

Behaviour of materials under the combined effects of high strains and high strain-rates

11th Technical Meeting, 1998
Dijon, France

MODELLING OF THE PERFORATION PROCESS ON METALLIC-CERAMIC MULTILAYER ARMORS

Karol JACH, Maciej MROCKOWSKI, and Robert ŚWIERCZYŃSKI

*Military University of Technology
2, Kaliskiego Street, 00-908 Warsaw 49, Poland*

I – INTRODUCTION.

In this paper the nonstationary, two-dimensional complex physical model and the results of computer simulations of tungsten rod perforation onto alumina-aluminium metallic-ceramic armor are presented. The models of tungsten, and aluminium are based on elastic-plastic theory [23,24,25] completed with Steinberg's constitutive models of materials [14,18,19] and model of cracking [6,2,12,21]. For ceramics the new approach to the processes of forming and growth of cracks is presented. In his papers [15,16] Steinberg describes a new constitutive model for fully dense ceramics. The main purpose of this paper is to present the modification of this model including alumina [1,3,4,5,13] with the original approach to the problem of the microcracks formation. Equations, describing the dynamics of microcracking, consider: fracture degree of the material, value of plastic strain and degree of exceeding beyond Hugoniot Elastic Limit (HEL)[1,3,20,22]. As a result of an increase of the degree of ceramic fracture the Steinberg's model has been modified to the model of porous, granular substance. It is interesting, that this model has been prepared with only a few "free" parameters.

Below we would like to present the usefulness of a complex physical model and a computer code HEFP [6] based on the "method of free particles" for modelling the perforation onto metallic-ceramic armor. This method, used earlier by authors in the numerical analysis of shape charge jet formation, explosively formed projectile and hypervelocity planetological impacts [6-11], gives vast possibilities in the analysis of wide spectrum of dynamic phenomena, where large deformations of the body occur. The method is very effective and convenient when initial or boundary conditions need to be changed.

II - PHYSICAL MODEL OF BEHAVIOUR OF CERAMICS UNDER HIGH DYNAMIC LOADING.

The model describing dynamic deformations of metals (the penetrator and the layer of the armor) is based on elastic-plastic theory [6-11,23,24]. It is supplemented with semi-empirical relations necessary for description of the behaviour of the metal under high dynamical loading:

-equation of state (EOS) [6,23,24],

-the Steinberg-Guinan model describing the behaviour of the yield strength [14,18-20],

- the model of cracks forming in the structure of metal [2,6,12,21,25],
- the model of the influence of cracks on yield strength and shear modulus [6,23,24],

In construction of the model describing the behaviour of ceramics the authors used information available in literature referring to the behaviour of the elastic-plastic/brittle materials. The model is based on elastic-plastic theory and includes conservative equations and constitutive relations:

$$(1) \quad \frac{d\rho}{dt} + \rho \nabla \cdot \vec{w} = 0$$

$$(2) \quad \rho \frac{d\vec{w}}{dt} = \nabla \cdot \hat{\sigma}$$

$$(3) \quad \rho \frac{dE}{dt} = \hat{\sigma} \cdot \nabla \vec{w}$$

$$(4) \quad \nabla S_{ik} = 2\mu \cdot \left(\dot{\varepsilon}_{ik} - \frac{1}{3} \dot{\varepsilon}_{ll} \delta_{ik} \right)$$

$$(5) \quad S_{ik} S_{ik} \leq \frac{2}{3} Y^2$$

here p is the pressure, ρ is density and E denotes the specific energy per unit mass.

The model is supplemented with the following models describing elastic-plastic/brittle characteristics of ceramics: (1) EOS, (2) the model describing the effect of the plastic strain rate, pressure, density and temperature on the yield strength, (3) the model of cracks forming in crashed ceramics.

EOS was adopted according to [2,6,23,24]:

$$(6) \quad p = K \cdot \left(\frac{\rho_s}{\rho_0} - 1 \right) + \gamma \rho_0 E$$

where K is the bulk modulus, ρ_0 is the initial density, ρ_s is the density of the solid phase. For $\rho < \rho_s$ K was assumed to be multiplied by $\frac{\rho}{\rho_s}$.

Temperature of ceramics is derived from the relation:

$$(7) \quad T = \frac{E - E_0}{3R}; \quad R = -\frac{E_0}{900}.$$

The model, describing elastic-plastic characteristics of ceramics including the modifications allowing to take into account the growth of cracks in the latter, is proposed as:

$$(8) \quad Y = \left[D \cdot (\dot{\varepsilon}^p)^n + Y_A \right] \left[G(V_C^*, \varepsilon^p, p^*) + A \cdot p \cdot \left(\frac{\rho_0}{\rho_s} \right)^{1/3} - B \cdot (T - 300) \right], \quad D \cdot (\dot{\varepsilon}^p)^n \leq Y_L :$$

$$(9) \quad \mu = \mu_0 \cdot \left[G(V_C^*, \varepsilon^p, p^*) + A \cdot p \cdot \left(\frac{\rho_0}{\rho_s} \right)^{1/3} - B \cdot (T - 300) \right],$$

$$(10) \quad \varepsilon^p = \frac{\sqrt{2}}{3} \left[(\varepsilon_{\pi\pi}^p - \varepsilon_{zz}^p)^2 + (\varepsilon_{\pi\pi}^p - \varepsilon_{\varphi\varphi}^p)^2 + (\varepsilon_{zz}^p - \varepsilon_{\varphi\varphi}^p)^2 + \frac{3}{2} (\varepsilon_{rz}^p)^2 \right]^{1/2}$$

The model enables to include the influence of yield strength, plastic strain rate, volume of cracks, density, pressure and temperature.

The function $G(V_C^*, \varepsilon^p, p^*)$ permits the transition from the Steinberg model for solid body [15,16,17] to the model of the crushed body of the "powder" type. The set of equations describing the dynamics of the growth of cracks volume is assumed like for metals with only the modification of liminal values for cracks formation in the medium.

$$(11) \quad \frac{dV_C}{dt} = -k_s \cdot \text{sign}(p) \cdot \left[|p| - \sigma_0 G(V_C^*, \varepsilon^p, p^*) \right] \cdot (V_C + V_{C0}), \quad \text{for} \quad |p| \geq \sigma_0 \frac{V_{C1}}{V_C + V_{C1}}$$

$$(12) \quad \frac{dV_C}{dt} = 0, \quad \text{for} \quad |p| < \sigma_0 \frac{V_{C1}}{V_C + V_{C1}}; \quad \text{and:} \quad \frac{1}{\rho} = V_C + \frac{1}{\rho_s},$$

where V_C is the volume of cracks per unite mass, V_C^* is the maximum volume of cracks, which appeared in the given element of the medium, p^* is maximum pressure, which appeared in the given element of the medium, ρ is the mean density.

Function $\sigma_0 G(V_C^*, \varepsilon^p, p^*)$ gives a current value of the liminal value of cracks growth for every element of ceramics. It is proposed as:

$$(13) \quad G(V_C^*, \varepsilon^p, p^*) = \frac{V_{C1}}{V_C^* + V_{C1}} \cdot F_1 \cdot F_2$$

where:

$$(14) \quad \begin{array}{ll} F_1 = 1 & \text{for } p^* \leq \sigma_{\text{HEL}} \\ F_1 = \left(\frac{\sigma_{\text{HEL}}}{p^*} \right)^{\alpha_1} & \text{for } p^* > \sigma_{\text{HEL}} \end{array}, \quad \text{and:} \quad \begin{array}{ll} F_2 = 1 & \text{for } \varepsilon^p \leq e^{kr} \\ F_2 = \left(\frac{\varepsilon^{kr}}{\varepsilon^p} \right)^{\alpha_2} & \text{for } \varepsilon^p > e^{kr} \end{array}$$

other notations: σ_{HEL} - HEL, ε^{kr} - critical value of the plastic strain after exceeding of which the damage of the ceramic structure occurs. Then, function $G(V_C^*, \varepsilon^p, p^*)$ defines liminal value which depends on: maximum value of cracks V_C^* , that appeared in the given element of the medium during the deformation, maximum pressure p^* that appeared anytime in the element of the ceramics, and plastic strain ε^p . Function G ranges from 1 (initial undamaged structure) to 0 (structure entirely destroyed). If in the Steinberg's formula for Y function G reaches 1 We obtain the original model for undamaged ceramics. If G equals 0, Steinberg's model changes into the model for the powder-type structure, for which $Y=0$ for $p<0$ and $Y>0$ for $p>0$.

The available materials data were based on literature [1,3,4,5,13]. The remaining data were found in the course of numerical experiments.

III - COMPUTER SIMULATIONS.

The set of differential equations and relations describing the properties of the materials, presented in a foregoing section with the relevant initial-boundary conditions have been solved numerically by means of what is referred to as a "method of free points". This method may be used for solving various non-stationary, two-dimensional problems of the continuous media. The scope of the present paper being limited, so we shall only present some examples of results concerning penetration of the projectile into ceramics-metal targets to illustrate the possibilities of our computer code.

In the Fig. 1. the comparison of computations with experimental data [26] is shown, for impact of tungsten rod from 25 mm APDS projectile at 1309 m/s onto a 20 mm alumina tile backed by a 19 mm aluminium plate. The examples above show possibilities of the application of the numerical code HEFP [6,10,11] to the modelling of the processes including large deformations of the affecting media, and the damages of their structure.

IV – CONCLUSIONS.

1. The results obtained in numerical simulations and presented in this paper demonstrate that it is possible to simulate, the processes of perforation of a metal backed ceramic target in by the "method of free particles".
2. The model for ceramic (alumina) is a modification of Steinberg's model of fully dense ceramics [14,15], and presents the new approach to modelling of the processes of forming and growing of cracks for the porous, granular substance.
3. The comparison with experimental data shows remarkable agreement . However, some problems related to precise determination of some of material constants used in the constitutive model and the model of cracks formation (e.g. ε^{kr} , V_{C0} , σ_0) still remain unsolved, mainly because there are not all necessary data available.
4. We can say that "method of free points", was found to be useful for explaining some interesting stages of the processes of perforation of metall-ceramic multilayer armor.

V – REFERENCES.

1. Ahrens T.J, W.H. Gust and E.B. Royce, Material strengths effect in the shock compression of alumina, J. Appl. Phys. 39, 1968, p. 4610.
2. Barbee T.W., Jr., L. Seaman, R. Crewdson, D. R. Curran, Dynamic fracture criteria for ductile and brittle metals, J. Mater., 7, 1972, p. 393.
3. Gust W.H. and E.B. Royce, Dynamic yield strengths of B₄C, BeO and Al₂O₃ ceramics, J. Appl. Phys. 42, 1971, p. 276.
4. Gust W.H., A.C. Holt, and E.B. Royce, Dynamic yield, compressional, and elastic parameters for several lightweight intermetallic compounds, J. Appl. Phys. 44 (2), 1973, p. 550.
5. Heard H.C. and C.F. Cline, Mechanical behaviour of polycrystalline BeO, Al₂O₃ and AlN at high pressure, J. Material Sci., 15, 1980, p. 1889.
6. Jach K., Modelowanie komputerowe zjawisk kumulacyjnych, WAT, Warszawa, 1990.
7. Jach K., E. Włodarczyk, Numerical simulation of multidimensional cumulation and driving problems of deformable bodies, J. Tech. Phys., 1986, 27, 1-2.
8. Jach K., E. Włodarczyk, Computer modelling of the target penetration process, J. Tech. Phys., 1991, 32, 1.

8. Jach K., E. Wlodarczyk, Computer modelling of the target penetration process, *J. Tech. Phys.*, 1991, 32, 1.
9. Jach K., E. Wlodarczyk, Solutions of the initial-value problems of the viscoplastic - nonstationary theory for the description shaped charge jet formation and target penetration, *Ballistics' 92*, Proceedings of 13th International Symposium on Ballistics, Stockholm, Sweden, June 1992.
10. Jach K., R. Swierczynski, E. Wlodarczyk, Computer simulation of the process of shaped charge jet formation and its penetration into armour, *Ballistics' 93*, Proceedings of 14th International Symposium on Ballistics, Quebec, Canada, September 1993.
11. Jach K., J. Leliwa-Kopystyński, M. Mroczkowski, R. Świerczyński and P. Wolański, Free Particle Modelling of the Hypervelocity Asteroids Collisions with the Earth, *Planetary and Space Science*, Vol.42, No. 12, pp.1123-1137, 1994.
12. Johnson J. N., Dynamic fracture and spallation in ductile solids, *J. Appl. Phys.* 52, 1981, p. 2812.
13. Lankford J., Comparative study of the temperature dependence of hardness and compressive strength in ceramics, *J. Material Sci.* 18, 1983, p.1666.
14. Steinberg D.J., Equation of state and strength properties of selected materials, Lawrence Livermore Nat. Lab. February 1991, UCRL-MA-106439
15. Steinberg D.J., Computer studies of the dynamic yield strength of ceramics, The 18-th International Symposium on Shock Waves, Sendai, Japan, July 21-26, 1991, p. C17.
16. Steinberg D.J., Computer studies of the dynamic strength of ceramics, *J. de Physique IV*, Coll. C3, Suppl. au Journal de Physique III, vol.1, Oct. 1991, p. C3-837.
17. Steinberg D.J., Computer studies of the dynamic strength of ceramics (II), *J. de Physique IV*, Coll. C8, Suppl. au Journal de Physique III, no 9, vol.4, Sept. 1994, p. C8-183.
18. Steinberg D.J., S.G. Cochran, M.W. Guinan, A constitutive model for metals applicable at high-strain rate, *J. Appl. Phys.* 51, 1980, p. 1498.
19. Steinberg D.J., C.M. Lund, A constitutive model for strain rates from 10^{-4} to 10^6 s^{-1} , *J. Appl. Phys.* 65, 1989, p. 1528.
20. Sternberg D.J., Material properties determining the resistance of ceramics to high velocity penetration, *J. Appl. Phys.* 65 (9), 1989, p. 3417.
21. Sugak S.G., G. I. Kanel, V. E. Fortov, A. L. Ni, B. G. Stelmah, Cislennoe modelirovanie dejstvia vzryva na zeleznuju plitu, *FGV*, 1983, 19, 20.
22. Tranchet J.-Y., A plasticity model for the shock-wave behaviour of pure aluminas, *J. de Physique IV*, Coll. C8, Suppl. au Journal de Physique III, no 9, vol.4, Sept. 1994, p. C8-289.
23. Wilkins M.L., Mechanics of penetration and perforation, *Int. J. Engng Sci.*, vol. 16, 1978, p. 793.
24. Wilkins M.L., Modelling the behaviour of materials, Structural impact and crashworthiness: Proc. Intern. Conf., London 1984, New York 1984, vol.2
25. Zukas J.A., T. Nicholas, H.F. Swift, L.B. Greszczuk, D.R. Curran, *Impact dynamics*, A Wiley - Interscience Publication, New York, 1982.
26. Briaies C., Cortes R., Zaera R., Martinez M.A., Sanches-Galvez V., An experimental and numerical study on the impact of ballistic projectiles onto ceramic/metal armours, *Ballistics' 95*, Proceedings of 15th International Symposium on Ballistics, Jerusalem, Israel, May 1995.

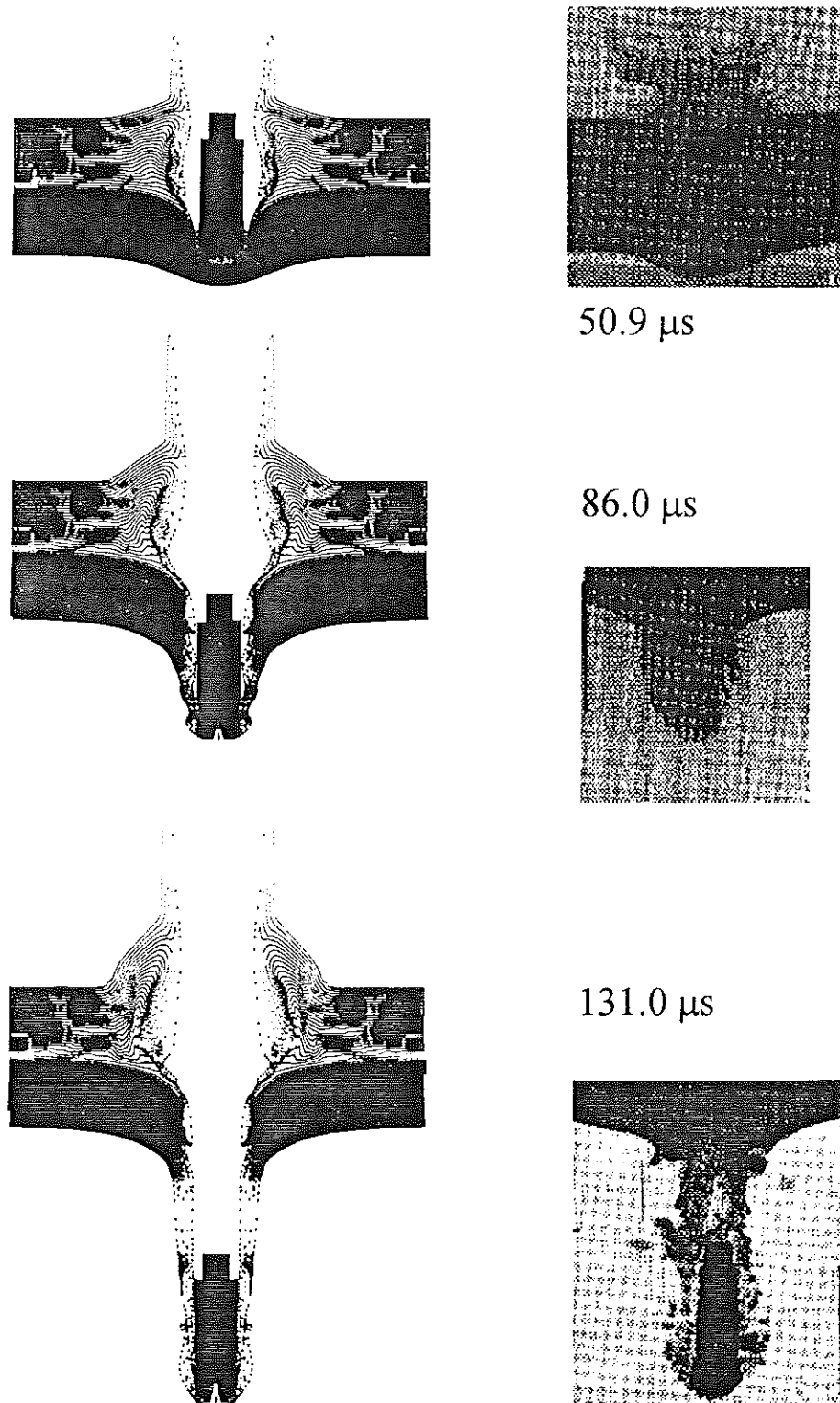


Fig.1. The comparison of computations with experimental data [26], for an impact of tungsten rod from 25 mm APDS projectile at 1309 m/s onto a 20 mm alumina tile backed by a 19 mm aluminium plate. Armor was completely perforated. Experiments were monitored by use a shadow-graph X-ray technique.

Validation of constitutive relations by comparing experimentation to calculation for elementary configurations

J. PETIT

DGA / DCE / Centre d'études de Gramat. 46500 Gramat, France.

I - INTRODUCTION

Numerical simulation has become an essential tool for designers who are able to test multiple options without resorting to as much experiments. Equally, numerical simulation is a privileged tool of physical analysis because it gives access to the evolution of non measurable parameters. The reliability of the results depends on the accuracy of the selected constitutive relations and particularly on that related to the behavior of inert materials.

Behavior modeling relies on a previous step of characterization. Tensile, compression, expansion or torsion tests provide stress-strain curves for different temperatures but for limited strain and strain rate ranges. The loading field reached in the numerical simulation of ballistics experiments corresponds to high strains ($\epsilon_p > 1$) with high strain rates ($\dot{\epsilon}_p > 10^4 \text{ s}^{-1}$) and the extrapolation of the models used has to be validated to justify their reliability in these domains. The aim of this work is to analyze two tools of validation which are the Taylor test and the electromagnetic cylindrical compression test. This work was performed on a conventional material : copper.

II - CHARACTERIZATION AND MODELING OF COPPER

The material used in this study is Cu-OFE-OK copper and is hot forged in rods (\varnothing 30 mm). The average grain size is 35 μm and the average hardness is 52 HV1. Compression tests (\varnothing 6 mm and 6-mm long samples) were performed at CTA for different strain rates and temperatures. The sampling of the stress-strain curves representative of each test condition gives a set of data σ , ϵ_p , $\dot{\epsilon}_p$ and T. The even low increase of temperature occurring during the adiabatic tests has been taken into account.

The experimental data were then processed to determine the coefficients of the different constitutive relations. The constitutive relations selected in this study are firstly the Johnson-Cook model [1] :

$$\sigma_y = \left(A + B\epsilon_p^n \right) \left(1 + c \text{Ln}\dot{\tilde{\epsilon}}_p \right) \left(1 - \tilde{T}^m \right) \quad (1), \text{ J-C 83}$$

$$\text{with } \dot{\tilde{\epsilon}}_p = \dot{\epsilon}_p / \dot{\epsilon}_0, \dot{\epsilon}_0 = 1 \text{ s}^{-1}$$

$$\text{and } \tilde{T} = (T - T_{\text{room}}) / (T_{\text{melt}} - T_{\text{room}})$$

and the Zerilli-Armstrong model in its original version for a cubic face centered material [2] :

$$\sigma_y = C_0 + C_2 \sqrt{\epsilon_p} \exp \left[\left(-C_3 + C_4 \ln \dot{\epsilon}_p \right) T \right] \quad (2), \text{Z-A 87}$$

These models are validated for moderate strains and strain rates ($\epsilon_p < 0.5$ and $\dot{\epsilon}_p < 10^4 \text{ s}^{-1}$) and are usually employed because they are implemented in numerous codes and the determination of their coefficients is easy. The counterpart of the simplicity of implementation of these models is the difficulty to represent with accuracy the behavior of a material in every domain of loading with a single formulation.

Different physical phenomena would need an enhancement of the models in view of a reliable extrapolation in the not well-known domain of high strains and high strain rates which is studied here. Zerilli and Armstrong proposed modifications of their initial relations as the case may be. A formulation has been developed to take into account the viscous displacement of dislocations between two obstacles [3] even if the strain rate corresponding to this phenomenon, $10^3 - 10^5 \text{ s}^{-1}$, and its importance remain controversial.

$$\sigma_y = 0.5 \sigma_{th} \left[1 + \sqrt{1 + 4 C_d \dot{\epsilon}_p T / \sigma_{th}} \right] + C_0 \quad (3), \text{A-Z 88}$$

$$\text{with } \sigma_{th} = C_2 \sqrt{\epsilon_p} \exp \left[\left(-C_3 + C_4 \ln \dot{\epsilon}_p \right) T \right]$$

Recently, another version of this constitutive relation has been proposed, in particular for tantalum materials, in order that the stress at 0 K does not increase indefinitely with the plastic strain since the defects density has to admit a limit [4]. In the case of a cubic face centered material, the relation (2) becomes :

$$\sigma_y = C_0 + C_2 \sqrt{\epsilon_r \left(1 - \exp(-\epsilon_p / \epsilon_r) \right)} \exp \left[\left(-C_3 + C_4 \ln \dot{\epsilon}_p \right) T \right] \quad (4), \text{Z-A 97}$$

A limited number of compression tests ($\epsilon_p < 0.5$ and $\dot{\epsilon}_p < 10^4 \text{ s}^{-1}$) which exhibit inevitably a spreading phenomenon does not allow the evaluation of the interest of relations (3) and (4) which particularities appear only at the boundaries of the characterization field. The use of suitable validation tests can only demonstrate the interest of these relations.

For each model, all the coefficients have been simultaneously optimized. The variation experimentation-model remains of the same order of magnitude for relations (1), (2) and (3). An example is given in figure 1. It shows the difficulty to adjust with accuracy a model to a set of data. For model (3), the coefficients have been optimized by fixing the value of C_d to 10 Pa, i.e. the value proposed in the initial paper [3]. The use of formula (4) reduces the difference between the experimental data and the model, particularly for the higher strains. Optimizing the coefficients leads to a value of ϵ_r equal to 0.75 which is entirely compatible with a saturation of the stress for a plastic strain equal to about 1.5-2 as observed by Taylor and Quinney [5].

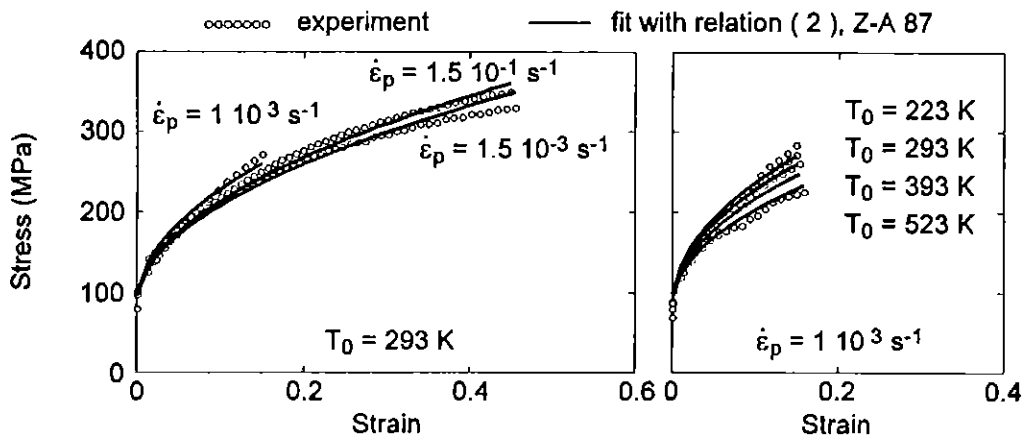


Figure 1. Comparison experiment - fitted relation (2) Z-A 87.

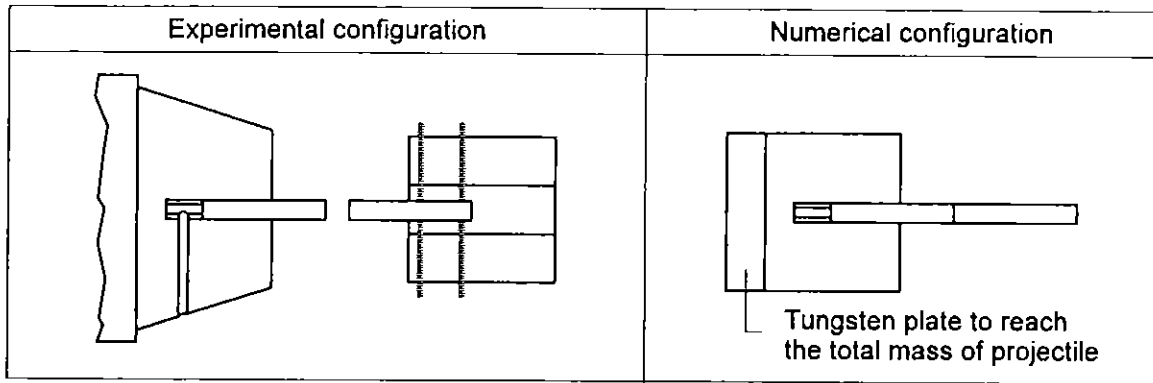


Figure 2. Taylor test configuration.

III - Validation tests

III - 1. Taylor test

The Taylor test is often used to validate constitutive relations from experimentation-simulation comparisons of the final shape of cylindrical test-pieces. The configuration used in this study is of symmetrical type : it avoids the problems of friction at interfaces which appear in the direct or inverse configuration cylinder-rigid wall. This configuration, developed by Erlich *et al* [6], is presented in figure 2.

The initial parameter of the numerical simulation is the impact velocity measured with a 1% accuracy. The initial shape of the soft-recovered cylindrical test piece was determined with a three-dimensional control equipment. The inaccuracy on the radius value is estimated to 0.05 mm by taking into account the accuracy of the measuring equipment and the circularity of the test-piece. The inaccuracy on the maximal diameter value at the interface is higher : it is estimated to 0.1 mm.

The impactor cylinder is set inside a Plexiglas block which ensures its behavior during the acceleration phase (figure 2). The block as well as the total mass of the projectile are taken into account in the numerical simulation (figure 2) even if their influence on the final shape of the target cylinder remains weak. The numerical simulation was performed with the hydrocode Ouranos [7] in its 2D Lagrangian version.

To reach the largest strains and strain rates possible, the impact velocity has to be the highest possible without any internal rupture nor ruptures at the periphery of the impact surface. A compromised is reached with an impact velocity of 275 m/s.

A comparison between experimentation and numerical simulations is illustrated in figure 3. The

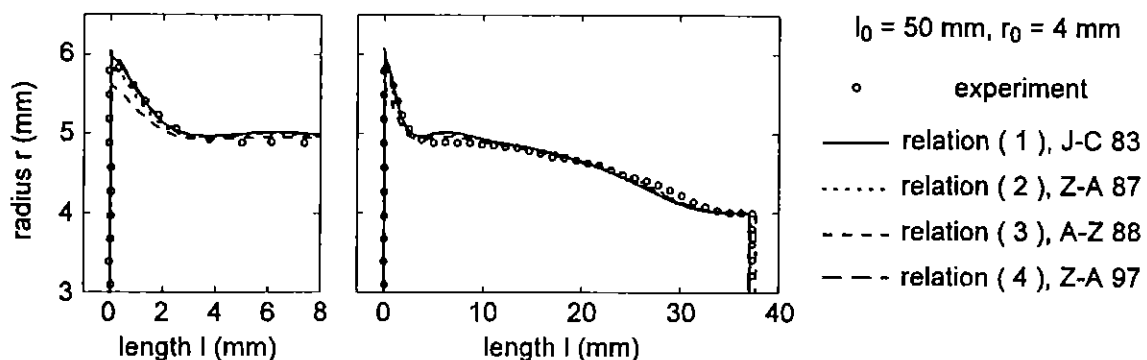


Figure 3. Taylor test results.

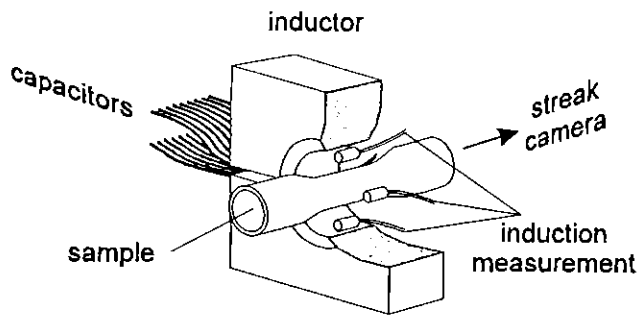


Figure 4.
Principle of the
electromagnetic cylindrical compression.

different models lead to neighboring and satisfying results for the major part of the cylinder which exhibits strains and strain rates lower than 0.5 and 10^4 s^{-1} respectively. Close by the interface, the strain can reach 1 most locally and the strain rate a few 10^4 s^{-1} . In this area, only model (3) gives results different from the others. The fast increase in stress as a function of the strain rate leads in this model to an overestimation of the stress and consequently to a significant underestimation of the test-piece radius.

III - 2. Test of electromagnetic cylindrical compression

The difference between the models (1, 2 or 4) is not easily revealed by the Taylor test. More, the validation domain reached in this test is limited as shown by the preceding results although obtained with copper, a ductile material. To reach higher strains and strain rates, a test of electromagnetic cylindrical compression has been developed at CEG in collaboration with a team of the Kurchatov Institute of Moscow [8, 9].

The principle of the experiment is presented in figure 4. A sample tube is placed at the center of a single-turn inductor through which a capacitor bank is discharged. The combination of the magnetic field to the current induced in the sample tube results in its cylindrical compression under the effects of Laplace forces. During the test, the magnetic field is recorded in four equidistant points. The evolution of the inner diameter of the sample as a function of time is controlled by a streak camera which slit is perpendicular to the inductor cut. As the magnetic field is slightly lower in the vicinity of the inductor cut (3-4 %), some defects of circularity are likely to appear in the final phase of the tube closure. A complementary recording with a frame camera ensures the control of the tube circularity and, if it is necessary, gives the usable running time of the test.

The input parameter of the numerical simulation is the magnetic field measured during the test. The measurement accuracy of the magnetic field is evaluated to 2 %. The numerical simulation is performed with the unidimensional fast dynamics code Unidim which involves the electromagnetic diffusion : it allows calculations of the electromagnetic forces and heating through Joule effect. A comparison of the experimental and simulated radius versus time curves provides the validation of the different constitutive relations in the reached loading field. The experimental measurement accuracy of the radius as a function of time has been evaluated to 0.05 mm.

Three different values of the tube wall thickness with an identical inner diameter of 18.6 mm were used to investigate different domains of loading (figure 5). The strains and strain rates are higher than those reached with the Taylor test and afford an investigation beyond the characterization domain of the compression tests presented in section II. The experimentation-simulation comparisons are shown in figure 6. For the lowest strain rates, the differentiation between the four models used here appears clearly after the phase of acceleration. Contrarily, it vanishes in the case of faster closure of the sample tube : in this case, the influence of the plastic work on the kinematics of the tube becomes insignificant. At the present time, it is the usable limit of this test.

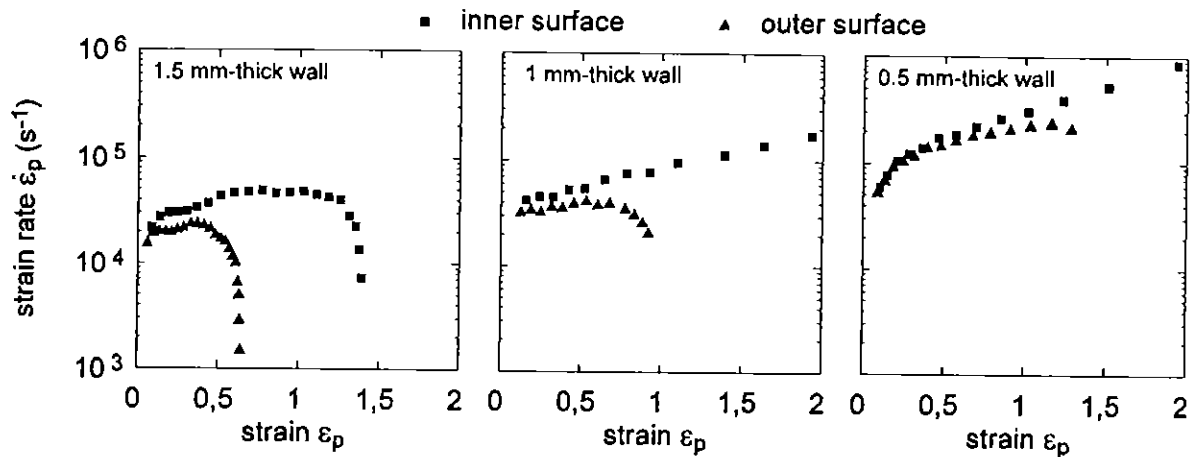


Figure 5. Strain rate and strain reached with electromagnetic cylindrical compression.

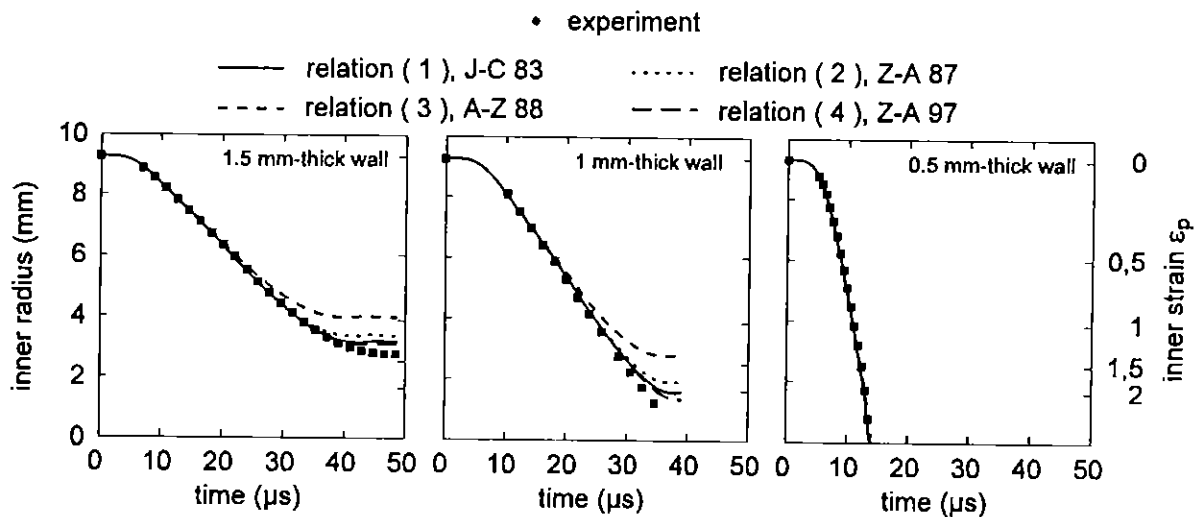


Figure 6. Constitutive relations evaluation. with electromagnetic cylindrical compression.

The test of electromagnetic cylindrical compression confirms that, for the copper material used in this study, it is not necessary to take into account the effects of the viscous displacements of dislocations for strain rates lower than 10^5 s^{-1} . More, it shows the interest to limit the increase of the athermal stress with the plastic strain to describe correctly the material behavior for high strains.

IV - Conclusion

Conventional tests of characterization cannot reach the domains of high strains and high strain rates which are characteristics of ballistics applications. The extrapolation of the existing models has to be validated to be used with confidence in this extreme domain. A test of electromagnetic cylindrical compression has been developed to be used as a tool of model validation by comparing experimentation to simulation. The first tests conducted on a copper material previously characterized in the usual domain of compression tests ($\epsilon_p < 0.5$, $10^{-3} < \dot{\epsilon}_p < 10^3 \text{ s}^{-1}$ and $223 < T < 523 \text{ K}$) show that :

- this test can validate models for strains higher than 1 and strain rates ranging from 10^4 to 10^5 s^{-1} , i.e. farther than with a test of Taylor. At the present time, the processing mode which is based on the evolution of the radius of the sample tube versus time impedes from

going beyond 10^5 s^{-1} . As a matter of fact, for higher strain rates, the plastic work becomes too low compared with the electromagnetic energy.

- in the particular case of the copper material tested in this study, there is no abrupt increase of stress for strain rates up to 10^5 s^{-1} . Moreover, a saturation effect of the athermal stress as a function of the plastic strain seems to enhance the accuracy of the model for high strains.

Acknowledgments

The author would like to thank P. Longère of CTA for the performing and processing of the compression tests, A. Halgand and Y. Sarrant of CEG for the performing of the electromagnetic cylindrical compression tests and of the Taylor test, Y. Lagarde of CEG and F. Gil of CISI for their help in the numerical simulation of the Taylor test.

References

- [1] G.R. Johnson, W.H. Cook. "A Constitutive Model and Data for Metals Subjected to Large Strains, High Strain Rates and High Temperatures". Proceedings of the 7th International Symposium on Ballistics, The Hague, pp 541-547, 1983.
- [2] F.J. Zerilli, R.W. Armstrong. "Dislocation-mechanics-based constitutive relations for material dynamics calculations ". J. Appl. Phys., Vol.61, No.5, pp 1816-1825, 1 March 1987.
- [3] R.W. Armstrong, F.J. Zerilli. "Dislocation mechanics based analysis of materials dynamics behavior ". Journal de Physique Colloque C3, Supplément au n° 9, Tome 49, pp C3-529 à C3-534, septembre 1988.
- [4] F.J. Zerilli, R.W. Armstrong. "Dislocation Mechanics Based Constitutive Equation incorporating Dynamic Recovery and Applied to Thermomechanical Shear Instability". Paper submitted to the American Physical Society 1997 Conference "Shock Compression of Condensed Matter", Amherst, Massachusetts, July 27-August 1, 1997.
- [5] G.I. Taylor, H. Quinney. "The Latent Energy Remaining in a metal after Cold Working". Proc. Roy. Soc. N° A143, pp 307-326, 1934.
- [6] D.C. Erlich, D.A. Shockey, L. Seaman. "Symmetric Rod Impact for Dynamic Yield Determination". Shock Waves in Condensed Matter-1981, AIP Conference Proceedings, Series Ed. H.C. Wolfe, Number 78, pp 402-406, 1982.
- [7] H. Jourden, J.-M. Sibeaud, M. Adamczewski-Cauret. "Logiciel Ouranos : présentation générale et utilisation en détonique". Revue Scientifique et Technique de la Défense, N° 4, pp 51-58, 1995.
- [8] J. Petit, Yu.A. Alexeev, S.P. Ananiev, M.N. Kazeev. "Compression of Metallic Tubes in Pulsed High Magnetic Fields to Test Behavior Modeling at High Strain Rate". To be published in the Proceedings of the Seventh International Conference on Megagauss Magnetic Field Generation and related Topics, Sarov (Arzamas-16) Russia, August 5-10, 1996.
- [9] J. Petit, Y.A. Alexeev, S.P. Ananiev, M.N. Kazeev. "The Electromagnetic Cylindrical Compression : a Tool to Test Behavior Modeling under Large Strain at High Strain Rate". pp C3-109 C3-114, J. Phys. IV France 7, Colloque C3, Supplément au Journal de Physique III d'août 1997.

Influence of precipitations on the dynamic ductility of aluminium alloy AA7075

M. BRODMANN and E. EL-MAGD

LFW Department of Material Science, RWTH Aachen University of Technology, 52062 Aachen, Germany

I INTRODUCTION

Under quasi-static loading, strain hardening causes an increase of force and acts to stabilise to the deformation process while the reduction of area as a destabilising influence decreases the force. In the case of dynamic loading, four additional influences on the ductility of the material have to be taken into consideration. With rising deformation rate, the strain rate sensitivity increases leading to an increase of the local value of the flow stress in the neck zone and acts to stabilise the deformation. On the other hand the adiabatic character of the deformation process reduces the flow stress and promotes instability. Mass inertia forces in the lateral direction arising in connection with the radial acceleration due to the reduction of area cause the initiation of either lateral tensile or lateral compressive stresses depending upon the time function of specimen elongation. Lastly, with increasing strain rate the local failure strain decreases resulting in a higher notch sensitivity under dynamic loading than under quasi-static conditions.

II INCREASED STRAIN RATE AND DUCTILITY

The influence of material parameters and deformation conditions on ductility and mechanical stability in the case of tension tests can be discussed by using the theory of imperfections. Local diameter deviations of a cylindrical test bar are found to cause non-uniform deformation by growing during the tension test. At the beginning of deformation the local stress at the narrowest cross-section is first slightly higher than in other regions. Beginning with plastic deformation, the smallest diameter decreases more than the others and leads to neck formation [1][2]. The adiabatic character of the deformation process promotes this effect because higher deformed regions are more softened by the deformation heat. However, the appearance of neck formation leads to an increased local value of strain and strain rate leading to higher local flow stress so that other specimen regions undergo additional deformation. In the case of dynamic loading with strain rates higher than 2000 s^{-1} , the influence of strain rate is given by a linear relation $\sigma = \sigma_h + \eta \dot{\epsilon}$ according to the damping mechanism. The strain rate influence can be studied quantitatively simply by considering a test bar, whose cross-sectional area is not constant along the gauge length but is given by $S_0 = S_{\min}[1 + \alpha(x)]$, where $\alpha(x)$ could be represented by a parabolic function. The material behaviour is described by

$$\sigma = [K(B + \epsilon)^n + \eta \dot{\epsilon}] \exp \left[-\beta \frac{(T - T_0)}{T_m} \right], \quad (1)$$

with the material constants B , K and η . T_m , T_0 and T are the absolute melting point, room temperature and actual temperature. β is a material constant which can be set for most of the materials to 3 [3]. Assuming that the deformation energy is partly transferred to heat during a dynamic deformation process and the remaining part is consumed by increasing the internal energy e.g. due to dislocation multiplication, the temperature increases by $dT = \kappa\sigma / (\rho_d c) d\varepsilon$ where $\kappa = 0.9$ represents the fraction of energy transferred to heat and where ρ_d and c_m are the density and the specific heat capacity of the material. With the dependency between the flow stress and temperature according to equation (1) the increase of temperature can be determined as a function of strain by integration. The stress-strain relation for an adiabatic tensile test results from the substitution of the temperature:

$$\sigma_{ad} = \frac{K(B + \varepsilon)^n + \eta\dot{\varepsilon}}{1 + a \int [K(B + \varepsilon)^n + \eta\dot{\varepsilon}] \dot{\varepsilon} dt}, \quad (2)$$

with $a = \kappa\beta / (T_m \rho_d c)$. The force $F = \sigma_{ad} S_0 \exp(-\varepsilon)$ is equal for any cross-section of the specimen so that the strain at any arbitrary cross-section is given by numerical solution of the relation

$$\frac{K(B + \varepsilon)^n + \eta\dot{\varepsilon}}{1 + a \int [K(B + \varepsilon)^n + \eta\dot{\varepsilon}] \dot{\varepsilon} dt} \exp(-\varepsilon) = \frac{S_1}{S} \frac{K(B + \varepsilon_1)^n + \eta\dot{\varepsilon}_1}{1 + a \int [K(B + \varepsilon_1)^n + \eta\dot{\varepsilon}_1] \dot{\varepsilon}_1 dt} \exp(-\varepsilon_1), \quad (3)$$

where ε_1 , $\dot{\varepsilon}_1$ and S_1 means the strain, strain rate and cross-section area in the smallest cross-section.

For lower deformed regions elastic unloading has to be considered after reaching the maximum load. The global extension results from the integration of $[\exp(\varepsilon) - 1]$ over the total length of the specimen so that the relation between force and elongation can be calculated. The influence of the material parameters η/K (a), n (b) and $a \cdot K$ (c) in equation (3) is represented in **Figure 1**.

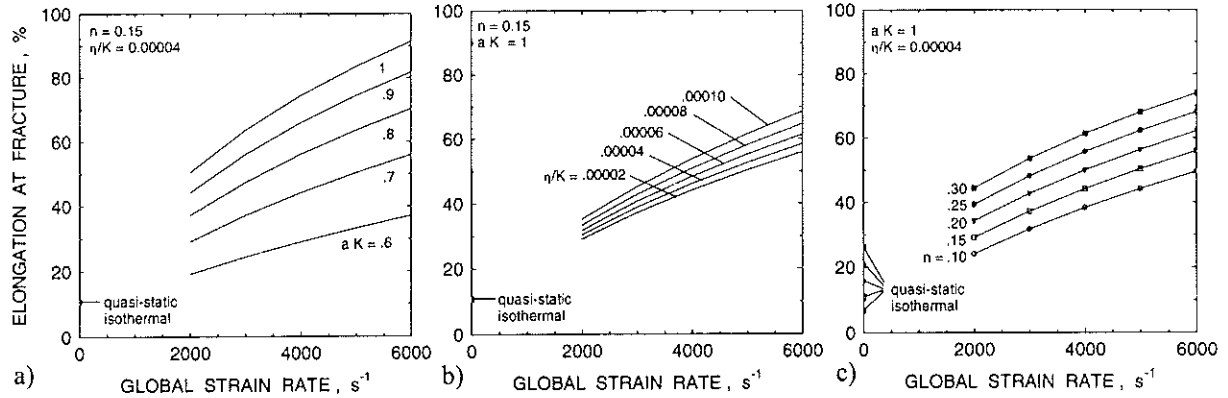


Figure 1: Influence of the material parameter a) $a \cdot K$, b) η/K and c) n on the elongation at fracture of a specimen having a parabolic profile with a maximum diameter deviation of 4%

Figure 2a shows the experimental and computational example of a tensile specimen with a maximum diameter deviation of 4% of the steel 42 CrV 6 using equation (3). A lot of other materials can be described just as well as it is represented in **Figure 2b**. But tensile tests with the aluminium alloy AA7075 shows, that its material behaviour deviates from that described with equation (3) (**Figure 2c**). Therefore other influences have to be discussed (see paragraph IV).

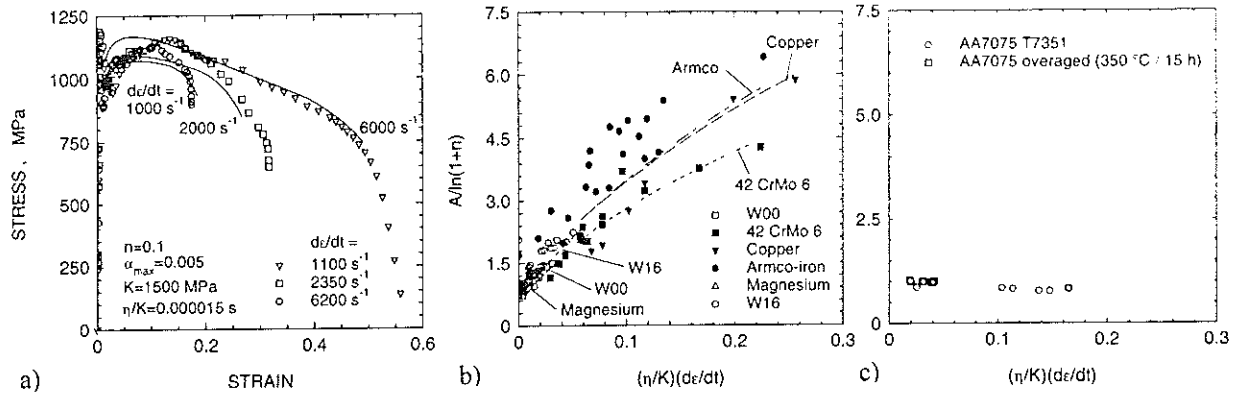


Figure 2: a) Experimental (markers) and computational (curves) results for different strain rates for a tensile specimen of steel 42 CrV 6 [4]
b) Experimental (markers) and computational (dashed lines) results for different materials [4]
c) Experimental results for aluminium alloy AA7075 in two heat treatment conditions

III CONDITIONS FOR DUCTILE FRACTURE

Ductile fracture usually starts in material regions with a high local strain and a high hydrostatic tension. Therefore the failure criterion is defined by the local failure strain $\varepsilon_f(\sigma_m / \bar{\sigma})$ as a function of the ratio between the local mean stress σ_m and the local equivalent stress $\bar{\sigma}$. Such a criterion is deduced considering that ductile fracture occurs due to nucleation, growth and coalescence of micro-cavities [5]-[7]. The rate of void growth can be determined as a function of $(\sigma_m / \bar{\sigma})$ by applying the theory of plasticity. A closed-form analytical solution for the rate of growth of cylindrical cavities with an elliptical cross-section in a strain-hardening material as a function of $(\sigma_m / \bar{\sigma})$ was inferred by McClintock [8]. Rice and Tracy [9] deduced the relation for the rate of change of the radius of a spherical void in an ideal plastic material. Using this modified relation Hancock and Mackenzie [5] introduced their failure criterion

$$\varepsilon_f = \varepsilon_n + \alpha \exp\left[-\frac{3\sigma_m}{2\bar{\sigma}}\right], \quad (4)$$

where the failure strain ε_f is given as a sum of the strain up to the nucleation of voids ε_n depending mainly on the purity of the material and the strain between void nucleation and fracture. Combined experimental and computational investigations [10] showed a great influence of the volume fraction of inclusions so that the factor 3/2 should be replaced by a material constant depending on inclusions.

Equation (4) was deduced for ideal plastic materials, but was also used for deformation conditions that do not hold assumption. Johnson and Cock [11] introduced correction factors considering influences of strain rate and temperature to apply equation (4) to the range of high strain rates.

For non-linear visco-plastic behaviour of a strain-hardening and -sensitive material the relation

$$\bar{\sigma} = \sigma_h + K\varepsilon^n \left(\frac{\dot{\varepsilon}}{\dot{\varepsilon}^*}\right)^m : \quad \frac{1}{R} \frac{dR}{d\varepsilon} = \frac{1}{2} \left[\frac{3(m+n)}{2(1-f^{m+n})} \frac{\sigma_m}{\bar{\sigma} - \sigma_h} \frac{2}{3} \sigma_h \ln\left(\frac{1}{f}\right) \right]^{\frac{1}{m+n}} \quad (5)$$

was deduced [12], where f is approximately equal to the volume fraction of voids in the material. Presuming pure viscous behaviour for very high local values of strain rate as in the neck or at a notch root for impact loading, σ_h can be ignored so that with $m = 1$ as a special case and for $f \ll 1$ the failure criterion for dynamic ductile fracture reads:

$$\bar{\sigma} = \eta \dot{\epsilon} : \quad \epsilon_f \approx \epsilon_n(\dot{\epsilon}, T) + \frac{\alpha}{(\sigma_m / \bar{\sigma})}. \quad (6)$$

Figure 3 shows the results of a FEM simulation of different notched specimen of iron and steel. Using the experimentally determined extension of the specimen at fracture, the corresponding values of $\bar{\epsilon}$ and $(\sigma_m / \bar{\sigma})$ are computed for different values of the radius in the narrowest cross-section and are represented as a continuous curve for each geometry (**Figure 3a**). The resulting failure criterion for quasi-static and dynamic loading of each material is represented in **Figure 3b**.

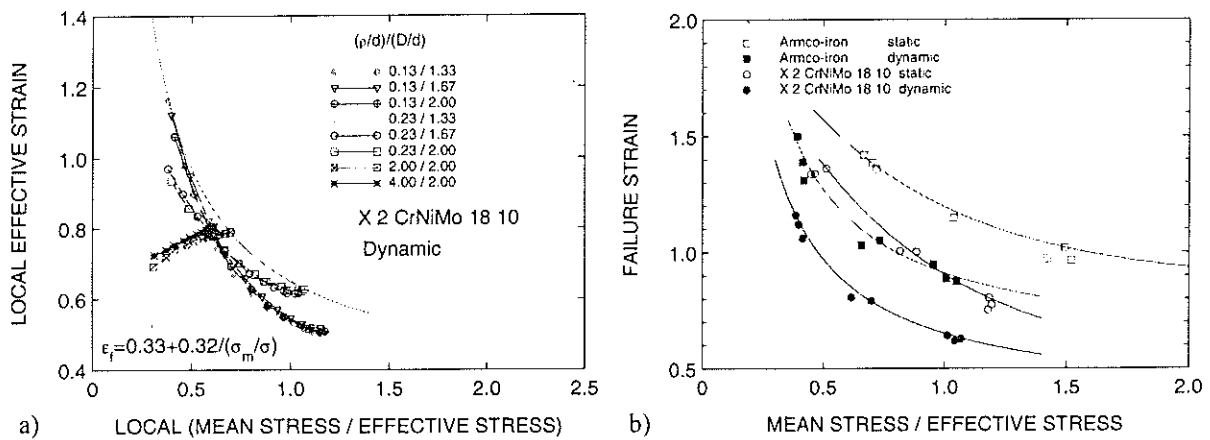


Figure 3: a) Local effective strain as a function of the ratio of the hydrostatic stress to the flow stress along the specimen radius at the narrowest cross-section of the austenitic steel X 2 CrNiMo 18 10 [12]
 b) Failure criterion for ductile fracture under quasi-static and dynamic loading of iron and austenitic steel [12]

IV BEHAVIOUR OF ALUMINIUM ALLOY AA7075

Quasi-static and dynamic tensile tests were carried out on specimens of aluminium alloy AA7075 in two heat treatment conditions: the T7351 condition (**Figure 4a**), which means a precipitation hardened material, and an overaged condition (**Figure 4b**), where the material is aged for 15 hours at a temperature of 350 °C. With an image analysing system the size and fraction of precipitations within the material in these two conditions could be determined. The precipitation hardened material shows a disperse distribution of smallest particles within the grain and at the grain boundaries having a mean size of 10 μm^2 with an area fraction of 2.4 %. The particles in the overaged condition have grown up to a mean size of 27 μm^2 with an area fraction of 1.3 % and are placed mainly on the grain boundary. The dynamic tests were carried out by using a horizontal Split-Hopkinson bar arrangement with a pneumatic acceleration unit. The experimental results of the tensile tests for the two heat treatment conditions show, that the stress reduction with increasing deformation is much higher than it could be described just with the influence of deformation heat. One explanation for this behaviour is the assumption of successive structural damage during the deformation process. The influence of damage on the flow curve can be taken into consideration by the introduction of a damage function $f(D)$:

$$\sigma = [K(B + \epsilon)^n + \eta \dot{\epsilon}] \exp\left[-\beta \frac{T - T_0}{T_m}\right] \cdot f(D). \quad (7)$$

$f(D)$ accounts for a reduction of the effective cross-sectional area due to increasing damage. Therefore this function is represented by $f(D) = 1 - D$. The damage parameter $D = D(\epsilon)$ can be assumed to increase with increasing deformation e.g. due to nucleation and growth of microcavities around inclusions and initiation of microcracks within the material. According to the increase of temperature $dT = \kappa \sigma / (\rho_d c) d\epsilon$ equation (7) leads to the relation

$$\int \exp\left(\beta \frac{T - T_0}{T_m}\right) dT = \frac{\kappa}{\rho_d c T_m} \int \{ [K(B + \epsilon)^n + \eta \dot{\epsilon}] \cdot (1 - D(\epsilon)) \} d\epsilon, \quad (8)$$

that allows the formulation of the adiabatic stress in consideration of damage

$$\sigma_{ad} = \frac{[K(B + \epsilon)^n + \eta \dot{\epsilon}] \cdot (1 - D(\epsilon))}{1 + a \int \{ [K(B + \epsilon)^n + \eta \dot{\epsilon}] \cdot (1 - D(\epsilon)) \} \dot{\epsilon} dt}. \quad (9)$$

For the determined aluminium alloy AA7075 T7351 the damage parameter $D(\epsilon)$ is found to be:

$$D(\epsilon) = 0.3 \left\{ 1 - \exp\left[-\left(\frac{\epsilon}{\epsilon^*}\right)^4\right] \right\}, \quad (10)$$

with $\epsilon^* = 0.05$ for the precipitation hardened condition T7351 and $\epsilon^* = 0.15$ for the overaged condition. In consideration of this damage function and the theory of imperfections using equation (9) the computational results for aluminium alloy AA7075 are represented in **Figure 4a** for the T7351 heat treatment condition and in **Figure 4b** for the overaged material. To justify the implementation of such a damage function the presence of damage has to be indicated. **Figure 5** shows the result of a light microscopical interference investigation of a dynamically deformed etched tensile specimen of the aluminium alloy AA7075 in the T7351 condition. Additionally to the main crack within the material there are other inter- and transcrystalline cracks initiated under participation of particles.

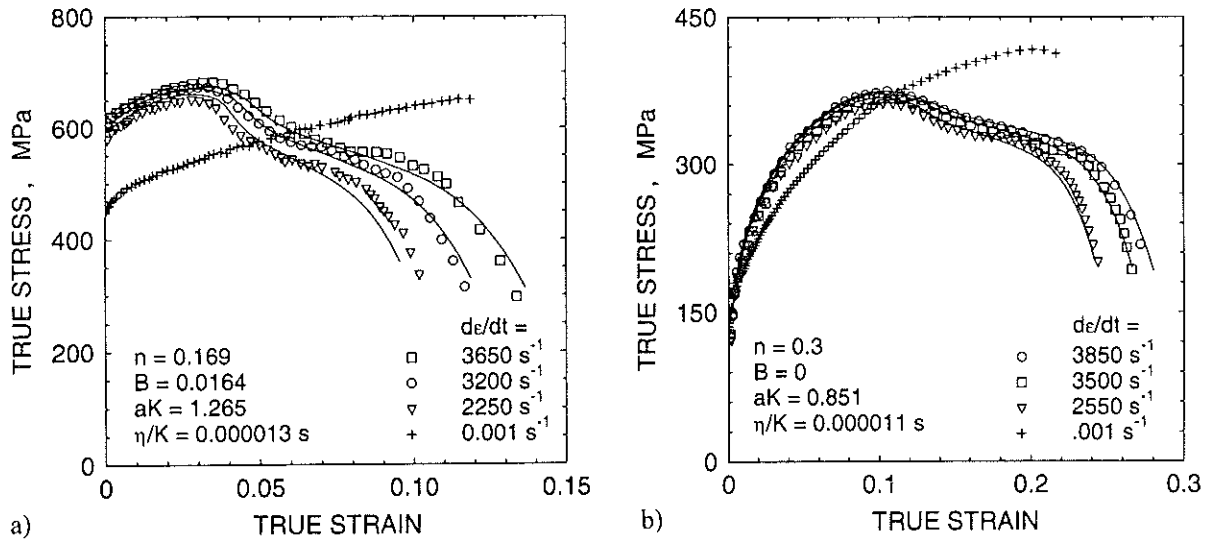


Figure 4: Experimental and computational results at different mean strain rates $d\epsilon/dt$ for a specimen with a maximum diameter deviation of 4% in consideration of damage of aluminium alloy AA7075 a) in the precipitation hardened condition T7351 and b) in the overaged condition (350 °C / 15 h)

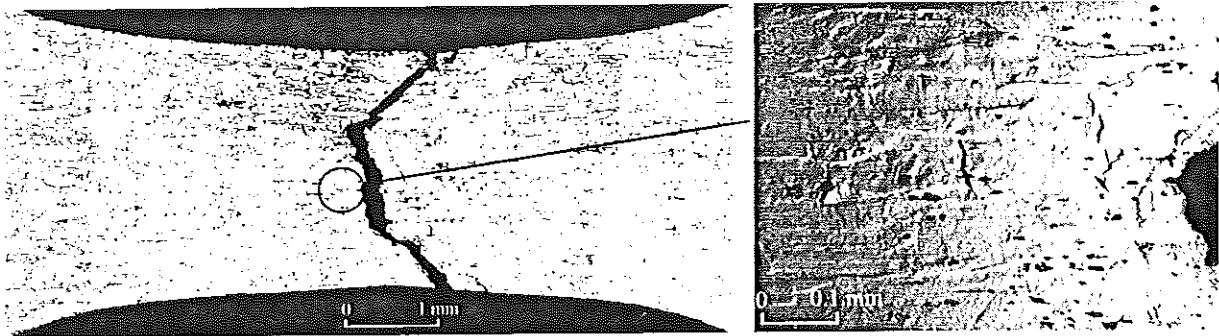


Figure 5: Damage within a dynamically deformed specimen of aluminium alloy AA7075 T7351
 a) overview of a longitudinal ground, polished and etched section of a broken specimen (left)
 b) Magnification of damaged area (interference contrast micrograph, right)

V CONCLUSIONS

With impact loading the strain rate sensitivity increases with rising strain rate. As neck formation occurs the local strain rate increases and stabilises the deformation process although the increase in temperature caused by the adiabatic character of the deformation process reduces the stress. However the notch sensitivity ascends with higher strain rates. With aluminium alloy AA7075 the stress reduction under impact loading is much higher than it could be described by the influence of deformation heat as strain dependent damage has to be taken into account. There precipitations are often the origin for nucleation and growth of voids leading to inter- and transcrystalline cracks additional to the main crack within the specimen which causes a decreased elongation at fracture.

VI REFERENCES

- [1] El-Magd, E.: *Materialprüfung* 15(1973), pp. 90-95
- [2] El-Magd, E.: *Archiv Eisenhüttenwesen* 45(1974), pp. 83-89
- [3] El-Magd, E.: *J. Phys. IV, suppl. J. Phys. II*, 4(1994), pp. 149-170
- [4] Weisshaupt, H.: *Dr.-Ing. Diss., Aachen*, 1995
- [5] Hancock, J.W., Mackenzie, A.C.: *J. Mech. Phys. Solids* 24(1976), pp. 147-169
- [6] Needleman, A.; Tveergard, V.: *J. Mech. Phys. Solids* 32(1984), pp. 461-490
- [7] Tveergard, V.; Needleman, A.: *J. Mech. Phys. Solids* 34(1986), pp. 213-241
- [8] McClintock, F.A.: *J. Appl. Mech.* 35(1968), pp. 363
- [9] Rice, J.R.; Tracy, D.M.: *J. Mech. Phys. Solids* 17(1969), pp. 201-217
- [10] Holland, D.; Halim, A.; Dahl, W.: *Steel Research* 61(1990), pp. 504-506
- [11] Johnson, G.R.; Cook, W.H.: *Eng. Fract. Mech.* 21(1985), pp. 31-48
- [12] El-Magd, E.: *Steel Research* 68(1997) No. 2, pp. 67-71

Fracture analysis in a multidimensionnal lagrangian hydrodynamics code : Application to spalling

F.DUFOUR

CEA, BP.12, 91680 Bruyères-Le-Chatel France

INTRODUCTION

Much progress has been made in the understanding of the processes leading to dynamical fracture of metals. Thus, models describing dynamical fracture ([1], [2], [3], [4],...) now make it possible to account for some experimental results (simple traction, ring expansion, spalling...). However, these models are often adapted to a given type of loading, even if one can note some research works towards more comprehensive models, notably for ductile fracture [5].

But the lack of such a unique modelling makes rather hazardous each attempt for the prediction - even qualitative - of results obtained for combined loadings.

In the field of multi-dimensionnal hydrodynamics involving shock waves in metals, an other problem lies in the numerical treatment of fracture in hydrodynamics codes, and that of the recovery of a fully damaged metal. Indeed, common treatments chosen for unidimensionnal (1D) codes are difficult to adapt to multidimensionnal codes.

As a consequence, we have opted at first for a simple treatment, compatible with the multidimensionnal hydrodynamics codes we use, and with well known fracture models and criterions. After the presentation of the treatment, a brief assessment shows its interest compared to similar approaches (see [6]). Finally, we use it in the calculation of an experiment of dynamic fracture through spalling, and the results are compared to experimental data.

1 DESCRIPTION OF THE FRACTURE TREATMENT

A treatment commonly used for fracture in unidimensionnal codes consists in creating a void between two cells of a material which state locally fills a given criterion. In multidimensionnal schemes, we have extrapolated this treatment by using local remeshing algorithms, in order to make the expected fracture surfaces correspond as nearly as possible to mesh surfaces [7]. Unfortunately, we have not been able to generalize this method to the treatment of a subsequent contact between the created surfaces (in the case of a recovery of a spalled sample for exemple). This is why we have opted for a less complex method through a cell treatment keeping the initial mesh.

In hydrodynamics shock waves, in which we are mostly interested, a lagrangian (or ALE) scheme is more adapted than an eulerian one. That is why we will give the detailed implementation of our treatment in a lagrangian code.

1.1 Fracture

The surfaces created by the fracture in a mesh cell are supposed to be the mesh surfaces around each "fractured cell". So, this cell is treated as if containing void. Consequently, we impose that its pression and deviatoric stresses equal zero, as well as its artificial viscosity - important point which we will emphasize later. Thus, we no longer use the equation of state of the compact material - or damaged material - for the "fractured cells". It is to be noted that such a treatment is compatible with any fracture criterion based on pressure, deviatoric stresses and plastic or total strains.

1.2 Recovery

We suppose that the material of the "fractured cells" passes again at its thermodynamic state at fracture. We also consider that it then follows its prior thermodynamic and elasto-plastic properties (no history damage): the equation of state and constitutive laws are used again.

However, the material of the fractured cell is not considered recovered until its pression goes positive again. This description is again compatible with any of the criterions listed before.

1.3 Implementation in a lagrangian hydrodynamics code

During the treatment of a "fractured cell", we let its density - given by the equation of momentum - evolve freely. We store the thermodynamic state of the material at the time when the fracture criterion is reached. It is used when the cell density equals again its value at fracture (no damage history).

2 COMPARISON WITH COMMON 1D TREATMENT

The chosen common 1D treatment is the one described at the beginning of the previous chapter. It is used in order to show that the shift due to our cell treatment is small - with fine enough meshes.

For that purpose, we have calculated the spalling obtained from the plate impact of a polyethylen/copper(1mm thick) flyer launched at 875 m/s on a copper(2mm thick)/LiF target. The time origin is the instant of impact. The criterion used is a threshold for the principal tensile stress, which value (see [8]) is 12 kbar. The comparison on figure 1 shows that the velocities of the Copper/LiF interface computed with both methods are identical, and that our treatment describes the fracture quite well.

The influence of the annulation of the artificial viscosity of a "fractured cell" is to be noticed. Indeed, the formulation of the artificial viscosity we use consists of space derivatives of velocity components (through gradient or divergence terms). This introduces a term

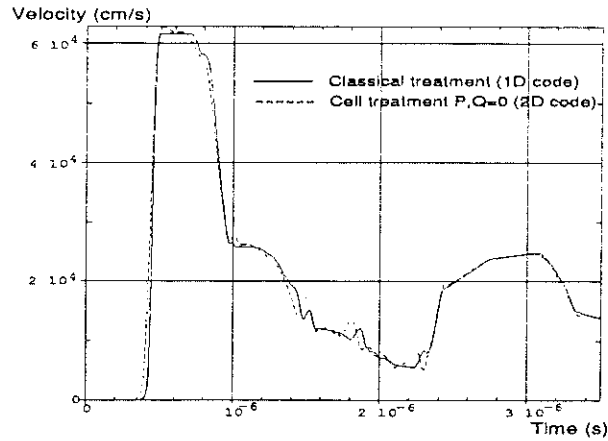


FIG. 1 - Velocity of the copper/LiF interface with two treatments for the fracture

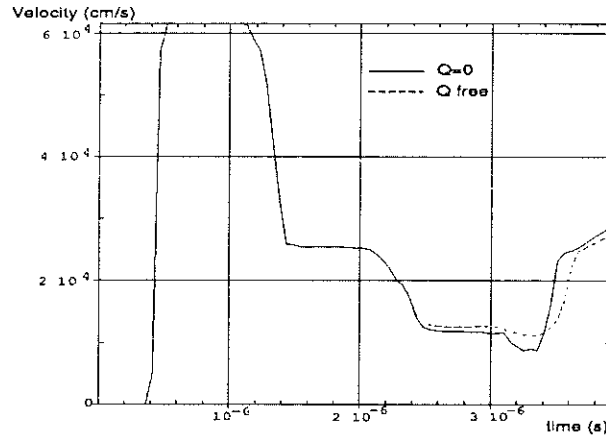


FIG. 2 - Influence of the treatment of the artificial viscosity Q

equivalent to a pressure in the discretized hydrodynamics equations, as soon as the cell is compressed. This term leads to an early compression and recovery, which can be seen on the velocity curves (see figure 2). Starting at about $1.35 \mu\text{s}$, this unphysical compression is clear at around $2 \mu\text{s}$. By zeroing this term, we agree with the result from the common treatment. We can now try to calculate a bidimensionnal spall experiment.

3 CALCULATION OF A 2D SPALL EXPERIMENT

In the experiment we want to reproduce numerically, spalling is obtained in the copper sample of a stainless steel/copper bicouche, launched by a high explosive. The precise geometry of the edifice is shown on figure 3. The velocity of the axial part of the free surface has been measured by means of doppler laser interferometry. It shows a velocity step characteristic of spalling (full fracture) without subsequent recover of the copper (figure 4).

A particular care has been brought into the calculation conditions (mesh, artificial vis-

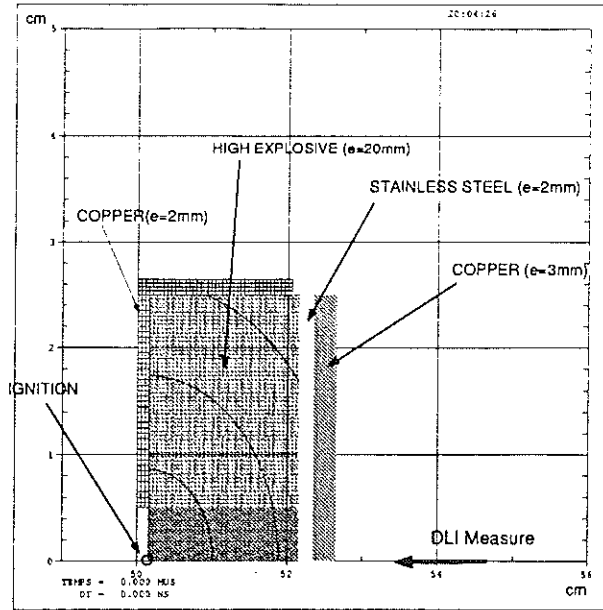


FIG. 3 - Geometry of the bidimensionnal experiment, with thicknesses e

cosity,...). These have been obtained through bidimensionnal calculations of the previous experiment, and make it possible to obtain a proper calculation of the shock waves.

By using the spall stress of the copper from plate impact experiments, the value of the calculated velocity step is higher than the experimental one. A spall stress of 40 kbar is needed to reproduce the data (see figure 4). We note oscillations around the velocity step - due to waves in the external fragment of copper, which are not found in the experiment. Moreover, the calculation suggests a multiple spalling of the copper, starting from its free surface and progressing back into the sample, as already mentioned in [4]. The bidimensionnal spreading of the spall planes at $5 \mu\text{s}$ is illustrated on figure 5, where the fractured cells - of very low density - are marked with daggers.

The use of the Johnson model makes it possible to get a more progressive relaxation of the stresses and thus eliminates the previous oscillations in the computed velocity. It confirms a multiple spalling of the copper, but its development differs from the previous one obtained with tensile threshold criterion. Moreover, the parameters from [4] - which enable us to fit properly measures from unidimensionnal experiments of plate impact [9] - do not reproduce exactly the experimental value of the velocity step. A lowering - even strong - of the porosity at spall (here equal to 30 %, from [4] and [5]) is not sufficient to obtain the proper velocity step.

However, on account of the complex phenomena involved in that experiment and their modelling (equation of state of detonation products, initiation of the detonation, constitutive laws,...), and because of too few measures (no stress measures, analysis of the sample after test,...), it seems difficult to put into question a particular point of the fracture models to account for this slight shift.

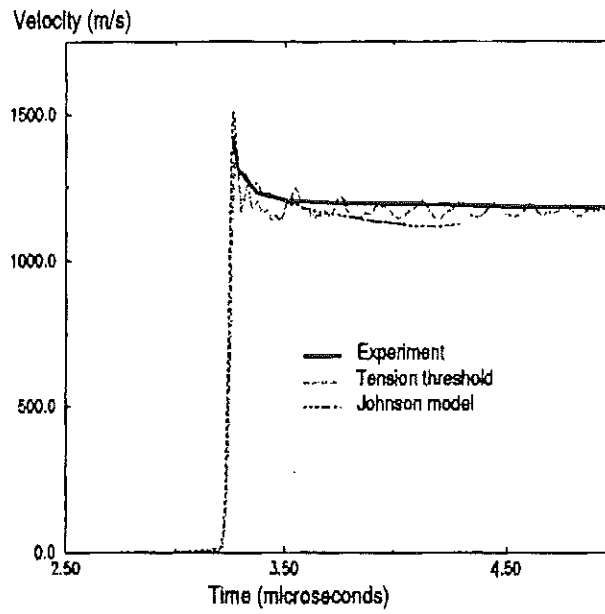


FIG. 4 - Comparisons between calculations and experimental results

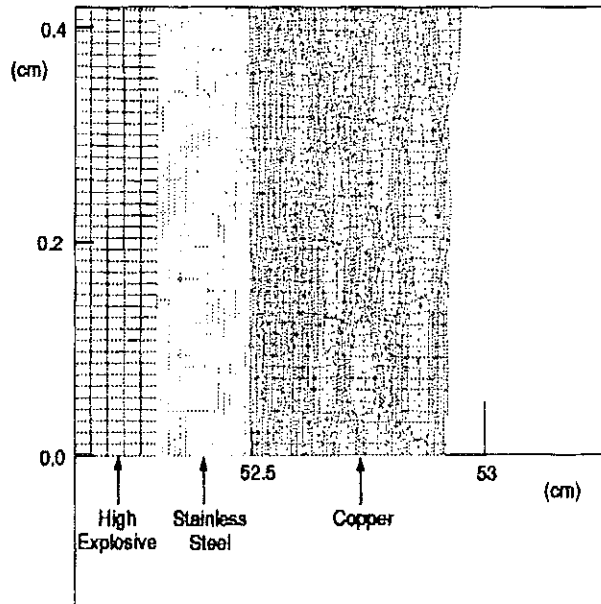


FIG. 5 - Calculated spalled regions (+) at $5 \mu s$ with the tensile threshold criterion

CONCLUSION

The treatment we have presented here makes it possible to simulate simply a fracture with a multidimensionnal hydrodynamics code. Implementation in a unidimensionnal code has shown its agreement with a common 1D treatment. Its application to the calculation of a bidimensionnal experiment of spalling in copper gives rather good results, either with a criterion of tensile threshold or the Johnson model, even if they suggest values of the parameters different than the ones used for plate impacts. Thus, other experiments, with improved instrumentation (recovering the samples for analysis [10], radiographic measures, history of the stress,...) are planned to determine the proper coefficients of various models of damage and fracture for copper and other metals (e.g. tantalum). We will then be able to assess the reliability of these models in the prediction of experiments involving high explosives and the subsequent recovery of spalled metals. In case of excessive discrepancy with experimental results, we consider some extensions of the Johnson model (introduction of a more realistic elastoplastic model, of the inertia terms in the solving of the equation of the porosity,...). At last, the implementation of that fracture treatment enables us to deal with experiments involving combined loadings, which are useful in the search for comprehensive models.

Références

- [1] **F.L. Tuler**
Int.J.Fract.Dyn.vol4 (4) (1968)
- [2] **H.M. Carroll, A.C. Holt**
J.Appl.Phys.43 (4) (1972)
- [3] **S.G. Cochran, D. Banner**
J.Appl.Phys.48 (7) (1977)
- [4] **J.N. Johnson**
J.Appl.Phys.52 (4) (1981)
- [5] **A.K. Zurek, J.N. Johnson, C.E. Frantz**
DYMAT 1988, p.269
- [6] **J.R. Maw, A.R. Giles**
Shock Compression of Condensed Matter 1995, p.295
- [7] **M. Khelifi, P. Simon, D. Techer**
Internal Report (1993)
- [8] **D.J. Steinberg**
J.Appl.Phys.64 (12) (1988)
- [9] **R. Dif, G. Talabart**
Internal Report (1995)
- [10] **A.K. Zurek, W.R. Thissel, D.L. Tonks, R. Hixson, F. Adessio**
DYMAT 1997, p.903

PROPAGATION OF ADIABATIC SHEAR BANDS

the plane
S. MERCIER and A. MOLINARI

Laboratoire de Physique et Mécanique des Matériaux.

I.S.G.M.P., Université de Metz, Ile du Saulcy, 57045 Metz, France

I- INTRODUCTION

Narrow layers of intense shearing, called adiabatic shear band, appear in solids sustaining high rates of deformation. Most of the analysis in the literature consider a shear band as an entity infinitely extended in the shear direction, so as the evolution problem is one dimensional. In such an approach, the propagation of the shear band tip cannot be analysed. In the present approach the shear band is modeled as a two dimensional entity.

II- KINEMATIC OF THE PROPAGATING BAND

The specimen is infinitely long with uniform properties and uniform thickness $2h$. Constant velocities $\pm V$ are prescribed at the boundaries $y = \pm h$. A shear band is assumed to have formed at some point along the specimen and then to have spread a distance sufficient to ensure the shear band tip is advancing under steady-state conditions. The band thickness is supposed to be well characterized and has the value $2h_0$. The material, far ahead of the tip is taken to be sheared uniformly while the medium far behind the tip is pulled at velocity $\pm V$ outside the shear band ($|y| \geq h_0$), and undergoes an uniform shear strain rate within the band ($|y| \leq h_0$).

A cartesian coordinate system (x, y, z) is used as reference. This system is placed at the

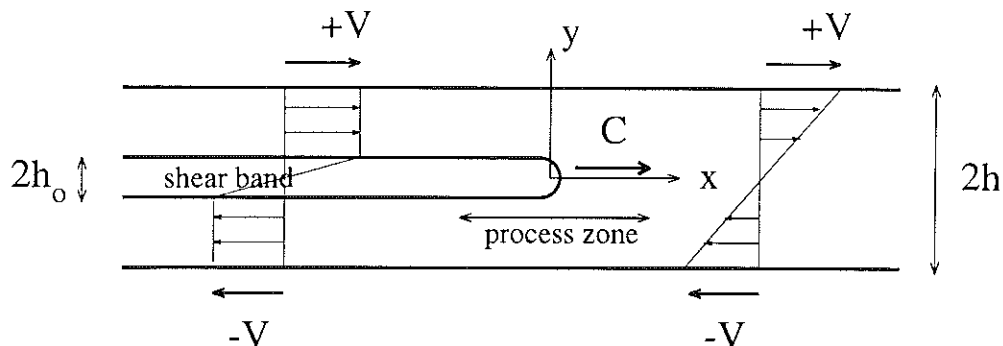


Figure 1: View of the sheared specimen and of the modelled velocity

tip of the band and is translated with it along the specimen axis at the constant tip velocity C . Plane strain conditions are assumed. An Eulerian formulation is used. Assuming incompressibility of the deformation, we introduce a stream function Φ to represent the

strain rate fields in the specimen. The kinematic of the flow is characterized by three parameters C , h_o and λ . The process zone, having a characteristic length defined by λ , is the region at the shear band tip, where a rapid change in the velocity profile is observed from linear ahead to piecewise linear behind. The stream function $\Phi(\lambda, C, h_o)$ defines a family of admissible velocity fields satisfying incompressibility and boundary conditions. Among these velocity fields, an estimation of the real solution is obtained using a variational approach. The width of the band $2h_o$ is considered as given; λ and C have to be optimized. The principle of virtual work leads to a set of equations for the two unknowns λ and C . They are solved using a Newton Raphson technique.

$$\int_{-\infty}^{+\infty} [s_{xy}]_{-h}^h dx + \int_{-h}^h [\sigma_{xx}]_{-\infty}^{+\infty} dy + \frac{4}{3} \rho V^2 (h - h_o) = 0$$

$$2 \int_{-\infty}^{+\infty} \int_{-h}^h \left(x [s_{xx} \frac{\partial \dot{\epsilon}_{xx}}{\partial x} + s_{xy} \frac{\partial \dot{\epsilon}_{xy}}{\partial x}] + s_{xx} \dot{\epsilon}_{xx} + s_{xy} \frac{\partial v_y}{\partial x} \right) dx dy - \rho C \int_{-\infty}^{+\infty} \int_{-h}^h \left(\left(\frac{\partial v_x}{\partial x} \right)^2 + \left(\frac{\partial v_y}{\partial x} \right)^2 \right) dx dy = 0$$

III- RESULTS AND CONCLUSION

Different constitutive behaviour are considered to capture the influence of various parameters on the shear band propagation. Heat conduction effects are neglected. The material is first consider as rigid perfectly plastic. In a second step, the behaviour is still supposed rigid but a thermal softening is accounted for. Finally elasticity is taken into account.

We analyze the effects of the material parameters and of the loading conditions on the structure of the process zone and on the tip velocity. Our results are compared with experimental measurements. The stabilizing effects of inertia, strain rate sensitivity, strain hardening, and the destabilizing effects of strain softening, thermal softening and elasticity have been analysed and quantified. Elastic energy release appears to have an important role, and could lead, if neglected, to a large underestimation of the shear band velocity.

IV- REFERENCES

- Gioia G., Ortiz M.,(1996), The two-dimensional Structure of Dynamic Shear Bands in Thermoviscoplastic Solids *J. Mech. Phys. Solids*, **44**, 251-292.
- Marchand A., Duffy J.,(1988), An Experimental Study of The Formation Process of Adiabatic Shear Bands in a Structural Steel, *J. Mech. Phys. Solids*, **36**, 251-283.
- Mercier S., Molinari A. (1998), Steady-State Shear Band Propagation under Dynamic Conditions, *J. Mech. Phys. Solids*, **46**, 1463-1495.
- Zhou M., Rosakis A. J., Ravichandran G.,(1996a), Dynamically Propagation Shear Bands in Impact-Loaded Prenotched Plates I- Experimental Investigations of Temperature Signatures and Propagation Speed, *J. Mech. Phys. Solids*, **44**, 981-1006.
- Zhou M., Ravichandran G., Rosakis A. J.,(1996b), Dynamically Propagation Shear Bands in Impact-Loaded Prenotched Plates II- Numerical Simulations, *J. Mech. Phys. Solids*, **44**, 1007-1032.

High strain, high strain rate material properties : development of the freely expanding spherical shell test

A. JUANICOTENA, F. LLORCA

CEA Valduc, DRMN/HPC, Laboratoire Comportement et Modélisation
21120 Is-sur Tille - FRANCE

1. INTRODUCTION

Many problems setting in the design of some civil, military or spatial structures are connected to the mechanical behavior of materials in the area of large strains and high strain rates. When the loading is highly dynamic, the prediction of dynamic structural response by means of numerical calculations needs optimized constitutive relations to describe plastic behavior of metallic materials. These models are determined from mechanical tests conducted in a wide range of thermomechanical conditions. Usually, tests are performed on classical hydraulically driven machines in the domain of low strain rates whereas for higher levels, the well established Split Hopkinson Bar technique is often used. This experimental method is classically dedicated to the study of material behavior at strain rates from 10^2 to 5.10^3 s^{-1} and strains up to 0.4. In order to extend the domain of strain rate and strain, free expanding structure tests are particularly suited to model evaluation by virtue of their inherently homogeneous stress state [1]. Because of its relative simplicity, the expanding ring test has received most of the attention of investigators to date. However, in this experiment the final strains are limited to 0.5. So, we have chosen to develop a new expanding spherical shell test for its potential capability to reach high strain rates and large strains. In this paper, we discuss the principle, the design, the development of the test and, finally we propose the first results in the case of tantalum.

2. GOVERNING EQUATIONS AND EXPERIMENTAL PROCEDURE

The test is derived from the classical expanding ring experiment : it consists to impose a free dynamic expansion to a thin object. Kinetic energy is then consumed in plastic work so that expanding velocity decreases. Through mathematical operations, the time-velocity data gives the stress-strain-strain rate state within the sample.

2.1. Governing equations

Let us consider a elementary volume of a spherical shell at radius r . Under the assumptions of free radial expansion, thin shell and spherical symmetry, the fundamental dynamic relation simply resolved itself and the stress-strain-strain rate relations are given by :

$$\sigma_r = 0 \quad \text{and} \quad \sigma_\theta = \sigma_\phi = -\rho \frac{r \ddot{r}}{2} \quad (1)$$

where σ_r and $\sigma_{\theta,\phi}$ are respectively the radial and the tangential stresses, ρ the material mass density, r the current sphere radius and \ddot{r} the radial acceleration. We assume that volume is conserved (plastic

deformation), density is unchanged during free expansion and relation (1) is verified for any current cross-sectional area. Also, σ_θ and σ_ϕ represent true stresses and the sphere material is subjected to an equibiaxial tension state of stress. True strains are given by

$$\epsilon_\theta = \epsilon_\phi = -\frac{1}{2}\epsilon_r = \ln\left(\frac{r}{r_0}\right) \quad (2)$$

where r_0 is the initial sphere radius.

The tangential true strain rate then becomes :

$$\dot{\epsilon}_\theta = \frac{\dot{r}}{r} \quad (3)$$

It is clearly shown that the measurement of displacement or velocity allows to determine stress, strain and strain rate second-order tensor at any time during the experiment. For example, it is possible to calculate displacement and acceleration by integration and differentiation with respect to time of the expanding velocity data. Stress and strain tensors are then reduced to effective scalar values according to Von Mises criteria :

$$\sigma_{eff} = \sigma = \sqrt{\frac{3}{2}\left(\sigma_{ij}\sigma_{ij} - \frac{1}{3}\sigma_{kk}^2\right)} = \sigma_\theta \quad \dot{\epsilon}_{eff} = \dot{\epsilon} = \sqrt{\frac{2}{3}\dot{\epsilon}_{ij}\dot{\epsilon}_{ij}} = 2\dot{\epsilon}_\theta \quad (4)$$

2.2. Experimental technique

The principle of the experimental procedure is based on the original expanding ring test [3-4]. The free radial expansion is imposed by means of an explosive set-up. A shock wave is generated by the detonation of a high explosive and transmitted outward through a steel driver. Therefore, the shock wave propagates within the sample which expands at high speed, by virtue of its own inertia, i.e. without the action of external forces. Under this motion, the thin sphere undergoes large plastic deformations as its initial kinetic energy is dissipated into plastic work. Technical difficulties associated with explosively driven devices in spherical geometry (initiation, complete sphere machining processes) have led us to restrict the test to the expansion of hemispherical shells. The design of the experimental set-up has been defined using 1D and 2D hydrocodes [5]. First, 1D numerical calculations are used to evaluate shock pressure levels in the sample material in order to limit damage phenomena like spalling. In 2D simulations, the apparatus has been designed in order to minimize bidimensionnal effects due to the hemispherical geometry. These results have also been used to plan measurements. Finally, the experimental set up is constructed as shown in Figure 1.

The driver material is XC38 steel with a 330 MPa yield strength. The driver size and the explosive diameter are chosen to launch the sphere at an initial strain rate of 10^4 s^{-1} . Dimensions of the principal elements are : explosive diameter from 38 to 44 mm, sphere inner diameter 100 mm and thickness from 1.5 to 3 mm. The radial sphere velocity is measured with the Doppler Laser Interferometry technique (DLI) for different locations in order to record bidimensionnal effects. Furthermore, expansion of the material sample is observed by means of ultra high speed cameras.

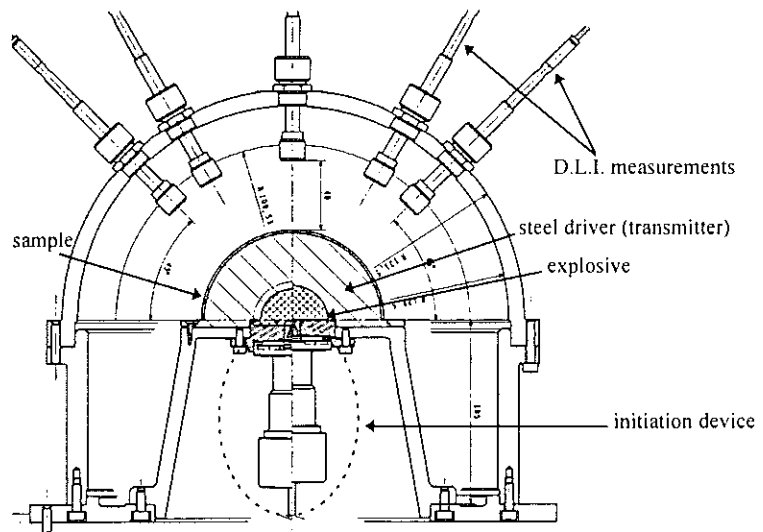


Figure 1 - Cross-sectional view of the experimental set up.

2.3. Numerical simulations

The objective of numerical simulations is to define the characteristics of the dynamic loading applied to the spherical sample (levels, chronology ...). Most of calculations were performed with a CEA hydrocode named Hesione. Figure 2 shows the simplified computational grid of the set-up. It is the axisymmetric representation where the x-axis is an axis of symmetry. Lagrangian calculations are performed : inert materials are modeled with Mie-Gruneisen equations of state and Steinberg-Cochran-Guinan constitutive relations [6].

Figure 3 shows the detonative and shock wave propagation across the elements.

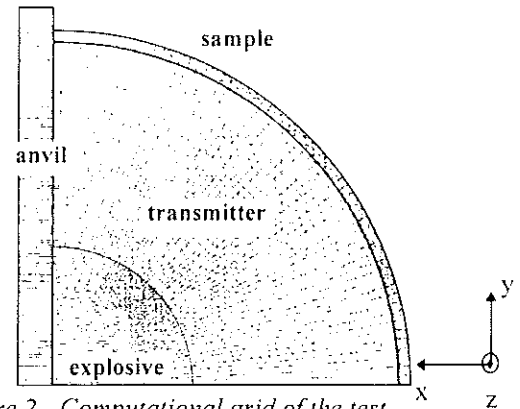


Figure 2 - Computational grid of the test.

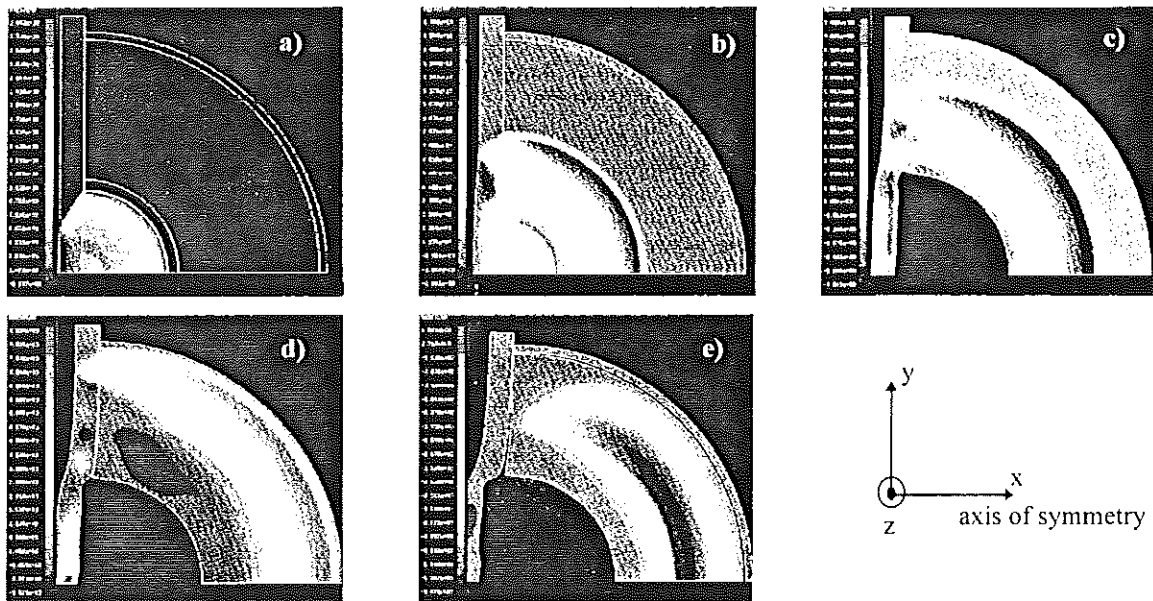


Figure 3 - The different stages of waves propagation and deformation phenomena given by a 2D numerical simulation - a) $2\mu s$, b) $4\mu s$, c) $6\mu s$, d) $8\mu s$, e) $12\mu s$.

The spherical sample separates from the driver approximately $10\mu s$ after detonation of the explosive. Calculated pressure and deviatoric stress levels in the spherical shell are reported in figures 4 and 5. These plots confirm that the applied loading is divided in two stages :

- first, the shock wave travels across the sample, in which the loading is close to uniaxial deformation in the x (\vec{e}_r) direction. In this case, $S_{yy} = S_{zz} = -0.5 S_{xx}$.
- then, the free radial expansion by plastic flow begins, the material is subjected to a dynamic equibiaxial tension in the y (\vec{e}_θ) and z (\vec{e}_ϕ) directions. Again we have the relation $S_{yy} = S_{zz} = -0.5 S_{xx}$.

In the previous example (Fig. 4), the peak shock pressure is about 6 GPa for a corresponding rise time of about $1.4\mu s$. In all performed calculations, initial shock pressure level has been found lower than 10 GPa. It is well known that application of a shock wave can lead to modify the mechanical properties like yield strength or work-hardening rate. For example, behavior of tantalum becomes to be sensitive to peak pressure effects between 20 Gpa and 45 GPa [7].

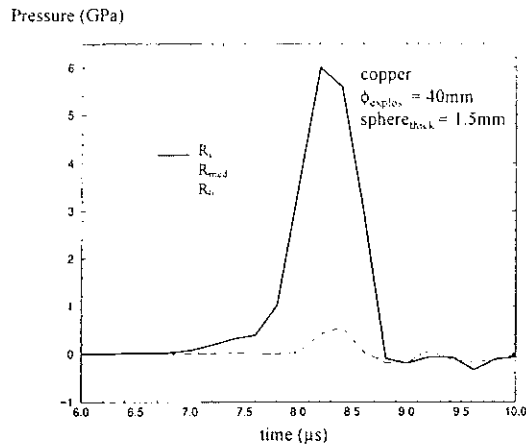


Figure 4 - Spherical component of the stress tensor.

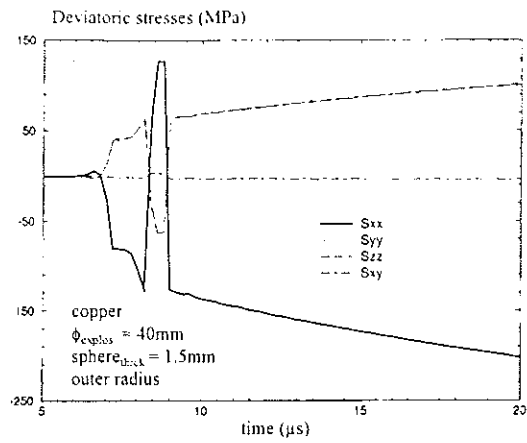


Figure 5 - Deviatoric components of the stress tensor.

Figure 6 is a plot of the radial velocity versus time for the three locations of DLI measurements. We can observe the oscillatory phenomenon caused by the waves reflections from the inner radius to the free surface of the sample. This ringing motion is damped out in time and the decreasing of velocity with plastic deformation becomes considerably smoother. Restoration of elastic energy at the end of plastic deformation is observed in the numerical simulations. In the case of the hemispherical geometry, it is due to bidimensionnal effects which propagate along the object, starting from the 45° location to the pole. In the case of real experiments, observation of elastic restoration depends on the appearance of damage and fracture phenomena. No damage law is included in the numerical simulation. Nevertheless, applying equations (1-2-3-4) at the pole location is justified because due to the axisymetrical geometry of the test, the state of stress at this point is always equibiaxial.

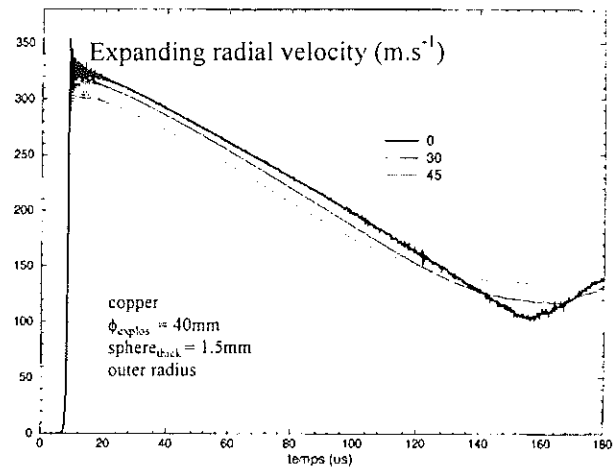


Figure 6 - Calculated radial velocity versus time.

3. TANTALUM RESULTS

Two tantalum spheres were expanded to strain rates up to $1.2 \cdot 10^4 \text{ s}^{-1}$. This material is very attractive in particular due to its high density, superior strength and excellent ductility over a wide range of strain rates and temperatures [8]. Tantalum used in the present study was produced by Cabot Performance Materials Company. the two hemispheres have been machined from an ingot (70 mm diameter), in accordance with a particular procedure to elaborate objects with homogeneous microstructure [5]. The grain size of the as-received tantalum spheres was approximately $35 \mu\text{m}$.

3.1. Results

Two tests have been performed. Table 1 shows the geometrical characteristics selected for the explosive and the thickness of the sphere.

Table 1 - Characteristics of the elements.

test number	ϕ explosive (mm)	sphere thickness (mm)
106	40	2
107	44	2

Figure 7 presents four pictures for the 106 shot. The origin of time is fixed as the detonator is initiated. The film shows the clean and apparent axisymetrical expansion of the hemisphere (pictures

a, b and c) until the time when first damages appear (pictures c and d).

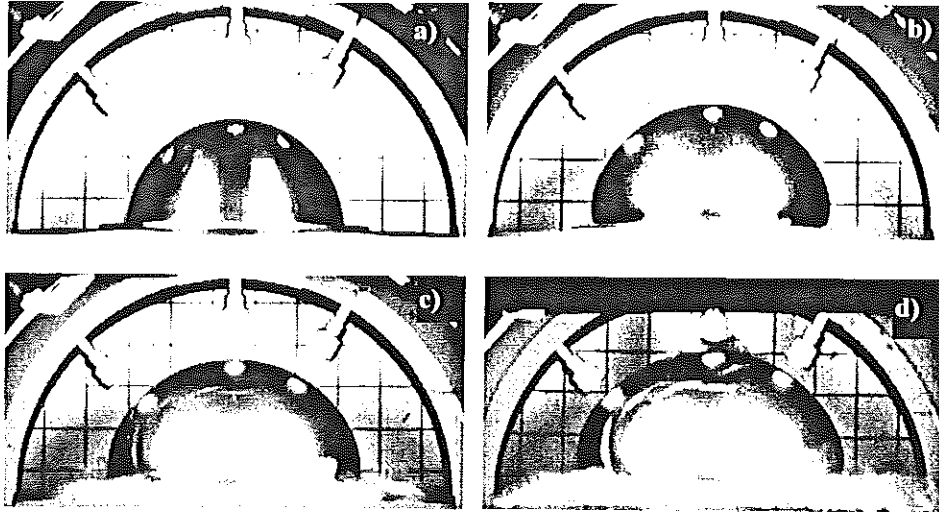


Figure 7 - Expanding spherical shell test - Tantalum - Shot 106.
a) 9.4 μs , b) 50.1 μs , c) 77.2 μs , d) 117.8 μs .

Figure 8 is a plot of the time velocity curves obtained for the two tantalum experiments. The same phenomena are to be found in the previous numerical simulations, that is to say a ringing motion after launch, followed by a decrease of the velocity with time. At the end of the test, there is no « elastic rebound », indicating that the material fractures before bidimensionnal disturbances appear. Shock pressure at the driver/sphere interface may be estimated with the next shock relation [9] :

$$P = \rho_0 D u_s = \frac{\rho_0 D u_s}{2}$$
 where ρ_0 is the mass density, $D = C_0 + S u_s$ the shock wave celerity and u_s the free surface velocity. With the values of $C_0 = 3367 \text{ m}\cdot\text{s}^{-1}$ and $S = 1.2$ [10], shock pressure levels for shot 106 and shot 107 are estimated : respectively 7.85 GPa and 9.06 GPa. Influence of peak shock pressure is then neglected according to literature.

3.2. Data processing and analysis

Using the equations (1-2-3) to transform experimental velocity curves into stress-strain curves requires integrating and differentiating operations. Considerable difficulty is usually encountered with the single differentiation of raw data. Various methods are then applied in order to reduce scatter. In this study, two ways were investigated. The first way consists in fitting the velocity time data within the usable data window to a quadratic function of the form : $v(t) = a + bt + ct^2$. Acceleration is then obtained by differentiating the analytical formula and is consequently a linear function of time. In the second way, by differentiating the velocity curve about a time period of approximately 2 μs (finite elements method), we eliminate the highest frequencies information in order to smooth the final results. We fit then the stress-strain curve by a quadratic function. These two techniques are not very sophisticated but we do not choose to focus on this problem at this time.

Figure 9 present plots of the effective strains and strain rates during the two experiments. For test 107, the stress-strain curve is calculated and proposed in figure 10.

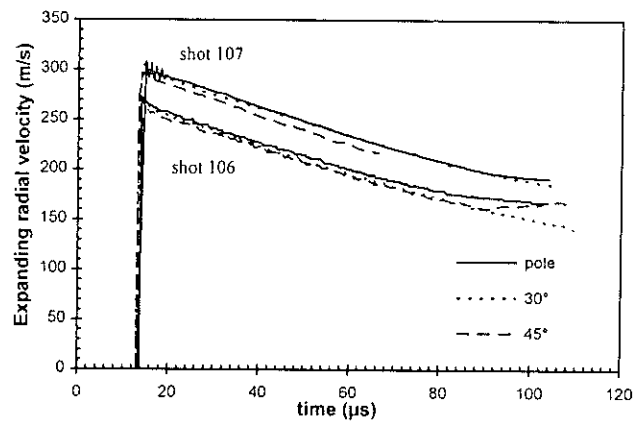


Figure 8 - Shot 106 and 107 : velocity-time curves.

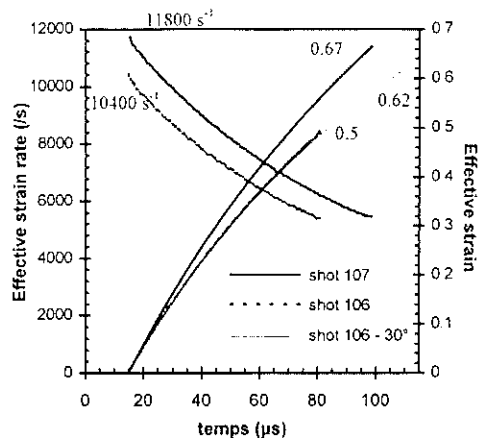


Figure 9 - Strain and strain rate time-evolution.

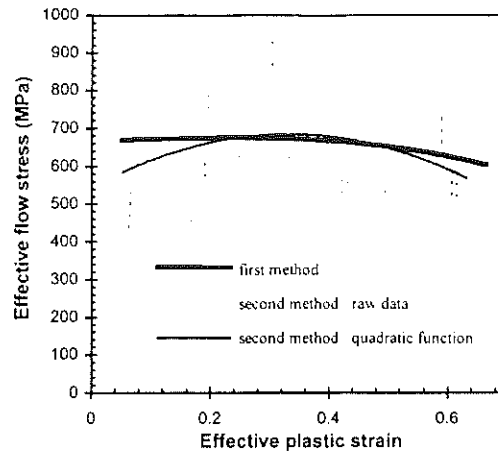


Figure 10 - Shot 107 : stress-strain curve.

Higher strain rate at the starting of the expanding stage of the shell varies from 1 to $1.2 \times 10^4 \text{ s}^{-1}$. The maximum plastic strain is achieved for shot 107, with a final level equal to 0.7. So, we confirm that the initial objective proposed for the design of this new experimental technique is reached. As regards the stress-strain curve, its shape puts in evidence short work hardening stage followed by a steady state and a final softening stage. The two first zones are currently observed in classical mechanical experiments ; the last stage is more original for evaluating models because it is the result of the action of two distinct phenomena : adiabatic heating and saturation of flow stress. Decreasing of strain rate is not sufficient to explain such a stress collapse. The measured stress levels for tantalum are in a good accordance with those obtained by means of the SHPB technique [5]. Evaluation of the plastic behavior of tantalum by means of various constitutive relations is presented by the authors in [11].

4. CONCLUSION

A new test for dynamic evaluation of viscoplastic models at high strains and high strain rates has been designed by means of numerical simulations. The freely expanding spherical shell test subjects the material to equibiaxial loading, and the stress - strain - strain rate function can be obtained from the radial velocity versus time function. The first experimental results in the case of tantalum show the test is perfectly adapted to the evaluation of plastic models at high strains and high strain rates.

ACKNOWLEDGMENTS

The authors gratefully acknowledge MM Patrice ANTOINE, Jacques MATHIAS and the REF/EM team for their contributions to the conducting of the expanding tests.

REFERENCES

- [1] WARNES R. H., DUFFEY T.A., KARPP R.R., CARDEN A.E., *Shock waves and high strain rate phenomena in metals*, Ed. Meyers and Le Murr, Plenum Press, pp. 23-36, 1981.
- [2] DORMEVAL R., ANSART J.P., *Proc. of the Int. Symposium on Intense Dynamic Loading and its effects*, pp. 608-613, Beijing, China, June 3-7, 1986.
- [3] HOGGATT C.R., RECHT R.F., *Experimental Mechanics*, pp. 441-448, October 1969.
- [4] WARNES R. H., KARPP R.R., FOLLANSBEE P.S., *J. de Phys.*, C5, Tome 46, pp. 583-590, août 1985.
- [5] JUANICOTENA A., *Thesis of University of Metz*, 1998.
- [6] STEINBERG D.J., COCHRAN S.G., GUINAN M.W., *J. of Appl. Phys.*, 51(3), pp.1498-1504, March 1980.
- [7] LASSILA D.H., LEBLANC M., GRAY III G.T., *Shock wave and high strain rate phenomena in materials*, Ed. by Meyers, Murr, Staudhammer, pp. 587-595, 1992.
- [8] BUTTNER F.H., BACON F.E., BANCROFT R.K., *Columbium and Tantalum*, Ed. by SISCO F.T. & EPREMIAN E., John Wiley & Sons, pp. 560-597, 1963.
- [9] THOUVENIN J., *Détonique*, Collection du C.E.A., Eyrolles, 1997.
- [10] STEINBERG D.J., *Equation of state and strenght properties of selected metals*, Lawrence Livermore National Laboratory, UCRL-MA-106439, 1996.
- [11] LLORCA F., JUANICOTENA A., *Modeling of high strain, high strain rate behavior of Mars 190 armor steel and tantalum*, 11th Journées Techniques DYMAT, Dijon, 1998 (this issue).

Fatigue of cold forging tools affected by high strains and strain-rates

CH. HINSEL, U. ENGEL

*Chair of Manufacturing Technology, University of Erlangen-Nuremberg
Egerlandstr. 11, 91058 Erlangen, Germany*

I - INTRODUCTION

Cold forging is characterized by high material efficiency and high production rates at short process times, net shape capability, and improved material properties due to cold hardening and favourable material flow [1]. Therefore cold forging is well-established where precise components have to be produced at high productivity.

The steadily increasing demands on this precision and productivity lead to high strains and strain-rates in the billet. Even if the tool speed is relatively low, for example in the range from 0.1 to 1 ms⁻¹ for a punch in backward can extrusion, the billet material can be subjected to strain-rates of 100 s⁻¹ and more. This is due to the fact that the die geometry causes the workpiece material to plastically deform in an inhomogeneous manner in order to be deformed to the desired shape [2].

Furthermore, the increasing industrial demand for improved productivity leads to higher speeds which can elevate the strain-rate in excess of 100 s⁻¹ [2] in local areas of the workpiece. In addition to the improved productivity, high-speed forging provides advantages with regard to enhanced surface quality and increased precision [3].

A consequence of these rising strains and strain-rates in the billet is that the load on the cold forging tools is significantly increasing as well, which leads to wear and fatigue fracture. In order to obtain economical tool life, enhanced tool design is required using advanced methods such as numerical analysis by finite elements. Based on the characterization and analysis of material flow, tool load and tool strength, this paper shows ways towards the appropriate design of tools for cold forging at high strains and strain-rates.

II - METHODS OF TOOL LAYOUT IN COLD FORGING

The appropriate layout of cold forging tools is supported by empirical, knowledge-based, statistical and deterministic methods. Empirical knowledge, compiled in various guidelines [4,5] and technical books [3], allows the estimation of tool load by analytical equations and by nomograms. The knowledge-based approach, which provides systems to design tools and forging sequences, is based on deterministic and empirical knowledge [6]. Statistical approaches take into consideration that all parameters of influence are subject to deviations, causing scattering in tool life [7].

In recent years, deterministic methods have gained in importance, especially due to the further developments in numerical process simulation. Therefore the following investigations mainly

concentrate on examples for the deterministic design of cold forging tools. The basic idea of this method is to trace back both the load and the strength to their origins, i.e. to the primary parameters of influence [7]. The material flow (see III-1) determines the external load which is given by the normal stresses, friction stresses and displacements between tool and billet. The internal load is caused by the external load and additionally influenced by tool design. The external and the internal load can be quantified by numerical simulation (see III-2) [8]. The strength of the tool elements is affected by the damaging mechanisms of wear and fatigue (see IV-1) which are controlled by the load. The damaging mechanisms can be modelled by applying concepts of tribology, damage and fracture mechanics (see IV-2). Tool life is determined by the period of time in which the strength of the tool exceeds the load. Due to its stochastic nature, however, tool life can be used for an appropriate criterion for the tool layout only if it is connected with an information about the probability of its occurrence [7].

III - EFFECTS OF HIGH STRAIN-RATES ON TOOL LOAD

III - 1. Analysis of material flow at high strains and strain-rates

Calculation of the tool load in a metal forming process requires the thorough knowledge of the properties and flow of the billet material. Contrary to simplified approaches, constitutive equations for modelling of the material behaviour should consider the flow stress as a function of strain, strain-rate, and temperature [2]. Heating of the workpiece in cold forging results from the plastic deformation and the strain-rate. Equations which are provided by finite element systems to model the material behaviour range from simple stress-strain-curves to more comprehensive models, taking into account strain-rate and temperature effects.

Software packages for numerical simulation can be considered in two broad groups: general (ABAQUS, MARC) and special purpose (MARC/AutoForge, DEFORM, FORGE2/3) programs. Special purpose codes gain increasing popularity due to the demands in industry. However, it is seldom recognised that increasing complexity of the problems needs complicated coupled models, which are rarely supported by special purpose programs [9]. In the following, material definitions used in the commercial FE codes DEFORM and ABAQUS are discussed.

Fig. 1 shows an example for a combined forward rod backward can extrusion process calculated by DEFORM. Based on a punch speed of 1 ms^{-1} , strains of up to 2 and strain-rates of more than 500 s^{-1} can occur locally, in this case for a punch speed of 1 ms^{-1} .

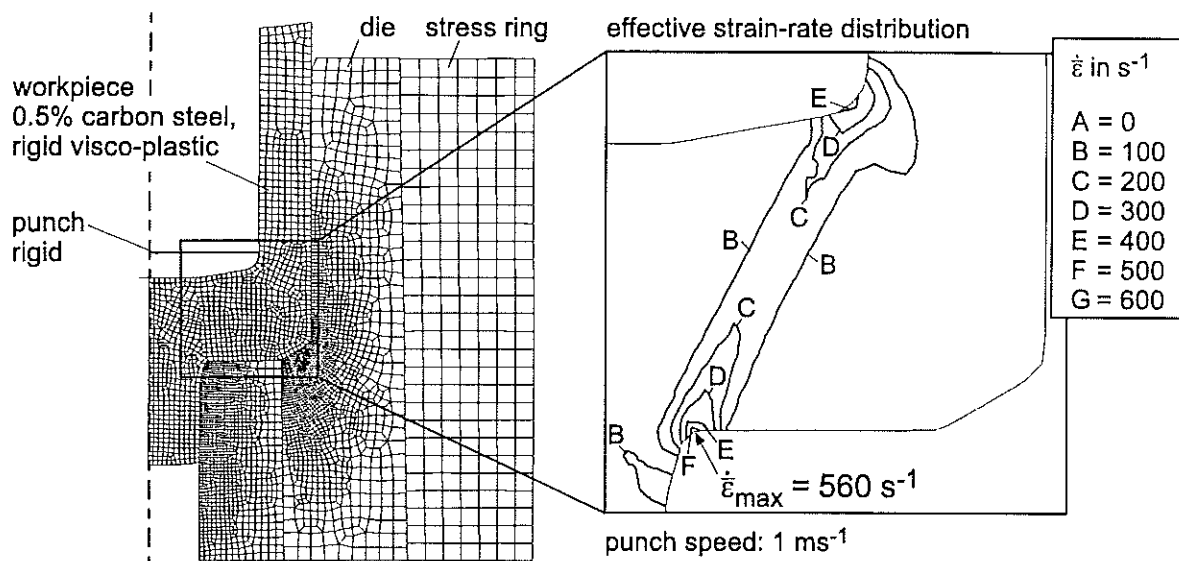


Fig. 1 Strain-rate distribution in combined forward rod - backward can extrusion

DEFORM [10] is a special purpose code designed for process simulation in cold, warm and hot forging of steels and non-ferrous metals. DEFORM provides the following built in functions for defining the flow stress in dependence of strain and strain-rate:

$$\sigma_f = C \cdot \varepsilon^n \cdot \dot{\varepsilon}^m \quad (1)$$

$$\dot{\varepsilon} = A \left[\sinh(\alpha \sigma_f) \right]^n e^{(-\Delta H / (RT_{abs}))} \quad (2)$$

$$\dot{\varepsilon} = A \sigma_f e^{(-\Delta H / (RT_{abs}))}, \quad (3)$$

Function (1) defines the flow stress in terms of strain and strain-rate only. The dependency of strain-rate is given by m which normally increases with temperature. In the functions (2) and (3), ΔH is the activation energy for plastic flow, used mainly for aluminium alloys. DEFORM offers the material models linear thermo-elastic material, rigid-viscoplastic material, porous material and thermal-elastoplastic material, all assuming isotropic material behaviour.

ABAQUS is a general purpose code for manifold applications in engineering. The material library in ABAQUS includes more metal plasticity models than DEFORM. The main options are a choice between rate independent and rate dependent plasticity, and a choice between the Mises yield surface for isotropic and Hill's yield surface for anisotropic materials.

ABAQUS allows to define a strain-rate dependent yield stress in two ways. First, test data can be provided as tables of yield stress values versus equivalent strain at different equivalent plastic strain-rates $\dot{\varepsilon}^{pl}$. Second, ABAQUS allows the user to enter only one hardening curve, the static hardening curve, and then to express the rate-dependent hardening curves in terms of the static relation, i.e.

$$\sigma_f(\varepsilon^{pl}, \dot{\varepsilon}^{pl}) = \sigma_0(\varepsilon^{pl}) R(\dot{\varepsilon}^{pl}) \quad (4)$$

where σ_0 is the static yield stress, ε^{pl} is the equivalent plastic strain, $\dot{\varepsilon}^{pl}$ is the equivalent plastic strain-rate, and R is a ratio defined as $R=1.0$ at $\dot{\varepsilon}^{pl}=0$. This material model is limited to isotropic hardening again [11].

In addition, ABAQUS optionally allows for plastic dissipation to result in the heating of a material. The option is typically used in the simulation of bulk metal forming or other high-speed manufacturing processes involving large amounts of inelastic strain where the heating of the material caused by its deformation is an important effect. The option is applicable only to adiabatic thermal-stress analysis or coupled temperature-displacement analysis.

To come to a conclusion, this comparison of functions provided by two commercial FE codes shows that the modelling of material at high strain-rates is still limited to simplified approaches, e.g. not taking into account anisotropic hardening. Therefore, the improvement of accuracy in numerical modelling of the material behaviour, taking into account the effects caused by high strains and strain-rates, requires two approaches. First, suitable constitutive equations have to be implemented into commercial software packages. Second, appropriate material parameters for typical cold forging steels have to be determined and disseminated.

In future, the modelling of microstructural behaviour will become more and more important to describe anisotropic hardening and damage [12]. These concepts are currently not included in the simulation of bulk metal forming processes. However, various studies (e.g. [13]) show that the yield stress for orthogonal and reversed (Bauschinger effect) reloading can differ up to 30% [9]. Such a difference can not be ignored if the accuracy of simulation must be high. Furthermore, these considerations are necessary for the innovative forming of microparts [14].

III - 2. Analysis of tool load

The material flow distribution yields the distribution of external load on the tool, represented by the normal stresses, the friction stresses and displacements between the tool elements and the billet. The internal load, represented by stress and strain distribution, is directly resulting

from the external load caused by the transfer of the contact conditions. Fig. 2 shows the effective stress distribution inside the die for the same process as in Fig. 1. The maximum effective stress represents the location where fatigue fracture occurs in the real tool.

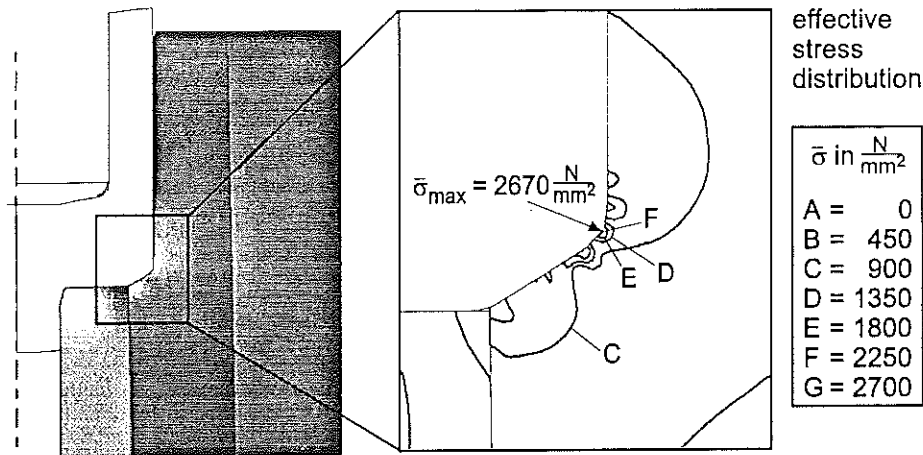


Fig. 2 Tool load: effective stress distribution in a cold forging die

IV - EFFECTS OF HIGH STRAINS AND STRAIN-RATES ON TOOL LIFE

IV - 1. Failure of cold forging tools

In cold forging, tool life is mainly constrained by fracture, wear, and plastic deformation. Wear and fatigue fracture are mechanisms affecting the tool simultaneously. Wear is a process starting immediately during the first forming operation; its accumulation determines the tool life. The criterion for that may be the decreasing surface quality of the billet or exceeding tolerance limits. Despite a high degree of hardness of tool material (high-speed steels, cemented carbides [1]) and modern coating technologies [15], wear always takes place in forming operations [16]. Fracture can be divided into forced rupture, which can be avoided by proper tool layout following appropriate guidelines [4,5] or empirical knowledge, and fatigue fracture. Fatigue fracture is the main danger in cold forging production because of the high costs arising not only from the tool replacement but also from the resulting damage which may be caused by the broken tool in automatic production.

IV - 2. Experimental and numerical analysis of tool strength

The strength of the tool elements is affected by the damaging mechanisms of wear and fatigue. These mechanisms can be taken into account in the numerical simulation by applying concepts of tribology, damage and fracture mechanics. With regard to fatigue, various concepts for the estimation of tool strength and thus tool life are available [17]:

The *Woehler approach* is based on uni-axial fatigue tests which yield a relation between the number of load cycles N_f and the stress amplitude σ_a for high-cycle fatigue:

$$N_f = N_D \left(\frac{\sigma_a}{\sigma_D} \right)^k \quad (5)$$

with σ_D as the fatigue limit and N_D as the corresponding lifetime.

The *local energy approach* takes into account multi-axial stress conditions by adding the directional-dependent damage portions. Assuming that the plastic strain components can be neglected, only the so-call modified elastic strain energy density ΔW^{e++} has to be considered:

$$\Delta W^{e++} = \frac{1}{2} \left(\frac{\Delta \sigma}{2} + \Delta \sigma_m \right) \left(\frac{\Delta \varepsilon}{2} + \varepsilon_m \right) \quad (6)$$

The *local strain approach* can be derived according to *Coffin et al* by

$$\varepsilon_{a, tot} = \varepsilon_{a, el} + \varepsilon_{a, pl} = \frac{\sigma_f' - \sigma_m}{E} (2N_f)^b + \varepsilon_f' (2N_f)^c \quad (7)$$

with ε_a strain amplitude; σ_f' cyclic stress coefficient, b cyclic stress exponent, ε_f' cyclic strain coefficient, c cyclic strain component. $2N_f$ is the number of load cycles until the initiation of fatigue cracks. In case of neglecting of plastic strain, ε_f' and c are not required.

For all of these approaches, however, it is difficult to get the necessary material data even for well-known tool materials. Nevertheless, especially the energy based approach provides an efficient instrument to estimate tool life if fatigue is the dominating failure mechanism [17].

V - APPROPRIATE DESIGN OF COLD FORGING TOOLS

The increasing loads caused by cold forging at high strains and strain-rates require advanced tool design. Due to the diversity of parameters of influence, there are many approaches to improved tool performance. Most of the measures aim at decreasing the load on the tool and/or at increasing the strength of the tool [7]:

Tool material: The optimum tool material combines high fracture toughness with high hardness. For cold forging punches, mainly cold/hot working steels (e.g. AISI D2, i.e. DIN X155CrVMo12 1) and high speed steels (e.g. AISI M2, i.e. DIN S6-5-2) are used [18]. The steadily increasing demands on tool strength lead to modern powder-metallurgical tool steels (e.g. ASP2000) which provide a high purity with almost no carbide concentrations that may lead to premature crack initiation; thus the fatigue strength can be improved significantly [19]. The use of cemented carbides (e.g. ISO G40) has become common for many cold extrusion dies where pre-stressing of the die minimizes the risk of cracks by tensile stresses in the die.

Surface and coating technologies: Surface and coating technologies, especially plasma technologies (physical vapour deposition, plasma-nitriding) and chemical vapour deposition, have become well-established in industry to improve the wear resistance of cold forging tools. However, due to the increasing demands on the performance and functionality of coatings, current developments aim at combining the advantages of various surface and coating technologies. For example duplex coating, i.e. plasma-nitriding with subsequent PVD coating, helps to increase not only the wear resistance but also the fatigue strength of tool steels [15].

Pre-stressing: Usually cold forging dies are pre-stressed by a stress ring to avoid crucial high tensile stresses in critical regions of the die. Pre-stressing technology by strip winding allows intensified pre-stressing by which the internal load can be further reduced, finally yielding an increase in tool life as well as a reduction in scattering of tool life [20].

Shape optimization: Stress and strain concentrations in cold forging tools mainly arise in areas with sharp corners or small radius respectively, being affected by wear as well as by fatigue. Such tool features are potential areas of crack initiation and require special attention in tool design as well as in tool manufacturing. While the quantitative interpretation of simulation results is rather difficult to evaluate, various examples have proven that the qualitative interpretation is very helpful to detect the most critical locations in a tool. This way numerical process simulation is the appropriate tool for shape modification and optimization.

Approaches to enhanced tool design meeting the demands of higher loads are not only related to high speed forging. Other trends in cold forging such as net shape forging, ecological manufacturing [21] and forging of light-weight materials (e.g. magnesium) put pressure on advanced tool design as well.

VI - CONCLUSIONS

Cold forging at high strains and strain-rates confronts proper process design in various ways. Concerning the billet, material properties such as strain-rate dependent yield strength are taken into account in the layout of cold forging processes, especially in numerical process simulation. However, in most cases these material models are still simplified, e.g. limited to isotropic hardening. Concerning the tool, the detection of critical tool areas and the relevant maximum loads is significantly supported by numerical process simulation. Together with experimental determination of the strength of the tool material, the calculation of damage parameters allows at least a qualitative estimation of the tool life today.

VII - REFERENCES

- [1] VDI Guideline 3138: Cold forging of steels and nonferrous metals - fundamentals of cold forging (*in German*). VDI, 1998
- [2] Dodd, B.: Strain Rate and Temperature Effects in Metalforming. DYMAT meeting St. Jean de Luz, September 1996
- [3] Lange, K. (ed.): Handbook of Metal Forming. McGraw Hill, New York, 1985
- [4] ICFG Doc. 4/82: General aspects of tool design and tool materials for cold and warm forging.
- [5] ICFG Doc. 6/82: General recommendations for design, manufacture and operational aspects of cold extrusion tools for steel components.
- [6] Cser, L.; Geiger, M.: A Generalized Life-Time Model for Cold Extrusion. CIRP Annals 40 (1991) 1, 299-301
- [7] Engel, U.: Load and strength of bulk metal forming tools (*German*). Meisenbach, Bamberg, 1996
- [8] Altan, T.; Vazquez, V.: Numerical process simulation for tool and process design in bulk metal forming. CIRP Annals 45/2, 599-615
- [9] Tekkaya, A.E.: Status and Developments in Simulation of Forming Processes. WIRE 1/98, 31-36
- [10] DEFORM 4.1 User's Manual. Scientific Forming Technologies Co., 1995
- [11] ABAQUS 5.6 Theory Manual. Hibbitt, Karlsson & Soerensen Inc. 1996
- [12] Kim, H.-S.; Im, Y.-T.; Geiger, M.: A Study of Prediction of Ductile Fracture in Cold Forging. In: Kaftanoglu, B. et al (edtrs.): Int'l Conf. and Exhibition on Design and Production of Dies and Molds, Ankara, Turkey, Matim, 1997, 305-310
- [13] Teodosiu, C.; Hu, Z.: Evolution of the Intragranular Microstructure at Moderate and Large Strains: Modelling and Computational Significance. In: Simulation of Materials Processing - Theory, Methods and Applications, 1995, 173-182
- [14] Engel, U.; Meßner, A.; Geiger, M.: Advanced concept for the FE simulation of metal forming processes for the production of microparts. In: Altan, T. (ed.): Advanced Technology of Plasticity, Columbus, Ohio/USA, Vol. II, 903-907
- [15] Hinsel, Ch: Advanced Surface and Coating Technologies for Improved Tool Life in Cold Forging. Presented at the 31st Plenary Meeting of the International Cold Forging Group ICFG, Göteborg, September 8, 1998 (*to be published in WIRE*)
- [16] Lange, K.; Cser, L.; Geiger, M.; Kals, J.A.G.; Hänsel, M.: Tool Life and Tool Quality in Bulk Metal Forming. Annals of the CIRP Vol 41 (1992) 2, 667-675
- [17] Falk, B.; Engel, U.; Geiger, M.: Estimation of Tool Life in Bulk Metal Forming Based on Different Failure concepts. J. Mater. Proc. Technol. Vol. 80-81 (1998) 602-607
- [18] VDI Guideline No. 3186: Tool materials for cold forging (*in German*). VDI, 1997
- [19] Broendsted, P.; Skov-Hansen, P.: Fatigue Properties of High Strength Materials Used in Cold Forging Tools. Presented at the 30th Plenary Meeting of the International Cold Forging Group ICFG, s'Hertogenbosch, September 9, 1997 (*to be published in Journal of Fatigue*)
- [20] Birker, T.; Groenbaek, J.: High-stiffness stripwound containers. WIRE 1/98, 37-42
- [21] Engel, U.: Basic Research in Manufacturing and its Contribution to an Eco-friendly Application of Cold Forging. In: IMechE Conf. Transactions - Forging and Related Technologies (ICFT'98, 27-28 April 1998, Birmingham) Bury St. Edmunds, London: Profess.Engng.Publ.Ltd.1998, 25-36

Dynamic characterisation of low impedance materials at large strains.

G. GARY & H.ZHAO

*Laboratoire de Mécanique des Solides, Ecole Polytechnique,
91128 PALAISEAU, FRANCE*

SUMMARY

This paper presents a review of results found in our Laboratory, these few last years, about new techniques allowing for a valuable analysis of strain rate effects on the behaviour of soft viscous materials. Those results concern the use of Hopkinson bars: -a) the waves' dispersion correction for viscoelastic 3D bars; -b) the extension of the SHB technique to long time measurements using a two-gauges measurement method taking account of the correction of wave dispersion effects, as it is indeed indispensable in that case; -c) inverse calculation methods that are needed for the analysis of the results of transient tests when the hypothesis of homogeneity in the specimen is not valid.

I - INTRODUCTION

The Split Hopkinson Pressure Bar (SHPB), or Kolsky's apparatus, is a commonly used apparatus for testing materials at high strain rates, in the range of approximately 300 to 3000 s⁻¹. Historically, the first use of a long thin bar to measure the pulse shape induced by an impact is considered due to Hopkinson [1]. This method has been well established after the critical work of Davies [2]. The experimental set-up with two long bars and a short specimen has been introduced by Kolsky [3]. The Split Hopkinson bar technique, which has been initially used in compression, has been extended to the tension (Harding et al., [4]) and to the torsion (Duffy et al., [5]). To increase the measuring duration of SHPB, some earlier workers (Campbell and Doby [6]; Lundberg and Henchoz [7]) have analysed the multiple reflections in bars, using two signals recorded at two different cross-sections in a bar.

This paper will focus on some particularly important points when soft materials subjected to high strains are considered. : In sections II & III we consider measurement problems that are directly related to the SHPB arrangement. In section IV, we consider the identification problems relating material behaviour to experimental measurements.

II - SHPB MEASURING TECHNIQUES. VISCOELASTIC DISPERSION CORRECTION

II - 1. SHPB measuring technique.

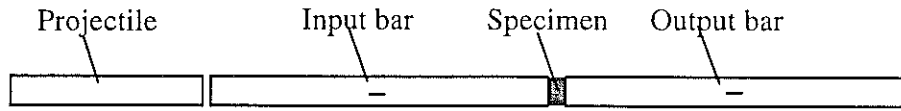


Fig. 1. SHPB test set-up

A typical SHPB set-up is outlined in Fig. 1. It is composed of long input and output bars with a short specimen placed between them. The impact of the projectile at the free end of the input bar develops a compressive longitudinal incident wave $\varepsilon_i(t)$. Once this wave reaches the bar specimen interface, a part of it, $\varepsilon_r(t)$, is reflected, whereas another part goes through the specimen and develops in the output bar the transmitted wave $\varepsilon_t(t)$. Those three basic waves recorded by the gages cemented on the input and output bars allow for the measurement of forces and velocities at the two faces of the specimen.

This measurement technique is based on the wave propagation theory and on the superposition principle. According to the wave propagation theory, the stress and the particle velocity associated with a single wave can be calculated from the associated strain measured by the strain gages. Using the superposition principle, the stress and the particle velocity in one section are calculated from the two waves propagating in opposite directions in this section. When the waves are known at bar-specimen interfaces, the forces and the velocities at both faces of the specimen are given by the following equations (1).

$$\begin{aligned} V_{input}(t) &= C_0 (\varepsilon_i(t) - \varepsilon_r(t)) & F_{input}(t) &= S_B E (\varepsilon_i(t) + \varepsilon_r(t)) \\ V_{output}(t) &= C_0 \varepsilon_t(t) & F_{output}(t) &= S_B E \varepsilon_t(t) \end{aligned} \quad (1)$$

where S_B , E and C_0 are respectively the bar's cross-sectional area, Young's modulus, and the elastic wave speed.

As the three waves are not measured at bar-specimen interfaces in order to avoid their superposition, they have to be shifted from the position of the strain gages to the specimen faces, in time and distance. This shifting leads to two main perturbations. First, waves change in their shapes on propagating along the bar. Second, it is very difficult to find an exact delay in the time shifting to ensure that the beginnings of the three waves correspond to the same instant. Those perturbations, if not controlled, can introduce errors in the final result, especially in the range of small strains.

The input force is proportional to the sum of the incident and the reflected wave recorded in the input bar. A correct measure of this force needs that the reflected wave is significantly different of the opposite value of the incident wave. The impedance of the specimen cannot then be too small compared to that of the bars. When soft materials are tested, this condition leads to the use of low impedance bars which are necessarily made of a viscoelastic material.

II -2. Correction for wave dispersion

The wave dispersion effects on longitudinal elastic waves propagating in cylindrical bars have been studied experimentally by Davies [8]. On the basis of the longitudinal wave solution for an infinite cylindrical elastic bar given by Pochhammer [9], and Chree [10], a dispersion correction has been proposed and verified by experimental data. Even though the Pochhammer-Chree solution is not exact for a finite bar, it is found easily applicable and sufficiently accurate [8].

Using the same assumptions, this approach is generalised to the case of bars made of any linear viscoelastic material. As it is presented in [11], the complete solution of the governing equation, with boundary conditions on the external surface of the bars, leads to a frequency equation that gives a relation between the wave number ξ and the frequency ω . This equation takes the same form as the classical one obtained in elasticity. However, in the present case, the argument ξ in the equation is a complex number that represents the complex change in phase function of the frequency ω . Its real part gives the relation between the frequency and the associated phase velocity and its imaginary part gives the relation between the frequency and the associated attenuation coefficient.

The explicit relation $\xi(\omega)$ is found numerically from the frequency equation. The shifting function is then carried out using the Fast Fourier Transformation (FFT) technique [12]. The associated dispersion correction is more important than the correction for an equivalent purely elastic system, in particular because of a significant dumping effect. An example of the influence of this correction is shown in fig. 2a and 2b.

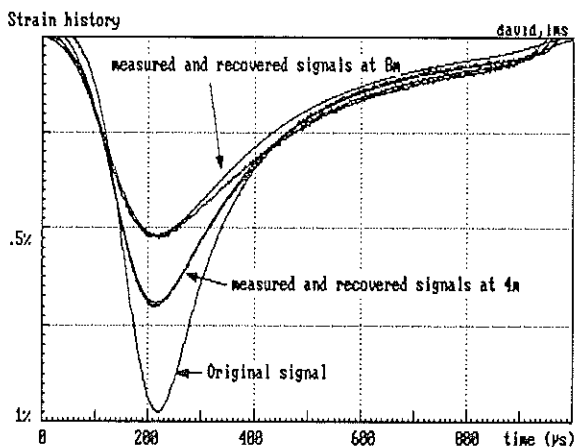


Fig. 2a Example of dispersion effects in a 40 mm diameter PMMA bar.

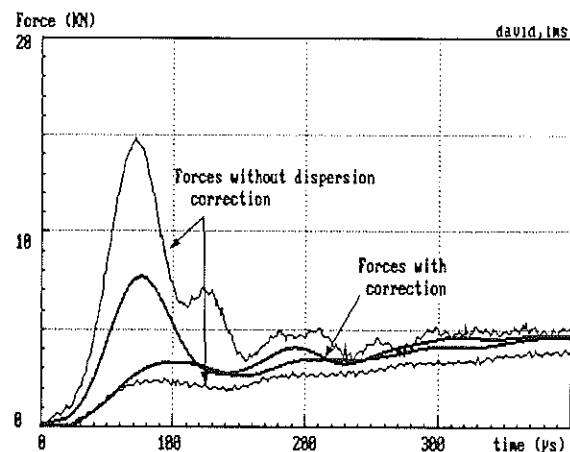


Fig. 2b Influence of dispersion correction on forces measurement (for a 3m long input bar)

III - LARGE STRAIN RANGE TESTING AND MEDIUM STRAIN-RATES.

The measuring technique using bars relies on the knowledge of the two elementary waves propagating in opposite directions. Once they are known, they can be time-shifted to the desired cross-section (barspecimen interfaces for example) to calculate forces and velocities. The SHPB technique uses long bars and a short loading pulse so that there exists a cross-section where the total incident pulse and the first part of reflected waves (of the same duration) can be recorded separately. There exists then a maximum observation duration depending on the length of the bars.

To increase the measuring duration of SHPB, some earlier workers have analysed the multiple reflections in bars. Campbell and Duby [6] have reported a method on the basis of one dimensional elastic wave theory. Lundberg and Henchoz [7] have also proposed a simple explicit formula (within one-dimensional wave propagation assumption) to separate the two elementary waves and to measure the particle velocity after the observation window, using two signals recorded at two different cross-sections in a bar. Recently, this method has found a new application [13] in the prediction of the wave propagation in a bar with a non-uniform impedance (due to a temperature gradient, for instance) and successfully used in high temperature SHPB testing [14,15]. However, as indicated by those authors [6,7], such a method is valid only if the wave dispersion effect can be neglected. This situation is found when the bar is thin and the measuring duration is short (the duration in those works is about 1 ms for a bar of 10 mm diameter).

A new measuring method has been proposed on the basis of a similar analysis but without above limitations [16,17]. An iterative formula allowing for the calculation of the two virtually separated elementary waves for the total desired testing duration is presented, using two signals recorded at two different cross-sections in each bar. It takes into account the wave dispersion effects which are very important for the accuracy of long time measurements. When soft materials are tested, it uses low impedance bars made of a viscoelastic material. The viscoelastic dispersion presented in section II is then very important as shown in [17].

III - 1. TWO STRAIN GAUGES WAVE SEPARATION METHOD

Considering the two elementary waves in a bar, the wave propagating in the positive direction (arbitrarily defined) is named the "ascending" wave and the other one the "descending" wave. The strain $\varepsilon(t)$ at each section is the sum of the contribution of the elementary "ascending" wave $\varepsilon_{asc}(t)$ and that of the elementary "descending" wave $\varepsilon_{des}(t)$.

$$\varepsilon(t) = \varepsilon_{asc}(t) + \varepsilon_{des}(t), \text{ where } C_0 \text{ is the wave speed.} \quad (2)$$

At the section where the strain is measured, a prior knowledge of the contribution of one elementary wave will allow for the calculation of the other one. Knowing how the waves propagate, the "ascending" wave at point B is found by applying the shifting function to the "ascending" wave at point A. In order to exhibit "ascending" and "descending" waves from measurements at two points A and B, an iterative process is built based on the solutions of equ. (2) written at points A and B.

An iterative formula is then constructed and both "ascending" and "descending" waves can be calculated for all the time intervals.

III - 2. APPLICATIONS TO THE DYNAMIC TESTING OF POLYMERIC FOAM.

Recently, the knowledge of the behaviour of low impedance materials (like foams) under crash situations has been needed in the automotive industry and has appeared as an important goal. One particular feature of foam testing is the need for a large maximum strain (up to 80%) in order to study the densification part of the response, associated with a significant increase of the stress. In a conventional SHPB test at quite high strain rates of about 300/s, it is not possible to measure such strains, even if they are easily reached after the measuring phase because of the very low resistance of foam. The difficulty lying in a limited measuring duration is solved with the wave separation method presented above.

A test on polymeric foam (a specimen of 40 mm of length and 40 mm of diameter) using a common Nylon SHPB with two 3m bars of a diameter of 40 mm is taken for an example. The measurable duration is about 12 ms, which is 10 times the initial SHPB measuring duration (about 1.2 ms) for this set-up. In terms of measurement duration, it is as if two bars of 30m long had been used. The deduced average stress-strain relation is shown in Figure 3. The material behaviour is measured up to a strain 3 times larger than for a conventional SHPB. Since there is a periodic loading due to the round trip of the incident wave in the input bar, 4 loading-unloading cycles are observed. Unloading and reloading curves do not follow exactly the same path, which is in agreement with known material characteristics and gives confidence in the accuracy of the measurement. If the unloading has to be avoided, one just has to use a different and better adapted loading device such as the "slow bar" [17], which allow tests at medium strain rates (5/s to 50/s). A comparison of results at 250/s and at 30/s is given in the figure 4, showing the strong rate sensitivity of the tested foam.

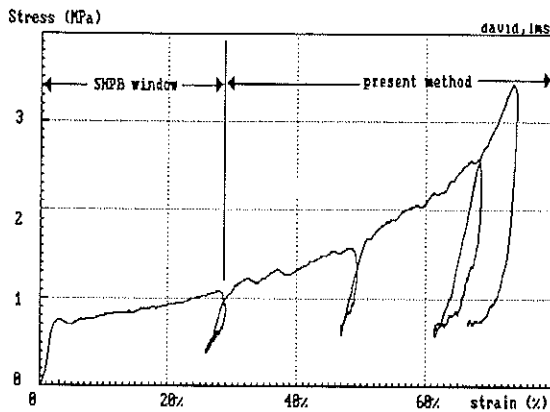


Fig.3 Average stress-strain relation of the foam

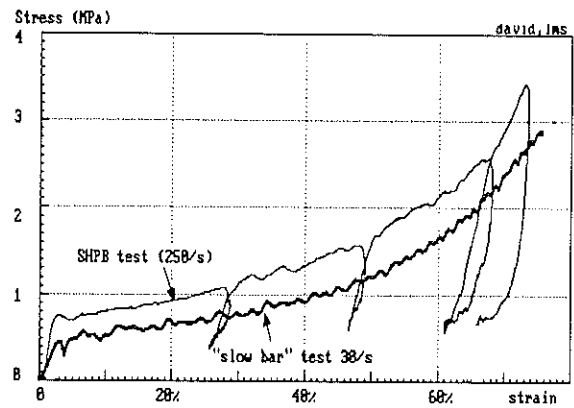


Fig.4 Strain rate effects on foam at medium strain rates

IV. MATERIAL BEHAVIOUR IDENTIFICATION

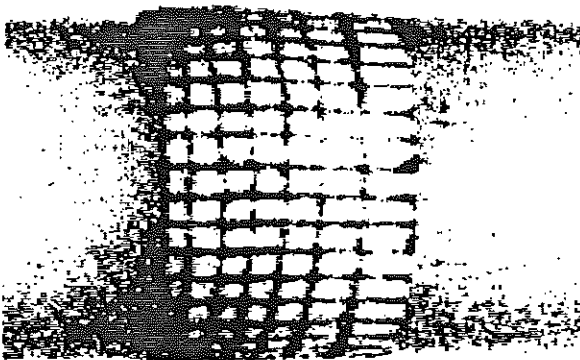


Fig. 5 High speed camera frame of a foam specimen under dynamic loading. (black lines are equidistant in the unloaded state)

The Split Hopkinson pressure bar arrangement can give very accurate measurements of forces and velocities at both sample faces if the data processing is carefully performed. There remains the second kind of problems of SHPB mentioned in the introduction, which consist of relating material properties to measured forces and velocities at the two specimen faces. The classical analysis assumes the axial uniformity of stress and strain fields in the specimen. Such an hypotheses is no more valid, at least when input and output forces are no more equal as shown in fig 2b, at least in the first third of the test. It can be deduced that strain-rate and strain fields will be also non-homogeneous as it is observed in fig. 5.

It is then necessary to develop a method which permits relating the material behaviour to the measured forces and velocities without assumption of uniformity.

A SHPB test provides superabundant measurements that are forces and velocities at both ends of the specimen. Accordingly, an identification technique based on an inverse calculation method [18] can be introduced. The complete theoretical process is presented in [19] and [20].

An obvious key point of the method is that a parametric model of the tested material is needed. For the foam we have tested (a test result is presented in fig. 2b), we have not yet found such a model. An example of the inverse approach is then presented for a Hopkinson test of salt-rock.

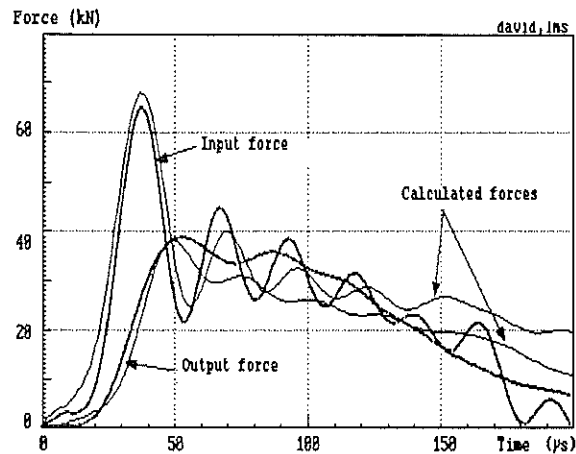


Fig. 6a. Simulated forces and real forces for salt

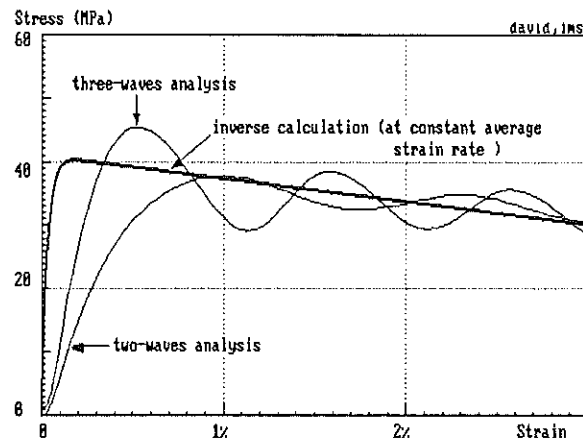


Fig. 6b Stress-strain curves from different analyses

In Fig. 6a, comparison for salt rock between the measured forces and the calculated ones is shown. The chosen model, with the set of parameters that give the best agreement with experimental data, can be considered as the representative model of the specimen in this test. As a result, the stress and strain fields in the specimen are known so that a stress-strain curve is found and can be given for a constant strain rate through the identified model. In our example, the stress-strain curve obtained with this method is compared with those of *two-waves* or *three-waves* classical SHPB analysis. Those two curves are quite far from that of the present method (Fig. 6b). As a result, the inverse calculation technique is the only way to obtain accurate results for this type of materials.

V. CONCLUSION

Some foam materials used in automotive industry dummies are low impedance materials that can support large strains and show a strong strain-rate effect. Testing and modelling such materials at high strain rates leads to solve special difficulties.

- a) Because of low impedance, Hopkinson bars made of low impedance materials are used.
- b) Because of large strains and low strain-rates often requested, a two strain gauges wave separation method is used.

In both cases, the use of a visco-elastic waves' correction dispersion theory is needed.

- c) Because of the strong strain-rate effect, measured input and output forces are sometimes significantly different and SHPB analysis has to be done using an inverse method.

Those techniques are available in our laboratory allowing for a valuable testing of soft materials at large strains and high and medium strain-rates.

REFERENCES

- [1] B. Hopkinson, A method of measuring the pressure in the deformation of high explosives by the impact of bullets, *Phil. Trans. Roy. Soc.*, 1914, Vol. A213, pp. 437-452.
- [2] R.M. Davies, A critical study of Hopkinson pressure bar, *Phil. Trans. Roy. Soc.*, 1948, Vol. A240, pp.375-457.
- [3] H. Kolsky, An investigation of the mechanical properties of materials at very high rates of loading, *Proc. Phys. Soc.*, 1949, Vol. B62, pp. 676-700.
- [4] J. Harding, E.D. Wood, J.D. Campbell, Tensile testing of materials at impact rates of strain. *J. Mech. Engng. Sci.*, 1960, Vol. 2, pp. 88-96
- [5] J. Duffy, J.D. Campbell, R.H. Hawley, On the use of a torsional split Hopkinson bar to study rate effects in 1100-0 aluminium, *J. Appl. Mech.*, 1971, Vol. 38, pp. 83-91
- [6] Campbell, J.D. and Duby, J. (1956), The yield behaviour of mild steel in dynamic compression. *Proc. R. Soc. Lond.*, **A 236**, 24-40.
- [7] Lundberg, B. and Henchoz, A. (1977) Analysis of elastic waves from two-point strain measurement. *Exper. Mech.* **17**, 213-218.
- [8] R.M. Davies, A critical study of Hopkinson pressure bar. *Phil. Trans. Roy. Soc.*, 1948, Vol. A240, pp. 375-457.
- [9] L. Pochhammer, Uber die fortpflanzungsgeschwindigkeiten kleiner schwingungen in einem unbergrenzten isotropen kreiszylinder, *J. für die Reine und Angewandte Mathematik*, 1876, Vol. 81, pp. 324-336.
- [10] C. Chree, The equations of an isotropic elastic solid in polar and cylindrical coordinates, their solutions and applications, *Cambridge Phil. Soc. Trans.* 1889, Vol. 14, pp. 250-369.
- [11] H. Zhao G. Gary, A three dimensional longitudinal wave propagation in an infinite linear viscoelastic cylindrical bar. Application to experimental techniques, *J. Mech. Phys. Solid*, Vol 43, 1335-1348, 1995
- [12] H.ZHAO, G.GARY, J.R. KLÉPACZKO, On the use of a viscoelastic split Hopkinson pressure bar, *Int. J. Impact Engng.* **19**(1997), 319-330.
- [13] Lundberg, B., Carlsson J. and Sundin K. G., Analysis of elastic waves in non-uniform rods from two-point strain measurement. **137** (1990), 483-493.
- [14] Bacon, C. Färm, J. and Lataillade, J.L. Dynamic fracture toughness determined from load-point displacement, *Exper. Mech.*, **34**(1994), 217-223.
- [15] Lataillade, J.L., Bacon, C., Collombet, F. and Delaet, M. Wave Propagation and Emerging Technologies. (Eds. W.K.Kinra, R.J. Clifton and G.C. Johnson). AMD-Vol. 188, (1994). 85-93.
- [16] H.ZHAO, G.GARY, Large strain range dynamic testing at high and medium strain rates, using a common scale SHPB. *Journal de Physique IV*, **7**(1997), C3, 341-346.
- [17] H.ZHAO, G.GARY, A new method for the separation of waves. Application to the SHPB technique for an unlimited measuring duration. *J.Mech.Phys.Solids.* **45**(1997), 1185-1202.
- [18] H.D. Bui, Introduction aux problèmes inverses en mécanique des matériaux. Editions Eyrolles, Paris 1993 // English translation, Inverse problems in the mechanics of materials: an introduction, CRC Press, Boca Raton, 1994.
- [19] L. Rota, An inverse approach for identification of dynamic constitutive equations, Proceedings of the 2nd international symposium on inverse problems - ISIP'94, A.A.Balkema, Rotterdam, Brookfield, 1994.
- [20] L.ROTA, Application de Méthodes Inverses au Dépouillement de l'Essai aux barres de Hopkinson, *Thèse de Doctorat de l'Ecole Polytechnique*, 21 février 1997

High strain rate deformation of polymers; Inverse method

N. BILLON

*CEMEF – EMP, UMR CNRS 7635, BP 207 06904 Sophia Antipolis
(France)*

I – INTRODUCTION

Due to their process ability and specific mass, polymers are more and more used in engineering applications. In that field, considerable attention must be paid to their performance for impact loading situations.

In parallel, many engineering thermoplastics exhibit a large deformation even during impact (e.g., 100 to 1000 s⁻¹)¹⁻⁸, whereas their mechanical behaviour at high strain rate and large strain is not yet modelled in a satisfactory way.

This study deals with this particular point and concerns different types of ductile polymers. It will be first stated that simple laboratory tests are inaccurate to model the performance of polymeric parts under actual loading. The main remaining problems will be described and the use of inverse methods, which appears to be a convenient alternative, will be illustrated

II – MECHANICAL BEHAVIOUR OF POLYMERS

II – 1. Description

Typical behaviour of ductile polymers in their solid state (excluding rubber-like materials) consists of four or five successive phases, the relative importance of which depend on the material, the strain rate and the temperature.

Low deformations (up to approximately 0.1 to 0.2) are mainly reversible and visco-elastic. Above an apparent yield point the deformation is irreversible (at least in the time scale of the experiment) (fig. 1). As plastic deformation is initiated a strain softening process (fig. 1b) is sometime observed. Then, an important plastic flow occurs (up to strain of 2 or 3) which induces an important anisotropy in the material and very specific strain hardening effects. This often results in stable neck propagation during tensile tests but also during impact¹⁻⁸.

This schematic description is valid whatever the loading conditions are (tension, compression or torsion). But, aside from this qualitative agreement, significant differences exist. Compressive yield stress is higher than others are. Strain hardening, which is related to induced anisotropy, is noticeably dependent upon loading conditions (fig. 1b).

In parallel, this behaviour depends on strain-rate and temperature even at very low strain rate and for small difference of temperature (fig. 1a). Due to relaxation phenomena (e.g., glass transition) this dependence can be more or less important, depending on the range of strain

rate or temperature encountered. Additionally, dependence upon strain rate, temperature and pressure are so tightly linked that it is often difficult to even predict whether the polymer will be in its glassy or in its rubber state during impact.

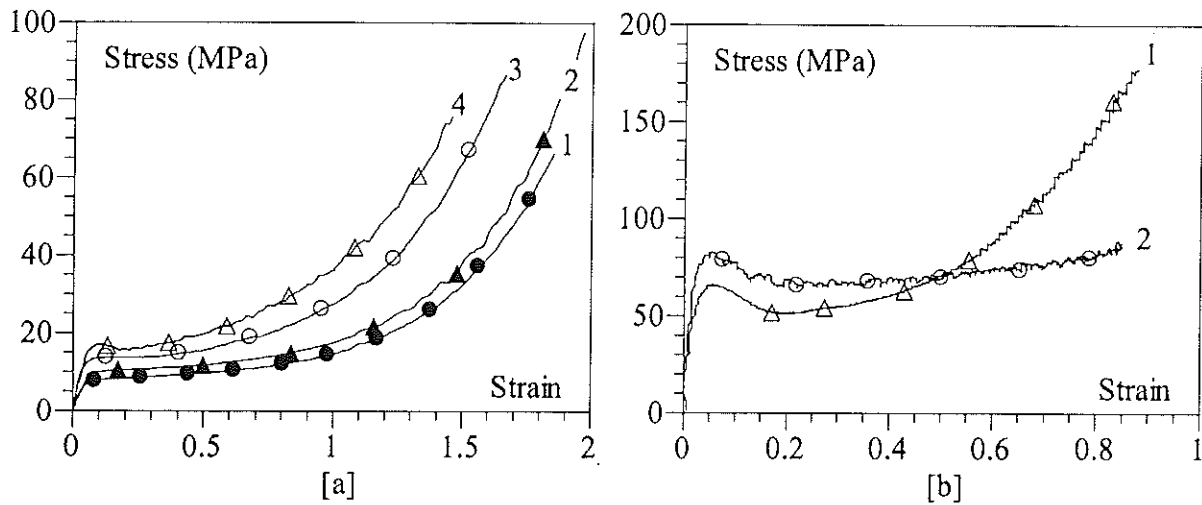


Figure 1. Typical behaviour of ductile polymers.

- a) Dependence upon strain rate and temperature: case of a toughened polypropylene¹; (1) 50°C, 10⁻⁴ s⁻¹; (2) 50°C, 10⁻³ s⁻¹; (3) 25°C, 10⁻⁴ s⁻¹; (4) 25°C, 10⁻³ s⁻¹.
- b) Dependence on loading conditions: case of a polycarbonate² (25°C, 10⁻⁴ s⁻¹); (1) Tension; (2) Compression

II – 2. Characterisation

The way in which a polymer can be (and must be) experimentally characterise is mainly conditioned by the above physical characteristics. Strain hardening effects make its necessary to perform measurement at high level of strain and with different loading conditions. Necking implies the uses of specific devices to determine local mechanical parameters. Dependence upon strain rates imposes to explore a wide range of strain rate.

Unfortunately, plastic flows at high strain-rate are not isothermal experiments. As a matter of fact, heat dissipation occurs. Due to the low thermal conductivity of polymers this results in a significant increase of the average temperature of the polymer and in an important thermal gradient in the sample. Taking into account usual evolution of constitutive parameters versus temperature, this effects can induce a significant thermal softening of the material and a none homogeneous deformation in the specimen. It is then impossible to unambiguously deduce intrinsic data from the measurements.

This can be illustrated using infrared analysis during tensile tests. The temperature of the lateral surface of the sample is then estimated without disturbing the test. As soon as the yield point has been reached the measured temperature increases (fig2. a). This effect, which can be noticeable (several tens of degrees) for strain-rate as low as 10⁻² s⁻¹, depends on the strain rate (fig2. b) and can result in a significant softening of the material.

Consequently, experimental characterisation of polymers should be performed accounting the fact that thermal softening can be important at rate higher than 10⁻² s⁻¹. Adiabatic assumption, considering "usual" samples a few millimetres thick, is valid above 1 s⁻¹.

To conclude, polymers have to be characterised using *local measurements* for the strain (due to the neck), *simple loading* to enable both local measurements and simple manipulations of data, *controlled temperatures and low strain-rates* to avoid self-heating. Conversely, complex and rapid loading should be analysed in order to promote accurate deformation mechanisms (i.e., equivalent to impact).

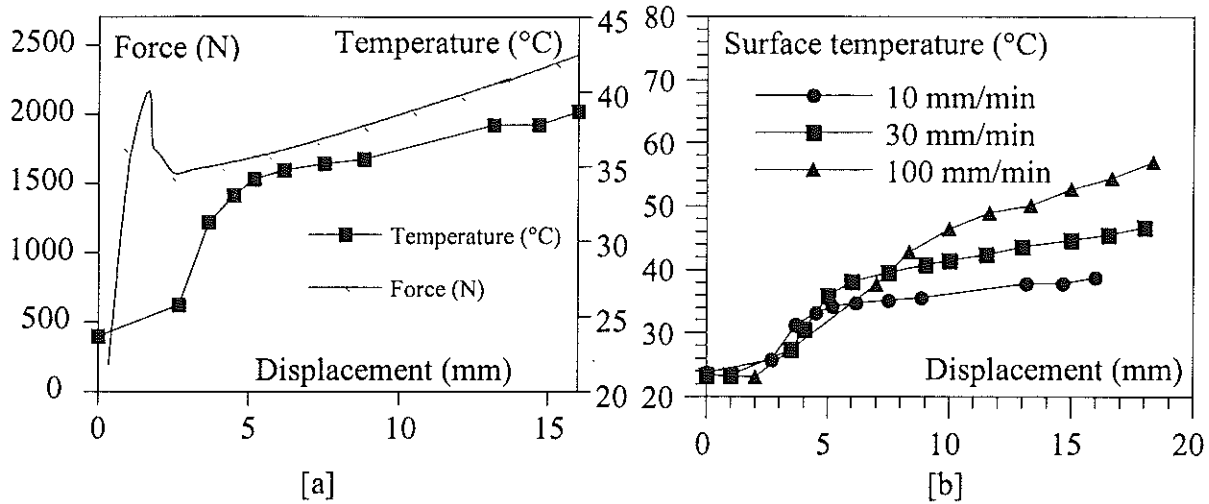


Figure 2. Tensile behaviour of a polycarbonate⁹; Sample diameter and initial temperature are 6 mm, and 23 °C, respectively.

- a) Comparison between the force (○) and the temperature at the surface (■) vs. displacement; Cross-head velocity is 10 mm/min (initially 0.02 s⁻¹).
- b) Temperature vs. displacement as a function of cross head velocity.

At this stage, a solution to characterise impact properties of polymers consists in the extrapolation and in successive adjustments of simple (and rigorous) measurements to complex loading. This implies the use of numerical simulations and, consequently, of constitutive models.

II – 3. Modelling

Each stage of the behaviour (visco-elasticity, yield) has been partly modelled using physical approach in the past. As far as the total behaviour (including low strain as well as high strain) is concerned, the most complete approaches are, nowadays, phenomenological laws. Several models exist whose accuracy is often equivalent¹⁰⁻¹⁴. They are either purely viscoplastic equations or combination of an initial linear elastic deformation and a viscoplastic flow. This latter is often modelled assuming the polymer to be homogeneous, isotropic and to obey the von Misès flow rule. Some examples are given below:

$$\sigma = \sigma_s + \sigma_0 \left(\exp\left(\frac{\epsilon^p}{\epsilon_c}\right) - 1 \right) + \beta \ln\left(\dot{\epsilon}\right) \quad (1) \ 10$$

$$\sigma = K_1 \left[\exp(2\epsilon^p) - \exp(-\epsilon^p) \right] + K_2 \left[\exp(\epsilon^p) - \exp(-2\epsilon^p) \right] - \beta \ln\left(\frac{\dot{\epsilon}}{\dot{\epsilon}_0}\right) \quad (2) \ 8, \ 11$$

$$\sigma = K \exp\left(\frac{a}{T}\right) (1 - \exp(W\epsilon)) \exp(h\epsilon^n) \dot{\epsilon}^m \quad (3) \ 12, \ 13$$

$$\frac{d\sigma}{d\dot{\epsilon}} = E \left[1 - \exp \left[\frac{W(\sigma - K_1 [\exp(2\epsilon^P) - \exp(-\epsilon^P)] - K_2 [\exp(\dot{\epsilon}^P) - \exp(-2\dot{\epsilon}^P)] - \sigma_e^*)}{kT} \right] \frac{\epsilon}{\dot{\epsilon}_e^*} \right] \quad (4)^{14}$$

$$\sigma = K_s \left(1 + \vartheta \epsilon_p \exp(-w \epsilon_p^2) \right) + K \exp\left(\frac{a}{T}\right) \exp(h \epsilon_p^2) \dot{\epsilon}^m \quad (5)^8$$

where σ , ϵ , ϵ^P , $\dot{\epsilon}$, E and T are the stress, the total strain, the plastic part of the strain, the strain rate, the Young's modulus and the temperature, respectively.

III – APPLICATION TO IMPACT

III – 1. Introduction

Whatever the chosen "constitutive" equation is, the modelling of impact implies two steps of extrapolation for the data: from low to high strain rate and from simple to complex loading.

Concerning the "strain rate extrapolation", it must be emphasised that the range of rate that can be analysed is very narrow compared to the range encountered during impact. Generally, simple equations which can be deduced from low velocity measurements (e.g., power law (eq. (3) or (5)) or Eyring law (eq. (1) or (2)) do not allow to reproduce the behaviour of polymers over more than six decades of strain rates. This is well illustrated with a polycarbonate at room temperature (fig. 3a). Measurements are performed in compression, combining a hydraulic apparatus and the Split Hopkinson Pressure Bar technique. It is verified that stress wave propagation effects are negligible at high strain rates¹⁵. Taking into account temperature and strain rate it can be stated that the material is always in its glassy state. Even in that "simple" case, extrapolation of low velocity measurement over strain rate is almost impossible.

Concerning the "loading extrapolation", it is obvious that simple laws, as those presented here, cannot model behaviour where induced anisotropy is important. Generally, tensile measurements are not accurate to model impact loading.

Consequently, one generally fails in modelling rapid and/or complex loading using data obtained during low velocity tensile tests (fig. 3b and 4). From a scientific point of view constitutive equation should be revisited. An alternative solution is to adjust the parameters to get a better agreement. In both these two cases, data have to be re-identified at strain rates and loading equivalent to those to be modelled.

III – 2. Inverse methods

To achieve that point, inverse methods have been developed accounting heat dissipation and none homogeneous deformation. It is based on a 2-D axisymmetrical FEM direct model (FORGE2[®]) in which the equilibrium equations are obtained by the minimisation of a dissipation functional, with respect to velocity. Incompressibility is enforced using a penalty method. Friction between the material and the experimental device can be taken into account. The temperature in the polymer is calculated assuming a Fourier conduction law and taking into account energy dissipation, thermal conductivity of the polymer and thermal exchanges with metallic clamping device (conduction) and surrounding air (involving convection and radiation phenomena). The air and the metal are assumed to be isothermal. A Galerkin method is used. The calculations are performed using small steady-like deformation steps.

The parameters are adjusted by minimising a cost function using a gradient method. This function accounts the force and optionally (for tensile tests only) the diameter. Its derivatives with respect to constitutive parameters are estimated using a finite difference scheme.

This technique enables to identify constitutive parameters and to reproduce rapid tensile tests (fig. 3b) using classical constitutive model (Eq. (3)). In the case of more complex loading, such as dart test experiments (impact of a hemispherical mass falling on a plaque (fig. 4)), quantitative agreement can be obtained only by revisiting equation, i.e. Eq. (3), to take into account a less important strain hardening process, e.g.:

$$\sigma = K_p (1 - \exp(W\epsilon)) (1 + h_1 \epsilon + h_2 \epsilon^2) \dot{\epsilon}^m \quad (6)^9$$

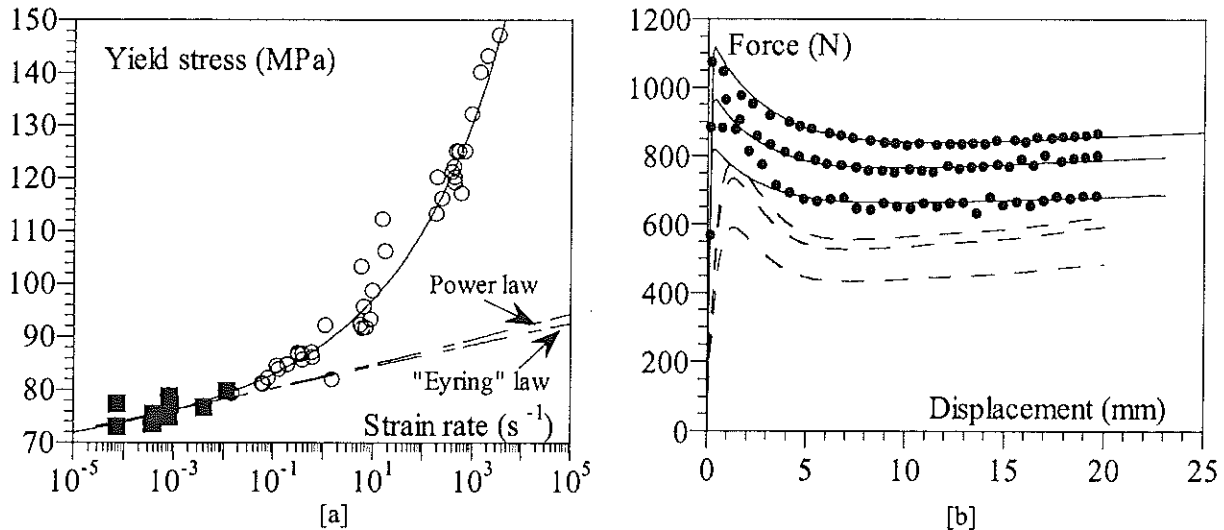


Figure 3. Behaviour of polymer over a wide range of strain rates.

- Case of a polycarbonate¹⁵: comparison between experimental yield stress (symbols) and extrapolations of simple laws (dotted lines) determined using low strain rate measurements (black squares).
- Case of a polyethylene⁹: Tensile tests at constant cross-head velocities; Comparison between experiments (symbols) and simulations (Eq. (3)) using low velocity measurements (dotted lines) or data identified using inverse method (plain lines). *Velocities are 2.5 mm/min (initially 5 10⁻³ s⁻¹), 5 mm/min (initially 10⁻² s⁻¹), 10 mm/min (initially 2 10⁻² s⁻¹), respectively.*

It must be noticed that in such a case, mechanical measurements require a good knowledge of physical properties of the material on one hand (density, heat capacity, heat conductivity and amount of work transformed into heat) and of the thermal exchanges with the surrounding medium on the other hand. Unfortunately, the fraction of work stored within the material is generally partly unknown, especially at high strain rates. This represents a key point to be studied in the future.

IV – CONCLUSION

Characterisation of impact behaviour of polymers cannot be done using simple laboratory tests. High strain rate test involving complex loading should be performed. These experimental conditions do not allow to extract accurate data using classical methods. Consequently, the development of inverse methods seems to be necessary.

Nevertheless, these methods only make it possible to determine parameters. They are not able to propose more accurate constitutive equations. Three main problems have to be solved in that field:

- evaluating the amount of work transformed into heat;

- accounting the effect of hydrostatic stress;
- accounting the strain hardening process.

In conclusion, work has to go on in three main directions:

- the determination of physical mechanisms involved in the plastic deformation;
- the proposal of more accurate constitutive equations;
- the experimental determination of parameters.

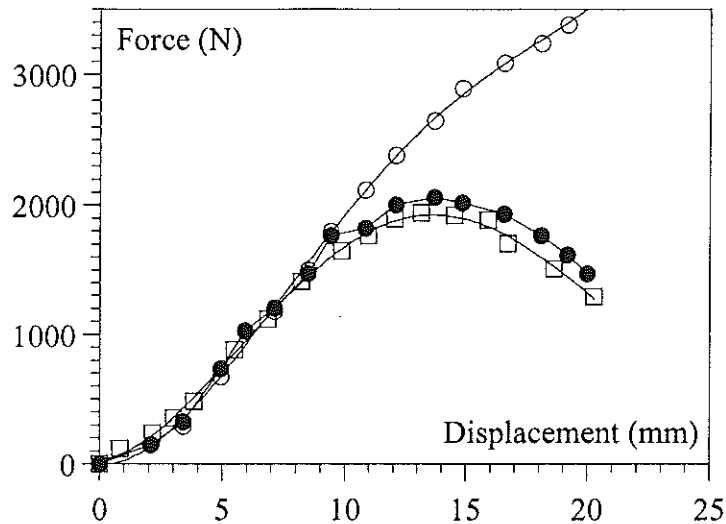


Figure 4. Behaviour of a polypropylene⁹; 50 mm/min, 2 mm-thick plaque; Comparison between experiments (●) and simulations using data obtained in tension at equivalent strain rate (○) and with the inverse analysis of puncture test (□).

- [1] N. Billon , L. Maurin, Y. Germain, In Proc. 1st International Conference on Mechanics of Time Dependent Materials, SEM, Ljubljana (Slovenia), 293(1995)
- [2] N. Billon, J. M. Haudin, Polym. Eng. Sci., **37**, 1761 (1997)
- [3] R. P. Nimmer, Polym. Eng. Sci., **23**, 155 (1983)
- [4] S. D. Sjoerdsma, J. P. H. Boyens, J. J. Mooji, Polym. Eng. Sci., **25**, 250 (1985)
- [5] W. M. Lee, W. W. Predebon, M. L. Jurosek, in “ Instrumented Impact Testing of Plastics and Composite Materials “, ASTM STP 936, 302 (1987)
- [6] T. M. Liu, W. E. Baker, Polym. Eng. Sci., **31**, 753 (1991)
- [7] O. Schang, J. M. Muracciole, F. Fernagut, N. Billon, Polym. Eng. Sci., **36**, 541 (1996)
- [8] M.L. Bisilliat, Thesis, Ecole des Mines Paris, France (1997)
- [9] Y. Tillier, Thesis, Ecole des Mines de Paris, France (1998)
- [10] M. Belcadi Thesis U. de Poitiers, ENSMA (1990)
- [11] J. M. Andrew, I. M. Ward, J. Mater. Sci., **5**, 411(1970)
- [12] C. G'Sell C, J.J. Jonas, J. Mater. Sci., **14**, 583(1979)
- [13] C. G'Sell,, Revue de Physique Appliquée **23**, 1085 (1988)
- [14] C. G'Sell, J.J. Jonas, J. Mater. Sci., **16**, 1956 (1981)
- [15] M.L. BISSILIAT, G. GARY, J.R. KLEPACZKO, N. BILLON. Proc. 10th Int. Conf. On Deformation Yield and Fracture of Polymers, Cambridge (UK) 203 (1997)

Effets des chargements dynamiques sur le comportement au crash des structures tubulaires.

Etude expérimentale et numérique.

ABAH L. *, LIMAM A. *

*URGC Structures, INSA-Lyon, France

email : abah@gcu-beton.insa-lyon.fr

Resumé:

Des tubes en alliage d'aluminium AA6060 T5 de sections différentes ont été testés pendant des chargements quasi statiques d'une part et dynamiques d'autre part, afin d'étudier l'influence de la vitesse de déformation sur leur comportement au crash ainsi que l'énergie cinétique absorbée sous forme d'énergie de déformation issue des cinématiques de membrane et de grandes rotations.

Les essais dynamiques présentent des imperfections provenant des interférences des vibrations d'une partie du banc d'essai dans l'acquisition des données. La modélisation numérique tenant compte de certains éléments adjacents à la structure permet de confirmer cette constatation.

Introduction

Ces dernières années, de nombreuses recherches sur le comportement au crash dynamique des structures de formes diverses ont été effectuées; elles ont toutes pour objet d'augmenter les chances de survie des passagers dans différents types de véhicules (voitures, trains, avions, ...). Ces chances de survie passent par la diminution de la charge (décélération) transmise à l'occupant par le véhicule quand celui-ci entre en collision avec un obstacle, soit en modifiant la structure assemblée en changeant la géométrie de ses éléments ou leur forme, soit en ajoutant sur ces structures des dispositifs « limiteur de charge » afin de mieux absorber l'énergie cinétique.

Dans l'optique de faire des voitures plus légères sans mettre en péril la sécurité des usagers, l'industrie automobile s'est penchée sur la conception des structures et des habitacles en alliages d'aluminium. Ces alliages présentent l'avantage d'avoir une masse volumique 3 fois moins élevée que celle de l'acier doux qui était jusqu'alors utilisé, ce qui permet d'avoir des gains de poids considérables comme le rapporte Nardini et Seeds [NAR 89]. Cette étude montre que l'alliage d'aluminium AA6060 T5 présente un comportement au crash différent de celui des structures en acier. Une constatation du même ordre a aussi faite par Langseth et Hopperstad [LAN 96] pour des structures en alliages d'aluminium AA6060 T4 , T4* et T6.

1. Caractéristiques mécaniques

Des essais de traction réalisés sur des éprouvettes normalisées ont donné des résultats reproductibles. Les valeurs obtenues sont résumées dans le tableau ci-dessous :

E (MPa)	ν	σ_L (MPa)	$\sigma_{0.2}$ (MPa)	σ_u (MPa)	ϵ_u
56500	0.34	90	194	239	9 %

Tableau 1: Caractéristiques de l'éprouvette n° 3.

E représente le module d'élasticité du matériau.

$\sigma_{0.2}$ est la contrainte à 0.2 % de déformation, ou contrainte limite d'élasticité.

σ_L est la contrainte à la limite de linéarité du matériau.

2. Essais statiques.

Des essais statiques ont été réalisés sur des éprouvettes de longueur variable. Deux types de sections ont été testés. Ces essais ont permis de connaître les caractéristiques de crash de ces structures tubulaires après un chargement axial.

2.1 Résultats expérimentaux et interprétations.

La sollicitation appliquée à la structure est de type compression axiale. La structure est soumise à des conditions aux limites sont de type encastrement parfait sur l'extrémité inférieure, tandis que la charge est appliquée sur l'extrémité supérieure.

La valeur de l'effort moyen P_{moyen} représentée dans les tableaux ci-dessous est calculée à partir de la formule suivante :

$$P_m = \frac{\int_0^{L_f} P dl}{L_f}, \text{ où } L_f \text{ est l'écrasement du tube.}$$

Le calcul sera fait pour une longueur L_f égale à 100 mm pour tous les tubes de section 48x48 mm² et 120 mm pour les tubes de section 78x78mm². L'énergie spécifique qui représente une caractéristique de la capacité d'absorption d'énergie d'un tube indépendante de la longueur d'écrasement. Elle est calculée de la façon suivante:

$$E_s = \frac{E_{abs}}{M_{L_f}}, \text{ } E_{abs} \text{ est l'énergie absorbée, } M_{L_f} \text{ est la masse de la longueur de tube déformée.}$$

2.1.1 Tubes carrés de section 48x48 mm².

Le mode d'écrasement symétrique compact quasi inextensionnel comme l'ont défini Abramovicz et Wierzbicki [ABR 89] a été observé. Le tableau ci-dessous résume les principales caractéristiques de crash qui ont été relevées et calculées à partir des essais statiques. Les valeurs moyennes obtenues et notées dans le tableau ci-dessous sont représentatives de tous les tubes, à cause du faible écart type de chaque caractéristique. Les écarts types constatés sur le premier pic et sur l'effort moyen permettent de déduire un comportement reproductible du carré sans ouverture soumis à une compression axiale.

TUBES SANS OUVERTURE						
N° ESSAI	Force (kN)					
Moyenne	78.1	27.3	203.4	2729	26.3	39.9
Ecart - type	0.76	1.02	1.9	114	0.98	2.2

Tableau 2.1.1 : Résultats obtenus.

2.1.2 Tube de section 78x78 mm².

La valeur moyenne du 1^{er} pic obtenue pour ces tubes est de 90.4 kN, elle est plus élevée de 14% par rapport aux tubes de section 48x48 mm²; Les figures ci-dessous montrent que pour certains tubes, il y a eu mélange de deux modes de déformation à savoir le mode compact et le mode non compact.

Le rapport épaisseur sur coté vaut $t/C = 0.0256$. Mahmood et Paluzny [MAH 83] avait déterminé de façon une valeur limite $t/C = 0.016$ en dessous de laquelle il y a développement du mode de déformation non compact de déformation. Pour ces tubes, ce rapport est légèrement supérieur à cette valeur limite, c'est pourquoi le mode de déformation de plusieurs tubes est un mélange des deux modes compact et non compact (voir figures ci-dessous).

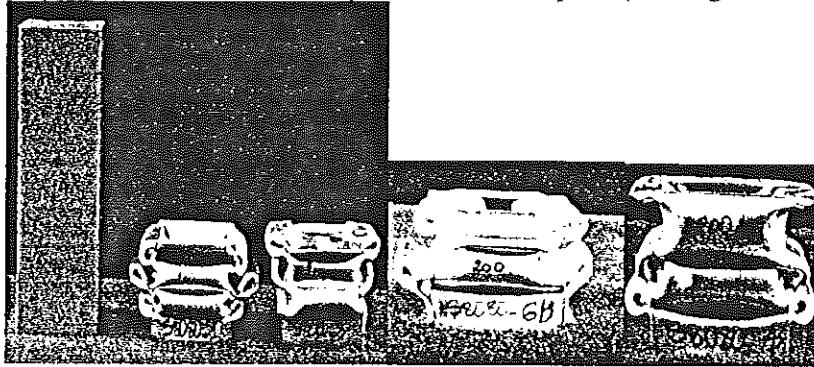


Figure 2.1.1: Déformées obtenues.

Dans le cas des tubes de section 80x80 mm², la longueur d'écrasement retenue pour le calcul d'énergie est de $L_f = 120$ mm. L'effort moyen est calculé comme dans le paragraphe précédent.

S8080	P_{max} (kN)	σ_{cr} (MPa)	P_{moyen} (kN)	E_{abs} (J)	E_s (J/g)	1 ^{er} pli (mm)
Moyenne	90.4	145	29.0	3499	17.2	65
Ecart type	4.8	7.7	3.1	353	1.8	5

Table 2.1.2 : Résultats obtenus.

2.2 Essais dynamiques

2.2.1 Tubes carrés 48x48 mm²

Les essais ont été réalisés à des vitesses d'impact variant entre 7 m/s et 15 m/s. Dans certains cas l'énergie cinétique a été maintenue constante, en modifiant juste la masse d'impact et sa vitesse.

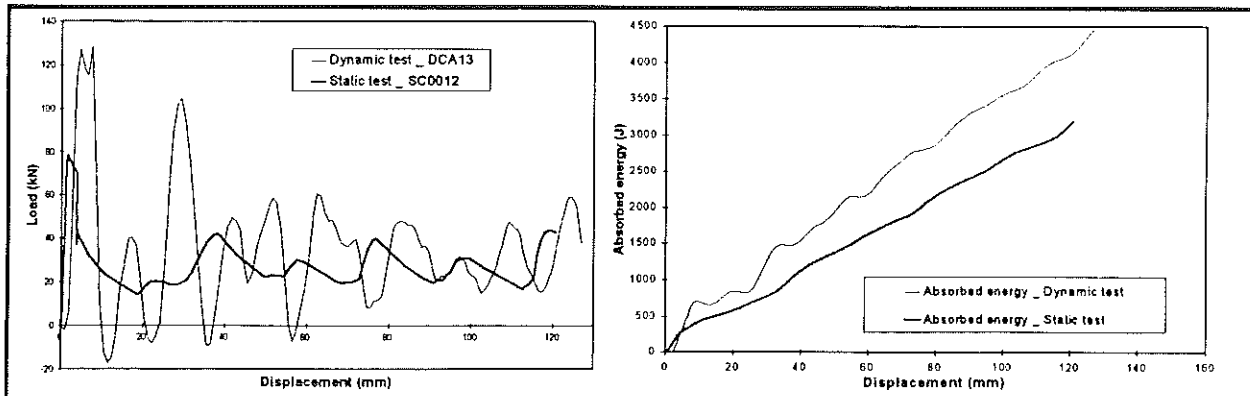


Figure 2.2.1 : Caractéristiques statiques et dynamiques.

La comparaison des résultats d'essais dynamiques et ceux des essais statiques montre des écarts de 40 % sur le premier pic et de 22 % sur l'énergie absorbée, comme le montre l'étude réalisée par Abah et Limam [ABA 98b].

La formule mise au point par Wierzbicki et Abramovicz [WIE 81] pour évaluer la vitesse de déformation a été utilisée. Sous les hypothèses du mode de déformation symétrique quasi inextensionnel [WIE 83], Abramovicz et Jones [ABR 84a] ont établie une formule directement applicable à partir des caractéristiques géométriques C de la structure extrudée et de la vitesse d'impact V: $\dot{\epsilon} = 0.33 \frac{V}{C}$.

Le graphe ci-dessous représente le rapport entre l'énergie spécifique dynamique et l'énergie spécifique statique en fonction des vitesses des déformation obtenues :

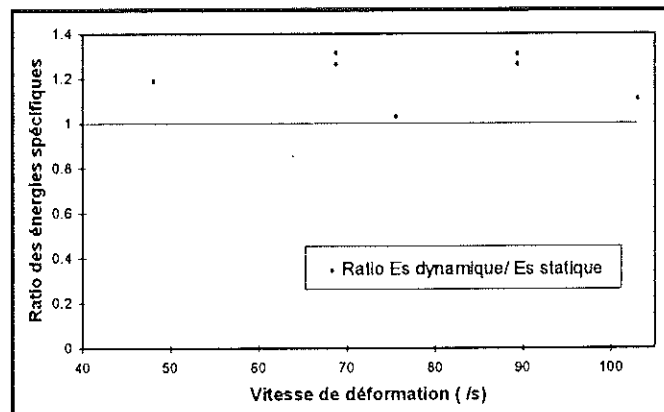


Figure 2.2.1: Effet de la vitesse de déformation.

Les différentes vitesses de déformation n'ont pas considérablement modifié l'énergie spécifique des structures impactées.

2.2.2 Tubes carrés 78x78 mm².

La vitesse de chargement a modifié le mode déformation des ces structures; pour des vitesses de l'ordre de 15 m/s, les tubes de longueur 530 mm ont développé un mode axial de déformation dès que l'impacteur est entré en contact avec l'éprouvette. Ce mode axial a influencé imposé la formation du mode compact de déformation. Les tubes qui n'ont développé ce mode axial, ont subi le flambage de type Euler.

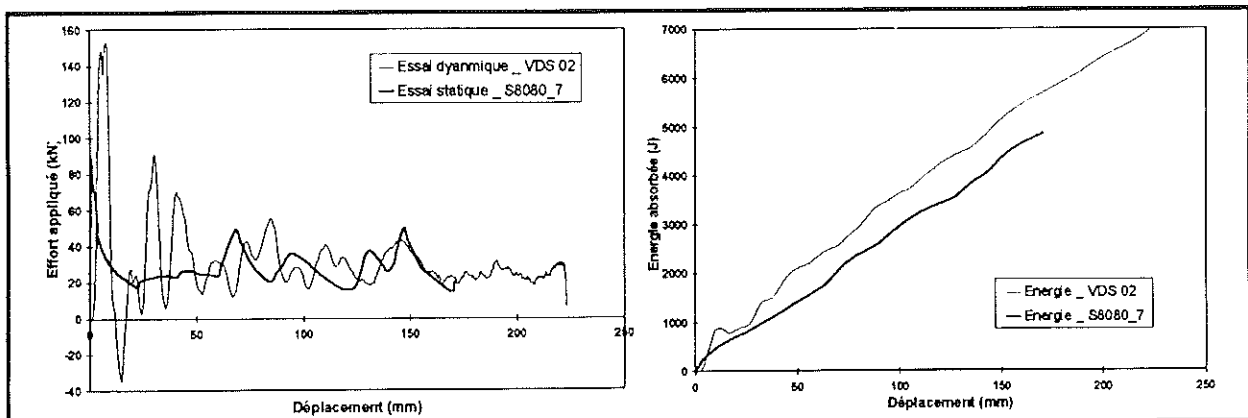


Figure 2.2.2: Comparaison des résultats statiques et dynamiques.

Les valeurs des caractéristiques dynamiques sont aussi plus élevées par rapport aux valeurs des caractéristiques statiques. Les écarts sont de 46 % sur le premier pic et de 18 % sur l'énergie absorbée.

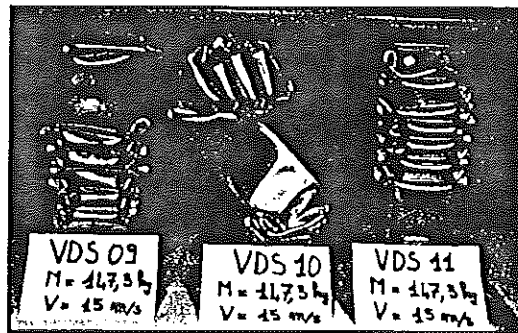


Figure 2.2.2.a: Modes de déformation.

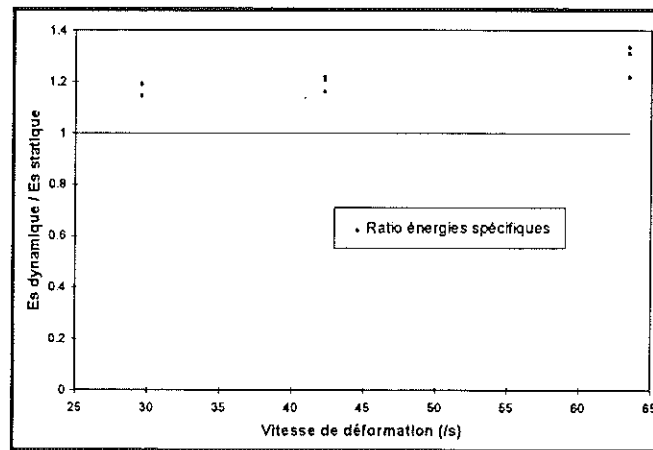


Figure 2.2.2.b: Effet de la vitesse de déformation.

La figure ci-dessus montre que l'énergie absorbée par les tubes impactés à 15 m/s est supérieure de 12 % en moyenne à celle des tubes impactés à 10 m/s.

Toutefois la vitesse de déformation n'influence pas beaucoup la capacité d'absorption d'énergie de ces tubes car pour les deux types de section, malgré le niveau atteint la vitesse de déformation, c'est uniquement les déformées des tubes qui sont différentes. L'énergie absorbée reste relativement constante. La différence entre les résultats statiques et dynamiques pourrait provenir des perturbations externes qui peuvent influencer l'acquisition des résultats expérimentaux. La modélisation dynamique pourra montrer qu'il faut tenir compte de l'interférence des différentes parties du banc d'essai.

2.3 Modélisation numérique.

Cette modélisation s'est effectuée à l'aide du code de calcul Pam-Crash. Le maillage de la structure extrudée a été effectué avec des éléments de coque à 4 nœuds. Pour tenir compte de l'interférence du banc dynamique dans l'acquisition des mesures d'essais, la plaque sur laquelle l'éprouvette est fixée pendant l'écrasement a été modélisée par des éléments volumiques afin de représenter au mieux les différents phénomènes de vibrations, d'amortissements qui ont lieu pendant le processus d'écrasement.

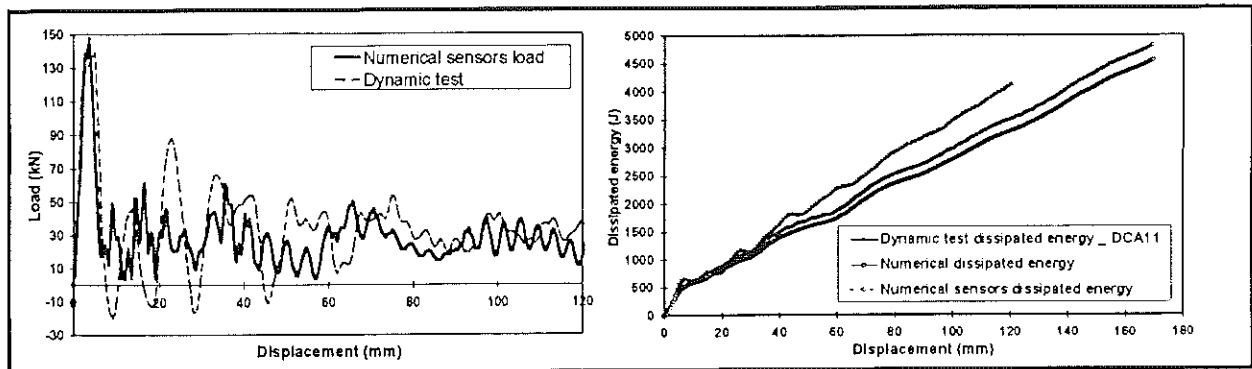


Figure 2.3 : Caractéristiques numériques.

Les résultats de cette modélisation explicités par Abah et al [ABA 98b] ont montré que la modélisation de la structure extrudée donne des résultats identiques à ceux des essais statiques. Pour des chargements quasi statiques et dynamiques. La prise en compte dans la modélisation des phénomènes vibratoires qui ont lieu pendant le processus d'écrasement augmente les valeurs des caractéristiques de crash de ces structures. La vitesse de déformation n'est donc pas à l'origine de la différence existant entre les valeurs des essais dynamiques et statiques.

Conclusion:

Cette étude montre que cet alliage d'aluminium n'est pas sensible à la vitesse de déformation, malgré la différence entre les résultats d'essais statiques et dynamiques. Cette différence est due aux vibrations de la plaque de fixation qui se traduisent par des oscillations des valeurs enregistrées et ainsi une augmentation des caractéristiques de crash.

Références:

- [ABA 98a] : Abah L., Limam A. and Dejeammes M. Effects of Cutouts on static and dynamic Behaviour of square Aluminium Extrusions. Proc. Structures Under Shock and Impact, June 24-26th, Thessaloniki - Greece (1998).
- [ABA 98b] : Abah L. and Limam A. Upon the Effects of Cutouts on the Behaviour of axially crushed Tubes. Proc. ASME/JSME Pressure Vessels and Piping Conference - Structures Under Extreme Loading Conditions, July 28-30th, San-Diego - USA (1998).
- [LAN 96] : Langseth M. and Hopperstad O.S. Static and Dyanmic Crushing of Square Thin-Walled Aluminium Extrusions. Int. J. Impact Engng, vol.18, n^{os} 7-8, pp.949-968 (1996).
- [NAR 89] : Nardini D., Seeds A. Structural Design Considerations for bonded Aluminium Structures Vehicules, SAE paper 890716 (1989).
- [ABR 83] : Abramovicz W. The effective crushing distance in axially compressed thin-walled metal columns. Int. J. Impact Engng. 1, pp. 309-317 (1983).
- [ABR 84a] : Abramovicz W. and Jones N. Dynamic axial crushing of square tubes. Int. J. Impact Engng., vol.2, n^o2, pp. 179-208 (1984).
- [ABR 89] : Abramovicz and Wierzbicki T. Axial crushing of multicorner sheet metal columns. J. of Applied Mechanics, Transaction of ASME, vol.56, pp. 113-120 (march 1989).
- [MAH 83] : Mahmood H.F. and Paluzny A. Design of Thin-Walled Columns for Crash Energy Management - their Strength and Mode of Collapse. Proc. 4th Int. Conf. Vehicule Struct. Mech., SAE, pp.7-18 (1982).
- [WIE 81] : Wierzbicki T. and Abramovicz W. Crushing of Thin-Walled Strain Rate sensitive Structures. Engng Transactions, 29, 1, pp.153-163 (1981).
- [WIE 83a] : Wierzbicki T. and Abramovicz W. On the Crushing Mechanics of Thin-Walled Structures. J. of Applied Mechanics, vol.50, pp.727-734 (1983).

Interpretation of flowstress curves of Al alloys at high rates.

BJØRN ANDERSSON, TOR E. JOHNSEN
*SINTEF Materials Technology, P.O.box 124 Blindern, N-0314 Oslo,
Norway*

I - ABSTRACT

Most forming operations are performed at strain rates $1-1000\text{s}^{-1}$ /1/, but the testing is normally done at much lower rates. There are several obstacles on the way to test at realistic rates so that the mechanical behaviour is adequately understood while keeping the experimental cost at low level. It is especially observed phenomena associated with artefacts in the measurement systems which may confuse the information about the actual material response. In this study, we have attempted to find ways to interpret readily accessible data so that the material response can be determine with an accuracy that is good enough.

It is found that the displacement can be measured by the ram position but a slight tuning is necessary. An important finding is that the specimen itself do not experience any strong plastic waves but a wave pattern is set up in the measurement system with the following characteristics: i) The severity of waves increase with increasing speed of testing but ii) does not depend on the load, iii) the wave pattern is very reproducible and iv) characteristic frequencies are recognised. The waves can be determined by a fitting procedure and subtracted from the recorded data so the material response can be found even for large oscillations.

The mechanical properties can not be found by extrapolating low strain rate results meaning that it is imperative to test at high (realistic) rates.

II- INTRODUCTION

It is in a way a paradox that most industrial forming operations involve rates in the range $1-1000\text{ s}^{-1}$ /1/, but nearly all testing is performed at much lower rates $10^{-5} - 10^{-1}\text{ s}^{-1}$. The reasons behind this is understandable: the rates in industrial surroundings must comply to the demands of high production rates, but in testing the strongest requirements are to high accuracy, readily accessible data and to low investment cost. This means that one is normally limited to lower strain rates. This leaves a gap between the actual strain rates in industrial forming operations and the ones used in testing. Since the industrial processes are given, the testing conditions must be adapted to yield correct information.

One may question the necessity of this. One common argument is that it is possible to extrapolate from typical testing rates. However, this will need an extrapolation over 2-3 orders of magnitude. The results must be evaluated i.e. high strain rate testing is needed - especially because the fundamental deformation mechanisms (dislocation movements, crossslip, tangling cell formations) are expected to respond strongly and differently on temperature and strain rate /2/. It should also be kept in mind that one reaches a regime where adiabatic heating starts.

The drawbacks of testing at high strain rates are that the data on load will contain artefacts even with sophisticated instrumentation. Also displacement measurements either calls for advanced instrumentation or must be derived from the bar movements. It is, however, essential to perform numerous tests to have good statistics and to map mechanical properties over a wide range of alloys, tempers etc. This is particular important since we are in regimes with many "white areas on the map".

In this study, it is attempted to find ways to interpret data that are readily obtained in order to derive the material response with a reasonable accuracy at low cost.

III - EXPERIMENTAL

The testing machine is a Schenk Hydropuls VHS100/10 with a maximum load of 100kN. The ram speed is 1 - 10 m/s. The strain rates are therefore in the range 17-170 s⁻¹ for standard tensile specimens which follows ASTM E8M which has a width of 12.5mm and parallel length of 60 mm. Higher rates are obtained with shorter specimens. The load is measured by piezoelectric crystal and the displacement by optically logging marks on a ruler attached to the lower cylinder. An ADAM transient recorder with sampling frequency 2-16 μs records time, load and displacement.

The Al-alloys have been DC cast, hot rolled and soft annealed at final thickness except for the Al1Mn0.5Mg that was rolled to 2 mm, backannealed (H28) and temper rolled 10 %.

IV - RESULTS AND EVALUATIONS

A curve based on the logged data for displacement and load is shown in fig. 1. The purpose is to show the different artefacts, which can be present. The pertinent questions are:

1. Do the strong oscillations in the measured load actually travel in the sample?
2. Is there uneven measured displacement and how does it affect the load?
3. Is the displacements measured correctly?

IV -1. Oscillations in the sample?

To investigate if the oscillation travels in the specimen or mainly in the clamping unit, and so disturbs the signal, Al1Mn0.5Mg and steel specimens were carefully measured: Elastic strain in the head of the specimen (the load experienced by the sample itself) was compared to the load signal from the piezoelectric crystal. The signals from the strain gauge in the head of the specimens oscillate much less than signals from the piezoelectric crystal except before loading. This has been referred in an earlier work /3,4/ with the conclusion that nearly all oscillations travel in the machine and not in the sample. This view is supported by the fact that similar oscillations are seen after the specimen has broken (fig. 1).

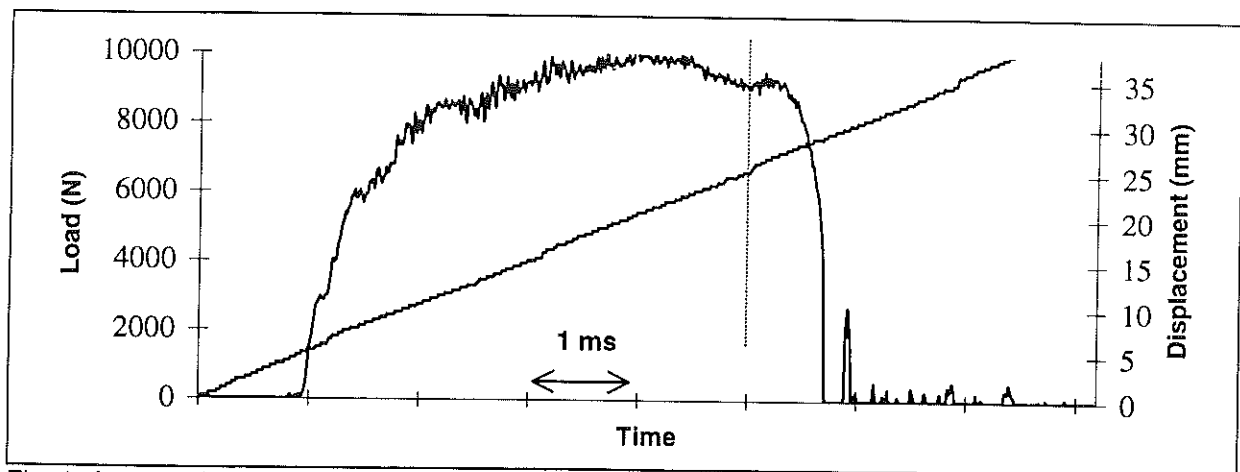


Fig. 1. As-recorded load and displacement as function of time using Al2.5Mg as example.

IV – 2. Uneven movement of the ram?

As shown in fig 1 by a broken vertical line, there can be a jump in the displacement. The optical method in itself is reliable but quite coarse since the markers are equidistant with spacing 0.3 mm. The jumps are larger and taken for real. The displacement - time relations can be found by a smoothing procedure.

The main worry is that it affects the load signal. Indications that the jump is a real one is of the type seen at the end of the load curve in fig. 1. The large jump in ram speed results in a jump in load. Since the strain rate sensitivity is positive at large strains at high rates¹, the load increase may stem from the rate increase or associated electronic noise.

IV – 3. Displacements measured properly by ram position?

The measurement of the movement of ram is in steps of 0.3 mm i.e. uncertainty of 0.5 % on a 60mm length. However, the movements are in reality slowly varying except for occasional jumps on some cases as mentioned above. Thus the logged displacement as function of time, can be smoothed and accurate data obtained. The displacement will include some deformation in the heads as well as in the tool. Such ram position measurements agree, however, very well with displacement measurement by the accurate optical contour method directly on the sample at Material Prüfung Anstalt in Stuttgart /3/, but a tuning is necessary. The measured uniform strains are normally 1-2% larger than the actual strain in the displacement in the deformation zone.

The total elongation of the specimen was measured by the length increase of a grid put on the sample. Comparison shows that the dynamic ram position measurement underestimates also the elongation by 1-2 %.

V- CORRECTION PROCEDURES

Following the discussion of the displacements, it seems that strain in the specimen itself can be found with a reasonable accuracy by fitting the displacement-time development to an analytical expression - normally a simple linear expression and then eventually tune this by subtracting a small fraction if necessary. It is also useful to measure the elongation manually to have a check on the displacement.

¹ This contrary to what is known from normal tensile testing

The remedy for the temporary rate changes is simply to be aware of it by combining displacement and load signal. Since these changes are transient and of short duration and not necessarily so serious as shown in fig. 1, this effect is not felt to be a serious one. In a fitting procedure, a lower weight on the data point should be used in such regions.

The characteristics of the wave patterns open for a correction by subtracting the systematic waves travelling in the measurement system. Instead of smoothing the fluctuations or subtracting by Fourier analysis /3/, it is found more useful to subtract dominant waves. In this way the major disturbances can be avoided at the same time it gives better control of the corrections made. First, it is obvious that the numbers of dominant waves are limited. This can be seen from a typical frequency spectrum as shown in fig. 2. The case chosen is a number of the weak AlFeSi alloys which displays the waves easily. As seen, there are two strong waves around 6000-7000 Hz. The weaker waves or doublet may be part of a system where the frequency is halved: 7000→3500→1750→775Hz, but more information and experience is needed to decide this. The strong doublets have been recognised for many alloys and materials centred around 5000-7000Hz. The pattern appears complex but is simply a result of constructive and destructive interference between two damped sinusoidal waves.

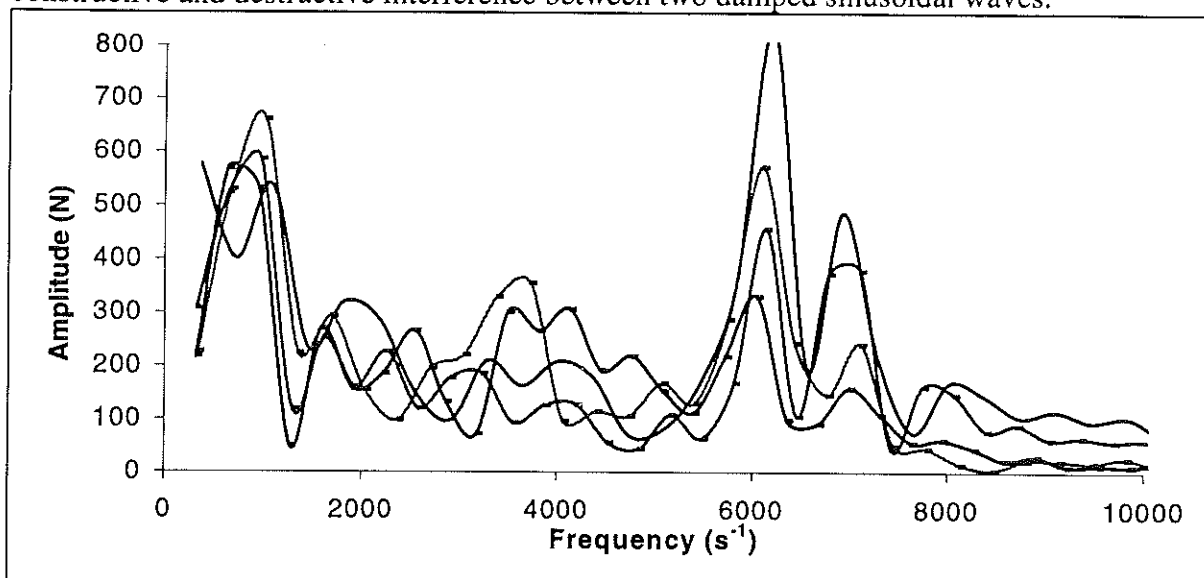


Fig. 2. The amplitudes of the Fourier components measured for four ALFeSi variants used in /5/.

V - 1. Correction of load signals.

At ram speed of about 1-3 m/s, the amplitudes of the oscillations are normally smaller than 5% and contain many periods of the waves so a fitting of the material response can be done directly. At higher speeds it is often necessary to subtract the dominant waves especially for weak materials or small specimens where the total load is below 1KN. The correction procedure for higher speed is described below. To illustrate the procedure a relatively soft material (Al1Mn0.5Mg) at the highest speed (10m/s) is shown in fig. 3 and 4.

Smoothing. A floating average over an interval of 1-3 wavelengths of high frequency waves can be used if this improves the robustness of the fitting procedure. A typical interval is 1/100 of the total deformation time.

Fitting. A material response function and 2 waves are first fitted to the recorded load data. The number of waves can be increased in order to refine the correction. The results of the previous fitting are then used or one may directly fit material response and 2-5 waves if good

initial values are known from previous experience. The fitting is done by using the Levenberg-Marquard method which is quite robust.

The material response function used is the Voce equation /6/: $\sigma = \sigma_0 + (\sigma_\infty - \sigma_0)(\exp(-\epsilon^b/\epsilon_c))$ where σ_0 is the initial flow stress, σ_∞ the saturation stress, ϵ_c a work hardening parameter and b a parameter to ensure correct overall shape of the material curve. The initial values for the parameters were estimated by judging the shape of the curve. The initial values for the parameters for the wave doublets and eventually the other waves i.e. wave lengths, phases and amplitudes are estimated either directly from the graph, by Fourier analysis or known from similar tests.

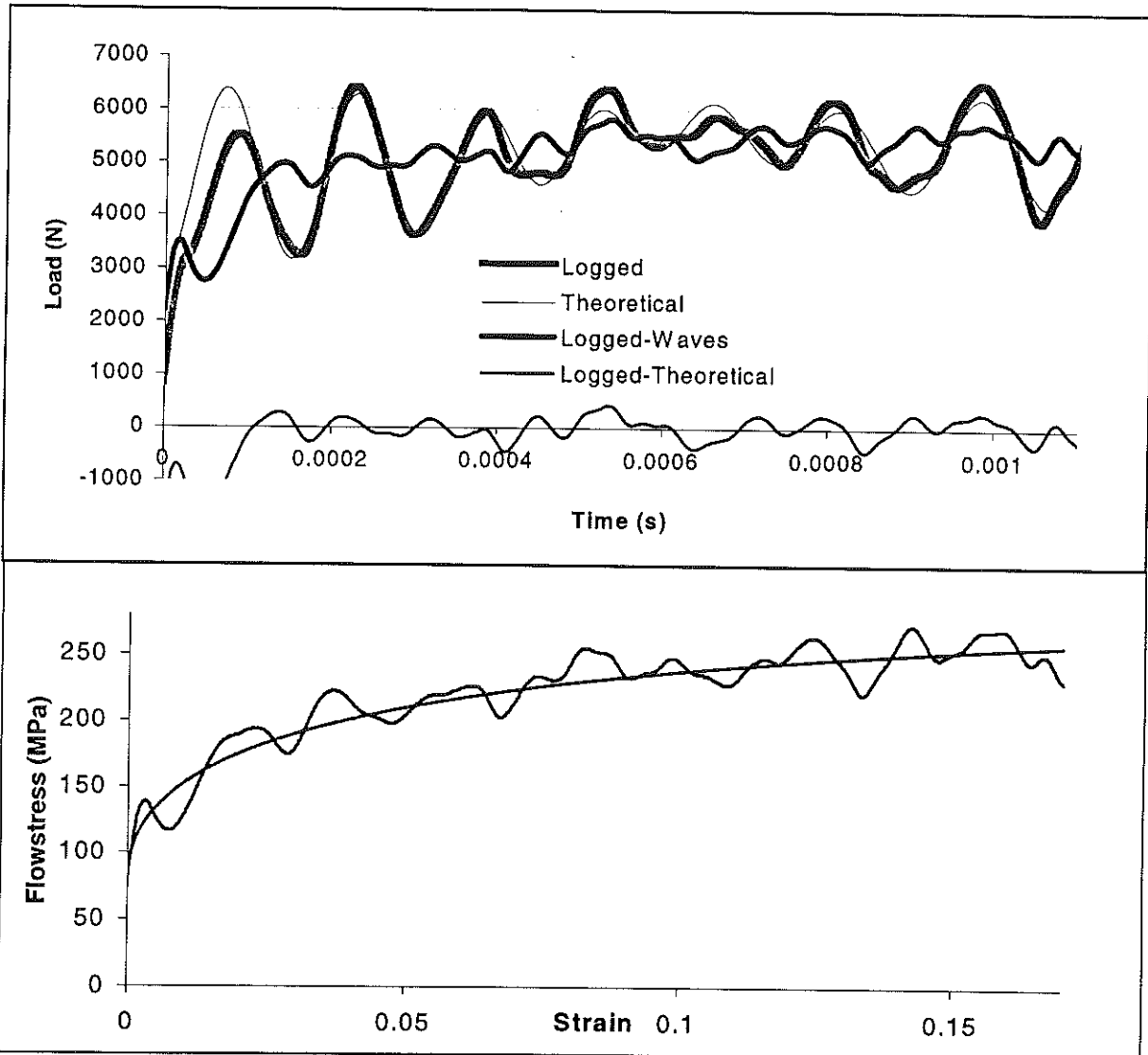


Fig. 3. Upper figure shows the as logged load data compared to the theoretical. Lower figure shows the corrected flowstress and a fitted material response using Voce equation.

In the given example (fig. 3 upper), the strong waves have amplitudes up to 1/3 of the material response. The fitted waves consist of a doublet of 6545 Hz and 5726 Hz and a weaker one at 1690Hz. These waves and the material response are seen to follow the logged data quite well, but some small systematic errors can be seen which is quite natural with this simple description. The main purpose is to reduce the oscillations so that the material response can be recognised more clearly and quantified. This can be done by using the original load signal and subtract the wave part and use this corrected signal to calculate

"experimental" flow stress. This is shown in fig. 3 lower as a separate figure, but can be included in the fitting step.

As seen above, a reasonable flow stress curve can be derived even in a "worst case" used as example.

However, it is important to ensure that the flow curves are real. Therefore tests are nearly always performed as series with rates changing from low to very high. Since it is expected that the physics change gradually, obvious wrongly fitted curves can be singled out. Another remedy is to impose the Considère relation in the fitting i.e. the $d\sigma/d\varepsilon = \sigma$ at uniform strain to ensure that the shape of the curve is physically correct.

Finally, it is important to remark that it is found beneficial to use the original Voce equation for high speed tensile testing because the strain hardening is very high at low strains and even if it decreases with strain it is still higher than in conventional testing /5,7/. This means that the overall shape of the curve is different and not so well fitted with the simplified Voce (with $b=1$) or even worse with Ludwigs law $\sigma=K\varepsilon^n$ since the work hardening coefficient n varies strongly.

VI – CONCLUSIONS

- The displacement can be measured by the ram position, but a slight tuning is necessary.
- The specimen does not experience any strong plastic waves.
- A wave pattern is set up in the measurement system with characteristics:
 - * The severity of waves increases with increasing speed of testing.
 - * The wave pattern is very reproducible.
- The waves can be determined and subtracted so the material response can be exhibited even if the amplitudes are large compared to the signal.
- For ram speeds below about 3 m/s no correction is needed.
- It is essential to test in systematic series to ensure the physical soundness of the results.
- Flow stress curves at high strain rates have shapes different from those at lower rates.

VII – REFERENCES

- /1/ J. Gil Sevillano, P. van Houtte, E. Aurnoudt: Prog. Mater. Sci., Vol. 25, p.69-4112, (1981).
- /2/ J.D. Campbell: "Dynamic Plasticity: Macroscopic and Microscopic Aspects", Mat.Sci. Eng. Vol. 12, p.3-21, (1973).
- /3/ I.H. Hove, B. Andersson and T.E. Johnsen: "High speed tensile testing", J. Phys. IV France, Vol 7, Supplement C3, p.229-234 , (1997).
- /4/ I. H. Hove, B. Andersson and T.E. Johnsen: "Tensile testing at high strain rates at Schenk Hydropuls VHS100/10", SINTEF report STF24 F97008, March 1997.
- /5/ F. Westvold, B. Andersson, Y. Langsrud, J.D. Evensen: "Effect of Alloying Elements on High-Strain-Rate Behaviour in Recycled Al-Fe-Si System Alloys", Proc. ICAA6, Vol.2, p.961-966, (1998).
- /6/ E. Voce: J. Inst. Metals, Vol. 74, p.537-62, (1948).
- /7/ Andersson, B. & Skjervold, S.E.: "Tensile Properties at Low to High Strain Rates of AlMgSi and AlZnMg Alloys", Proc. ICAA5, Vol. 4, p.153-158, (1996).

Microstructure associated with high strain and high strain rates.

J. BUCHAR (1), J. KREJČÍ (2) AND J. BREZINA (3)

(1) Institute of Physics, Mendels University, Zemedelska 2, 602 00 Brno, Czech Republic

(2) Institute of Material Engineering, FME, TU Brno, Technická 2, 616 69 Brno

(3) Institute of Physics of Materials, ASCR, Zizkova 22, 616 62 Brno

I - INTRODUCTION.

In the given paper we focused on the study of the microstructure of the slug and jet. The formation of the slug and jet during the collapse of the shaped charge liner represents a typical example of the high strain and high strain rate phenomenon where the strains are about 10 and the average values of the strain rates lie between 10^4 and 10^5 s^{-1} . The extensive study of slug and jet structure was published by Murr et al. [1,2]. They came to the conclusion that the final structure results from dynamic recrystallization. As there is nothing to be added to these articles as our results are identical, this contribution was focused on slugs that came in contact with steel targets.

II - EXPERIMENTS AND RESULTS

Two types of copper liners with apex angle 40° were used in experiments. The liners were made from OFHC copper, one type with diameter of cone base 32 mm, the height 33 mm, average mass was 15.8 g. The explosive (A IX-1), in this case, weighed 27 g. Second type had 65 mm diameter at base and weight 150.2 g. The shaped charges were shot against the steel targets with different structure (hardness), for details see [3]. All slugs and few jet residues were recovered. Smaller shaped charge slugs pierced in the perforation made by jet, second type slugs were stopped at the entrance of the perforation (see Fig.1). Light, scanning and transmission electron microscopy were used for structure evaluation. Hardness (HV0.1) was measured both on liners and slugs. The grain size of the liner material was checked on at least 50 liners and the value $75 \pm 5 \text{ } \mu\text{m}$ was obtained. The slugs had average grain size $15 \pm 5 \text{ } \mu\text{m}$, i.e., the grain size reduction was around 5:1. The size of grains differ considerably not only with position (near the surface or axis of the slug) but in the same region as well. The average dislocation cell size determined from TEM micrographs was 0.5 μm , the note about differences holds also for cells. The average weight of the first type slugs was 9.3 g, in second case 83.3 g. It means that approximately in the first case 40% and in the second case 45% of the shaped charge liners went into the jets. Initial hardness of the liners was $65 \pm 5 \text{ HV0.1}$, while the average hardness of slugs was $66 \pm 15 \text{ HV0.1}$.

Fig.1 shows an example of the recovered slug (second type). The part left of the "wings" penetrated into the perforation made by jet. On this part of slug, necking could be recognized. Axial section, Fig.2, exhibits the saw-like surface of the slug. In Fig.3, the region around the "wing" is shown. The slug moved from right to left. The "teeth" were apparently present before the material was pushed by the edge of the target perforation. Often, the slugs encompass the internal cavity, which also could be saw-like, Fig.4 (axial section). This cavity was observed in the first type also, but usually deformed.

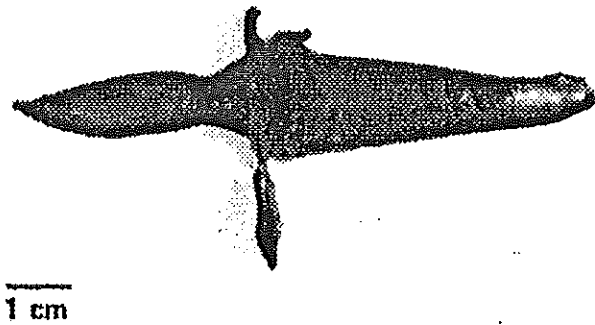


Fig.1 Slug recovered from steel target

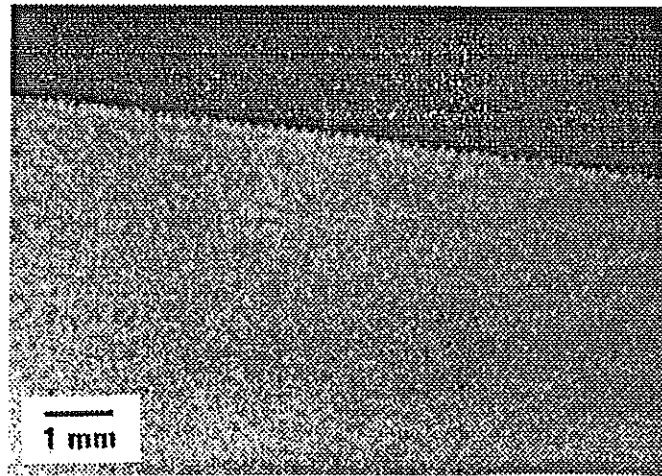


Fig.2 Axial section of slug. The outer surface exhibits teeth.

More frequently, the internal cavity looks like shrinkage (Fig.5) with columnar crystals at the surface (Fig. 6), axial section. Cross section of another slug is in Fi.7, detail in Fig.8. All these micrographs speak for solidification from melt in the interior of the slug.

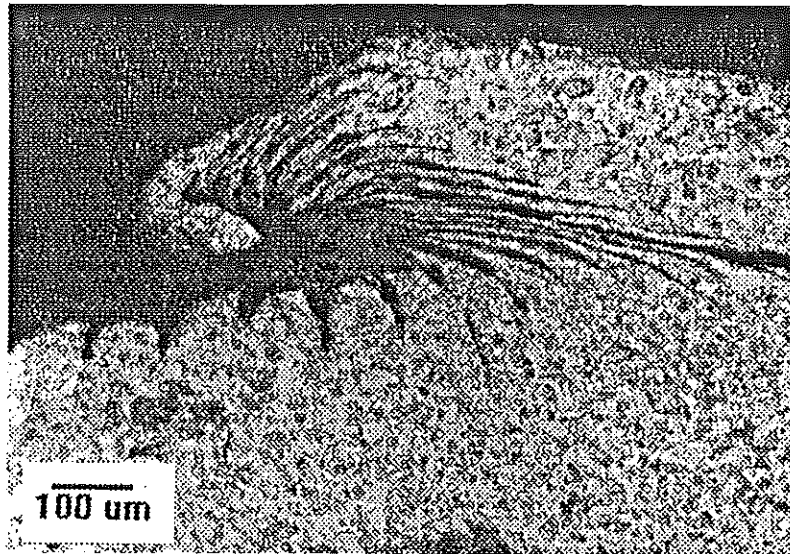


Fig.3 Axial section. Deformed "wing" and teeth.

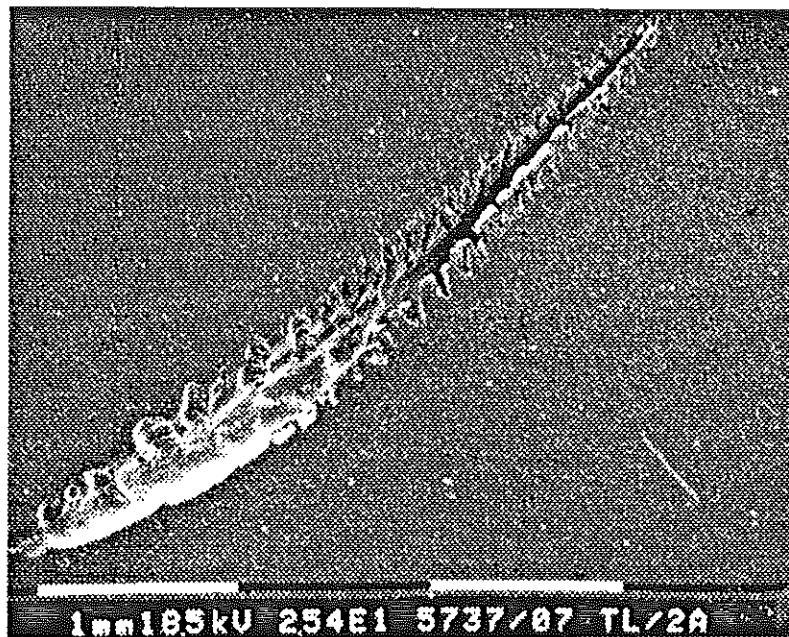


Fig.4. SEM of slug internal cavity. Axial section.

Transmission electron micrographs generally showed recrystallized structure with relatively high dislocation density (the slug were deformed upon contact with the target). Dislocation substructure (and density) depends on the distance from the surface of the slug (deformation decreases toward the slug axis). Only surprising is that the deformation structure seems to be inherited by new grains. Often twins were observed, again they seem to retain deformed dislocation structure.

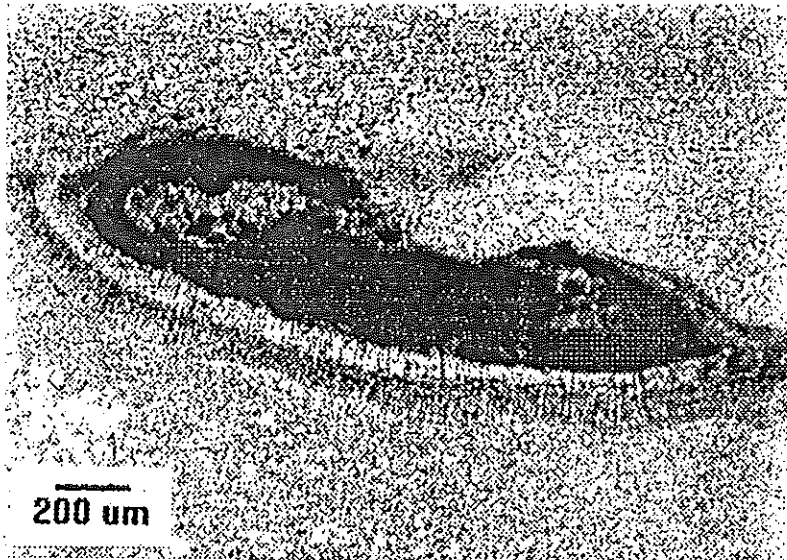


Fig.5. Cross section of with internal cavity.

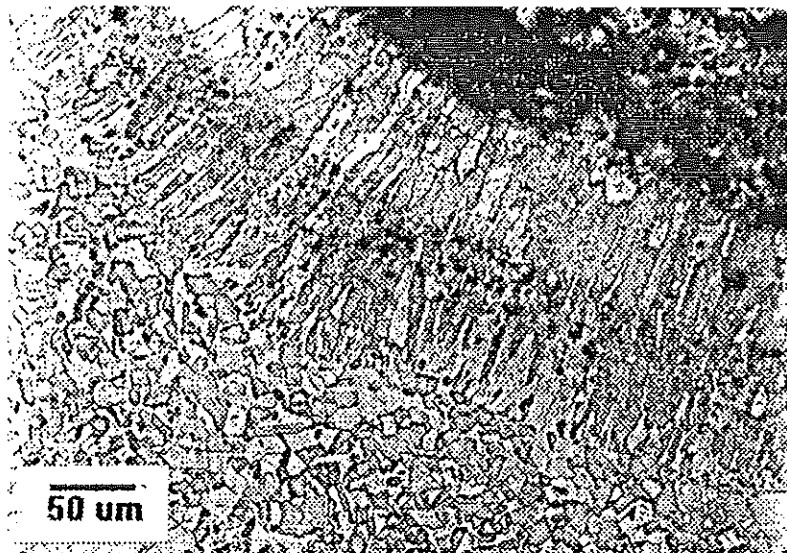


Fig.6 Detail of Fig.5 shows columnar grains at the surface of internal cavity.

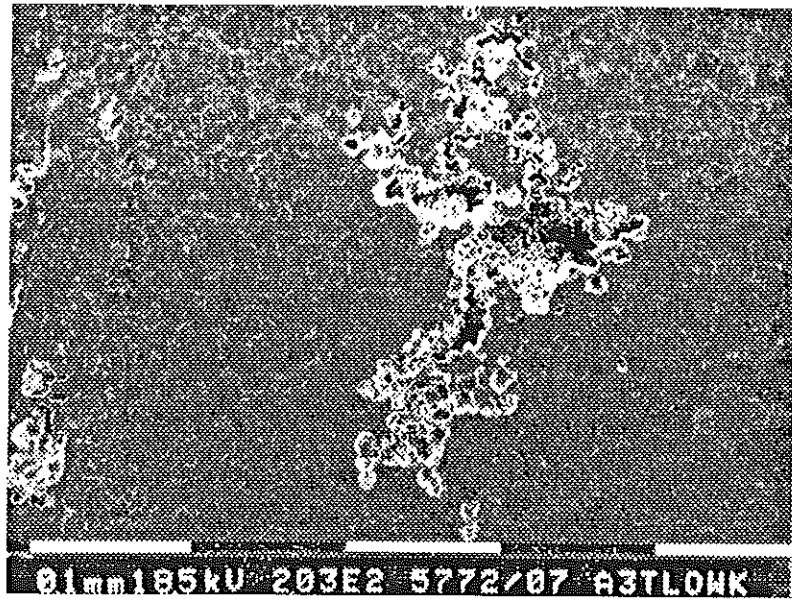


Fig.7. Scanning electron microscopy (SEM) of central region of slug with shrinkage

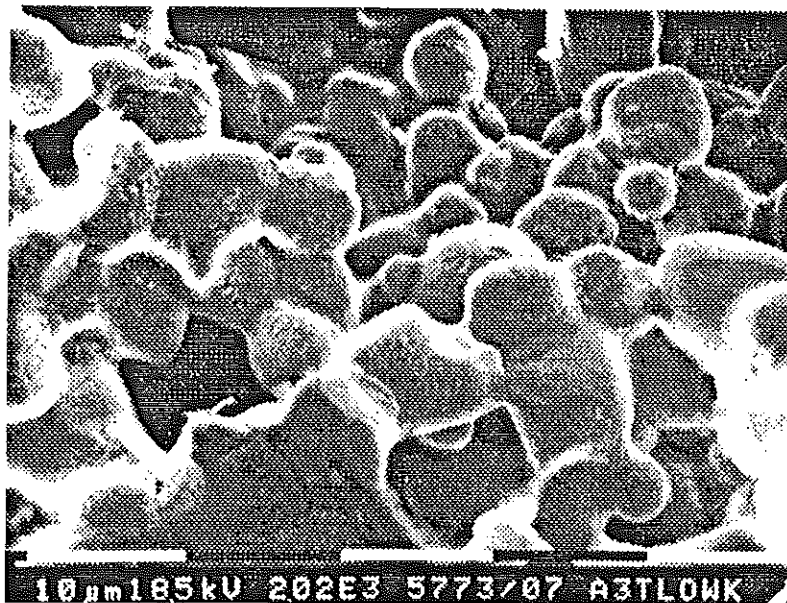


Fig.8. SEM , the surface of the shrinkage in Fig.7

III - CONCLUDING REMARKS

Two features observed on slugs are not in full agreement with existing opinion about solid slug and jet undergoing dynamic recrystallization during their formation. First is the saw-like appearance of the slug surface. It seems plausible to explain it as the consequence of shock waves arising from intensive deceleration when slugs comes to contact with perforated target. However to obtain teeth on the surface, we must assume that the material is in semi-solid state. This concerns larger shaped charges as the smaller one are deformed during piercing in the perforation made by jet. Second feature are columnar crystals on the surface of interior cavity of the slug. Columnar crystal together with shrinkage defects are typical for casting structures and can grow only from melted material. In smaller slugs recovered from the perforated target, only traces of the internal cavity were observed and therefore we cannot prove the melting of material.

It seems probable that the difference between our observations presented here and results of Murr and coworkers (who did not mention any traces of melting) lies in the liner dimensions (mass) and other shaped charge parameters (explosive). These results suggest that in relatively small experimental shaped charges both inner and outer surface layer of the liner are above solidus in some during the collapse and therefore it is probable that the jet also is not solid in the moment of formation. Both features mentioned above appear on the surfaces that are not in direct contact with target and they are separated from contact area by recrystallized material. The inner columnar crystals were observed on soft recovered slugs too.

ACKNOWLEDGMENT

The authors acknowledge the support of Grant Agency of Czech Republic through the grant No.106/94/0567

REFERENCES

- [1] Murr L.E., Shih H.K., Niou C-S., Zernow L.: Dynamic Recrystallization in the Shaped Charge Regime. *Scripta Metallurgica et Materialia* **29** (1993), 567-572
- [2] Shih H.K. Murr L.E., Niou C-S., Zernow L.: Dynamic Recrystallization in a Tantalum Shaped Charge. *Scripta Metallurgica et Materialia* **29** (1993), 1291-1296
- [3] Krejci J., Brezina J., Buchar J.: The influence of microstructure on the layered target response to shaped charge jet. Proc. of 13th Int. Symposium "Ballistics 92", Stockholm (1992). Vol.III, pp 25-32

Ability to model the saturation stress under different loading directions and strain rates

FARRE J. , BUY F.
CEA/VALDUC 21120 Is-sur-Tille

Abstract : We study the evolution of the saturation stress of a tantalum under different loading directions (torsion and compression) and strain rates (10^{-1} - 10^3 s⁻¹). Using a physical model we notice that this evolution is quite different from the yield stress one : a plateau is observed at low strain rates when the yield stress grows in a linear way. Macroscopic models confirmed our observation. Estrin model is able to describe high strain behaviour in all regimes whereas Voce model gives a good restitution only for smooth hardening behaviour. In terms of loading directions we notice different behaviours but sharper experiments have to be performed.

I - INTRODUCTION

During their life, structures are submitted to normal or accidental thermo-mechanical loading conditions that can be very complex. The modelling of their visco-plastic behaviour through constitutive equations is frequently based on experiments performed in a single direction of stress (compression or tension tests). Below some stress value, the material is purely elastic. Beyond this value, the material deforms plastically. The flow stress is related to the plastic deformation by a constitutive law. We have chosen in this paper to study the evolution of the saturation stress under different loading directions and strain rates and the ability of different models to predict this saturation stress for a b.c.c. metal. In fact, the saturation stress is the theoretical limit of the flow stress beyond which the material cannot consolidate. It corresponds to the maximum density of microstructure defects that the metal can bear before failure. This limit depends on strain rate and temperature but is very seldom reached through usual experimental techniques. It limit also sensitive to the stress state (loading direction). The material used in this study is high purity tantalum provided by Cabot Inc.. It has been forged in the three directions and then heat treated at 970°C for 1 hour. The subsequent hardness was 74 HV10, this value being representative of a well recrystallized material.

II - EVOLUTION OF SATURATION STRESS USING A PHYSICAL MODEL

II -1. Presentation of the model

Most constitutive equations describe the evolution of an equivalent flow stress with the cumulated equivalent plastic strain. The mathematical expression which arises from such an approach may fit the experimental results with a very good accuracy. However, the extrapolation of the simulations out of the experimental domain may be venturesome. In fact, the flow stress is subjected to the crystal defects. Moreover, these defects have kinetics of creation which depend on the loading conditions. Therefore, models that identify the phenomena at a microscopic scale and give evolution laws for microstructure defects with

strain fit better the mechanical behaviour of metals. In the present paper, we used a model based on the dislocation density evolution [Klepazcko75 & 87, Buy97]. It adopts the following assessments :

- in the domain of validity, viscous drag (very high strain rates) and creep (very low strain rates and high temperatures) have no effect ;
- the flow stress σ is the sum of an « internal » component σ_i and of an « effective » one σ^* ; the former, due to long range obstacles, depends on the lattice hardness and of the defects density ρ ; the latter is the result of obstacles with small activation volumes and is temperature and strain rate sensitive :

$$\sigma = \sigma_i + \sigma^*$$

The internal stress $\sigma_i = \alpha Gb\sqrt{\rho}$ depends on the shear modulus G , on the Bürgers vector b , and on a factor, α , which traduces both the interactions between dislocations and the loading direction effects. For b.c.c. metals, the effective stress $\sigma^* = \sigma_0^*(1 - \sqrt{kT \ln(vb^2\rho_m / \dot{\epsilon}) / \Delta G_0})$ depends on a frequency factor proportional to the vibration frequency of the lattice v (considered as constant) and to the mobile dislocation density ρ_m , on the short range obstacles maximum energy ΔG_0 , and on the contributions of temperature T and strain rate $\dot{\epsilon}$ to the overcoming of obstacles.

The parameters ρ and ρ_m follow the evolution expressions [Klepaczko87, Buy96] : $d\rho/d\epsilon = M - k_a(\dot{\epsilon}, T)(\rho - \rho_0)$ (M is the multiplication while $k_a(\rho - \rho_0)$ represents the annihilation) and $\partial\rho_m/\partial\rho = \beta/\rho$

II -2. Experimental results

In the frame of this work, torsion and compression tests have been carried out [Buy96, Buy97]. These two kinds of loading have been chosen for the following reasons :

- the development of models which consider that glide is the main deformation mechanism, leads to tests where the loading conditions are representative of this glide : shear or torsion ;
- most models coefficients are determined from compression tests ; the necessity to compare our results to literature data has motivated compression tests.

In this work, we only focus on the strain rate effects on the mechanical behaviour and don't take temperature effects into account.

II -2.1 Determination of the model parameters [Buy96, Buy97]

8 parameters are to determine : α , ρ_0 , M , k_a , σ_0^* , ΔG_0 , ρ_{m0} , et β .

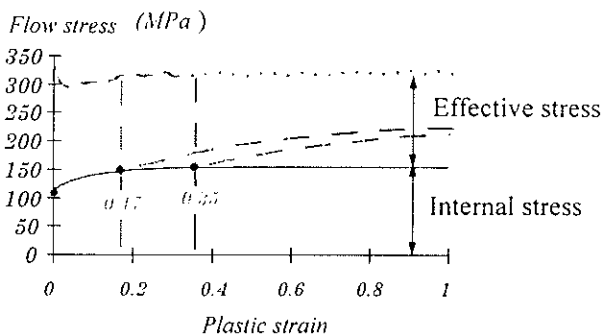


fig 1 : jump test results on tantalum (torsion)

A former article's goal [Buy97] was to explain the technique to determine these coefficients from jump tests in strain rate. Such tests enable to separate the internal and the effective components. We determined the sets of coefficients for the torsion and compression tests using the following interaction coefficients : $\alpha_{axial} = 1,53$ et $\alpha_{shear} = 0,88$.

II -2.2 Strain rates studied

In order to determine the miscellaneous coefficients, different tests have been carried out :

- constant strain rate tests in compression and torsion
- jump tests in compression and torsion.

The following table summarises the set of strain rates which were studied.

Loading	Strain rate (s^{-1})				
Torsion (γ)	3.10^{-4}	$1.5.10^{-3}$	$1.5.10^{-2}$	$1.5.10^{-1}$	3.10^{-2}
Compression (ϵ)	$1.5.10^{-4}$	2.10^{-3}	2.10^{-2}	2.10^{-1}	1.10^3

tab 1 : Set of constant strain rate tests

II -3. Yield and saturation stresses

From the experimental results and the model coefficients found for tantalum, we may determine (fig 1)

- the low elastic limit (just after the disanchorage of dislocations)
- the saturation stress from the saturation values of both total and mobile dislocation density at saturation.

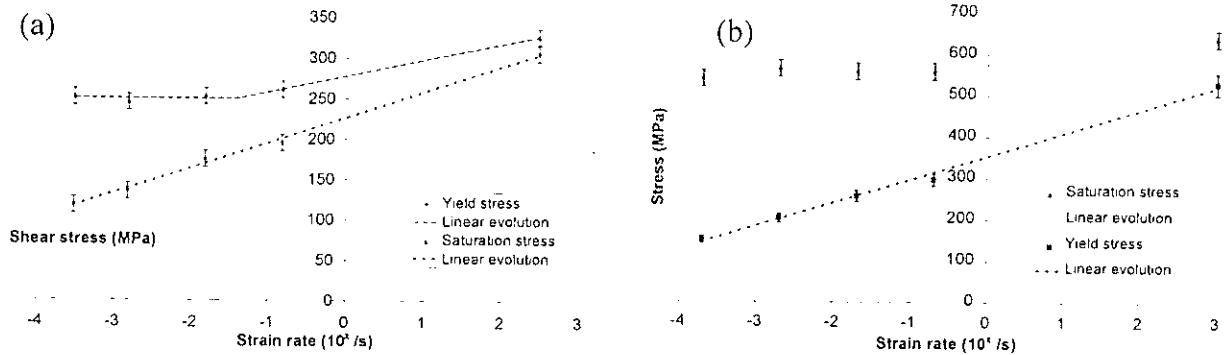


fig 2 : Yield and saturation stresses in torsion(a) and compression(b) versus strain rate ($\dot{\epsilon}$)

II -4. Discussion

In the range of strain rates that were studied, the yield stress seems to be a linear function of the variable $\log(\dot{\epsilon})$ as well for compression as for torsion (fig. 2). This evolution can be accounted for by thermally activated phenomena. Concerning the saturation stress, the evolution is quite different. In the low strain rates, the saturation stress is located on a plateau. Then, at strain rates beyond $10^{-1} s^{-1}$, the saturation stress increases in a quasi linear way with $\log(\dot{\epsilon})$. This observation can be explained by a competition between a fall in the internal stress due to the increasing annihilation of dislocations on the one hand and rise in the effective stress with the strain rate on the other hand.

One can notice that neither Tresca nor Von Mises criteria manage to fit yield or saturation stresses in torsion with the ones got in compression. This phenomenon has already been observed by several authors [Rogaush70, Kroupa68]. One of the reasons we can point out is the fact that screw dislocations split into sessile partial dislocations. To be able to move, they must combine into glissile partial dislocations (in a single plane), this process being orientation dependant. Moreover, the slip planes may differ between both loading directions causing different deformation textures and thus saturation stresses.

Although this physical model give very interesting results, the complete experimental procedure may be long and fastidious for a saturation stress at a specific strain rate. This is why we took an interest in the ability of more simple models to predict the saturation stress.

III - SATURATION STRESS ESTIMATED WITH MACROSCOPIC RELATIONS

III -1. Constitutive equations

When there is no drastic change in the structure of the material, the flow stress tends to a saturation value at constant temperature, strain rate and pressure. We have chosen to study two classical model : Voce law [Voce48 & 55], and Estrin-Mecking law [Estrin84].

III -1.1 Voce law

Voce proposed the simplest relation for a saturation stress : $\sigma = \sigma_0 + (\sigma_s - \sigma_0)[1 - \exp(-\frac{\epsilon}{\epsilon_r})]$

σ_0 being the yield stress, σ_s the saturation stress and ϵ_r a characteristic strain. This model in its differential form : $\frac{\partial\sigma}{\partial\epsilon} = \theta_0 [1 - \frac{\sigma}{\sigma_s}]$ has been a base for MTS [Follansbee88] and PTW [Juanicotena97] models whose much more complex expressions will not be discussed in the

present paper. Kocks [Kocks76] related the latter relation to a dislocation density evolution :

$\frac{\partial\sigma}{\partial\epsilon} = k_1\sqrt{\rho} - k_2\rho$ where the stress σ is proportional to $\sqrt{\rho}$, and the multiplication factor inversely proportional to the mean free path of a dislocation $\rho^{-1/2}$.

III -1.2 Estrin-Mecking law

Estrin and Mecking [Estrin84] considered that the multiplication factor hanged on the kind of obstacles that controlled plastic flow. In the case of « stiff » obstacles that do not evolve through strain (Peierls valleys, precipitates for instance), they assert that a constant multiplication factor is more appropriate and propose the relation : $\frac{\partial\sigma}{\partial\epsilon} = k_1 - k_2\rho$ that, once integrated gives :

$$\sigma^2 = \sigma_0^2 + (\sigma_s^2 - \sigma_0^2) \left[1 - \exp\left(-\frac{\epsilon}{\epsilon_r}\right) \right]$$

The latter relation is equivalent to the one we get for the internal stress in the physical model.

III -2. Optimisation

The parameters of Voce and Estrin-Mecking relations were optimised from constant strain rate loading conditions. The two following figures show the data used for torsion and compression.

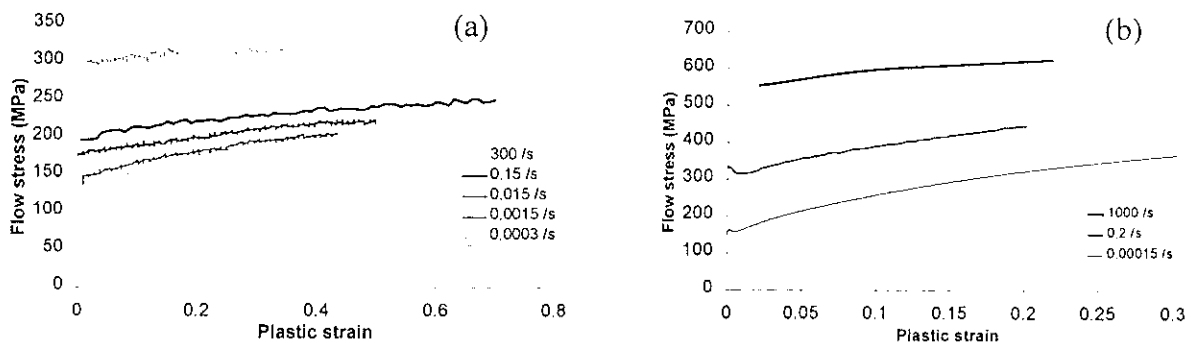


fig 3 : Experimental data in torsion (a) and compression (b)

The saturation stresses obtained via an optimisation of the coefficients for the different strain rates are the following (tab2). We used sets of coefficients so that the optimisation results remain in a 99% confidence interval :

Torsion

Strain rate (s^{-1})	Saturation stress (MPa)		
	Physical	Voce	Estrin
$3 \cdot 10^{-4}$	251 +/- 10	237 +/- 13	254 +/- 20
$1.5 \cdot 10^{-3}$	245 +/- 10	225 +/- 7	232 +/- 8
$1.5 \cdot 10^{-2}$	253 +/- 10	263 +/- 9	275 +/- 12
$1.5 \cdot 10^{-1}$	261 +/- 10	266 +/- 11	268 +/- 13
$3 \cdot 10^2$	326 +/- 10	315 +/- 8	316 +/- 8

Compression

Strain rate (s^{-1})	Saturation stress (MPa)		
	Physical	Voce	Estrin
$1.5 \cdot 10^{-4}$	541 +/- 15	435 +/- 5	530 +/- 4
$2 \cdot 10^{-1}$	559 +/- 15	548 +/- 16	600 +/- 27
$1 \cdot 10^2$	640 +/- 15	636 +/- 3	635 +/- 3

tab 2 : Saturation stresses under different strain rates with 3 models

For torsion tests, both Estrin and Voce models predict a saturation stress analogous to the one given by the physical model. This remark is valid for all the strain rates studied. One can nevertheless notice that the strain hardening is rather smooth, so that the modelling cannot go far from the experimental data. Furthermore, the saturation seems to stabilise around a plateau in the low strain rate regime. In the case of compression, the strain hardening is somewhat sharper. « Estrin saturation stresses » remain close from the values predicted by the physical model but the fit given by Voce model is much less accurate for low strain rates.

III -3. Validation

We have to confirm the two consistent conclusions : a better prediction of saturation stress with Estrin model and the existence saturation stress plateau at low strain rate. First, we present two stress-strain curves, one for smooth hardening behaviour (torsion), the other for sharper hardening (compression). We have optimised the Voce and Estrin relations until some limits and we have extrapolated the laws at higher strains.

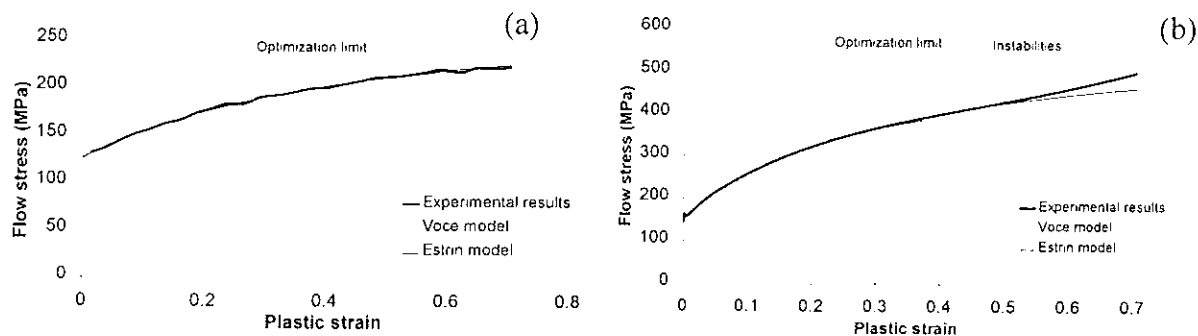


fig 4 : Extrapolation of laws (a) in torsion ($3 \cdot 10^{-4} s^{-1}$) (b) in compression ($1.5 \cdot 10^{-4} s^{-1}$)

For smooth hardening, extrapolations are agree with real behaviour, but for sharper hardening, only Estrin model can represent the real behaviour until instabilities.

Second, we have studied the evolution of saturation stress at low strain rate in tension.

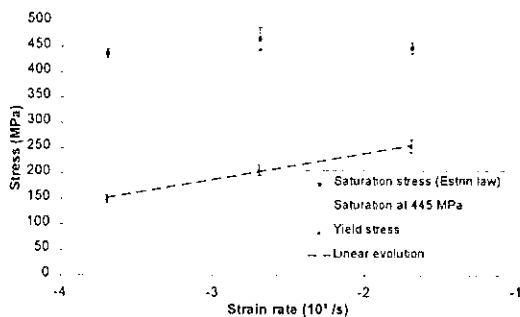


fig 5 : Yield and saturation stresses in tension

We observed the same behaviour :

- linear evolution of yield stress versus $\log(\dot{\epsilon})$
- saturation stress plateau at low strain rate

IV - CONCLUSION

In this work we used a physical model which has helped us to understand phenomena that can be observed at a macroscopic scale, and to develop macroscopic model. It also accounted for the evolution of the saturation stress with strain rate of the tantalum studied : a plateau in the low strain rate regime (that cannot be observed for yield stress), a rise for higher strain rates. Concerning macroscopic models, we concluded for this metal, that Voce law is able to describe high strain behaviour only for smooth hardening whereas Estrin model behaviours with a good accuracy in all regimes.

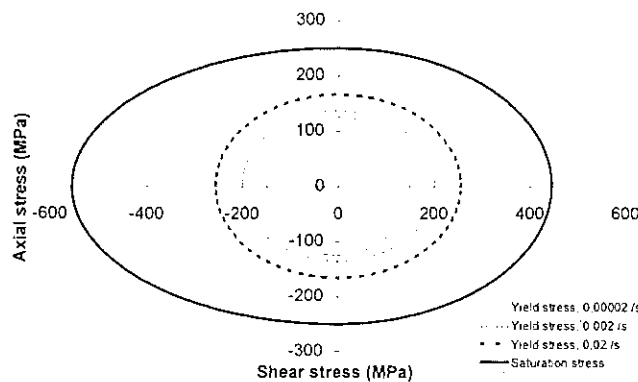


fig 5 : Hill's ellipses

We also studied the saturation stress under different loading direction. Different behaviours are observed according to the direction which can be described neither by Tresca nor Von Mises criteria. We can represent yield and saturation stresses with Hill's semi-ellipses (compression-shear and tension-shear) for different strain rates. We can observe an asymmetry of saturation stress in axial loading that is not noticed for the yield stress. Moreover, the semi ellipses do not present a uniform growth.

We intend to perform sharper experiments in order to study the loading direction effects : plasticity domain in axial/torsion mode, flow stress in monotone axial/torsion test .

Acknowledgements

The authors acknowledge the assistance of M. Antoine Juanicotena (CEA Valduc).

References

- [Buy96] Buy F., *Etude expérimentale et modélisation du comportement plastique d'un tantale. Prise en compte de la vitesse de déformation et de l'histoire du chargement*, Thèse de l'Université de Metz (SMZ9634) -1996.
- [Buy97] Buy F., Farré J., Klepaczko J.R. et Talabart G., Evaluation of the parameters of a constitutive model for b.c.c. metals based on thermal activation, *Colloque C3, Supplément au Journal de Physique III d'août 1997, J. PHYS IV FRANCE 7*, pp. 631-636 (1997)
- [Estrin84] Estrin Y., Mecking H., A unified phenomenological description of work hardening and creep based on one-parameter models, *Acta Metall.* **32**, pp. 57-70 (1984)
- [Follansbee88] Follansbee P.S., Kocks U.F., A constitutive description of the deformation of copper based on the use of the Mechanical Threshold Stress as an internal stress variable, *Acta Metall.* **36**, No. 1, pp. 81-93 (1988)
- [Juanicotena97] Juanicotena A., Llorca F., Contribution du test d'expansion d'anneaux à l'étude de différentes lois de comportement élastoplastique dans le domaine des grandes vitesses de déformation, *Colloque C3, Supplément au Journal de Physique III d'août 1997, J. PHYS IV FRANCE 7*, pp. 541-546 (1997)
- [Klepaczko75] Klepaczko J.R., Thermally activated flow and strain rate history effects for some polycrystalline f.c.c. metals, *Material Science and Engineering*, **18**, p 121, (1975).
- [Klepaczko87] Klepaczko J.R., Modeling of structural evolution at medium and high strain-rates, f.c.c. and b.c.c. metals, *Proceeding 8th Risø symposium, Constitutive relations and their physical basis*, p387, (1987).
- [Kock76] Kocks U.F., Laws for work-hardening and low-temperature creep, *Journal of Engineering Materials and Technology*, **98**, p 76, (1976).
- [Kroupa68] Kroupa F., Plastic deformation of b.c.c. metals with special reference to slip geometry, *Déformation plastique des métaux et alliages*, Masson ed, pp 29-66, (1968)
- [Rogaush70] Rogaush K.D., Mordike B.L., Asymmetry of slip in tantalum and tantalum alloys, *Strength of Metals and Alloys (2nd Conference) vol 1*, p 168, (1970).
- [Voce48] Voce E., The relationship between stress and strain for homogeneous deformation, *J. Inst. Metals* **74**, pp. 537-562 (1948)
- [Voce55] Voce E., A practical strain hardening function, *Acta Metallurgica* **51**, pp. 219-226 (1955)

Analysis of protective shell structure subjected to impulsive loading due to an explosion

K.CICHOCKI

Technical University of Koszalin, 75-620 Koszalin, Poland

I - INTRODUCTION

For important offshore structures (underwater tunnel crossings, pipelines, and the elements of plants in oil industry), their resistance against the load produced by the explosions is an important component of the entire structure safety. The exceptional character of this kind of load, its impulsive characteristics as well as the complex phenomena occurring due to reflection of incident wave on the flexible curved surface of the structure, make the analysis in real-life situations highly complex and difficult to perform, even using the modern and powerful professional general-purpose computer codes.

In spite of all these problems, described in details in [1-4], numerical simulation of dynamic response of such structures to the impulsive loads is a task of growing importance for many authors. Several works have been published recently [5-9], giving the review of last achievements and results, as well as many useful remarks considering the methodology of numerical analysis, its limitations, possible approximations and simplifications.

The numerical analyses are very useful to evaluate the efficiency of various protective means applied to prevent the damages of the main structure. One of the possible protection of important structures is the protective containment, realised as a shell placed in a certain distance to the main structure. This protective containment can be connected with the main structure by means of diaphragms, stiffeners and other structural elements. The main scope is to dissipate the maximum amount of energy, in order to minimize the energy dissipated by the main structure. This goal is achieved by the inelastic deformation of protective structure, up to its local or even total damage.

The additional protective effect is due to the offset between the containment and the main structure. This distance serves to diminish the value of peak pressure arriving after the damage of containment structure, and to prevent the early contact between the main structure and the damaged parts of containment.

The present work concerns the analyses of an underwater tunnel protected by an external containment structure subjected to a contact explosion, described in details in [5]. On the basis of former preliminary analyses presented in [8], the discrete finite element model was defined and applied in order to find the best configuration of protective structure, in terms of its efficiency. A portion of the structural system is illustrated in the Fig.1, through the schematic view of the entire structure and the mesh of a finite element model with adequate boundary conditions, applied in analysis.

II - DESCRIPTION OF THE PROBLEM

The main structure consists of a sandwich cylindrical wall with 25 mm thick steel sheets on the both inner and outer surface, massive plain concrete core 450 mm inside and transversal connections between steel sheets. The cylindrical sandwich wall is surrounded by a coaxial protective structure. This containment structure consists of a 35 mm steel sheet, externally coated by a concrete layer, and endowed with circumferential stiffeners on the inner side. The internal thick cylinder is connected to the external thin protective shell by steel diaphragms. The coaxial cylinders and diaphragms form an intermediate air chamber (1m wide in the radial direction).

The 40 kg spherical charge of trinitrotoluene (TNT) placed on the external surface of the entire structure was taken into account in the analysis. The load was modelled as a known field of pressure, variable in time and space, based on semiempirical relations published by Henrych [1]. To model the reflection of the incident wave on the curved surface of structure, the Henrych's relations were modified on the basis of empirical observations and analytical observations (Shrivastava [10]).

As regards the material model for steel, the von Mises yielding criterion with isotropic hardening and associative flow rule together with Hook's law of isotropic linear elasticity was assumed. The rate-sensitivity of steel was captured by Cowper-Symonds model (Ref. [12]) with well known in literature (Ref. [13]) parameters for ductile steel: $D=40 \text{ s}^{-1}$, $p=5$. As a failure criterion, the maximum value of plastic equivalent strain $\varepsilon_{eq}^{p,max}$ was assumed. This latter assumption, although controversial (Ref. [5]), was adopted and verified in trial computations in order to avoid serious errors and inaccuracies.

On the basis of preliminary analyses (Ref. [9]), the elastoplastic model with damage, based on considerations published by Comi et al. [14] was implemented for the plain concrete, as the user's subroutine into the ABAQUS/Explicit code.

III - CONCLUSIONS AND FINAL REMARKS

The results obtained in numerical analyses show that the damage of protective shell is localised in vicinity of explosive charge and limited by the presence of T-section stiffeners. Destroyed and fragmented parts of protective containment hit the external layer of the main sandwich structure with a relatively high velocity (up to about 900 m/sec). Considering the damages caused by the individual parts of protective containment it is clear that the main source of damages is the contact between the stiffener under the charge and the external steel layer of sandwich.

In the internal thick concrete layer the damages occur due to propagation of pressure wave through its thickness. When the pressure wave reaches the internal steel layer of sandwich, the reflected part of pressure wave starts to propagate in the opposite direction. Through this mechanism, the damages in concrete tend to accumulate, forming the zone of completely degraded material.

This phenomenon leads to practical conclusions regarding the possible means which should be undertaken to avoid excessive damages, particularly in the main bearing structure (i.e. internal cylindrical sandwich). First of all, the configuration of protective containment should be investigated. Although some its parts has to be considered constant due to structural and technological reasons (i.e. stiffeners, diaphragms), there are also possibilities to check the influence of thickness of external concrete cover of protective shell on the damages in various parts of main bearing structure. Four cases were taken into consideration: 0-5-10-15 cm thick plain concrete layer. Additionally the presence of 10 cm thick concrete layer on the external surface of main sandwich structure was also considered. Other parameters, as for example the

thickness of steel sheets, configuration of stiffeners, diaphragms, etc., were not analysed, although they have also the great influence on the protective effect of external containment structure.

The examples of final deformed shape of the structure under consideration for two chosen thicknesses of external concrete layer are given in Fig. 2. Damaged parts of structure were removed from the mesh. For the greater thickness of external concrete layer the damages in main bearing sandwich structure are reduced.

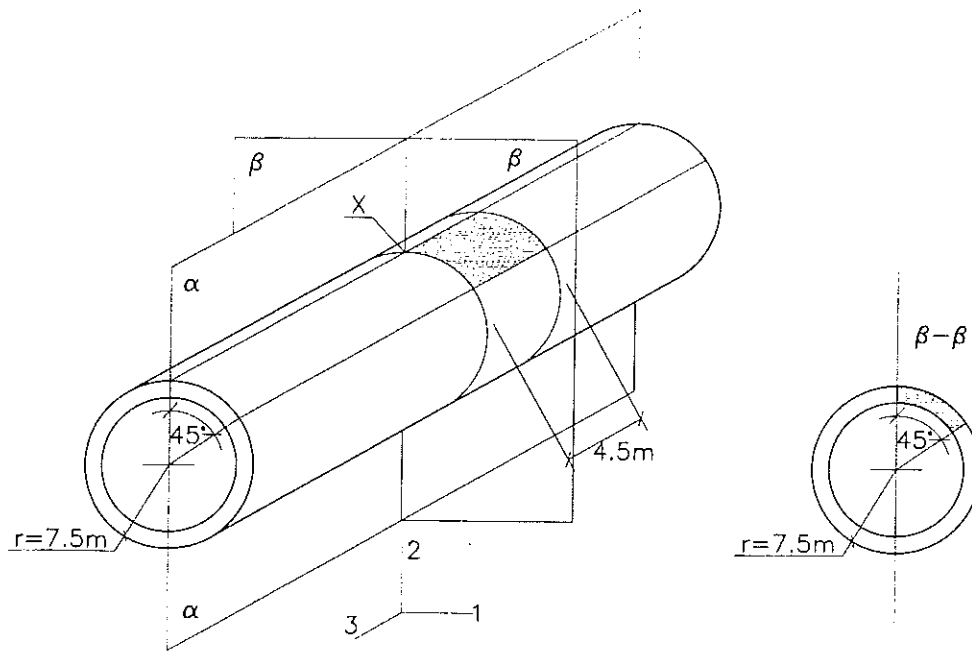
In Fig. 3 the values of total dissipated energy as well as the values of energy dissipated in various elements of entire structure are shown for two cases considered in Fig. 2. Also here one can observe the reduction on energy dissipated by bearing parts of structure (i.e. concrete, upper and lower steel layers in sandwich). Similar behaviour can be observed for other values of thicknesses of external concrete layer.

The influence of additional concrete layer applied on the outer surface of sandwich was investigated in [9].

REFERENCES

- [1] J. Henrych, *The Dynamics of Explosions and Its Use*, Elsevier, Amsterdam, 1979
- [2] Y.W. Kwon, P.K. Fox, Underwater shock response of a cylinder subjected to a side-on explosion, *Computers and Structures*, **48**: 637-646, 1993
- [3] M.Y.H. Bangash, *Impact and explosion - Analysis and design*, Blackwell Scientific Publications, Cambridge, 1993
- [4] F. Salvatorelli, Dynamic response and failure of singular and sandwich cylindrical shells under lateral blast loading, In: *Structure under shock and impact*, 381-395, P.S. Boulson (Ed), Elsevier, Amsterdam, 1989
- [5] K. Cichocki, G. Maier, U. Perego, Analysis of damages due to underwater explosions on a hybrid structures, *International Journal for Engineering Analysis and Design*, **1**: 341-361, 1994
- [6] K. Cichocki, G. Maier, U. Perego, On numerical simulations of explosions on sealines, In: J. Najjar, ed., *Proceedings of 9th DYMAT Technical Conference*, Munich, Germany, 1995
- [7] K. Cichocki, Computer analysis of dynamic response due to underwater explosion on a hybrid structure, In: HKS, ed., *Proceedings of ABAQUS Users' Conference*, 207-220, Newport, USA, 1994
- [8] R. Adamczyk, K. Cichocki, M. Ruchwa, Analysis of the Shock Response of an Underwater Structure Subjected to a Far-Field Explosion, In: HKS, ed., *Proceedings of ABAQUS Users' Conference*, Milan, Italy, 1997
- [9] K. Cichocki, R. Adamczyk, M. Ruchwa, Effect of protective coating on underwater structure subjected to an explosion, In: R. de Borst et al., ed., *Proceedings of EURO-C International Conference "Computational modelling of concrete structures"*, 623-631, Balkema, Badgastein, Austria, 1998
- [10] *ABAQUS Theory Manual ver. 5.7*, Hibbitt, Karlsson & Sorensen, Pawtucket, USA, 1997
- [11] R.S. Srivastava, *Interaction of Shock Waves*, Kluwer Academic Publishers, Dordrecht, 1994
- [12] W. Chen, *Constitutive Equations for Engineering Materials, Vol.2: Plasticity and Modelling*, Elsevier, Amsterdam, 1994
- [13] R.W. Hertzberg, *Deformation and Fracture Mechanics of Engineering Materials*, Wiley, New York, 1996
- [14] C. Comi, Y. Berthaud, R. Billardon, On localization in ductile-brittle materials under compressive loadings, *Eur. J. Mech. A/Solids*, **14**: 19-41, 1995

a)



b)

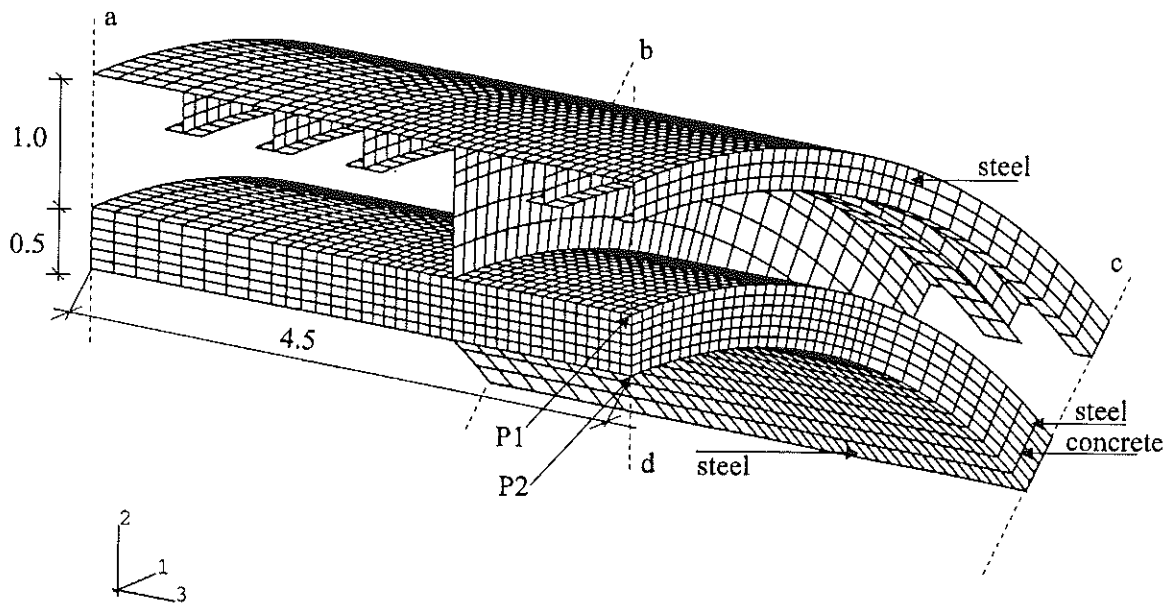


Fig. 1. Tunnel

a) Schematic view of structure (X - explosive charge)

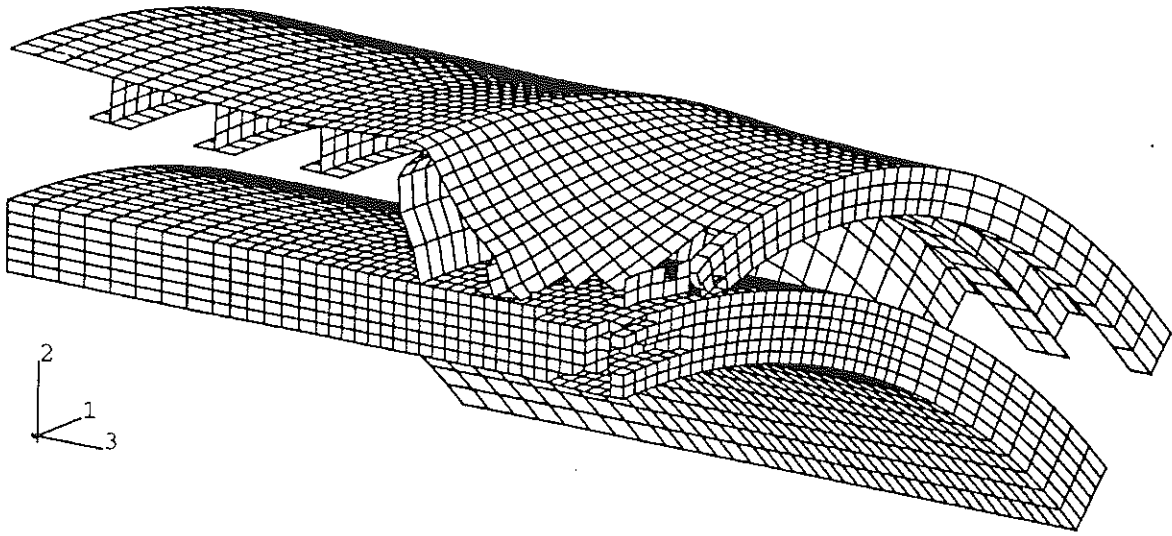
b) View of entire mesh

Boundary conditions:

Plane surfaces a - b, b - c; fixed nodes;

Plane surfaces c - d, a - d: symmetry

a)



b)

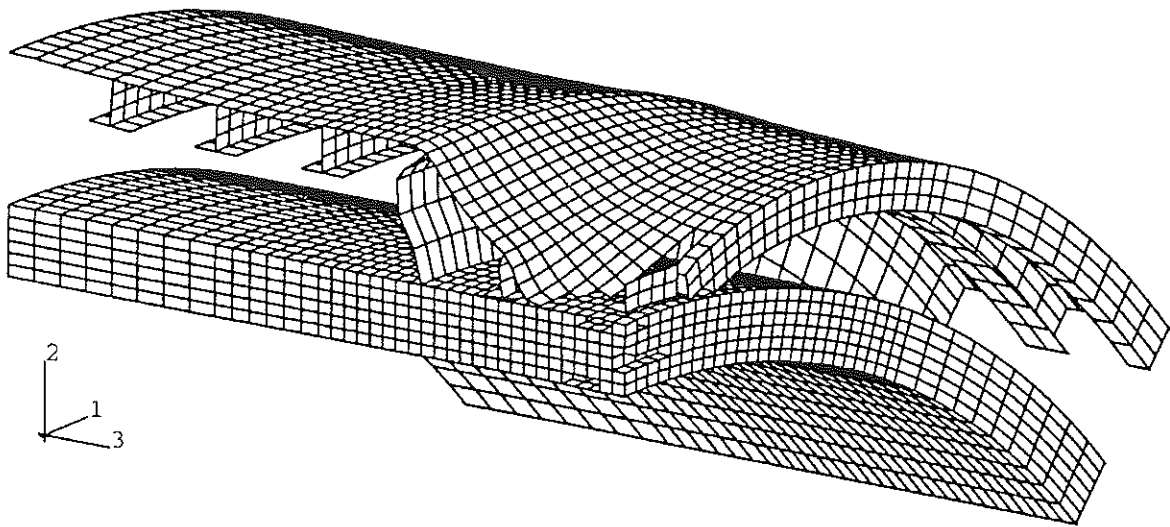
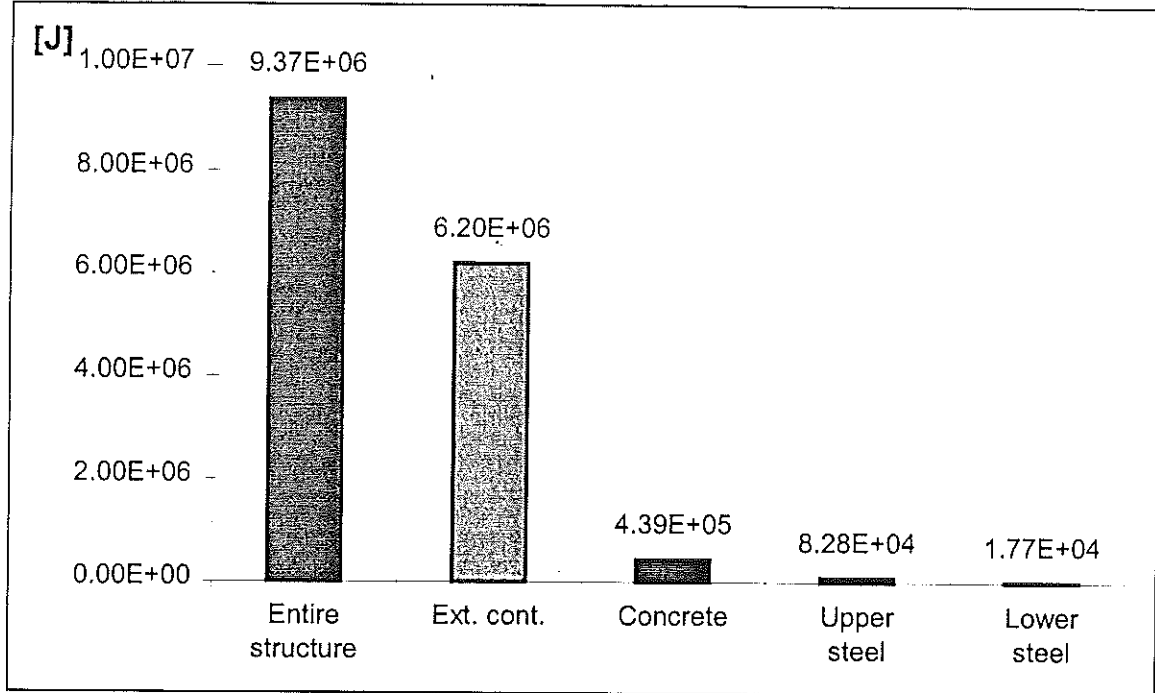


Fig. 2. Deformed structure
a) External concrete layer 10 cm
b) External concrete layer 15 cm

a)



b)

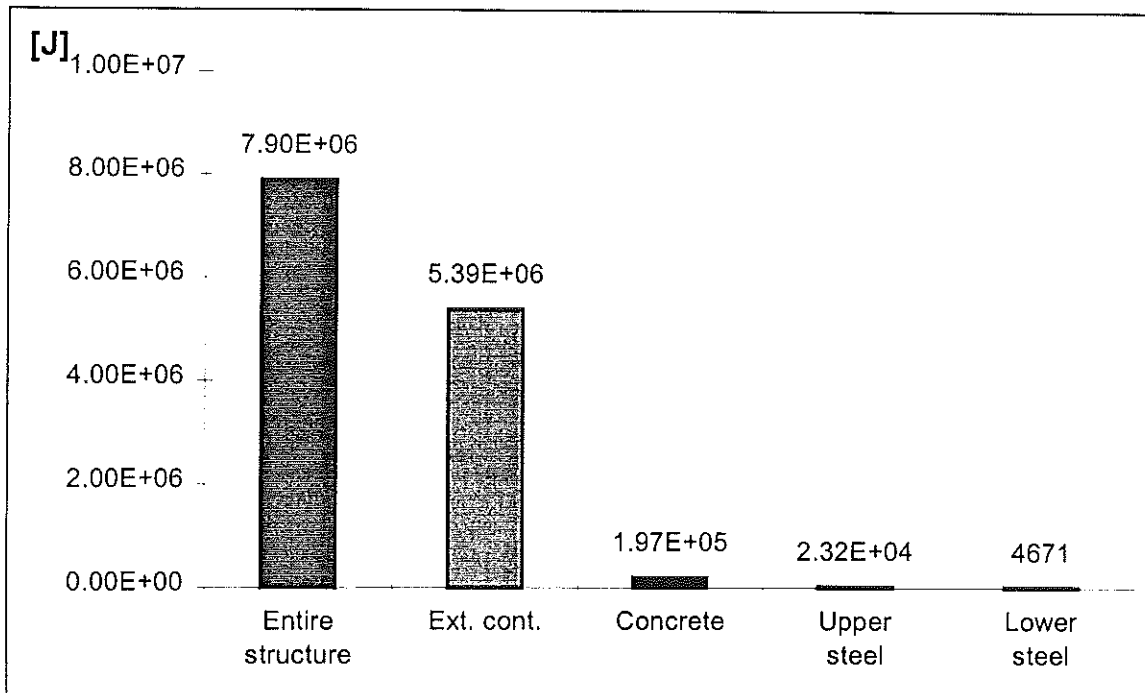


Fig. 3. Maximum dissipated energy

a) External concrete layer 10 cm

b) External concrete layer 15 cm

Hot shock wave compacting coated Tungsten powders.

L. JAPARIDZE, A. PEIKRISHVILI

Department for Science and Technology of Georgia, 38004 TBILISI, Georgia

Texte non reçu à la date de l'impression

The text has not been received by the printing date.

Micro- and mesostructures in composites under high strain-rates deformations

S.N.KULKOV

Ceramic Composite Laboratory. The Institute of Strength Physics and Materials Sciences of the Russia Academy of Sciences, Siberian Branch, 2/1, pr. Akademicheskai, Tomsk, 634021, Russia e-mail: kulkov@ispms.tsc.ru

Abstract

There carried out a study of regularities of deformation and fracture of the composite with structure-unstable binder, the peculiarities of inelastic behavior of the matrix having structural phase transformation.

It was shown that there was formed the ultra-fine structure with typical size of crystallites less 10 nm having high plasticity and high capacity to hardening. This structural state of the matrix lead to the effective transmission of external loading to hardener and a dislocation slides even in typical brittle particles, for example, titanium carbide on a microlevel and rotation of the carbide particles on a mesolevel result in multiple cracking of a plastically deformed particles and, finally, to the high value of the fracture toughness. The material fragmentation on the fracture surface was founded, and the presence of transformation leads to the amorphisation of the fracture surface.

1. Introduction

The composites with disperse hard particles being in a relatively soft metal matrix represent a special class of materials - the so called hard alloys, which are widely used in engineering both as structural and cutting tool materials with hard particles increasing strength and hardness and a plastic matrix giving rise to the high toughness and plasticity to the whole material. At low content the particles promote the higher yield stress of plastic deformation of a material (as carbides in steels for example). In other case the plastic matrix gives some plasticity and toughness to a brittle material (carbide for example).

From all the existing models only some of them (Almond [1]) pay a sufficient attention to a binding phase. Nevertheless, the problem becomes apparently principal firstly for physics of the deformation process of a such class of materials to be understood for correct modeling of mechanical behavior of such composites, and for increasing of the properties of the materials and new-generation composites with the highest properties to be worked out. The fact is that the non-uniform stresses in the disperse-hardened composite stipulate considerable mechanical constraint of deformation playing the leading part in the formation of the properties of the hard alloys. Taking into account a rather small (less then 1-2 μ) size of the interparticle distances

and the higher yield stress of a matrix as a result of the lower thickness of interlayers, it's difficult to expect that dislocation sliding should be effective under these conditions.

So, it is necessary to look for new materials as the binding phases that should provide the effective deformation of the composite under strained conditions and preserve its fracture as a result. In our previous work (Kulkov [2,3]) it have been shown, that the usage in a composite as binder of an alloy with structure transformation permits the essentially to increase its mechanical properties. The alloys with thermoelastic martensitic transformation may be taken to materials of such a class owing to their crystal structure instability with respect to shear, for example, NiTi (Kulkov [3]).

The our results have been demonstrated that the efficiently higher plasticity of an alloy can be achieved at the same level of strength due to the transformation of the structure-unstable binder, it being not important, in what way this is achieved - due to changing either of its composition or the deformation temperature. In any case the specific energy of plastic deformation increases approximately more than 3 times.

The main purpose of the work is to study a structures at a various scale levels, the phase composition, the deformation and fracture of TiC - TiNi composites with a structure-unstable binding phase at dynamic loading.

2. The experimental procedure and materials

The TiC-TiNi composite with martensitic transformation in binder was investigated. The material was obtained by powder metallurgy methods and was a cylinder form with the size 10*10 (mm), which were used as flyers for penetration to the half-infinite targets prepared from the aluminium alloy. After extraction flyers from target the analysis of its microstructure by the X-ray and TEM was carried out.

3. Results and discussions

On Fig.1 are shown the X-ray patterns, obtained in initial condition and from fracture surface of a flyer. As one can see, after shock loading the X-ray reflections, belonging to a binding phase are not practically visible, while reflections of carbide have a broadening. Such kind of X-ray lines permits to make the conclusion, that in volume of a binder material the amorphous structure is formed.

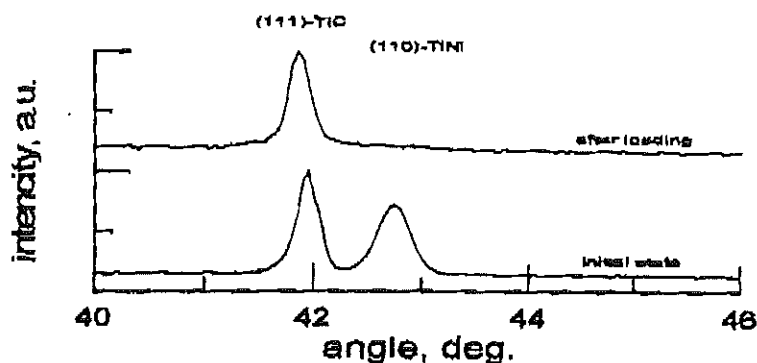


Figure 1.
The X-ray patterns of a
samples, CuK α .

For analysis of an internal structure of such material after shock loading the researches on thin foils, cutting from fractured samples were carried out by TEM investigations. The studies of the deformation and fracture processes of TiC-NiTi alloys with the structure transformation

showed for NiTi deformation to be accompanied by considerable changes of structure state when being lost shearing stability of its lattice. Already in the non-deformed TiC-NiTi samples the NiTi structure is inhomogeneous to a high degree. One can observe the characteristic ripple contrast at the light-field electron-microscopic patterns what testifies to NiTi was in a pre-transition state. Under loading still in a region of the composite elasticity the microstructure changed from a disperse domain into a banded contrasting one that is characteristic for the intermediate shear structure. Firstly, one can observe generation of diffraction peaks in the electron diffraction patterns and then extra-reflexes both in commensurable and incommensurable positions with the different parameter of commensurability in the different directions of axes of the reciprocal lattice, what testifies to several variants of the martensite domains each being generated with its own real structure. A such character of NiTi transformation is caused by highly inhomogeneous state arising near the hard particles of the composite under loading. Under the conditions of high stress gradients appearing in a matrix, the directions of atomic displacements in microzones stipulating local losses of B2 structure stability are determined by stressed states arising under loading at a moment in a given microvolume of the binding. These conditions determine the orientation of newly generating martensite domains too. NiTi transformations of a such character result in simultaneous decrease of the peak and the integral intensities of B2-phase lines in X-ray patterns not being accompanied by growing or arising of new martensite peaks.

Under deformation with the higher velocity there appears a disperse structure consisting of disoriented fragments of B2 phase and martensite domains. The electron diffraction patterns, Fig.2, taken from these zones have a characteristic ring shape of a different kind, mainly rings of point peaks and separate arcs arranged in one azimuth range of the wide (110) B2 ring against the weak diffuse (110)-B2 background. One can see the wide, highly intensive ring sharply standing out the others and being 0.201-0.240 nm in width corresponding to an interval of the interplanes distances of the most intensive (002), (111), and (020) peaks of a monoclinic phase and (110) peak of B2 cubic structure. Moreover, one frequently can see on electron diffraction patterns (especially in the vicinity of intercarbide boundaries) the rings of point peaks with reflections of B2 and martensite structures against the background of diffuse (110) ring of B2. Second-order peaks are very weakly. Diffraction of a such character corresponds to the quasiamorphous state, Fig.2.

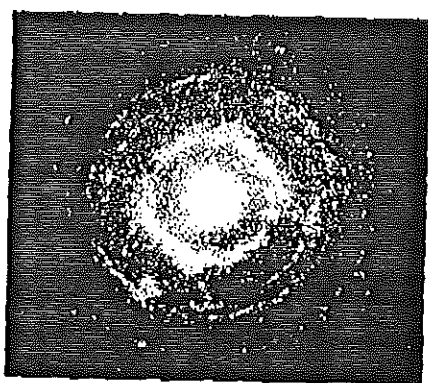


Figure 2a

The electron diffraction of deformed binder in composite

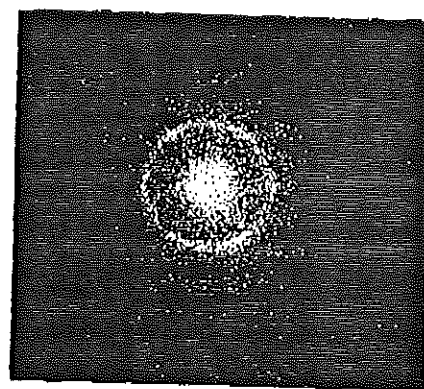


Figure 2b

The quasi-amorphous state of a binder

The binding phase on a micro-level is in two-phase state - on figures one can see both an austenitic phase, and martensitic one in a form of a plate. As it is possible to see, the plates have places in volume of a binding phase, and at approach to carbide particles closely adjoin to

border of "binder-carbide", Fig.3. The area of contact "martensitic plate - carbide grain" is different for carbides with the different size. On Fig.4 the angles measured on the various images of contact "martensitic plate - carbide grain" are shown. It is visible, that than it is less size of a carbide grain, that it is more angles of contact. It, as appear, testifies that in a loading process there is the rotation of the carbide grains that greater, than it is less their size.

Such rotation of the carbide grains cannot occur without formation of the specific internal structure of a binding phase. On Fig.5 the data on measurement of azimuth angles of binder fragments from degree of plastic deformation are shown. It is visible, that the coarse structure (as for TEM) in initial condition is broken with growth of strain into fragments with disorientation each other, and the angle of its rotation is increased exponentially with growth of deformation. It is characteristic, that in carbide grains the increase of dislocation density was observed.

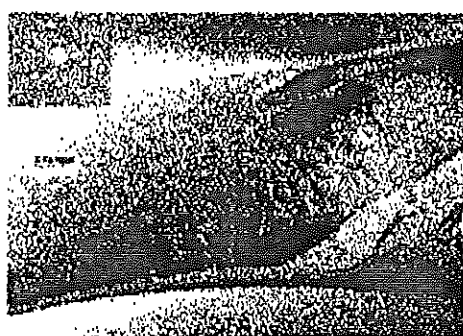


Figure 3
TEM image of composite after loading

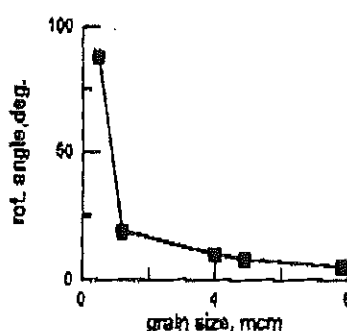


Figure 4
The rotation of a carbides
vs. its sizes

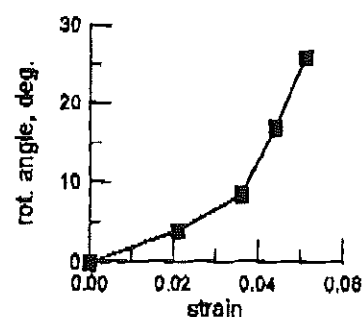


Figure 5
The angles between the
fragments of binder

So, it may be realized the following transformation scheme in the binder phase of the composite during deformation: $B2 \Rightarrow B2 + B19' \Rightarrow B2 + \text{"quasiamorphous state"}$, with formation of fine-grain, highly disoriented structure less then 10 nm in grain size, characterizing by high plasticity and strengthening and stipulating external loading effectively transferred onto a strengthener, causing simultaneous dislocation slipping even in typically brittle TiC particles. The subsequent loading increases the multiple cracking of plastically deformed hard particles and, finally, one can obtain the high value of fracture toughness of the material.

On Fig.6 are shown the optic microscopic images of a surface of cross-section of a flyer after its interaction with target. The analysis of microstructure of samples were shown, that in material there are many microcracks, concentrating in a form of strip-lines or "tracks", taking place through the whole sample are observed. The fact of occurrence of such "tracks" testifies to special condition of a binder at the moment of impact. Moreover, these "tracks" were formed at initial stage of fracture and only then were taken place a spall. As appear, it is connected to presence in composite of a disperse carbide phase. Really, if to plot a distribution of a carbides on its sizes $N(d)$ and a distribution of a distances between cracks, $N(h)$, it is possible to see the certain dependence, Fig.7. First of all on distribution $N(h)$ is displayed at least three maximum (which was marked by arrows) at $h=2, 4$ and 8μ , while the average size of a carbide grain is equal 1μ . The similar picture is observed for materials with other size of a carbide grain.

This dependence can be presented analytically in a form: $Y = \sum A_i \exp[-\alpha(x+2^i d)]$,

where d - average size of a carbide grain, and A_i - function, describing change of intensity of maxima. It can be write in a form:

$$A_i = I_i (x + b_0)^2$$

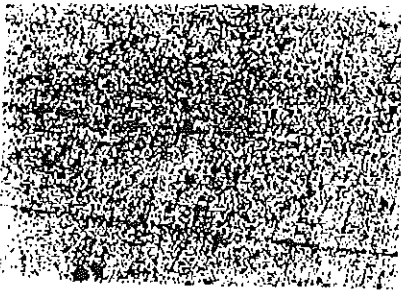


Figure 6a
"Tracks" in the samples after
shock loading. (x 200)



Figure 6b
"Tracks" in the samples after shock
loading. (x 800)

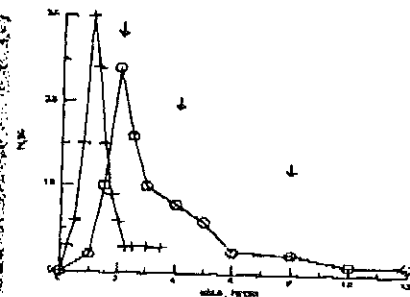


Figure 7
The size distributions of the
carbide particles (+) and distance
between the cracks (o)

This function depending on b_0 in positive area of argument can be or decreasing, or growing. In a first case b_0 is very great, in second - it is very small. Experimental data are shown, that b_0 - is great and, as appear, it is connected to length of a critical crack.

4. Conclusions

Thus, it is possible to point out a number of the main features of behavior of a composite with a structure-unstable binding.

1. Inhomogeneous deformation of the binding phase is able to change a structure under external loading causes its transformation. It should be noted for the latter to occur to the different degrees following the strain, the higher inhomogeneity of stressed state and plasticity of the binding material owing to transformation, the higher dispersion of the binding structure.
2. The combined influence of transformation and constraint of deformation results in the efficiently higher stress of martensite shear under deformation and in a binder arises the fine-grain structure that causes the high toughness of the whole composite.
3. The physical meaning of usage of the structure-unstable bindings in the composites is that to lower a scale of structure levels of plastic deformation and fracture owing to formation of a micro-crystal structure in the binding phase under inhomogeneous loading.

References

- [1] Almond E.A. Strength of Hard Metals. *Metal Science*, #12, pp.587-592, 1978.
- [2] Kulkov S.N., Poletika T.M., Chuhlomin A.Y. and Panin V.E. The Influence of the Phase Content of TiC-TiNi alloys on a Fracture Behavior and Mechanical Properties. *Poroshkovaya Metallurgiya*, v.8 (260), pp.88-92, 1984.
- [3] Kulkov S.N., Poletika T.M. Heterophase Materials with Structure Instabilities: Structure Levels of Deformation and Fracture. In: *Structure Levels of Deformation and Fracture*, Novosibirsk, Nauka, pp.187-203, 1990.

HIGH PLASTIC DEFORMATION OF NITROGEN ALLOYED STEELS UNDER DYNAMIC COMPRESSION LOADING

LICHTENBERGER A., LACH E. (ISL), COUQUE H. (GI)

ISL, Institut Franco-Allemand de recherches de Saint-Louis,

B.P.34, - 68301 Saint-Louis – France

Giat-Industries, Division des systèmes d'armes et de munitions,

7 route de Guerry -.18023 Bourges - France

I - INTRODUCTION

In dynamic compression of classical steels, the formation of adiabatic shear bands and the high level of hardness usually limits the plastic strain, especially at high strain rates.

With an unusual combination of strength, toughness, corrosion resistance, wear resistance and non magnetizability, nitrogen alloyed steels are a relatively late group of materials, which is still in development. They are produced by adding between 0.3 and 1% nitrogen in interstitial solution. Mn, Cr, Mo and V are increasing the solubility and Ni and Si are decreasing the solubility of nitrogen. The main property of nitrogen is to stabilize the austenitic structure, so that no formation of deformation martensite α' will occur. Since no strain-induced martensite occurs, nitrogen alloyed steels possess excellent cold workability up to very high strains, combined with high strength (between 1000 and 2000 Mpa). Deformation rates up to 95% were achieved without austenite becoming unstable [1].

The dynamical behaviour of very high strength nitrogen alloyed steels and the hardening capacity under shock waves have been investigated in previous works [2] [3]. Nitrogen in interstitial solution increases internal friction, which leads to very high strain rate sensitivity. With a very low stacking fault energy (10 mJ/m^2), high deformation leads to microstructure with high density of slip bands and/or twins. The aim of this work is to point out the large deformation capacity of nitrogen steels under high strain rate compression. This study was conducted with three dynamic compression techniques consisting of the Hopkinson bar test and two version of the Taylor test which are the single cylinder impact against a rigid anvil and the symmetric impact of two identical cylinders.

II – MATERIALS

Three different austenitic nitrogen alloyed steels were studied.

Steels A and B named as P900¹ (Z8CrMnN18-18) have the same chemical composition. They are composed of high amount of Mn and Cr to increase the solubility of nitrogen and do not have a strong nitride-forming tendency. The characteristics of this kind of steels depend on nitrogen in interstitial solution. The initial state was workhardened by a ring extension process (producer: VSG). Steel represents the initial state with a hardness of 380HV30. Some slip lines are present in the individual grains. Steel B has been annealed by a temperature of 1080°C. Its microstructure contains recrystallized grains without any slip bands but recrystallization twins. The hardness after solution annealing decreases to 280HV30.

Steel C, named Uranus² B66 is quite different from steel A and B because the main alloying element is Ni and Mn contents is reduced. This alloy has been developed especially for its improved corrosion resistance. Its hardness in the initial state is only 220HV30. The microstructure is very similar to that of steel B but with a larger grain size.

Compared to classical high strength martensitic steels with similar hardness, these steels possess a high flow stress, high strain hardening and they are also very sensitive to strain rate. The other particularity of this steel is the high amount of plastic deformation, up to 70%, which is also unusual for classical high strength steel.

III - EXPERIMENTAL RESULTS

III - 1 Testing Procedure

Different sizes of cylindrical specimens were machined with 4mm diameter and 2 to 5mm lengths. All the samples are lubricated with a special lubricant that minimizes the effect of friction during testing. True stress-strain curves are determined in the uniaxial compression state at various strain rates at room temperature.

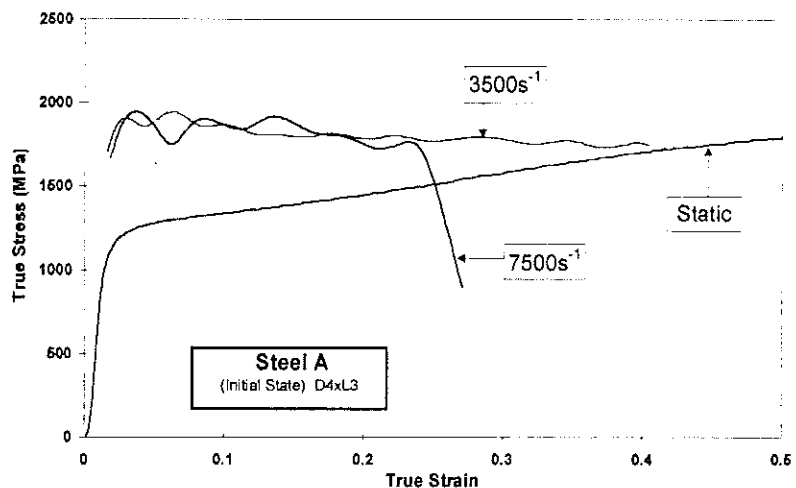


Fig. 1: Compression tests on steel A

Dynamical compression tests are conducted at high strain rate from 3000 s^{-1} to over 20000 s^{-1} using a split Hopkinson pressure bar. In order to obtain the deformation of the high strength steels without indentation of the bars, a sintered tool steel heat treated to a very high hardness of 67HRC was used. A good straightness has been achieved and tests have shown the ability of such materials to support high impact stresses without plastic deformation or rupture. Short rise time was used for the incident wave in order to get a rapid answer of the material behaviour.

Several single Taylor tests was conducted with cylinders having a 9mm diameter with 36mm length and at velocities ranging from 115 to 220m/s, against a rigid tungsten carbide target. A symmetric Taylor test has also been used in order to investigate the influence of friction [4].

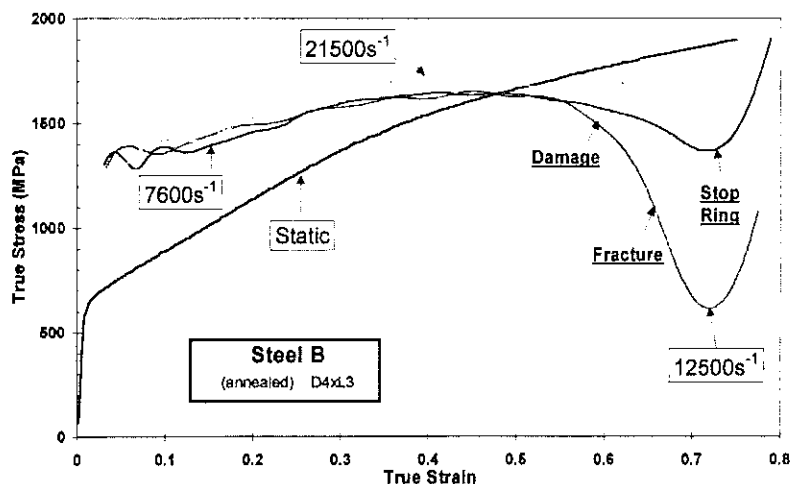


Fig. 2: Compression tests on steel B

¹ Registered Trade Mark of VSG Energie und Schmiedetechnik GmbH, Westendstr.15, D 45143 Essen

² Registered Trade Mark of Creusot loire, BP 56, F-71202 Le Creusot

III - 2 Compression stress-strain behaviour

The stress strain behaviour in dynamic loading for the three types of steels is given in figures 1, 2 and 4. In static compression the materials can be loaded to very high deformation without rupture (more than 100% true strain could be achieved), but a begin of some inhomogeneities can be seen above 70 to 80%.

For steel A (figure1) dynamic loading leads up to 50% increase in the flow stress with the absence of any strain hardening. A slight decrease of the true stress is due to the thermal softening by adiabatic condition of the test generating some increase in temperature. The maximal deformation before rupture (for the defined size of specimens) is much smaller than in the static condition and seems to be reduced with increasing strain rate.

Steel B shows much higher strain rate sensitivity than steel A; the flow stress at small plastic deformation reaches twice the corresponding value in quasi-static condition. Compression tests, with stop ring could be conducted up to very high true strain (70%) without any fracture in the specimen. By strain rate of $12\,500\text{ s}^{-1}$, fracture begins at about 65%. The curves in figure 2 shows clearly the different domains of deformation. At the beginning of plastic deformation a small strain hardening is observed which decreases with strain up to about 60%. A first important decrease of stress is due to a damage in the specimen, followed by a second change in the slope of stress curve, indicating the development of fractures. The following increase in the transmitted wave is due to the influence of the stop ring that avoids further deformation of the specimen and allows microscopic observations of existing damage. During each test the specimen average strain rate is relatively constant (see figure 3).

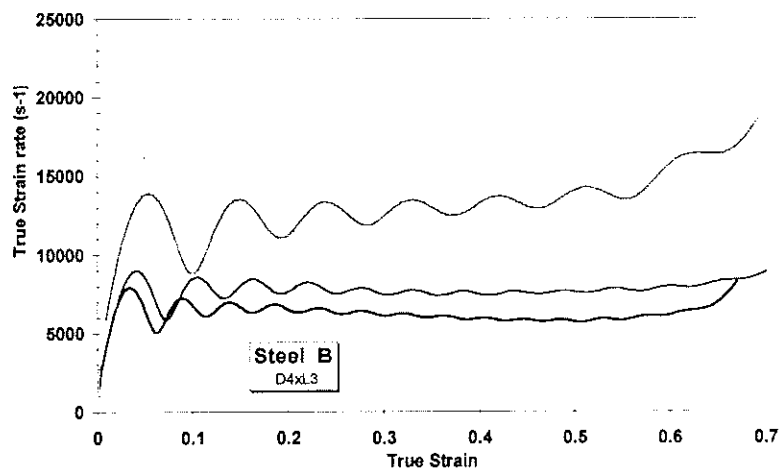


Fig. 3: Variation of the strain rate with strain

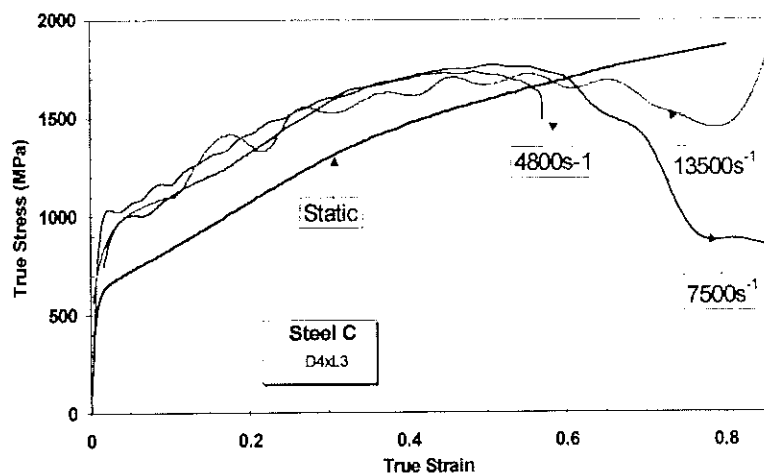


Fig. 4: Compression tests on steel C

The behaviour of steel C is similar to the previous annealed steel, but with a high strain hardening in the dynamic condition. Very high deformation (up to 60%) could be also observed even at very high strain rate (figure 4). Strain rate up to more than 20 000 m/s could be achieved with smaller specimen (4mm diameter and 2.2 mm length). In this case, the

assumptions made in the treatment of Hopkinson bar data must be verified. Stress inhomogeneities appear in the specimen and the inertial stresses and velocities are no more negligible. Different approach have been proposed [5], [6], leading to the following equations:

$$\sigma_i = \rho \left(\frac{r^2}{16} + \frac{h^2}{6} \right) \dot{\epsilon}^2 + \rho \left(\frac{h^2}{6} - \frac{r^2}{8} \right) \ddot{\epsilon} \quad (1) \quad V_r = \frac{\dot{\epsilon} r}{2} \quad (2)$$

$$\sigma_z - \sigma_0 = \frac{2\mu r \sigma_z}{3h} + \rho \left(\frac{h^2}{12} - \frac{r^2}{16} \right) (\dot{\epsilon}^2 + \ddot{\epsilon}) + \frac{3\rho r^2}{16} \ddot{\epsilon} \quad (3)$$

h, r : height and radius of the specimen

$\dot{\epsilon}, \ddot{\epsilon}$: strain rate and acceleration

σ_i, V_r : inertial component of the stress and radial velocity

The influence of $\ddot{\epsilon}$ can be important but only at the beginning of the deformation and no more at high strains.

Friction can also be neglected [7]. The outer profile of the specimens after a high deformation have been measured and figure 5 shows a final geometry which remains very close to the cylindrical shape with only very small barrelling.

For the present tests, with the geometry of our specimen:
 at $20\,000\text{ s}^{-1}$: $\sigma_i=6.6\text{Mpa}$;
 $\sigma_z/\sigma_i=1.6\text{Mpa}$; $V_r=20\text{ m/s}$.

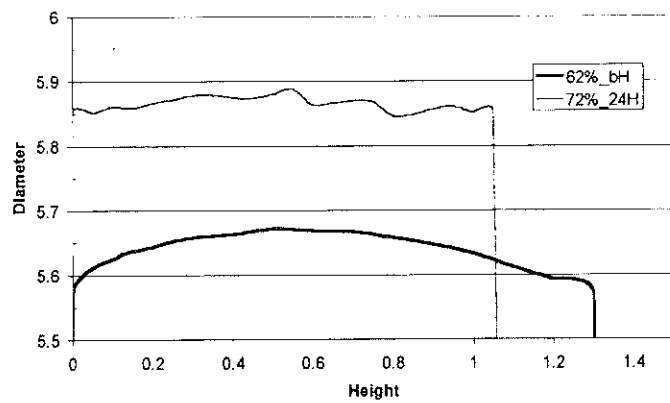


Fig. 5: Profile of a specimen after high compression.

These evaluations indicate that inertia can be important and cause some errors in the classical data processing. A careful analysis is necessary to estimate the remaining inertial contribution and to obtain the corresponding correction. Simulations with code DYNA2D are running.

III - 3 Single Taylor test

Single Taylor tests were realized with steel A only. After impact at different velocities, the final profile was measured with a laser micrometer. Experimental results on the variation of the radius of the impacted projectiles are given in figure 6. The maximal velocity at 218m/s leads to a complete rupture of the specimen. At 200m/s some small cracks appears with 45° orientation at the front surface.

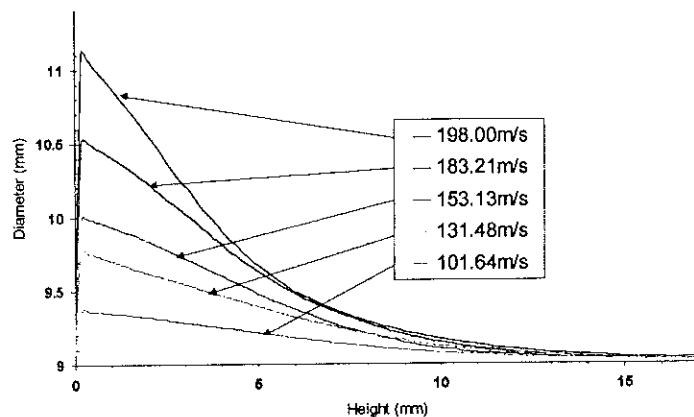


Fig. 6: Profile of the impacted cylinder at different velocities.

III - 4 Symmetric Taylor test

Along with single Taylor testing, symmetric Taylor testing of specimens 9 mm in diameter and 35 mm in length was conducted to investigate the effect of friction on deformation and fracture of impacted steel A cylinders. When compared to single Taylor testing, symmetric Taylor testing do not involve friction at the loading interfaces. Symmetric Taylor tests were generated with an improved testing procedure involving Teflon sabots [4]. The loading system consists of a 25 mm caliber gas gun launching one Taylor specimen guided with a Teflon sabot against a second Taylor specimen positioned with an identical Teflon sabot at the gun muzzle. The use of Teflon sabots during the loading phase facilitates planar and coaxial impacts. Because the Teflon has an impedance five times lower than steel A, the Teflon sabots have no interference during the specimen loading phase. To compare results generated with the two Taylor set-ups, an equivalent impact speed was introduced equal to half the launch speed for the symmetric Taylor test and equal to the launch speed for the single Taylor test.

At a given equivalent speed, larger final diameters were generated with the symmetric Taylor specimens resulting from the absence of friction at the impact, see Table 1 and Figure 7. Preliminary results from numerical simulations conducted at an equivalent speed of 131.5 m/s with the hydrocode AUTODYN indicate that the dynamic friction is of the order of 0.01. Shear bands were generated at higher final diameters and equivalent speeds for the single Taylor specimens when compared to the symmetric Taylor specimens. The higher final diameters of the single Taylor specimens indicate that higher equivalent plastic strains are needed to generate shear bands. Most probably, this is due to the friction at the impact plane implying higher pressures therefore delaying shear band formation.

Numerical simulations, currently being conducted, will bring indights of the state of stress of the two Taylor and friction characteristics at the steel/tungsten carbide target interface.

Table 1 : Comparison of single and symmetric Taylor test results for steel A.

Taylor test	Constant equivalent speed		Shear band initiation	
	Single	Symmetric	Single	Symmetric
Launch speed (m/s)	131.5	263.0	198.0	324.5
Equivalent impact speed (m/s)	131.5	131.5	198.0	162.3
Maximun final diameter (mm)	9.77	10.01	11.23	10.70
Shear bands	No	No	Initiation	Initiation

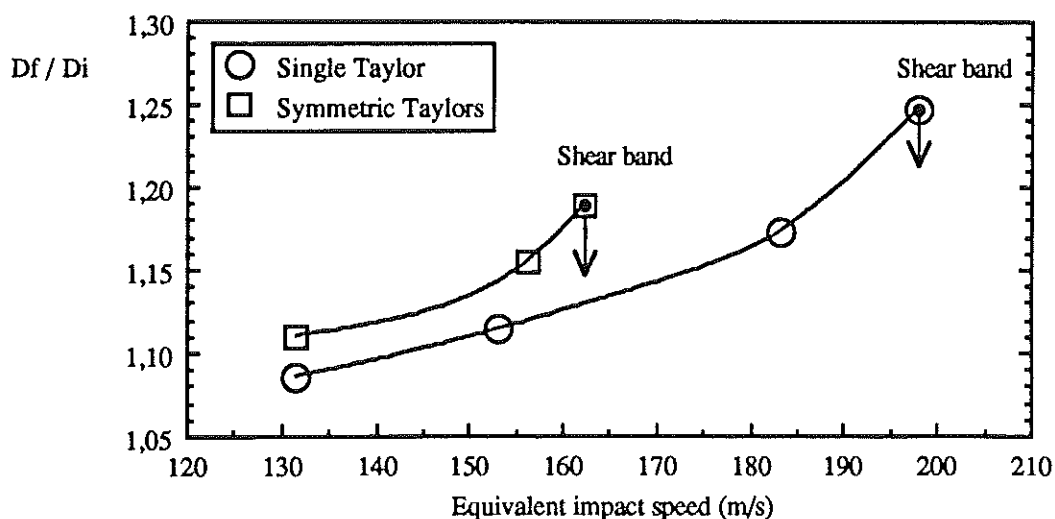


Fig. 7: Final to initial Taylor diameters ratio function of the equivalent impact speed for steel A.

IV - MICROSCOPIC OBSERVATIONS

Figure 8 shows a micrograph of a dynamically compressed specimen (steel B). Fine adiabatic shear bands begin to form at the edge of the specimen with a 45° orientation. The width of these adiabatic shear bands is about 5 μm and the microhardness 800 HV0.1. These shear bands lead rapidly to a catastrophic failure. In the edge regions the density of slip lines is higher than in the rest of the longitudinal cut, where the deformation of the structure seems to be relatively uniform. This observation contributes to the validity of the compression test by high levels of strains and stresses (over 60-70% and 1600Mpa).

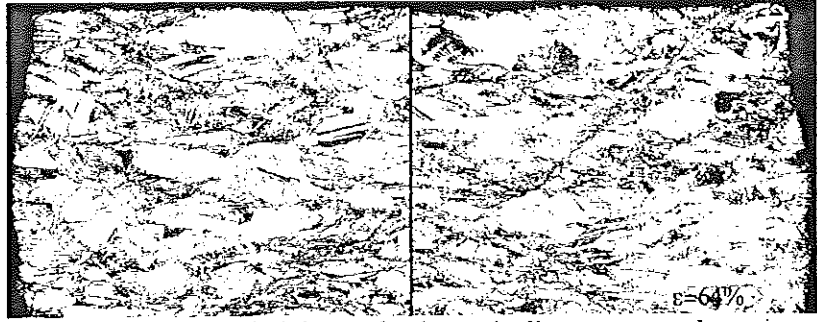


Fig.8: Axial cut of a dynamically compressed specimen

In the Taylor tests material near the impact region is subjected to very high deformation combined with high strain rate ($>10^4 \text{ s}^{-1}$) that can be calculated with simulation of this test [2]. At 200m/s, the first cracks can be observed on the impact surface of the mushroomed part with an angle of 45° towards the longitudinal axis (figure 9). High deformations can be seen on the microstructure in the impact region of highest radius, with the appearance of adiabatic shear bands in the early state.

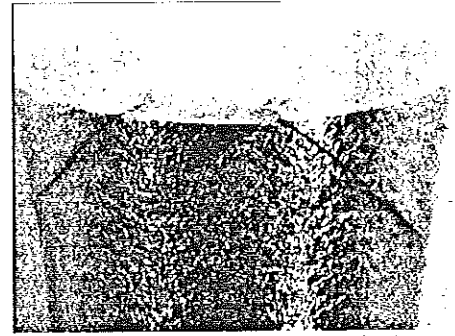


Fig. 9: Taylor test (steel B)

V - CONCLUSION

Dynamic compression behaviour of high strength nitrogen alloyed steels was investigated at high strain rate (up to $20\,000 \text{ s}^{-1}$) and at high deformation (up to 60% true strain without damage) using single and symmetric Taylor tests and Hopkinson tests. Damage in the specimens was observed to occur via adiabatic shear bands at strain varying from 60 to 70%.

The effect of friction at the specimen loading interfaces was investigated with the two types of Taylor tests and is being analysed through numerical simulations. Preliminary results indicate that friction implies a highly constrained stress state delaying shear band formation.

References

- [1] Speidel M.O., Uggowitzer P.J.: "Stickstofflegierte Stähle", Ergebnisse der Werkstoff-Forschung Band 4, Thubal-Kain, Zürich, 1991.
- [2] Lichtenberger A., Lach E., Rondot F., "Dynamical behaviour of very high strength Nitrogen alloyed steels", Eurodymat 97, Toledo, 22-26 Sept. 1997,
- [3] Lach E., Uggowitzer P. J., Rondot F., "Hardening of nitrogen alloyed steels by shock waves and their mechanical properties", Eurodymat 97, Toledo, 22-26 Sept. 1997.
- [4] Couque H., "On the use of the symmetric Taylor test to evaluate dynamic ductile compression fracture properties of metals, SUSI 98, Thessaloniki, p579, juin 98
- [5] Malinowski J.Z.; Klepaczko J.R., "A unified analytic and numerical approach to specimen behaviour in the split-Hopkinson pressure bar" Int. J. Mech. Sci. Vol.28, N°6, p.381, 1986.
- [6] Gorham D.A. "An effect of specimen size in the high strain rate compression test", Dymat 91, Strasbourg, Journal de physique, C3, Vol.1, Oct. 1991.
- [7] Lichtenberger A., Lach E., Bomann A., "Analyse du frottement dans les essais de compression sur barres d'Hopkinson", Eurodymat 94, Oxford, Sept. 1994.

Dynamic Testing on Gleeble Physical Simulator

S.T. MANDZIEJ
Advanced Materials Analysis
P.O.Box 3751, NL - 7500 DT Enschede

I - INTRODUCTION

The physical simulation is a way to gain physical data of material behaviour characteristic of a real industrial process. Such data can then be used for engineering calculations aiming to modify technology, design tools, etc., or for computer calculations to describe a behaviour of any workpiece during processing and to predict its properties after.

The history of physical simulation begins with the welding thermal cycle simulator, called Gleeble, which was made at Rensselaer Polytechnic Institute in USA just after the WW-II to study heat affected zone (HAZ) properties of welds on the novel at that time HSLA steels. This simulator, in its initial form, comprised:

- an AC resistance heating system with thermocouple feedback control,
- pneumatic displacement & loading system with appropriate sensors, and
- data recording devices.

An improvement added soon to more accurately reproduce the situation of HAZ where, due to thermal gradients, substantial local deformations occur, included dynamic servo-hydraulic mechanical system, thus giving rise to a modern thermal-mechanical simulator capable to execute simultaneously high rate thermal and mechanical cycles.

The Gleeble, after more than 40 years since its first appearance in research laboratories, has not much changed as to its principal idea, however it is now equipped with an up-to-date computer control and data acquisition. Having developed from a welding simulator into a modern dynamic multi-purpose simulating system, it can reproduce situations of many metallurgical processes, in which heating of a metal sample to any temperature including its melting point, is combined with deformation(s) at strain rates from 0.00001/sec up to 500/sec. The highest strain rates of this range are of particular interest to scientists and technologists occupied with contemporary high rate and high efficiency metal forming processes like hot- and warm- forging and rolling. To them, the Gleeble offers a significant advantage of exact studying multi-step deformations with a possibility to separate control strain and strain rate.

II - GLEEBLE / HYDRAWEDGE THERMAL-MECHANICAL SIMULATOR

When performing compression testing with high speed hydraulic systems, one typical problem that develops is overshoot strain. All hydraulic systems require a finite time and distance to stop, and even more time to revert their action. This problem can be minimized by using high speed hydraulic valves coupled with high speed computer control systems. The Gleeble systems series 3000 incorporate the highest speed valves and computers available.

However, even with the fastest valves and computer systems alone, overshoot strain can occur. To eliminate overshoot strains, the second hydraulic system called Hydrowedge, synchronized with the main / primary deforming system, acts as a flexible mechanical stop that allows the primary hydraulic ram to be stopped by running into an immovable object. Additionally, in order to perform exact multiple compressions sequentially, for which the specimen must be moved since the main hydraulic ram will stop at the same point in space each time, the Hydrowedge is used to program the necessary displacements. This allows to exactly control the amount of strain, while simultaneously and separately controlling the strain rate at which the sample is being deformed.

II-1. Hydrowedge system

The main purpose of the Hydrowedge system, schematically presented in Fig.1, is to provide a superior method for performing high speed single or multiple step hot/warm compression testing when compared to conventional methodologies. Such tests are carried out to evaluate a material using thermal and mechanical variables that simulate real world processing or service conditions, in particular strain rates, strains, and interpass times that are equivalent to the real processing.

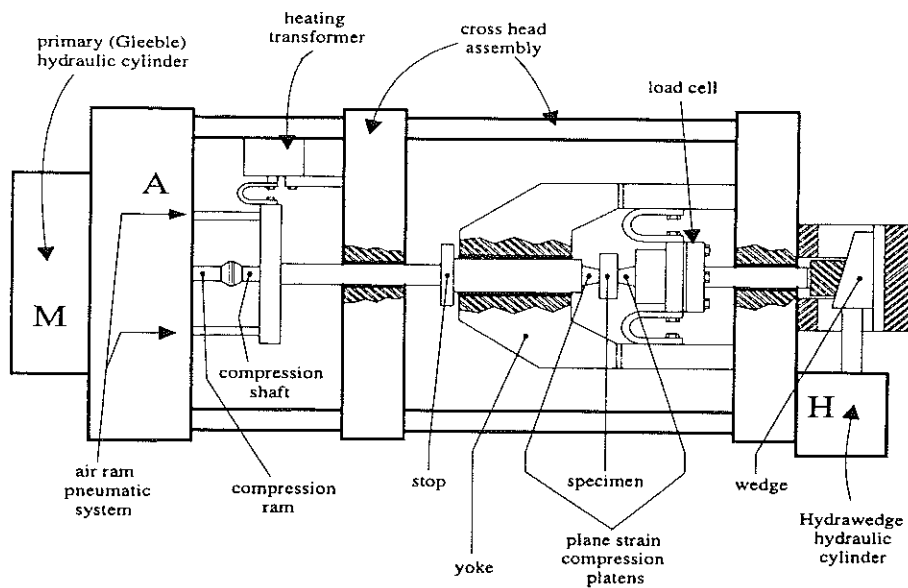


Fig.1. Schematic drawing of the Gleeble's Hydrowedge system

II-2. Operation of Hydrowedge

Hydrowedge system before deformation.

Schematic drawing of the Hydrowedge system before deformation, or between deformation steps, is given in Fig.2. The dashed lines represent the force path, while " Δl " represents the amount of deformation that will occur during compression.

Here the main hydraulic system "M" is not yet in contact with the deformation ram, there is a gap "g" between them. Also, the stop is not in contact with the yoke - " Δl " appears between them. In this position, the force, and resultant contact pressure the specimen is subjected to, are provided by the air ram system "A". The purpose of the air ram is to keep the specimen between the platens, and to maintain enough contact force to provide heating and cooling paths, otherwise between hits the specimen could fall out of the proper position between the platens.

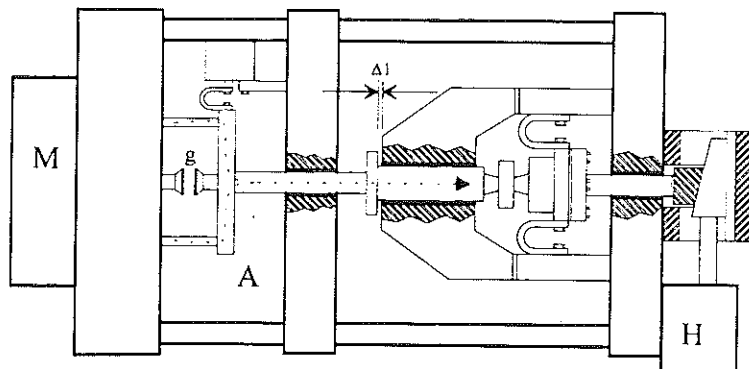


Fig.2 Hydrowedge system before deformation

Hydrowedge system during deformation.

To begin the deformation, the main hydraulic loading system “M” accelerates within the gap “g”. The deformation begins when it gets in contact with the deformation ram, and loads as great as 20 metric tons can be applied to the specimen (peak available load will depend on what Gleeble system model is rated for). The measured load on the specimen at this point would be the load required by the flow stress of the material under the programmed deformation conditions. The amount of allowed deformation, would be exactly like the “ Δl ” shows. In this step, the force path is straight from the main hydraulic system to the deformed sample, and it stays like that till the stop engages the yoke.

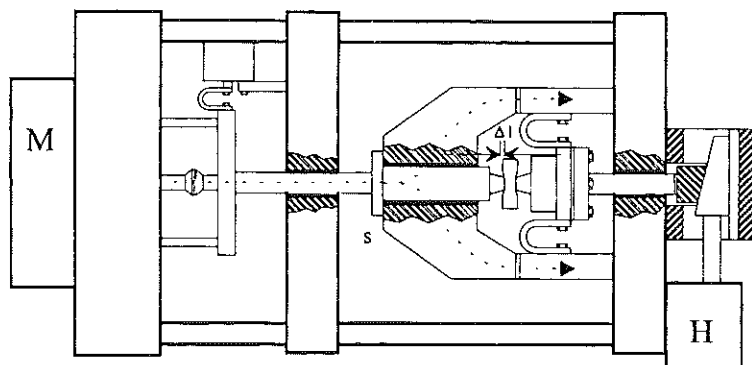


Fig.3 Hydrowedge system at the end of deformation.

Fig.3 shows the Hydrowedge system at the end of a deformation step. Here the main hydraulic loading system is still in contact with the deformation ram, but the load applied from the main hydraulic system is not being applied to the specimen. Instead, since the stop is in contact with the yoke, the load is being transferred around the specimen through the yoke. The purpose of the stop and the yoke is to end the deformation regardless of how fast the deformation ram is moving. The force to stop the ram is transferred to the crosshead via the stop and yoke. When the stop and yoke are in contact with each other there is no significant load on the specimen.

Hydrowedge system preparation for another deformation step

At the beginning of preparation for another deformation step, or in preparation for controlled cooling, the main hydraulic loading system backs away from the deformation ram to the pre-deformation position. At this moment, as presented in Fig.4, there is no force being applied to

the specimen since the main hydraulic system is no longer in contact with the deformation ram, and because the force exerted due to the air ram system is being transferred around the specimen through the yoke. In order to prepare for another deformation step it is necessary for the whole Hydrawedge system to return to the "prior to deformation position".

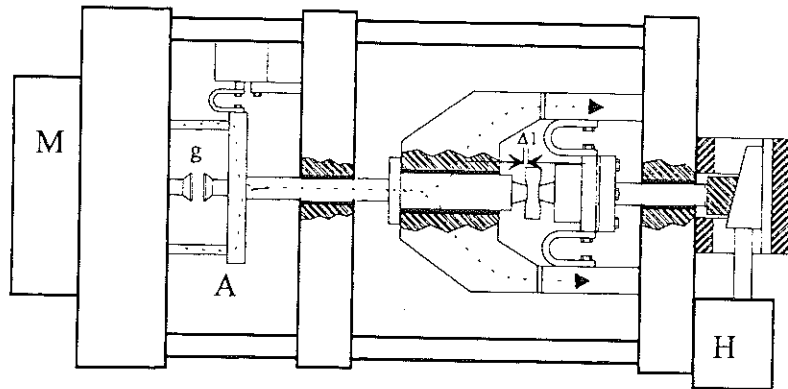


Fig.4 Hydrawedge system preparation for subsequent deformation step

To achieve this, it is necessary for the Hydrawedge secondary hydraulic system "H" to move the specimen toward the main hydraulic system. As the Hydrawedge moves the specimen, the stop will be removed from contact with the yoke, and hence the load from the air ram system will again be applied to the specimen thus securing its firm position between the platens. The load from the air ram system must be applied to the specimen rather than the yoke in order to have adequate heating and cooling. The Hydrawedge is programmed to move the specimen for the next value of strain ($\Delta\epsilon_i$) for the subsequent deformation step. In this position heating and cooling are continually controlled between deformations.

III - PERFORMANCE OF GLEEBLE / HYDRAWEDGE SIMULATOR

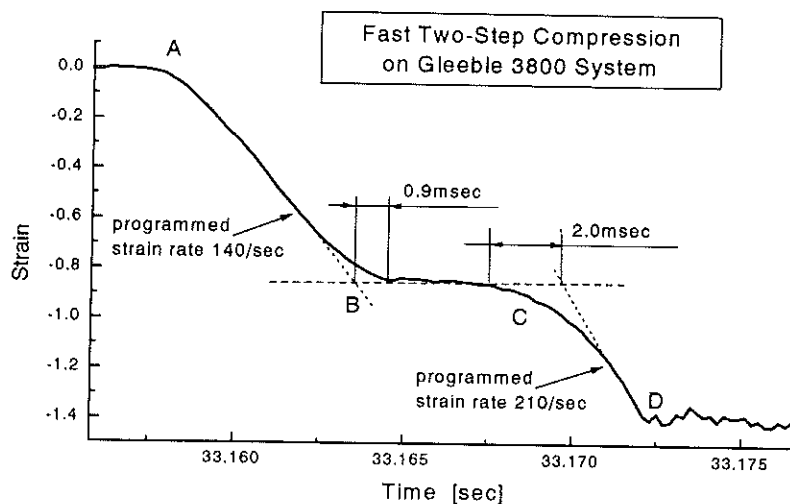


Fig.5 Accuracy of strain rates during two step compression on Gleeble 3800 system

The performance of an up-to-date Gleeble's main servo-hydraulic unit, can be showed in the test like presented in the following Fig.5. This figure shows the reaction times of the main hydraulic cylinder, and also of the fast stop exerted by Hydrawedge.

The material tested here was AlSi27Ni6 PM alloy, which during deformation at high strain rates generates a substantial adiabatic heat, giving rise to a self-healing of the material and to a decrease of its susceptibility to cracking.

To show the performance / speed of the servo-hydraulic valve itself, both deformation steps were executed without Hydrawedge operating; the Hydrawedge in this deformation test only provided the exact total amount of strain and the instantaneous stop at the end of it.

The main hydraulic system, which accelerates before the first hit as the free gap "g" allows it, is engaging the sample as it is visualized at the point "A" of the graph and deforms it with the first programmed strain rate of 140/sec. But to minimize the overshoot and to reach exactly the programmed strain of 0.85 in the first step, the hydraulic system has to slow down, as shown at point "B" of the graph, by partly closing the valve for about 1 millisecond. Then, after the hold time of about 3 msec, during which the main piston was not backed (as it was programmed like that), the subsequent acceleration of the piston, as shown at point "C" of Fig.5, takes more time, and the delay of about 2 milliseconds appears before the deformation can reach the second programmed strain rate of 210/sec. The Hydrawedge's stop at the end of both deformation steps caused the deformation to end with almost no delay, as shown in point "D" of Fig.5, and the total strain reached quite accurately the programmed value of 1.4. The use of such a high strain rate, and its fast stop, resulted of course in certain "ringing" in the whole deformation system, which has been mainly due to an elastic deformation of the yoke and lasted for a few milliseconds after the stop, as it can be seen in Fig.5 after the point "D".

From this graph, practical reaction times of the "plain" Gleeble system can be read, which are in the order of a few milliseconds. In the Gleeble plus Hydrawedge system, these reaction times are much shorter, like for example is shown at point "D" of Fig.5.

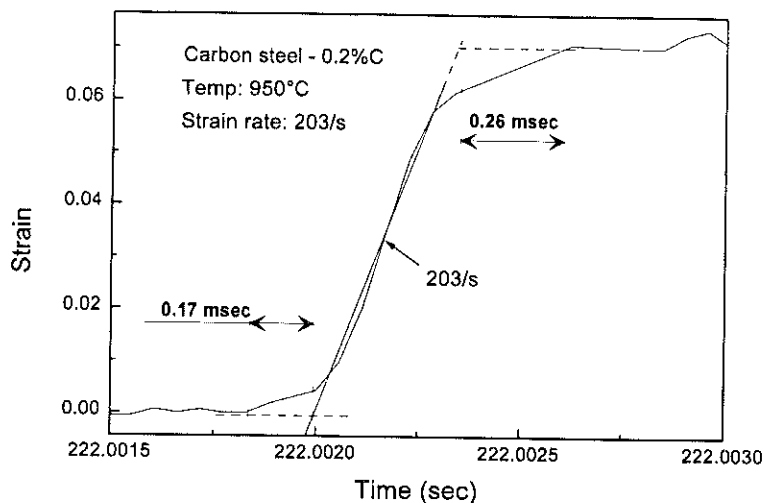


Fig.6 Practical performance limits of Gleeble 3800 / Hydrawedge system

An example of the ultimate performance of the Gleeble / Hydrawedge system, is given in Fig.6. Here, a plain carbon steel sample of an initial height 5.0 mm, was hot compressed in a single hit with the strain rate of about 200/sec, to the final height of 4.66 mm. As it can be seen, both the initial delay of 0.17 msec to reach the programmed strain rate, and the "slow down" at the end of the hit, are in the range much below one millisecond. And about one-half

of the deformation applied here, i.e. 0.15 to 0.20 mm of sample's height, can be treated as the reproducible accuracy of the Gleeble / Hydrawedge system for the strain rates of 200 to 300/sec. If the accuracy of the height reduction is acceptable in the range of 0.30 to 0.40 mm, then the maximum available at present programmed and controlled strain rate of the Gleeble plus Hydrawedge system is of about 500/sec.

Another issue of the performance is the time required for the main hydraulic system to pull back to the pre-deformation position and for the secondary Hydrawedge hydraulic system to set up the next programmed strain. For the typical heights from 5 to 25 mm of samples for plane strain compression tests, and for the strains between 0.2 and 1.5, the 20T force Gleeble 3800 system requires from 20 to 200 milliseconds time before the next hit can be executed.

The following graph, Fig.7, shows a three-step compression of plain 0.2% carbon steel at 1075°C. As the displacements recorded in it were measured by a longitudinal "jaw-to-jaw" strain gauge, it is possible to see from it how the main and secondary hydraulic systems cooperate during the whole three-hit deformation test.

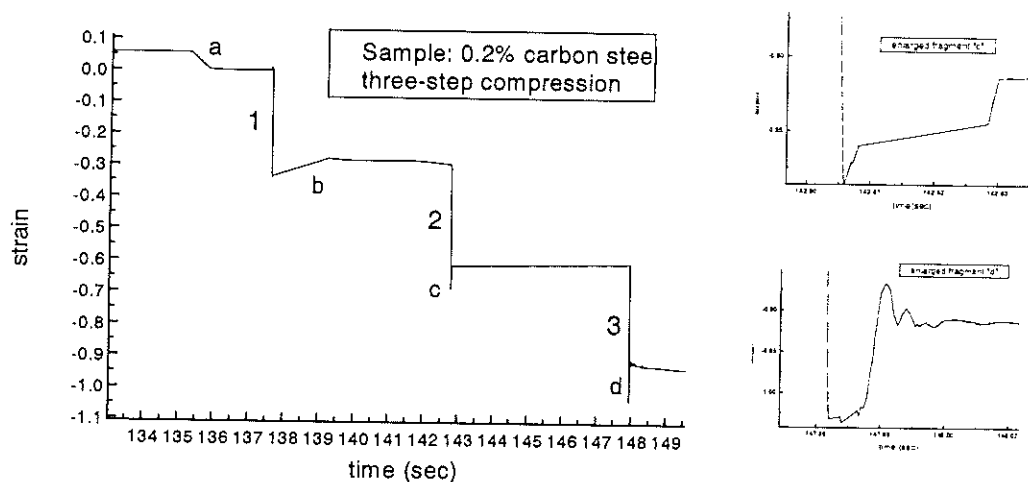


Fig.7 Reaction times of Gleeble 3800 with Hydrawedge, In three-step hot compression of carbon steel.

The displacement curve of Fig.7, shows at point "a" the setting up provided by Hydrawedge and correction of existing backlash, which took about 0.5 sec. After the first deformation, to a strain about 0.3, the backing away of the main hydraulic system, and the setting of the next deformation by Hydrawedge, were executed slowly and this took about 1.5 sec (point "b"). The preparation for the third step was made in a fast mode, as shown at point "c", and the whole preparation took about 25 msec for the main piston to pull back and for the Hydrawedge to set the programmed strain for the third stroke. This last figure of 25 msec is about the practical lower limit for the Gleeble / Hydrawedge system to prepare for the next deformation step.

Concluding remark.

As this article is mainly of an informative type, therefore the author reserved for himself the right not to draw out any scientific conclusions, leaving the whole issue open for an eventual discussion.

COMPORTEMENT MECANIQUE

D'UN EXPLOSIF COMPOSITE

P. Racimor, M. Quidot, P. Chabin

SNPE -Centre de Recherches du Bouchet 91710 Vert-Le Petit

Résumé

Les matériaux énergétiques de défense de type composite ont un comportement mécanique complexe que l'on peut qualifier de viscoélastique non linéaire. Une première méthode approchée de dimensionnement des explosifs composites est directement dérivée du domaine de la propulsion et utilise le principe de l'équivalence temps - température. Cette méthode s'avère trop approchée compte tenu des besoins actuels et futurs en matière de dimensionnement mécanique des explosifs, en particulier dans le cas des têtes militaires. Nous présentons les moyens expérimentaux : barres de Kolsky-Hopkinson basse impédance, Taylor test inverse avec instrumentation VISAR, et numériques : modèle de Maxwell généralisé dans le code de dynamique rapide LSDYNA, mis en place à SNPE pour le développement d'un modèle de comportement mécanique des explosifs composites en régime dynamique.

1. INTRODUCTION

L'accroissement des performances des systèmes d'arme, en particulier des têtes militaires, se traduit par des accélérations en phase propulsion et des vitesses à l'impact sur cible plus importantes entraînant des sollicitations mécaniques extrêmement sévères pour l'explosif et pouvant conduire à des ruptures et des mouvements préjudiciables au bon fonctionnement du système.

Les problèmes potentiels liés à ces mouvements et donc directement dépendant du comportement mécanique de l'explosif peuvent être de différentes natures, par exemple :

- rupture de l'explosif pouvant entraîner un fonctionnement détonique non nominal ou un allumage prématuré par friction.
- action mécanique importante de l'explosif sur d'autres parties du système (corps, système d'amorçage,...).
- écartement de l'explosif par rapport au système d'amorçage.

Il est important d'utiliser la simulation numérique pour le dimensionnement mécanique des têtes militaires et la définition d'essais représentatifs à l'échelle du laboratoire.

Il est donc essentiel de bien caractériser le comportement des explosifs dans ce domaine de sollicitation dynamique afin de réaliser des simulations numériques réalistes.

2. MODELE DE COMPORTEMENT MECANIQUE

2.1. Caractéristiques mécaniques des explosifs composites

Les explosifs composites sont composés de charges cristallines de faible diamètre enrobées dans un liant polymère. Le taux de charge est très élevé et les surfaces d'adhésion entre le liant et les charges sont très importantes.

Les explosifs composites sont proches de par leur nature des propergols composites et ont donc des caractéristiques mécaniques qualitativement similaires et un comportement du type viscoélastique non linéaire endommageable [1] [2].

Une première méthode approchée de dimensionnement mécanique des explosifs composites est donc directement dérivée du domaine de la propulsion et utilise le principe de l'équivalence temps - température. Il importe de vérifier l'extrapolation de ce principe, qui n'est qu'approché pour les matériaux énergétiques de défense en raison du fort taux de charges cristallines, aux très fortes vitesses de déformation. C'est pourquoi nous avons développé des moyens expérimentaux et numériques pour l'évaluation du comportement dynamique des explosifs.

2.2. Implémentation et validation d'un modèle de Maxwell généralisé dans LSDYNA

Si au cours des 20 dernières années, de nombreux modèles de comportement mécanique plus ou moins complexes de matériaux énergétiques ont été développés, les modèles utilisés dans le monde au stade industriel pour le dimensionnement d'objets réels restent relativement simples en raison du coût de la caractérisation expérimentale de modèles complexes et de l'implantation et la validation dans des grands codes de calcul. Nous avons donc choisi d'utiliser, dans une première étape, un modèle simple viscoélastique de type Maxwell généralisé. Ce modèle s'exprime en petite déformation par :

$$\sigma'_{ij} = \int_0^t 2G(t-\tau) \epsilon'_{ij}(\tau) d\tau \quad (1)$$

Le modèle de MAXWELL généralisé implanté dans LSDYNA [3] suit la formulation générale des matériaux hypoélastiques.

SNPE dispose d'une large expérience de ce type de modèle dans les codes implicites ([4]) ; la formulation explicite adoptée dans LSDYNA est tout à fait identique. L'intégration est rendue praticable par une représentation du module de cisaillement en série de Prony :

$$G(t) = G_0 + \sum_{i=1}^n G_i e^{-\beta_i t} \quad (2)$$

On utilise alors une formulation récurrente ([5]) où on suppose la vitesse de déformation constante sur un pas de temps.

L'implantation du modèle est validée sur des cas tests élémentaires en statique : traction, traction-relaxation et fluage. La formulation non linéaire est validée par des tests de vérification de l'objectivité de la formulation et par un test de cisaillement. Pour ce dernier cas, nous avons développé une solution analytique en viscoélasticité.

3. CARACTERISATION MECANIQUE

3.1. Caractérisation en statique

Des essais de traction sont réalisés pour différentes conditions expérimentales : température, vitesse de traction. Les températures étudiées sont comprises entre -50 et +60°C, tandis que les vitesses de traction sont 5, 50 et 500 mm/min. Compte tenu de la valeur du coefficient de Poisson, le module de cisaillement est obtenu par $G=E/3$.

Le principe d'équivalence temps - température s'applique généralement pour les polymères, il a été mis en évidence en particulier par William, Landel et Ferry [5]. SNPE a appliqué ce principe non seulement pour le comportement mécanique de ses matériaux énergétiques, mais l'a étendu à leurs caractéristiques à la rupture. La méthodologie mise en place dans la propulsion a été reprise pour les explosifs composites. Ce principe d'équivalence temps - température est appliqué à la composition explosive étudiée. Il conduit pour chacun des paramètres de l'essai de traction à la relation :

$$P(T_1, \dot{\epsilon}_1) = P(T_{réf}, \dot{\epsilon}_{réf} a_T(T_1)) \quad (3)$$

Le paramètre P est le module de traction pour la suite de la présentation. C'est à partir de la courbe maîtresse ainsi obtenue que nous évaluons les coefficients du modèle de Maxwell pour des vitesses de déformation élevée.

3.2. Caractérisation dynamique

Il s'agit dans ce cas de réaliser des essais dynamiques à l'aide des barres de Hopkinson à des vitesses de déformation proche de celles estimées dans une tête explosible lors de son impact.

L'essai aux barres de Hopkinson consiste à placer une éprouvette cylindrique entre deux barres équipées chacune d'un pont de jauges de déformation. Une onde de choc est générée à l'extrémité de l'une des barres (barre d'entrée) à l'aide d'un impacteur projeté par un canon à air comprimé, cette onde de choc se propage le long de cette barre. Le pont de jauge de déformation caractérise cette onde dit « incidente » à son passage. A l'interface éprouvette - barre incidente, cette onde se décompose en une onde « réfléchi » et une onde « transmise ». L'onde réfléchi est mesurée par les jauges placées sur la barre d'entrée, l'onde transmise par celles placées sur la seconde barre (barre de sortie).

L'acquisition des signaux est faite à l'aide d'un oscilloscope numérique à mémoire.

Il est important de pouvoir distinguer ces différentes ondes, pour cela il faut principalement :

- optimiser la longueur de l'impacteur pour une longueur de barre d'entrée donnée,
- utiliser des barres dont la matériau est tel que son impédance acoustique soit adaptée à celle du matériau étudié.

Pour l'étude du comportement mécanique des explosifs composites nous utilisons des barres polymériques (P. M. M. A. ou Nylon), dont le caractère viscoélastique est pris en compte pour le traitement des ondes.

Les ondes sont mesurées à une certaine distance des interfaces avec l'éprouvette, et il est donc nécessaire de « transporter » ces ondes depuis leur lieu de mesure vers ses interfaces. Le logiciel DAVID [6] permet cette translation en tenant compte du comportement et de l'amortissement de barres polymériques ; il calcule également les forces, les vitesses aux interfaces.

L'une des difficultés lors du dépouillement est de bien recalibrer les débuts de l'onde réfléchie et de l'onde transmise. Ceci induit un léger écart dans ce recalibrage des ondes qui provoque les oscillations dans le début de la force appliquée à la face d'entrée de l'éprouvette. Ces oscillations sont également dues à l'aspect tridimensionnel des barres, elles sont visibles sur les ondes mesurées et plus particulièrement sur l'onde incidente.

A partir de ces résultats la contrainte moyenne et la vitesse de déformation moyenne sont évaluées dans l'éprouvette et un modèle de Maxwell à 5 branches est déterminé. La modélisation de l'essai en 1D statique avec le code LSDYNA permet de s'assurer de la représentativité du modèle. On montre que le modèle statique déduit de l'équivalence temps-température sous-estime largement les contraintes dans le matériau.

Des essais complémentaires ont été réalisés à des températures autres que l'ambiante. Nous constatons la forte influence de ce facteur sur le comportement des explosifs composites. La recherche d'un modèle devra prendre en compte cette constatation.

4. EVALUATION DE MODELES SUR LE TAYLOR TEST

4.1. Description du dispositif expérimental

Le Taylor test, dans sa configuration inverse-impact de projectile sur l'échantillon- a été mis au point à SNPE pour l'étude du comportement mécanique et de l'endommagement des matériaux énergétiques de défense [7]. Dans le cadre de cette étude, les essais sont réalisés à la vitesse la plus basse possible afin de rester, si possible, en dessous du seuil d'endommagement du matériau. On y a adjoint une mesure de vitesse matérielle en face arrière afin d'explorer un large spectre fréquentiel de la réponse viscoélastique du matériau. L'objectif de cet essai est d'évaluer le modèle statique déduit de l'équivalence temps-température et le modèle dynamique obtenu à partir des essais aux barres d'Hopkinson.

L'échantillon (\varnothing 15 h 30 mm) est maintenu sur un film Kapton (épaisseur de 0,1 mm) par un simple élastique. Le film Kapton est tendu de manière à ce que la face d'impact de l'échantillon soit bien parallèle à celle de l'impacteur. Ce système de fixation de l'échantillon est supposé avoir une influence négligeable sur les phénomènes observés.

La géométrie de l'impacteur et plus particulièrement sa longueur (\varnothing 40 h 90 mm, Aluminium 5083 H 111) a été définie de façon à assurer le maintien de la vitesse d'impact. L'impacteur lié à un sabot reste guidé dans le tube du canon au cours de l'essai, assurant une bonne planéité d'impact.

Un montage en PMMA, placé entre le réservoir de récupération et le montage de maintien, permet de visualiser l'échantillon avant et après l'impact. La mesure de la déformation est réalisée par ombrographie. Un système interférométrique de type VISAR push-pull a également été utilisé lors d'un tir, ce qui nous a permis de mesurer la mise en mouvement de la face arrière de l'échantillon testé.

4.2. Résultats

Deux tirs ont été réalisés. Les vitesses et les planéités à l'impact sont les suivantes :

TIRS	VITESSE	TILT
Tir 1	48 m/s	3 mRad
Tir 2	48.6 m/s	2 mRad

Pour le tir 1, l'examen de l'échantillon récupéré après tir a permis de vérifier l'absence d'endommagement et de déformation résiduelle pour la vitesse d'impact choisie. Le dépouillement des films réalisés avec une caméra DYNAFAX permet de montrer une très faible déformation de l'échantillon au cours de l'essai. La précision des résultats expérimentaux ne permet pas de ce fait une exploitation quantitative.

L'essai est simulé à l'aide du code LSDYNA en utilisant les deux modèles statique et dynamique. On constate que le modèle dynamique donne des résultats plus proche de l'expérience. Néanmoins, l'écart calcul-expérience est significatif et révèle la présence de phénomènes non linéaires et/ou visqueux non pris en compte dans la modélisation.

5. CONCLUSIONS

Des moyens expérimentaux et numériques ont été mis en place pour l'étude du comportement dynamique des explosifs composites. On a montré, sur le test de Taylor, qu'un modèle viscoélastique linéaire déterminé à partir d'essais aux barres d'Hopkinson apportait une amélioration par rapport à un modèle déduit de l'équivalence temps-température. Toutefois, cette amélioration reste insuffisante et il convient de compléter ce modèle en prenant en compte des non linéarités de comportement du matériau afin de rendre plus réaliste les simulations numériques de têtes militaires. D'autre part, des travaux sont actuellement en cours pour améliorer la modélisation de l'essai aux barres d'Hopkinson afin de mieux déterminer le modèle de comportement dynamique.

Références

- [1] A. Davenas : Technologie des Propergols Solides Masson, 1989
- [2] B. Gondouin et coll. : Progrès dans les Méthodes de Dimensionnement Thermomécanique.
Revue Scientifique et Technique de la Défense, 1997-3.
- [3] Hallquist J.O., Stillman D.W, Lin T-L.
LSDYNA3D User's Manual, Version 930.
- [4] M. Quidot
Traitement du Comportement Viscoélastique Linéaire Incompressible en Formulation de Hermann, Note SNPE N° 164/80/CRB, 1980.
- [5] M.L. Williams, R.F. Landel, J.D. Ferry
The Temperature Dependence of Relaxation Mechanics in Amorphous Polymers and other glass-forming Liquids.
J. Amer. Chem. Soc. 77, 3, 701, 1955
- [6] G. Gary
Manuel d'Utilisation du Logiciel DAVID
Laboratoire Mécanique des Solides - Ecole Polytechnique.
- [7] P. Chabin, P. Cognot, S. Lecume
Mise au Point du Taylor Lest Inverse au Canon à Gaz Léger.
CR N° 36/98/CRB, 1996

Development of an explicit dynamic code : application to metal cutting

O. PANTALE - R. RAKOTOMALALA - S. CAPERAA
Laboratoire Génie de Production CMAO, ENIT - 47 Av d'Azereix
65016 Tarbes cedex - France

I - INTRODUCTION

Experimental observations of metal cutting processes show that the phenomena associated to the chip formation is full of complexities. Many research projects about finite element simulation of cutting processes have been done last few years and a number of models are presented in literature [2]. The cutting tool is subjected to very localized high pressures and temperature gradients, and the influence of the cutting temperature distribution on tool wear is a well known factor. The aim of our study is therefore to develop a predictive numerical model suitable for giving stresses and temperatures distributions in the tool-chip contact zone, from the set of cutting material parameters.

This work is the continuation of a research project concerning simulation of cutting process done by the authors last few years [3], [5] and [4]. The main conclusions deduced from those previous studies concern the need to have a very flexible Arbitrary Lagrangian Eulerian (ALE) finite element code dedicated specially to dynamics computations and including several performant constitutive and contact laws suitable to model the very localized phenomena occurring near the front edge of the tool.

The development of this finite element code (named **DynELA**) is also motivated by the need for a code which could serve as a testbed for research into numerical algorithms and new constitutive and contact models for nonlinear materials.

II - THE FINITE ELEMENT CODE

DynELA is written completely in C++. The code contains no mesh generation capabilities (the finite element meshing is imported from a CAD). We developed a language for the input which allows the user to define the meshing, material properties, boundaries conditions... A home made graphic interface has been developed to serve as a pre-processor and post-processor. The current version uses a Lagrangian formulation, the ALE motion description will be added in a future version.

II - 1. Explicit time integration scheme

DynELA uses an explicit scheme for the time integration algorithm. Quantities at time $t + \Delta t$ are deduced from the corresponding known quantities at time t by respect of the conservation laws given in paragraph II-2. We introduced a predictor-corrector algorithm in the time integration scheme. The unknown quantities at time $t + \Delta t$ are given by the following set of relationships below:

$$\begin{cases} \rho_{t+\Delta t} = \rho_t + \dot{\rho}_t \Delta t \\ e_{t+\Delta t} = e_t + \dot{e}_t \Delta t \\ v_{t+\Delta t} = v_t + \frac{1}{2} (\dot{v}_t + \dot{v}_{t+\Delta t}) \Delta t \\ u_{t+\Delta t} = \Delta t v_t + \frac{1}{2} \dot{v}_{t+\Delta t} \Delta t^2 \end{cases}$$

In the above relationships, ρ is the mass density, e is the specific internal energy, v is the material speed and u is the material displacement.

II - 2. Conservation laws

Conservation laws are discretized using a Lagrangian finite element formulation. The matrix forms of the equations which govern the continuum in Lagrangian description are the three conservation laws given here after:

$$\dot{\rho}_{t+\Delta t} = - (M_t^\rho)^{-1} K_n^\rho \tilde{\rho}_{t+\Delta t} \quad (mass) \quad (1)$$

$$\dot{e}_{t+\Delta t} = (M_t^e)^{-1} (r_{t+\Delta t} - g_t) \quad (momentum) \quad (2)$$

$$\dot{v}_{t+\Delta t} = (M_t^v)^{-1} (f_{t+\Delta t}^{ext} - f_t^{int}) \quad (energy) \quad (3)$$

In the above equations, M^ρ , M^e and M^v represents the three mass matrices, K^ρ is the stiffness matrix, r is the body heat generation vector, g is the heat flux vector, f^{ext} and f^{int} are the external force vector (including contact effects) and internal force vector respectively.

II - 3. Constitutive law

Concerning the constitutive law treatment, the Cauchy stress tensor may be decomposed into the deviatoric stress tensor \mathbf{S} and the hydrostatic pressure p .

$$\sigma = \mathbf{S} - p\mathbf{I} \quad (4)$$

where \mathbf{I} represents the unary tensor δ_{ij} (Kronecker delta). \mathbf{S} and p are given by the rate constitutive equation

$$\dot{\mathbf{S}}_{ij} = C_{ijkl}^e v_{(k,l)} + \mathbf{S}_{kj} v_{[i,k]} + \mathbf{S}_{ki} v_{[j,k]} \quad (5)$$

and the equation of state

$$M^p \dot{p} + N^p p(\rho, e) = u \quad (6)$$

respectively. In the two above equations $p(\rho, e)$ is the function for the equation of state, $v_{(i,j)}$ and $v_{[i,j]}$ are the symmetric and anti-symmetric parts of the material speed gradient and C_{ijkl}^e is the material response tensor given by:

$$C_{ijkl}^e = 2\mu \left(\frac{1}{2} (\delta_{ik}\delta_{jl} + \delta_{il}\delta_{jk}) - \frac{1}{3} \delta_{ij}\delta_{kl} \right) \quad (7)$$

where μ is one of the two Lamé coefficients.

II - 4. Contact law

DynELA currently supports on type of contact surface boundary condition: a deformable against rigid surface. Development of a deformable/deformable contact algorithm is currently in progress. Contact is treated as a kinematic constraint by **DynELA**, so the contact algorithm apply a correction to the acceleration vector of the contacting nodes. Friction treatment and heat generation at the interface is supported by the code.

Concerning the kinematic part of the contact treatment, the predicted acceleration vector ($\dot{\hat{v}}_{n+1}$) of all contacting nodes of the structure (calculated using the momentum conservation law) is to be corrected using the procedure described below:

First, if a node of the slave surface is penetrating an element of the master surface at the end of an increment, we evaluate the force vector needed to cancel this penetration defined by:

$$\vec{f}^e = f^n \cdot \vec{n} + \vec{f}^t \quad (8)$$

where the normal component is deduced from the penetration value δ of the node in the master element using the relationship:

$$f^n = m \cdot \frac{\delta}{\Delta t^2} \quad (9)$$

m is the equivalence nodal mass of the penetrating node and Δt the time increment of the step. The tangential component \vec{f}^t is evaluated with respect on the friction law used. From this, we can deduce the value of the corrected acceleration $\dot{\hat{v}}_{n+1}$ of the slave node at the end of the increment

$$\dot{\hat{v}}_{n+1} = \dot{v}_{n+1} + 2 \frac{\vec{f}^e}{m} \quad (10)$$

and of course, we obtain finally the result here after for the normal component of the displacement:

$$u_{n+1}^n = \bar{u}_{n+1}^n + \delta$$

Thus the corresponding node has been moved to the rigid surface.

III - APPLICATIONS AND TESTING

III - 1. Hertz contact problem

The Hertz contact problem is a classic example for verifying the contact algorithm of **DynELA**. The problem studied here consist of two identical, infinitely-long cylinders pressed into each other and a reference solution may be found in Abaqus/Explicit Example manual [1]. Because of the symetry, the problem can be modeled by a deformable cylinder pressed against a rigid plane surface and only one quarter of the upper cylinder has been meshed.

The cylinders have a radius of 254mm, are elastic with a Young's modulus $E = 206GPa$ and a Poisson ratio $\nu = 0.3$. No friction is assumed at the interface between the two rods. The nodes along the upper surface of the cylinder are displaced vertically down by 10.16mm. The prescribed displacement is ramped over a relatively long time (0.01s) to obtain a quasi-static computation. The mesh is the same to the one used in the reference solution.

Figure 1 shows the Von-Mises contourplot in the cylinder at the end of the computation. This plot verifies that the highest stress density occurs inside the body and not on the surface. The stress contourplot can also be compared to the one obtained using Abaqus/Explicit. A comparison of the stress values σ_{22max} and $\bar{\sigma}_{max}$ (Von-mises equivalent stress) obtained with **DynELA** and Abaqus/Explicit is given here after:

	DynELA	Abaqus Explicit
σ_{22max}	1,98e+10	1,92e+10
$\bar{\sigma}_{max}$	1,24e+10	1,22e+10

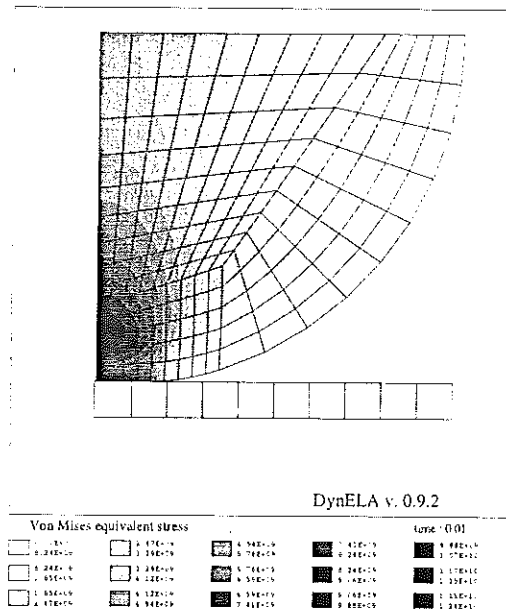


Figure 1: Von-Mises contourplot

The good level of agreement obtained when comparing **DynELA** and Abaqus/Explicit results allows us to validate the contact algorithm used in our finite element code.

III - 2. Cutting

The possibility to simulate orthogonal cutting processes has been tested using **DynELA**. The aim of such a calculus is just to verify the ability of the contact algorithm to simulate a sliding contact including the rupture of the contact. So we used a basic elastoplastic constitutive law and a Coulomb contact law (whithout friction) in our model for simplicity. We also have introduced a geometric node separation criteria (with a minimal distance measurement) at the front end of the tool edge to separate the material in contact with the tool. We assumed a Young modulus $E = 210GPa$ and a Poisson coefficient $\nu = 0.3$ for the material. Constitutive law used in our model is $\sigma = A + B\varepsilon^n$ with $A = 595e6$, $B = 580e6$ and $n = 0.133$. Cutting speed have been taken equal to $v_c = 4m/s$ and cutting advance to $v_a = 0.50mm/rev$.

Figure 2 shows two Von-Mises contourplots. The first one concerns the begining of the calculus, the second one the end (steady state cutting has been reached yet).Such kind of calculus shows the actual limitations of the Lagrangian formulation. Severe distortions occur for the elements of the chip when the tool penetrates the workpiece leading to a decrease of the time-step values from $5.58e^{-9}s$ to $2.80e^{-9}s$ as shown on figure 3.

IV - CONCLUSIONS AND PERSPECTIVES

We presented the first version of our finite element code. The very first simulations (Hertz contact, Taylor impact test) show that numerical results present a good level of agreement with referential solutions. Many developments including three-dimensional elements, addition of ALE terms in the conservation laws, and constitutive and contact law improvements are in progress. Futher versions of **DynELA** will extend the abilities of the code to simulate metal cutting process.

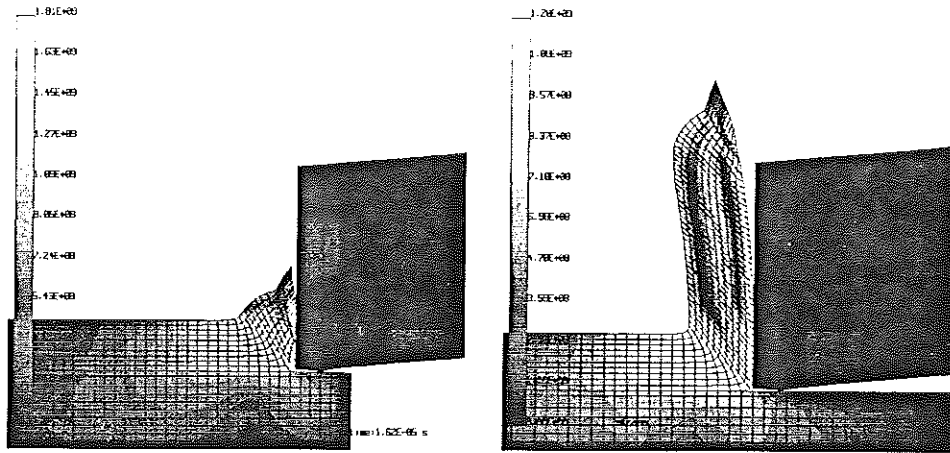


Figure 2: Von-Mises contourplot at the beginning and the end of the calculus

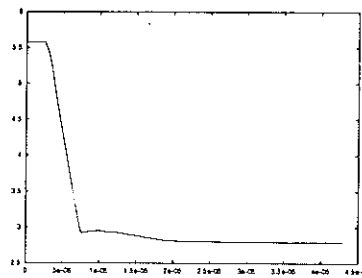


Figure 3: Time-step history (y axis $\times 10^{-9} s$)

References

- [1] Abaqus/Explicit *Example Problems Manual* version 5.7
- [2] T.H.C. CHILDS *Material property requirements for modelling metal machining* - 5th International conference on mechanical and physical behaviour of materials under dynamic loading - p21-36 - Euro DYMAT 97
- [3] P. JOYOT R. RAKOTOMALALA O. PANTALE M. TOURATIER and N. HAKEM A numerical simulation of steady state metal cutting Proc. Instn. Mech. Engrs vol 212 part C - p331-341 - IMechE 1998
- [4] O. PANTALE *Modélisation et simulation tridimensionnelles de la coupe des métaux* - Thèse Université Bordeaux I - Juillet 1996
- [5] O. PANTALE R. RAKOTOMALALA M. TOURATIER *A three-dimensional numerical model of orthogonal and oblique metal cutting processes* - 3rd Biennial European Join Conf. ESDA - Montpellier (1-4/07/1996) - PD Vol 75, ESDA vol 3, p199-206 ASME 1996

Modeling of high strain, high strain rate behavior of Mars 190 armor steel and tantalum

F. LLORCA, A. JUANICOTENA

CEA-Valduc, DRMN/HPC, Laboratoire Comportement et Modélisation
21120 IS-SUR-TILLE - FRANCE

ABSTRACT

In this paper, the capability of empirical and semi physical models to describe high dynamic material behavior is discussed. We propose to study two particular bcc materials : tantalum and Mars 190 armor steel. The materials parameters are estimated for the constitutive relations of Johnson-Cook, Zerilli-Armstrong and Preston-Tonks-Wallace from quasistatic and dynamic test data. The models are then evaluated by comparing analytical and experimental stress-strain curves from a new experiment : the free expanding spherical shell test.

1. INTRODUCTION

Description of high speed plastic flow in applied physics programs (Explosively Formed Projectiles ...) have a great need for physically realistic models of the behavior of metallic materials. Temperatures, pressures may increase substantially over ambient conditions (several hundred Kelvin ...) and plastic strains of several hundred percent are typical. Considerable progress has been made in understanding the role of rate controlling dislocation mechanisms on the temperature and strain rate dependence of the flow stress of metals and alloys (figure 1). At temperatures below that where diffusion controlled mechanisms become operative, metals usually deform by thermally activated mechanisms. Above some critical temperature, the behavior may become athermal. Under certain assumptions, the total flow stress is the sum of the athermal component and the effective activated stress. Otherwise, at very high strain rates, dislocation movement can be controlled by viscous drag mechanisms.

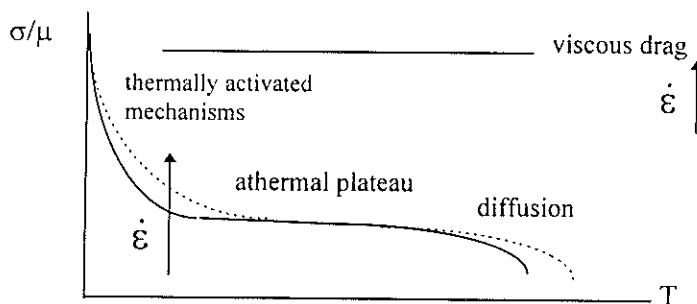


Figure 1. Deformation mechanisms as functions of strain rate and temperature.

In this paper, we limit our study to thermal and athermal activation mechanisms but we also investigate the behavior of metals at high strain levels which is classically associated to the phenomena of stress saturation.

Several attempts have been made in recent years to improve the description of these physical plastic mechanisms. Always used in computer codes, the purely empirical constitutive relations are curve fitting exercises to available experimental data [1]. At the other extreme, various authors have proposed theoretical relationships based on the micromechanical processes assumed to govern deformation in metals [2]. Between these two extremes, semi physical models offer the advantage of representing macroscopically effects of microscopic deformation mechanisms [3-4-5].

In this work, we attempt to determine the ability of Johnson-Cook, Zerilli-Armstrong and Preston-Tonks-Wallace models for two bcc materials (tantalum and Mars 190 armor steel). The evaluation of the models and data will be made by comparing analytical results with experimental data from a new test : the freely expanding spherical shell test [6-7].

2. CONSTITUTIVE RELATIONS

2.1. General considerations

Specification of a yield surface provides an equation relating the deviatoric stress s_{ij} to a yield limit or flow stress σ . Here, we use the Von Mises surface and several flow stress models. These relations are functionally dependent on equivalent plastic strain ε , strain rate $\dot{\varepsilon}$ and temperature T :

$$\frac{3}{2}s_{ij}s_{ij} = \sigma^2(\varepsilon, \dot{\varepsilon}, T) \quad (1)$$

2.2. Modeling flow stress

a) The Johnson-Cook model has the classical form $f(\varepsilon)g(\dot{\varepsilon})h(T)$:

$$\sigma = \left[\sigma_0 + B\varepsilon^n \right] \left[1 + C \ln(\dot{\varepsilon}/\dot{\varepsilon}_0) \right] \left[1 - \left(\frac{T - T_0}{T_m - T_0} \right)^m \right] \quad (2)$$

Athermal mechanism is not taken into account : the strain rate dependence is purely semi-logarithmic. The work hardening follows a power law where the exponent n is assumed to be constant with temperature and strain rate. It does not match reality for bcc materials : in general, stress usually reach saturation mechanisms at high strain-rate and the rate of work hardening decreases to zero. The third term in (2) describes the reduction of strength due to adiabatic heating during dynamic loadings.

b) The Zerilli-Armstrong model is expressed here in specific form for bcc metals $f(\varepsilon) + g(\dot{\varepsilon}, T)$:

$$\sigma = \Delta\sigma'_G + kd^{-1/2} + C_1 \exp(-C_3 T + C_4 T \ln \dot{\varepsilon}) + C_5 \varepsilon^n \quad (3)$$

Here again, the work-hardening function is assumed to be temperature and strain rate independent. Thermal activation mechanisms are described through the second term in equation (3). At the limit, the soft dependency of athermal stress with temperature (because shear modulus also decreases with temperature) is not described.

c) Preston and al. have largely refined a semi empirical approach based on an extension of the Voce work hardening relation : the flow stress varies from σ_y (yield stress) to σ_s (the saturation stress). For bcc materials, the initial rate of work hardening θ_0 is a constant. Then, the work hardening rate is expressed as :

$$\frac{d\hat{\sigma}}{d\varepsilon} = \theta_0 \frac{\sigma_s - \sigma}{\sigma_s - \sigma_y} \quad (4)$$

In the domain where plasticity is driven by thermal activation theory, the yield stress and the saturation stress are described as functions of temperature and strain rate :

$$\begin{pmatrix} \hat{\sigma}_s \\ \hat{\sigma}_y \end{pmatrix} = 2 \left[\begin{pmatrix} s_0 \\ y_0 \end{pmatrix} - \begin{pmatrix} s_0 - s_\infty \\ y_0 - y_\infty \end{pmatrix} \operatorname{erf} \left[\kappa \frac{T}{T_m} \ln(\gamma \dot{\varepsilon} / \dot{\varepsilon}_0) \right] \right] \quad (5)$$

The error function is well suited to describe a continuous transition from thermal to athermal mechanisms.

3. EVALUATION OF MODELS PARAMETERS

3.1. Experimental data

The parameters estimates in this section result from fitting quasi static and dynamic compression experimental data for each material. The test data are primarily obtained from compression tests over a wide range of strain rate and temperature (see table 1). Dynamic tests were performed on classical Split Hopkinson Pressure Bars while quasi static tests were conducted on classical hydraulically driven machines (a 100 kN Zwick universal machine for ambient temperature and a 100 kN MTS universal machine for elevated temperatures).

Table 1. Experimental conditions of mechanical tests used for the evaluation of model parameters.

<i>tantalum</i>								
$\dot{\epsilon} (s^{-1})$	10^{-4}	$2.2 \cdot 10^{-3}$	$2.2 \cdot 10^{-2}$	$2.2 \cdot 10^{-1}$	1000	1700	1400	1400
$T (K)$	293	293	293	293	293	473	673	873
<i>Mars 190 armor steel</i>								
$\dot{\epsilon} (s^{-1})$	10^{-4}	10^{-1}	10^{-2}	10^{-2}	1850	2500	1950	1750 $10^{-4}, 10^{-2}$
$T (K)$	293	473	293	473	293	473	673	873

The temperature dependence of flow stress with strain rate is shown in figure 2 for the two materials. For tantalum, thermal activation is well described while athermal mechanisms are not observed because of the lack in quasi static data above 473 K. In the case of Mars 190 armor steel, tests were performed in a wide range of temperature : at high temperatures (above 673 K), deformation mechanisms are diffusion controlled. As opposed to tantalum temperature dependence, the athermal stress component is high compared to the thermal activated component.

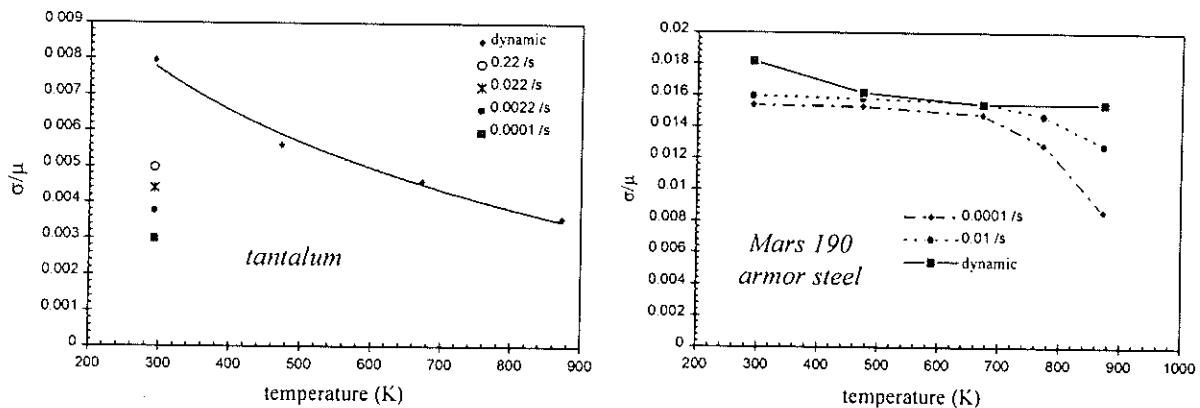


Figure 2. Flow stress at $\epsilon=0.05$ as a function of strain rate and temperature.

3.2. Parameter estimation

A specific software, developed at the CEA is used to estimate the material parameters for the two materials. It was shown previously [6], by means of manual updating operations, that the data sets contain sufficient information to evaluate a well-determined set of parameters. The semi-automatic software is based on a modified Levenberg-Marquart algorithm : the procedure of optimization requires, first, to assign initial values for all parameters ; then an iterative scheme reduces the distance between experimental and analytical data through the minimization of a quadratic cost function. Next tables give the estimated parameters for the three material models evaluated in this work.

Table 2. Johnson-Cook model constants for tantalum and Mars 190 armor steel.

Parameter	tantalum	Mars 190 armor steel
σ_0 (MPa)	183	1075
B (MPa)	290	427
n	0.59	0.28
C	0.077	0.0073
m	0.4	1.2
T_0 (K)	293	293
T_m (K)	3269	1752

Table 3. Zerilli-Armstrong model constants for tantalum and Mars 190 armor steel.

Parameter	tantalum	Mars 190 armor steel
$\Delta\sigma'_0 + kd^{-1/2}$ (MPa)	20	938
C_5 (MPa)	506	417
n	0.73	0.28
C_1 (MPa)	897	2295
C_3/K	0.00372	0.0079
$C_4/(Ks)$	0.00023	0.0002

Table 4. Preston-Tonks-Wallace model constants for tantalum and Mars 190 armor steel.

Parameter	tantalum	Mars 190 armor steel
γ_0	0.00522	0.0119
γ_∞	0.000107	0.00671
s_0	0.0053	0.0148
s_∞	0.0027	0.00801
κ	0.428	0.356
$\gamma \dot{\xi} / s$	$2.1 \cdot 10^6$	$3.69 \cdot 10^9$
θ	0.0091	0.0367

For tantalum, it is shown in figure 3 that the best fit is given by the PTW model all over the explored thermomechanical range. Zerilli Armstrong constitutive relation is found reasonably adapted so long as saturation mechanisms do not occur (see in particular the dynamic curve). Compared to those models, Johnson Cook constitutive law gives a relatively poor representation of experimental data (see the evolutions of the yield limit and the rate of work-hardening with strain rate).

For Mars 190 armor steel, all the models give a close representation of experimental stress-strain data (see figure 3). It is explained by the fact that saturation mechanisms are activated for very low levels of strain and strain rate and therefore, the models are forced to flatten rapidly.

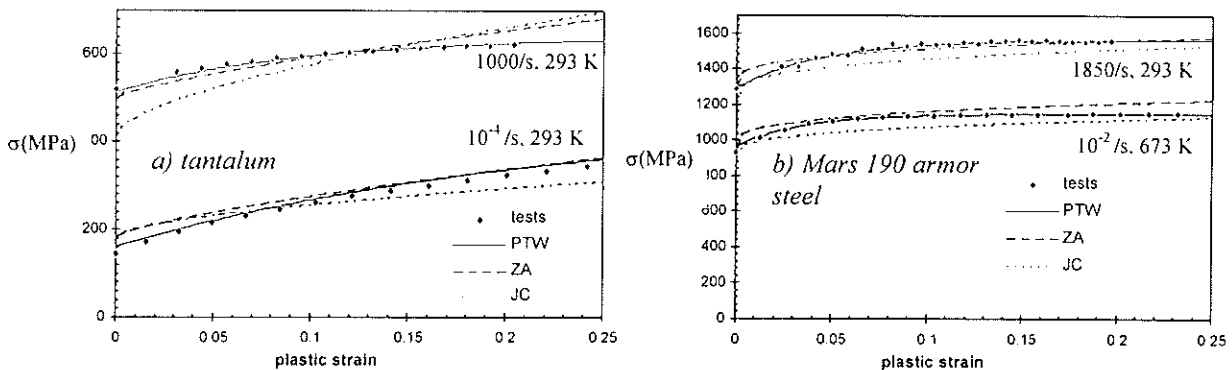


Figure 3. Comparisons between experimental data and models (isothermal curves) for various tests conditions.

For tantalum, an extrapolation of the models at high strain levels is shown in figure 4. In the range of high strains, differences between the models are magnified. From this curve, it is clear that for

numerical simulations of high strain dynamic applications (EFP...), it needs to make a choice between models. That can be done through the use of a new experiment developed to evaluate models at high strains : the expanding spherical shell test.

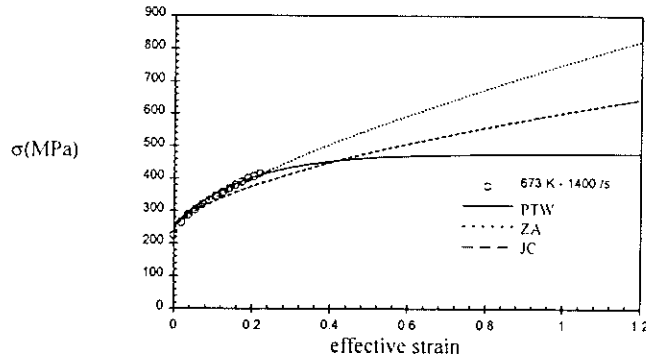
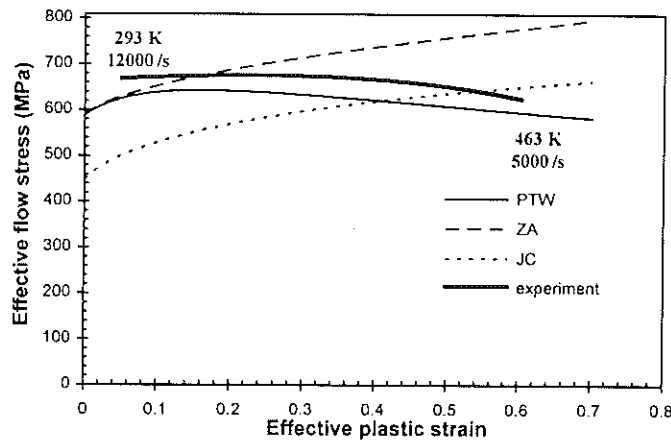


Figure 4. Models extrapolation at high strains for tantalum (isothermal curves).

4.VALIDATION

The dynamic expanding spherical shell test is described elsewhere [6-7]. The applied dynamic loading is a pure equibiaxial tension in the range of high strain rates (10^4 s^{-1}) and high strains. Measured stress strain curves are compared to those of analytical data given by models calculations. Comparisons are given in figure 5.

a) tantalum



b) Mars 190 armor steel

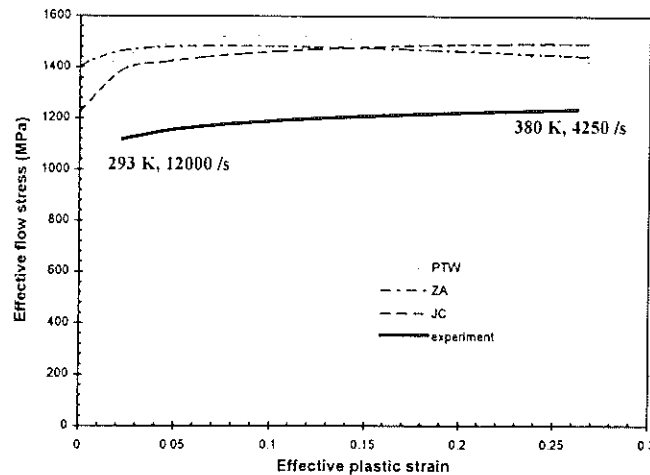


Figure 5. Comparisons between experimental and analytical data for expanding spherical shell tests.

For tantalum, we observe a direct thermal softening process while for Mars 190 armor steel, flow stress increases all along the expanding stage. For this material thermal softening is not a major piloting effect in this experimental configuration. All the models give a quasi identical behavior over the strain range for mars 190 armor steel. Therefore, in the case of tantalum, it is clearly shown that PTW model offers the best fit of the experimental stress-strain curve at high strain levels. For tantalum, ZA and JC models representations of high strain behavior are more difficult because saturation stress has not been observed during characterization.

For the two materials, we have commented the shape of the stress-strain curves. For the two materials, the differences between the models curves and the experimental data levels are explained by the large difference between the sphere materials and those used for characterization. For characterization, samples are cylindrical and electro discharge machined with dimensions 8 mm in height and 8 mm in diameter. Machining process used for the sphere fabrication is presented in [5]. In fact, comparing the micro hardness values, we can explain that, in figure 5, stress is under estimated for tantalum models while it is surestimated for Mars 190 armor steel.

Table 5. Characteristics of material samples used for characterization and evaluation of the models.

	tantalum		Mars 190 armor steel	
	cylindrical samples	spherical samples	cylindrical samples	spherical samples
micro hardness	74HV10	94HV10	366 HB	287 HB
grain size (μm)	60	35	-	-

5. CONCLUSION

Modeling of two bcc materials in the domain of high strain and high strain rates has been investigated in this paper. Zerilli Armstrong and Johnson Cook models have been compared to an original approach proposed by Preston Tonks Wallace. The main improvement in this model is the account of saturation mechanisms with temperature and strain rate dependence. For the two materials, comparison of analytical data and new expanding spherical shell test data show the ability of the PTW model to describe dynamic behavior at high strain levels.

ACKNOWLEDGMENTS

The authors would like to thank Professor A. Molinari (University of Metz) for his technical supervision of this work.

REFERENCES

- [1] Johnson G.R., Cook W.H., *A constitutive model and data for metals subjected to large strains, strain rates and high temperature*, 7th International Symposium on Ballistics Proceedings, 1983, pp 541-547.
- [2] Klepaczko J.R., *Constitutive modeling in dynamic plasticity based on physical state variables - a review*, Journal de Physique, C3, tome 49, 1988, pp 553-560.
- [3] Zerilli F.J., Armstrong R.W., *Dislocation mechanics based constitutive relations for materials dynamics calculation*, Journal of applied physics, Journal of applied physics, 61(5), 1987, pp 1816-1825.
- [4] Preston D.L., Tonks D.L., Wallace D.C., *PTW materials model*, rapport Los Alamos, 1992.
- [5] Juanicotena A., Llorca F., *Contribution du test d'expansion d'anneaux à l'étude de différentes lois de comportement élastoplastique dans le domaine des grandes vitesses de déformation - Application au cuivre et à l'acier Mars 190*, Journal de Physique, Colloque C3, 7, 1997, pp 541-546.
- [6] Juanicotena A., *Etude théorique et expérimentale du comportement viscoplastique des matériaux aux grandes déformations et grandes vitesses de déformation - Application à l'acier Mars 190 et au tantale*, Thèse de l'Université de Metz, 1998.
- [7] Juanicotena A., Llorca F., *High strain, high strain rate materials properties : development of the freely expanding spherical shell test*, 11th Journées Techniques DYMAT, Dijon, 1998 (this issue).

Calcul du module de compressibilité et de la polaire de choc d'un milieu hétérogène liquide/bulles sous sollicitation dynamique

Alain FROGER

*Commissariat à l'Energie Atomique - Centre d'Etudes du Ripault
BP 16 - 37260 Monts*

Résumé : Dans cet article théorique on considère une onde de choc maintenue qui traverse un milieu liquide hébergeant une population de bulles. Le front d'onde présente une structure très perturbée, du fait de la phase d'implosion des bulles. Cependant, au bout d'une durée caractérisée par la période d'oscillation des bulles, on peut définir dans le milieu amont un état stationnaire en moyenne. Pour cela on calcule le champ de pression moyen et la masse volumique moyenne dans une cellule centrée sur une bulle de référence, puis on corrèle ces grandeurs aux relations d'Hugoniot ce qui détermine la polaire de choc. En considérant des pressions de chocs de plus en plus faibles on définit le module de compressibilité *dynamique* du milieu. Il est essentiel de tenir compte de la compressibilité du liquide, même pour des sollicitations faibles.

Avant-propos : Considérons une bulle de gaz sphérique isolée dans un milieu liquide infini, et un choc maintenu parcourant ce milieu. Lorsque le choc arrive sur la bulle, celle-ci implose : son rayon diminue jusqu'à atteindre une valeur minimale. Puis elle entre en phase d'explosion. Son rayon croît jusqu'à une valeur maximale, puis un cycle implosion/explosion recommence. Dans le cas d'une bulle de cavitation le gaz se condense et la bulle se résorbe, souvent à la fin de l'implosion initiale. Dans le cas d'une bulle de gaz « étranger » le cycle perdure tant que la perturbation est maintenue, l'amortissement étant faible pour des liquides aux propriétés physiques (viscosité, conductivité thermique) comparables à celles de l'eau.

Au cours d'un cycle implosion/explosion la variation relative du rayon de la bulle est très grande, ainsi que la vitesse moyenne de sa paroi, cela même pour des perturbations de quelques dizaines de bars. Pour fixer les idées, une bulle d'air de 0,5 mm de rayon soumise à un choc de 100 bars dans de l'eau implose en 4,6 μ s, et la vitesse moyenne de sa paroi est de 96 m/s. D'autre part le rapport du rayon initial sur le rayon minimal est de 9, ce qui représente une très grande déformation. L'implosion est quasiment adiabatique, car les effets de la viscosité et du transfert thermique gaz/eau sont ici négligeables.

Bien entendu, une bulle isolée est un système physique, et non pas un matériau. Aussi nous nous intéressons ici à une population de bulles. Le sujet concerne donc un matériau hétérogène liquide/bulles, que nous cherchons à représenter par un matériau moyen homogène dont les caractéristiques sous *sollicitation dynamique* sont à définir, notamment le module de compressibilité et la polaire de choc.

I - INTRODUCTION.

L'étude de l'implosion d'une bulle est ancienne puisque déjà au début du siècle Lord Rayleigh s'est penché sur le sujet. Il s'agissait de comprendre pourquoi les hélices de navires s'érodaient, et l'explication fut trouvée dans la résorption (implosion) des bulles de cavitation. Depuis environ vingt ans ce sujet a repris de l'intérêt, à propos notamment de la signature acoustique des hélices marines qui résulte en partie de l'implosion des bulles de cavitation, et, plus récemment, à propos de l'érosion des surfaces portantes hydrodynamiques (hydrofoils). Le champ d'investigation s'est alors étendu à la prise en compte d'une population de bulles.

Les bulles de gaz étranger, mais aussi les bulles de cavitation, concernent aussi les problèmes de sécurité pyrotechnique des liquides réactifs (industrie chimique, industrie pyrotechnique, ergols liquides pour les lanceurs spatiaux).

Enfin, et plus généralement, la connaissance des propriétés sous sollicitation dynamique d'un milieu hétérogène liquide/bulles peut être déterminante dans le cas la conception d'installations hydrauliques, en particulier du fait des coups de bélier dans les conduites.

C'est dans ce dernier cadre que nous nous plaçons, et nous nous restreindrons ici à une population de bulles sphériques de gaz étranger, de petites tailles, et en faible quantité par unité de volume.

II - PHYSIQUE DE L'IMPLOSION D'UNE BULLE ISOLEE.

Soit une bulle sphérique de rayon initial R_0 dans un milieu liquide infini que nous admettons provisoirement incompressible - nous verrons plus loin comment échapper à cette hypothèse. On suppose que la bulle ne peut se déformer que radialement ; elle est donc géométriquement caractérisée par son rayon $R(t)$ seulement. Dans ces conditions la vitesse des particules de liquide dérive du potentiel $\varphi(r) = -\dot{R}R^2/r$, la coordonnée radiale $r=0$ étant le centre de la bulle et \dot{R} la vitesse de la paroi (on utilise la notation : $\dot{s} \equiv ds/dt$ pour tout symbole s). Lorsqu'une perturbation de pression P_∞ « venant de l'infini » traverse la bulle celle-ci se déforme, radialement par hypothèse. L'instant initial t_0 est ici l'instant où la perturbation atteint la bulle, et on note P_0 et T_0 les conditions initiales de pression et de température du système liquide/bulle au repos.

En appliquant le théorème des forces vives à l'ensemble du milieu liquide, et compte tenu du potentiel de la vitesse, on obtient, en négligeant la viscosité et la tension superficielle, l'équation d'évolution du rayon, soit :

$$\rho_\ell R \ddot{R} + \frac{3}{2} \rho_\ell \dot{R}^2 = P_g - P_\infty \quad (1)$$

P_g est la pression instantanée dans le gaz au niveau de la paroi, et ρ_ℓ la masse volumique du liquide ; la pression de perturbation P_∞ peut dépendre du temps. Cette équation a été établie par Lord Rayleigh dès 1917, et porte son nom. A partir de t_0 la bulle implose si $P_\infty > P_0$, ou explose si $P_\infty < P_0$.

Le potentiel de vitesse $\varphi(r)$ permet d'obtenir une intégrale première de l'équation de Groméko-Lamb, ce qui détermine le champ de pression dans le liquide :

$$P(r) = P_\infty + \rho_\ell \frac{R}{r} \left[\ddot{R}R + 2\dot{R}^2 - \frac{1}{2} \dot{R}^2 \frac{R^3}{r^3} \right] = P_\infty + \frac{R}{r} (P_g - P_\infty) + \frac{1}{2} \rho_\ell \dot{R}^2 \frac{R}{r} \left[1 - \frac{R^3}{r^3} \right] \quad (2)$$

En analysant l'équation de Rayleigh (1), et dans le cas où P_∞ est constant, on montre que la variation $R(t)$ du rayon est périodique. $R(t)$ évolue entre R_0 et $R_{\min} < R_0$ dans le cas de

l'implosion, et entre R_0 et $R_{\max} > R_0$ dans le cas de l'explosion. Bien entendu, pour un chargement $P_\infty(t)$ quelconque, l'évolution du rayon n'est pas nécessairement périodique. Dans le cas d'une implosion avec P_∞ constant, et pour un gaz parfait diatomique, en supposant la bulle de gaz uniforme à chaque instant et sans échange thermique avec le milieu liquide, Lord Rayleigh a pu estimer la demie période d'évolution de R_0 à R_{\min} , et inversement, soit :

$$\tau = 0,915 R_0 \left[\frac{\rho_\ell}{P_\infty - P_0} \right]^{1/2} \quad (3)$$

La forme constamment sphérique de la bulle constitue l'hypothèse forte du modèle de Rayleigh. En toute rigueur elle n'est vraie que pour une onde de perturbation sphérique convergente centrée sur la bulle. Dans le cas courant d'une perturbation de direction quelconque et de front d'onde pratiquement plan, elle n'est acceptable que si que si la durée $2R_0/c_l$ mise par la perturbation pour « traverser » la bulle est nettement inférieure à la durée d'implosion ou d'explosion, c_l étant la vitesse du son dans le liquide. Pratiquement P_∞ doit être inférieur à 200 bars dans le cas de l'eau, d'après (3).

A titre d'illustration, on peut voir sur la *figure 1* suivante l'évolution calculée du rayon d'une bulle d'air dans de l'eau pendant 3 oscillations, ainsi que sa vitesse dans l'espace des phases, pour une pression de perturbation de 100 bars indéfiniment maintenue. Les conditions thermodynamiques initiales sont les conditions normales. Nous verrons succinctement au paragraphe suivant la méthode numérique utilisée.

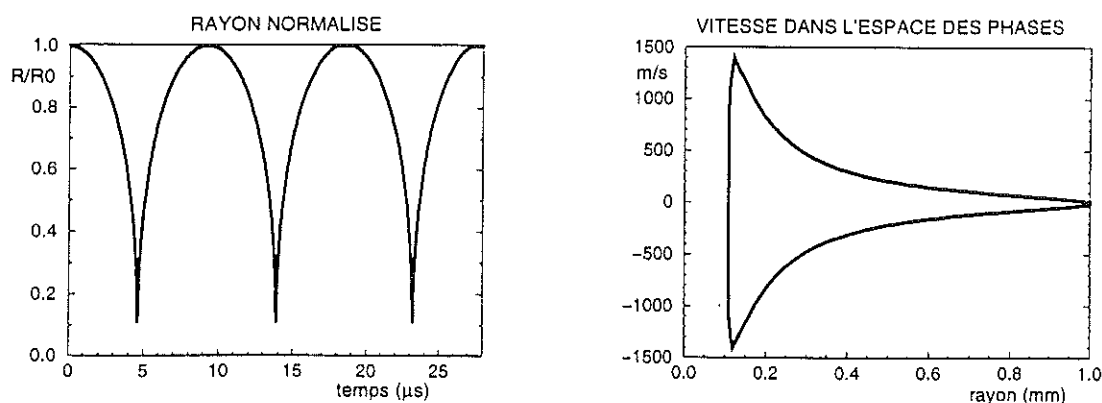


figure 1

La paroi atteint de très grandes vitesses. Néanmoins l'écoulement (radial) du gaz reste subsonique car la vitesse du son augmente avec la compression. En phase finale d'implosion le rapport R_0/R_{\min} est ici voisin de 9. La compression est considérable, aussi nous utilisons une équation d'état de type Abel-Noble pour représenter le gaz : $P_g(\rho, T) = \rho \mathcal{R} T [M(1 - \eta \rho)]^{-1}$, ρ étant la masse volumique, T la température, M la masse molaire, η le volume massique limite, et \mathcal{R} la constante des gaz parfaits.

III - BULLE GENERALISEE ET COMPRESSIBILITE DU LIQUIDE.

La pression dans le gaz peut atteindre des valeurs considérables en phase finale d'implosion, et, par continuité, il en est de même dans le liquide. L'hypothèse d'incompressibilité de celui-ci n'est alors plus valide. Cependant le champ de pression décroît selon (2) à partir de la paroi, de sorte que cette hypothèse est acceptable suffisamment loin de la bulle. L'établissement de la formule (1), ainsi que l'utilisation de la formule elle-même, ne nécessitent pas la connaissance détaillée de l'état du gaz dans la cavité, mais seulement sa

pression à la paroi. On peut donc définir une « bulle-généralisée », constituée du gaz entouré d'une coquille de liquide *compressible*, telle que sur la figure 2.

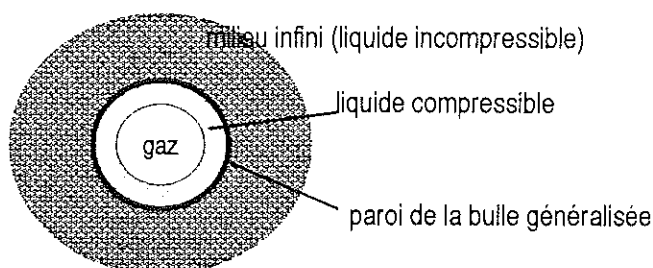


figure 2

Le calcul des caractéristiques cinématiques (position et vitesse matérielles) et thermodynamiques (masse volumique, pression, température) instantanées du système se font à l'aide d'une méthode numérique discrète ; la bulle généralisée est maillée en cellules lagrangiennes, qui sont ici des coquilles sphériques. Les équations usuelles de l'hydrodynamique compressible sont discrétisées et résolues sur ce maillage monodimensionnel selon le schéma bien connu de Richtmyer. La condition à la frontière du système est exprimée par la formule (1) qui est résolue numériquement. Pour l'eau compressible on utilise l'équation de Tait, soit $P=3,21 \cdot 10^8 [(\rho/\rho_0)^7-1]$, ce qui est une formulation du type Murnaghan bien connue dans le cas des solides sous haute pression. Enfin le champ de pression dans le milieu liquide infini incompressible est déterminé par (2). La viscosité et la conduction thermique sont prises en compte, ainsi que la tension superficielle du liquide à l'interface liquide/gaz. Cependant ces effets sont généralement négligeables.

IV - MODULE DE COMPRESSIBILITE DYNAMIQUE DU MILIEU.

On s'intéresse maintenant à un liquide hébergeant une population de bulles. On note f_v la fraction volumique de gaz, et on considère, momentanément, des bulles de même rayon initial R_0 . Si f_v est suffisamment petit on peut négliger l'interaction entre les bulles et représenter le milieu par un réseau cubique régulier, chaque cube élémentaire de côté $2L_0$ contenant une bulle en son centre. Ces grandeurs sont reliées par : $f_v=(\pi/6)(R_0/L_0)^3$.

Lorsqu'un choc stationnaire d'amplitude P_c traverse le milieu, dans chaque cellule la bulle va osciller radialement selon (1), et le champ de pression, *instationnaire mais périodique*, va y être défini par (2). A la surface des cellules la pression de perturbation P_* de (1) et (2) s'identifie à P_c (ceci résulte finalement de l'hypothèse de non interaction entre bulles).

Pour une valeur P_c donnée on calcule à chaque instant le rayon de la bulle généralisée et celui de la cavité de gaz (cf. §III), ainsi que le côté $L(t)$ de la cellule de référence par conservation de la masse de liquide dans celle-ci. On en déduit la masse volumique $\rho(t)$ de la cellule contenant le liquide et le gaz, ce qui permet de définir la masse volumique ρ_c de la cellule comme moyenne temporelle de $\rho(t)$ sur la durée d'au moins une oscillation.

De la connaissance de P_c et ρ_c , on tire directement des deux premières relations d'Hugoniot la vitesse D du choc d'amplitude P_c dans le liquide hétérogène.

Cette théorie est fermée, en ce sens qu'à partir du champ de pression $P(r,t)$ dans la cellule on calcule de façon appropriée la moyenne spatio-temporelle de la pression : cette valeur se trouve être égale à P_c .

Dans le cas de l'air et de l'eau, la figure 3 qui suit, présente D en fonction P_c pour $f_v=0,05\%$, puis en fonction de f_v pour différentes valeurs de P_c .

On constate qu'il est essentiel de tenir compte de la compressibilité du liquide, même pour de petites valeurs de P_c , faute de quoi D pourrait devenir supérieur à la vitesse des chocs faibles dans l'eau, soit 1500 m/s, ce qui n'est pas physique.

Enfin par extrapolation de la courbe $D(P_c)$ jusqu'à la valeur $P_0=1$ bar ici, on obtient la vitesse du son dans le milieu, ou, ce qui est équivalent, son module de compressibilité pour les perturbations infinitésimales. Il s'agit d'une valeur *dynamique*, différente de la valeur statique qu'on obtiendrait en considérant la compression statique du gaz.

On y voit aussi que pour des valeurs f_v trop grandes, le calcul produit des valeurs D inférieures à la vitesse du son dans l'air, soit 350 m/s ici, ce qui n'est pas physique. Cela signifie que pour de telles fractions volumiques de gaz l'hypothèse de non interaction entre bulles n'est plus acceptable. Par ailleurs on considère généralement cette hypothèse valide dès que $L_0/R_0 > 4$, ce qui correspond à $f_v=0,8\%$. Notre concept de bulle généralisée implique a priori des valeurs plus faibles, mais ce seuil reste à déterminer.

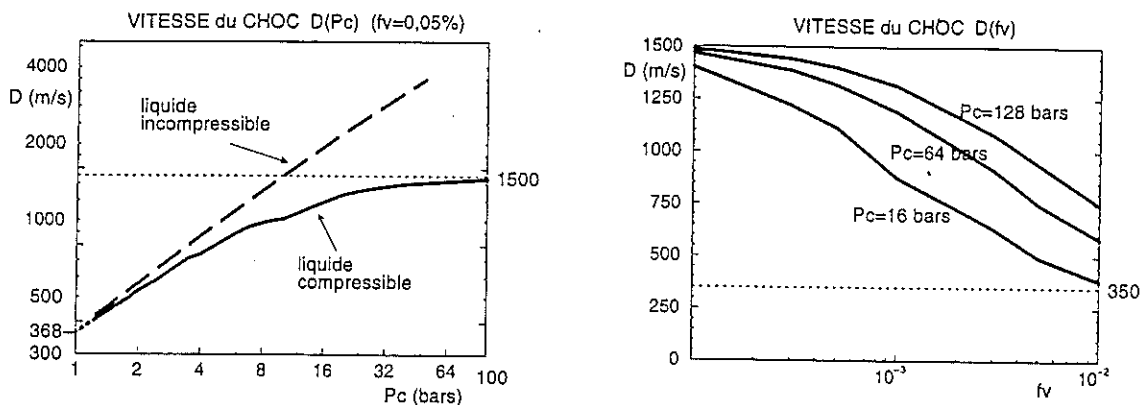


figure 3

Les relations d'Hugoniot permettent encore de déterminer la vitesse matérielle d'ensemble u , et donc la polaire de choc, puis de relier D à u . Dans le cas d'une fraction volumique de 0,1% d'air dans de l'eau les résultats sont présentés sur la figure 4.

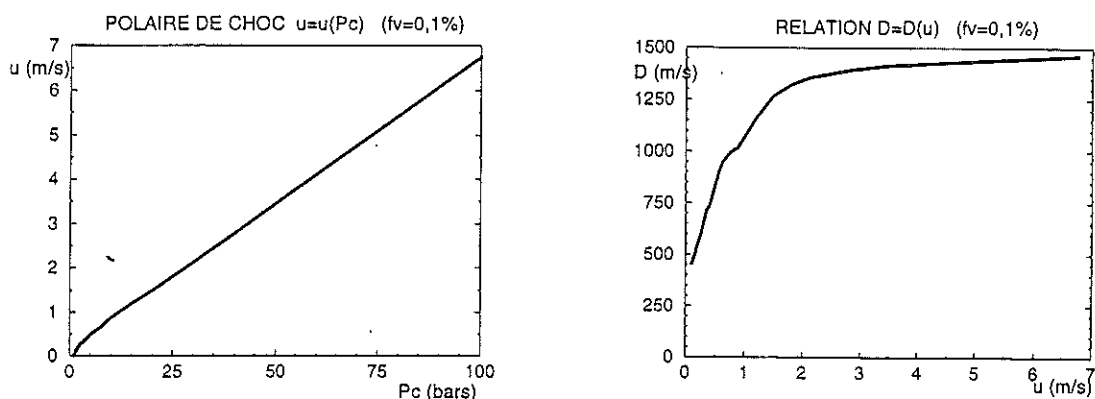


figure 4

En ce qui concerne la vitesse matérielle u , il ne s'agit évidemment pas de la vitesse instantanée des particules de matière, puisque celle-ci présente une composante radiale. Il s'agit de la vitesse moyenne dans la direction du choc de l'ensemble de la cellule considérée comme homogène.

Tous les calculs présentés ont été réalisés pour une valeur fixée $R_0=1$ mm du rayon initial de la bulle. La valeur de ce paramètre n'intervient pas directement dans la théorie, seule compte la fraction volumique de gaz f_v . On a vérifié qu'effectivement les résultats sont stables pour différentes valeurs de R_0 . En conséquence cette théorie s'applique à une population de bulles dont les rayons ne sont pas nécessairement égaux.

Enfin la connaissance du module de compressibilité et la connaissance de la relation $D=D(u)$ permet de définir l'équation d'état, sous sollicitation dynamique de type Murnaghan (cf. plus haut) du milieu hétérogène pour toute valeur f_v . On écrit $P=K[(\rho/\rho_0)^\gamma-1]$ avec $K=\rho_0 c_0^2/\gamma$, $\gamma=4B-1$ où B est tel que $D=c_0+Bu$. c_0 , vitesse du son dans le milieu hétérogène, et ρ_0 dépendent ici de f_v .

V - CONCLUSION.

A partir de l'équation de Rayleigh relative à l'évolution d'une bulle isolée dans un liquide infini incompressible, nous avons défini un concept de bulle généralisée qui permet de prendre en compte la compressibilité du liquide, et nous avons défini une représentation modèle d'un milieu liquide hétérogène hébergeant une population de bulles. Cette conception permet de calculer le module de compressibilité, la célérité des chocs, et la polaire de choc du milieu sous sollicitation dynamique. Dans le cas d'un milieu eau/air les calculs montrent que, même pour des fractions volumiques de gaz très faibles et des pressions de chocs inférieures à 100 bars, la célérité des chocs est nettement inférieure à la célérité des chocs faibles dans l'eau pure. La polaire de choc est ici une relation pratiquement linéaire entre la pression de choc et la vitesse matérielle moyenne. Pour des valeurs de pression plus élevées (>100 bars) le milieu se rigidifie et devient semblable à l'eau pure. Cette théorie est acceptable pour des valeurs limites de rayon initial de bulle, de fraction volumique de gaz, et de pression de choc voisines de 5 mm, 0,05% et 200 bars respectivement. Ces seuils restent encore à déterminer avec plus de précision.

Il n'est pas nécessaire que les bulles immergées dans le liquide soient de tailles identiques. D'un point de vue conceptuel on a montré qu'il est fondamental de prendre en compte la compressibilité du liquide, même pour des sollicitations de quelques bars. Enfin on peut déterminer l'équation d'état du type Murnaghan du milieu hétérogène sous sollicitation dynamique.

Quelques références sur le sujet.

M.S. Plesset, A. Prosperetti :

« Bubble dynamics and cavitation » Annual Review of Fluid Mechanics, vol. 9, 1977

L. d'Agostino, C.E. Brennen :

« Linearized dynamics of spherical bubble clouds » Journal of Fluid Mechanics, vol. 199, 1989

G.L. Chahine, R. Duraiswami :

« Dynamical interactions in a multi-bubble cloud » Transactions of the ASME, vol. 114, 1992

Y. Matsumoto, M. Kameda :

« Propagation of shock waves in dilute bubbly liquids » JSME International Journal, series B, vol. 39, n°2, 1996

Attenuating materials for weapon systems : modelling the dynamic compaction

Cyrille Kammerer

DGA/CTA, 16 bis avenue Prieur de la Côte d'Or, 94114 Arcueil Cedex

Résumé – Dans le domaine de la protection des systèmes d'armes, ces dernières années ont vu apparaître la nécessité de pouvoir amortir les effets d'un choc. Ce besoin a entraîné un intérêt croissant d'une certaine classe de matériau, les *matériaux amortissants*. Ceux-ci amortissent les effets d'une onde de choc en emmagasinant par déformation une certaine quantité de l'énergie incidente. Le niveau d'énergie consommée par compaction dépend des vitesses de sollicitation mais également des modes de déformation. Pour concevoir et optimiser les solutions amortissantes, différentes approches permettent la modélisation de leur réponse mécanique.

Abstract – In the field of the protection of weapon systems, during these last years the need of shock attenuations has appeared. This need induced an increasing interest in attenuating materials. By deformation, they attenuate the residual effects of a shock wave by storing a part of the incident energy. The level of consumed energy depends on both loading rates and deformation modes. In order to design and optimize the attenuating solutions, the modelling of their constitutive behaviour can be performed with different approaches.

1 – INTRODUCTION

Because of the diversification of the French army services, and because of the increasing levels of threats, the capacities of mobility and protection of weapon systems must be increased and strengthened. Then, the need of shock attenuations has appeared in order to both avoid damage (spalling or delamination) in structures and ensure a more important safety for personnels and boarded equipments. The mechanical study of such attenuating materials is required.

In the case of a plate impacting a plane structure, the main finalities of attenuating materials are to limitate the loading (stress levels) on the structure, and to increase the duration of this loading.

In a first part, we present the interest of shock attenuation by compaction. The Hugoniot shock waves theory allows us to suggest a sufficient condition to acknowledge an attenuating material. The last part presents different approaches to model their constitutive behaviour, in order to design attenuating solutions and concepts. Then, we present our analytic simulations based on energetic considerations.

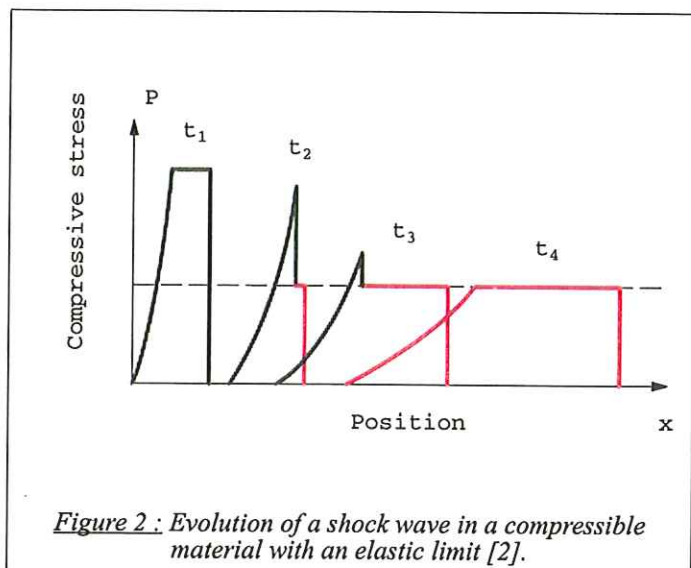
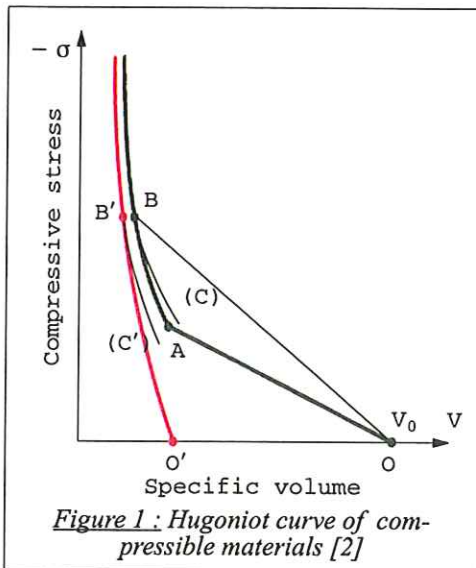
2 – ATTENATION OF SHOCK WAVES BY COMPACTION

2.1 – Shock waves and attenuation

With the Hognoniot theory, it is possible to show [1] that shock waves are stable and release waves are unstable. Then, it can be shown [1] that the release waves propagation speed is more important than the compression waves propagation speed. The attenuation of shock waves can be obtained when the release waves overtake the compression wave front.

The attenuation will be all the more important since the release waves propagation speed will be high in front of the compression waves propagation velocity. This is the interest of attenuation of shock waves by compaction : if the used material is compressible, its Hugoniot curve presents a steep concavity (figure 1) and then the gap between the compression and release waves propagation velocities is important. In fact, the propagation velocity of a compression wave is given [1] by the degree of slope of the Rayleigh line, (OB) segment which links the initial

state of the sollicitated material with its mechanical state behind the wave front. The release waves propagation speed is given by the slope of isentropic curves (C)(C').



On figure 1 the Hugoniot curve of a compressible material is presented in green lines. This curve tends, when the compressive stress has high values, towards an asymptotic Hugoniot curve (presented in red line). It is convenient to see that, for the corresponding material, the release waves propagation speed has the same order of magnitude that the one of the compressible material, while the compression waves propagation speed are by far higher. In the case of porous materials, the material of which the Hugoniot curve is the asymptotic curve constitutes the porous material ; it is named the constituent material.

If the compressible material has an elastic limit, it is interesting to remark that the evolution of the compressive stresses can be represented as figure 2 shows it. After a certain duration, only the elastic limit exists.

2.2 – Sufficient condition

Considering the last paragraph, we propose a sufficient condition which allows to classify a given material as an attenuating material :

Any material which is compressible and of which the Hugoniot curve tends toward the Hugoniot curve of a compact material, which has a less important concavity, can be called attenuating material.

Then, the efficiency of an attenuating material will be given by the wide of the area defined between the Hugoniot curve of the attenuating material and this one of the compact material. In the case of the representation of its constitutive behaviour in a (σ, ϵ) plane, its efficiency will be given by the deformation energy which it is able to store.

2.3 – Different kinds of attenuating materials

With this sufficient condition, several materials can be considered as attenuating materials. It is possible to classify them according to :

- “structural” materials : as honeycombs (the patented structures of [3] are a kind of honeycomb), sectional steel or aluminium alloys, hollow balls assemblies (these kinds of structures is the subject of a PHD thesis at CTA, [4]), etc ...
- porous materials : woods, glasses [5], expanded glasses, some polymeric materials, foams (polymeric foams, metallic foams), porous rocks, etc ...

Among these materials, results of mechanic characterisations can be found in open publications. Figure 3 presents the constitutive behaviour of two “high density” honeycombs, and several expanded concretes (tested at CTA). These materials are submitted to confined compression loadings. These “high density” honeycombs are obtained by welded plane and corrugated sheets, their densities are respectively 800 and 2900 kg.m^{-3} .

Generally, under compression loadings, these materials present an elastic field without permanent strains), a compaction phase (for which the stresses have a same order of magnitude), a densification phase (while the stresses increase rapidly compared with a little variation of volume).

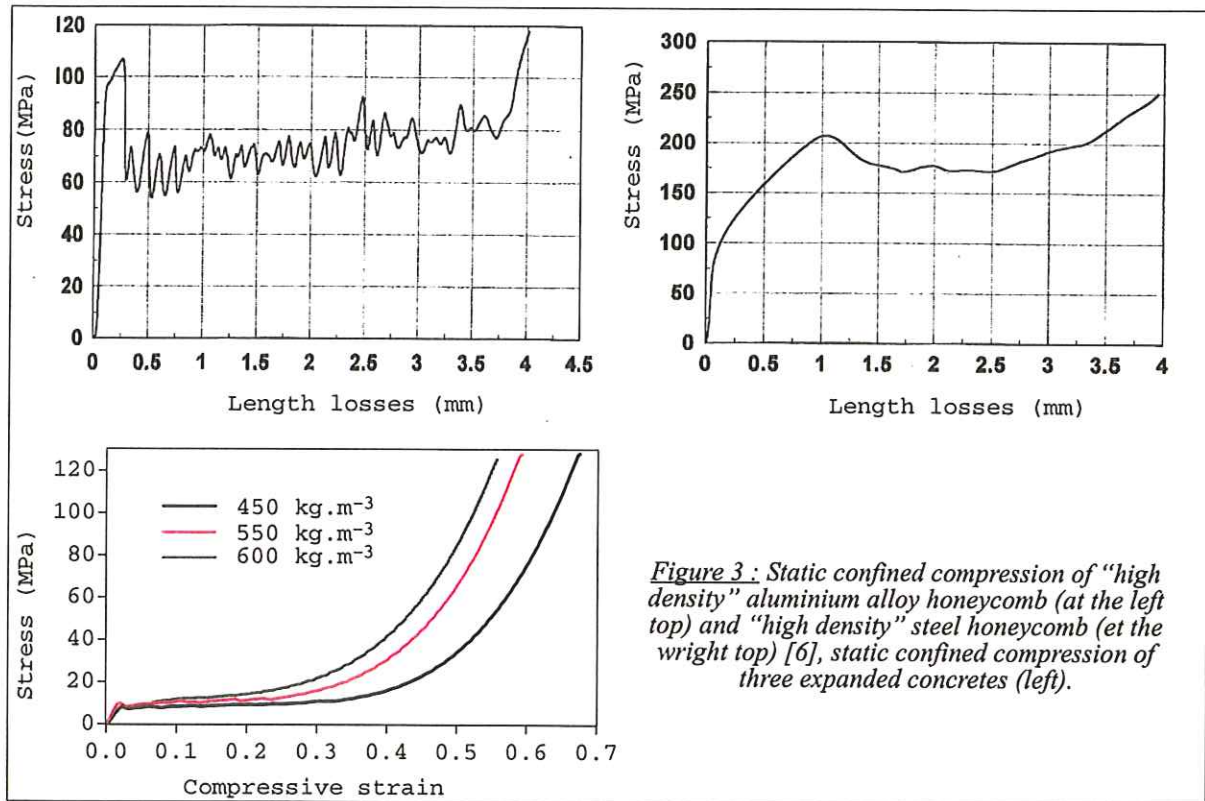


Figure 3 : Static confined compression of "high density" aluminium alloy honeycomb (at the left top) and "high density" steel honeycomb (et the wright top) [6], static confined compression of three expanded concretes (left).

3 – TEST CHARACTERISATIONS

We use two kinds of tests in order to identify the attenuating characteristics of materials.

The first kind concerns tests performed with hydraulic machine apparatus and/or split-Hopkinson bars apparatus. These tests give information about macroscopic constitutive behaviour of these materials under confined or free compression loadings, and about the possible effects of strain rates (for example, studies on hollow balls assemblies [7], or on expanded glasses [8]). Plate impact tests allow to know the Hugoniot curve of the studied material.

The second kind refers to ballistic tests. In these tests, the studied materials are in conditions of use. These tests can be instrumented in order to compare test results with simulations performed with the constitutive behaviour identified with the first kind of tests.

4 – NUMERIC APPROACHES

The aim is to describe and modelize the constitutive behaviour of attenuating structural solutions or concepts. In this part, we choose a unidimensionnal approach (we suppose that the compaction wave is plane).

4.1 – "Equation of state" approaches

These approaches are based on the Hugoniot theory : it assumed that an equation of state exists. This equation of state characterizes the loaded material and linked the specific internal energy with the applied hydrostatic pressure and the specific volume. Then, the main difficulty rests in the correct description of release waves, which governs the interest of a material in attenuating compression waves.

In this way, the Hermann approach [9] allows the description of porous materials constitutive behaviour : an internal variable describes the compaction ratio of the material in

which a compression wave goes through. The main difficulty rests here in the description of the evolution of this internal variable, during the loading. This approach has been the subject of studies at the Laboratoire de Combustion et de Détonique de l'ENSMA (Poitiers), [5] [10].

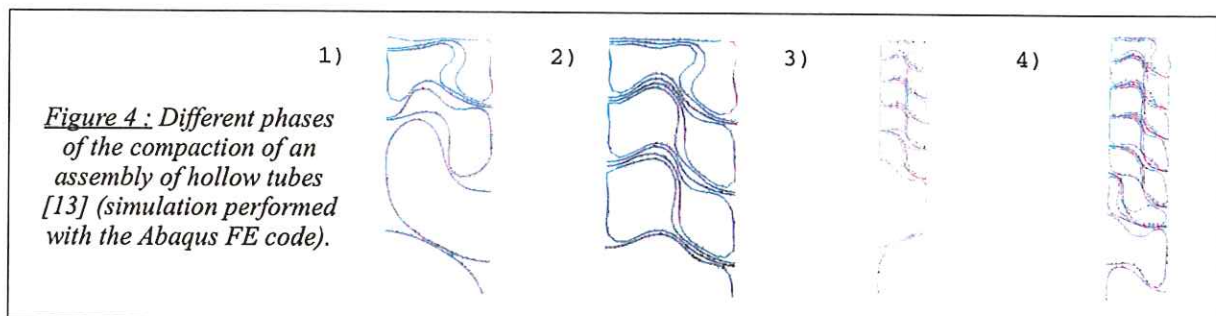
4.2 – Local approaches

In a same way, a constitutive relationship between stresses and strains can be written in using internal variables. In this case, the positivity of dissipation must be ensured. This approach is necessary if the use of an Lagrangian EF code is requisite (these codes are conventionally used by manufacturers). But, it does not exist, at the present time, some constitutive relationship or constitutive law in order to succeed in performing simulations with these codes. Then, there is a large field of open researches and studies in this way.

Two kinds of internal variables must be taken into account : it is important to describe the evolution of the compaction of the studied material and the evolution of its stiffnesses which increase because of the disappearing of voids. The need of the description of these two phenomena has been shown in studies at CTA [11].

4.3 – Macroscopic approaches

These approaches suit for all periodic structures and take place at the scale of the elementary mesh. They allow a good understanding of the compaction mechanisms of the periodic structure, and, if necessary, allow the optimisation of structural parameters in order to obtain the greater characteristics of shock attenuation. Such approaches have been used from about twenty years to a better understanding of buckling mechanisms of sectional steels or aluminium alloys and of honeycombs [12]. Such an approach is at the present time done at CTA, beyond the scope of a PHD thesis (figure n°4).



4.4 – Analytic approaches

Analytical approaches have already been used in order to describe the compaction of porous materials loaded by a compression wave. The reference [14] gives a good example of an analytical approach to describe the compaction of wood. In this way, we have developed three analytical approaches [7] [11]. The aim is to built an help for design and for the choice of attenuating solutions. We do the following assumptions :

- **H1** – it is a **unidirectional** approach, strains are **uniaxial**,
- **H2** – the constitutive behaviour of the **compacted** attenuating material looks like the constitutive behaviour of the snow in front of the ploughshare of a snowplough : the compacted attenuating material has a **homogeneous velocity**,
- **H3** – the other materials (different of attenuating materials) are considered as dimensionally stable,
- **H4** – about the constitutive relationship of the attenuating materials, we do three different assumptions :
 - H4.1** – its internal energy is evaluated from the Hugoniot equations [15],
 - H4.2** – its constitutive behaviour is rigid perfectly plastic,
 - H4.3** – its constitutive behaviour is rigid plastic.

4.4.1 – Impact of a plate projectile on a semi-infinite attenuating material

With these assumptions, on both sides of the compaction wave front, the energy balance and the momentum balance are written in order to obtain the loss of projectile speed versus time.

In the case of **H4.1** and **H4.2** assumptions, we obtain the analytic formulation of plate projectile velocity versus time [11] (x is the projectile position, μ and V_0 are its surface density and initial velocity respectively, ρ_0 and ρ_c are the surface density of the attenuating material and of the compacted attenuating material respectively, σ_0 is the compaction limit specific stress) :

H4.1 :
$$V = \dot{x} = \frac{V_0 \sqrt{\mu}}{\sqrt{\mu + 2 \rho_0 x}}$$

H4.2 :
$$V = \dot{x} = \sqrt{\frac{V_0^2 - Bx}{1 + Ax}} ; \text{ where } = \frac{\alpha \rho_0}{\mu (\alpha - 1)} , B = 2 A \sigma_0 \ln(\alpha) \text{ and } \alpha = \frac{\rho_c}{\rho_0}$$

In the case **H4.3**, a numeric integration is needed [11] : at time t , the specific stress behind the compaction wave front is the solution of the nonlinear equation $A(y) = B(y)$, in which the functions A and B are defined as (g is the compaction function : the evolution of specific stresses versus strain ; f is a function of $g(y)$ and y) :

$$\begin{cases} A(y) = (\mu + m_t)[g(y) - \rho_0] + 2 \rho_0 \left(E_{dt} - \frac{1}{2} \mu V_0^2 \right) \\ B(y) = - dt g(y) \sqrt{\frac{\rho_0 y}{g(y) - \rho_0}} [y[g(y) - \rho_0] + 2 \rho_0 f(y)] \end{cases}$$

dt , m_t and E_{dt} are the time increment, the compacted mass and the stored energy at time t .

Figure 5 presents a comparison between the results obtained with these three configurations, against a result obtained with the EF code Abaqus. It is shown that the **H4.1** is by far different. Figure 6 compares experimental results (it is a conventional aluminium alloy honeycomb impacted by a plane projectile) with the corresponding simulations (assumptions **H4.2**) : good results are obtained.

4.4.2 – *Impact of a projectile on an attenuating material laid on a free structural plate*

Two cases are possible : either the elastic forerunner is not negligible, then it must be taken into account two compaction wave fronts ; or it is, then a single wave front exists. We consider here the second case because we wanted little cpu times. In this way, the algorithm which we have written considers, with the latter assumptions on both sides of the compaction wave front, the energy balance and the momentum balance in order to obtain the loss of projectile velocity and the move of the free structural plate versus time. We have named this algorithm "Matamor".

Because we did not own high speed experimental data in order to validate this approach, we have performed numerical simulations with the EF explicit code Abaqus. Figure 7 and figure 8 present respectively the loss of projectile velocity (an 5 mm steel plate thick, with an initial velocity of 600 m.s⁻¹), the motion of the structural rear plate, and the applied stress obtained on this latter. There is a good comparison between the analytical and the EF code results. But the cpu time is very different : forty seconds with Matamor, two hours with the EF code Abaqus.

With this algorithm, we can obtain the loading on the rear structural plate, the duration of the interaction, and the acceleration of the rear structural plate. These results are interesting considering the main finalities proposed in introduction.

5 – CONCLUSION AND PROSPECTS

In first part, we have shown the interest of compressible materials in order to attenuate the effects of a compression wave. We have proposed a sufficient condition to define an attenuating material. In a second part, we have presented different approaches which allow to describe the compaction of an attenuating material, and then, to describe the attenuation of a compression wave. At last, we present analytical modelisations performed at CTA. With the analytical simulations of a fixed configuration (a projectile plate impacting a free structural plate which is protected by an attenuating material), we can obtain good results with very low cpu times on conventional computer.

The ongoing studies are the carrying out of high velocities experimental data. Then, we will compare them with Matamor simulations results. These analytical simulations can be incorporated into a larger algorithm allowing helps to design and choice attenuating technological solutions or concepts.

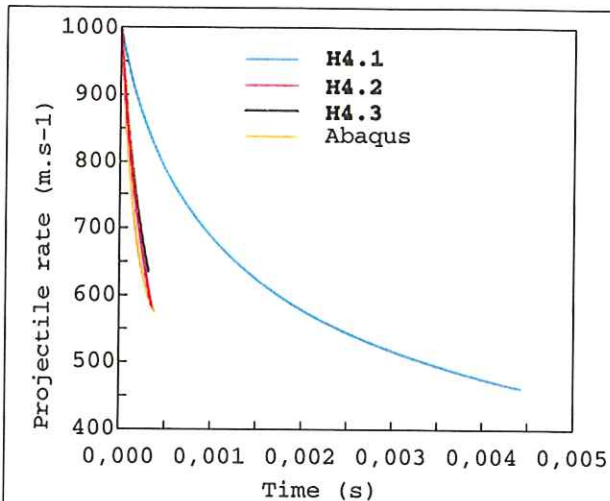


Figure 5 : Comparison of the three assumptions H4 with a EF code (Abaqus).

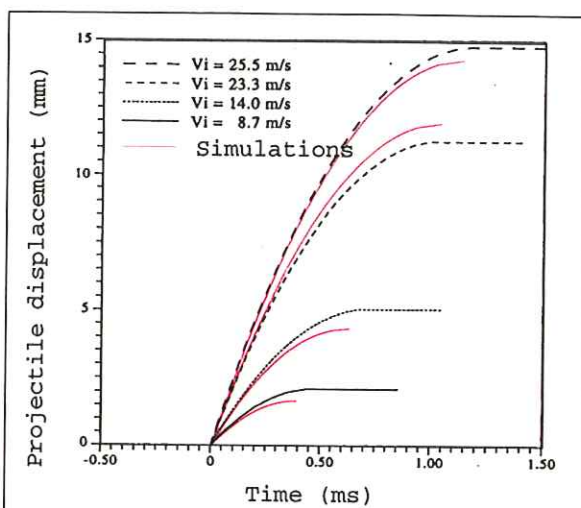


Figure 6 : Compaction of a honeycomb ; experimental data from [16].

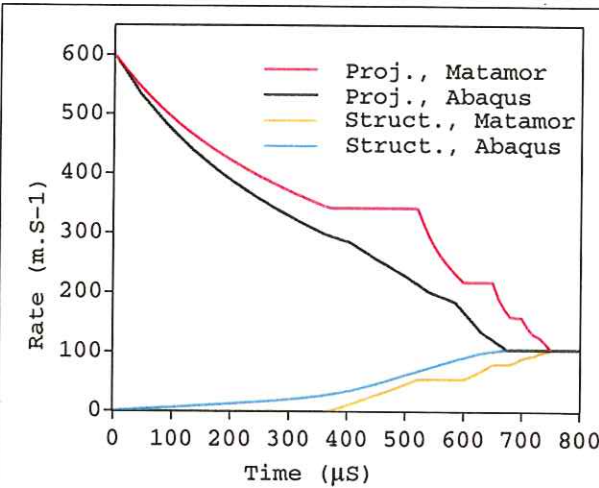


Figure 7 : Time evolution of projectile and structure velocities ; comparison Matamor - Abaqus [11]

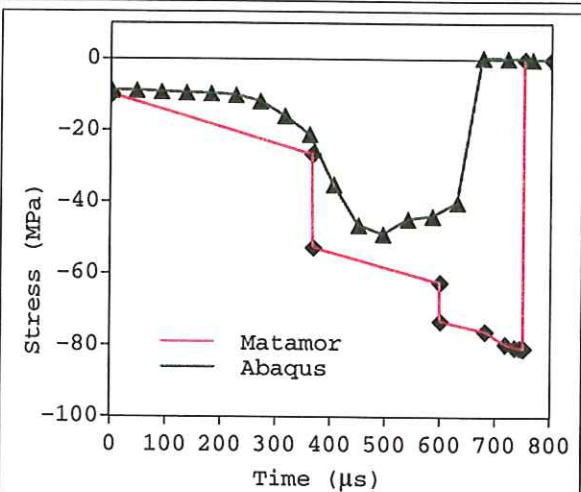


Figure 8 : Time evolution of stress on the structure plate [11].

REFERENCES

- [1] M. Defourneaux, "Théorie et mesure des ondes de choc dans les solides", cours polycopié de l'ENSTA.
- [2] M. Samirant, rapport ISL CO 32/74.
- [3] J. Lecaroz, brevet n° WO 87/01789, déposé le 26 mars 1987.
- [4] C. Seymarc, C. Kammerer, J.J. Marigo, SF2M, Journées d'automne, 27-29 oct. 1998.
- [5] T. de Rességuier & al., DYMAT Journal, 1, n°1, march 1994, pp. 31-46.
- [6] W.E. Baker & al., *Int. J. of Impact Engng.*, 21, n°3, pp. 149-163, 1998.
- [7] A. Meunier, rapport CREA 97 R 053, Juillet 1997.
- [8] N. Debrie, PV/CTA n°23/98, "Caractérisation mécanique de verres expansés", juin 1998.
- [9] W. Hermann, *Journal of applied physics*, 40, pp. 2490-2499, n°6, mai 1969.
- [10] D. Zagouri, *J. Phys. IV*, colloque C3, suppl. au *J. de Phys. III*, 1, p. 495, octobre 1991.
- [11] C. Kammerer, rapport CTA 98 R 056 (à paraître).
- [12] N. Jones, "Structural impact", Cambridge University Press, 1986.
- [13] R. Descamps, rapport CREA 97 R 077, Janvier 1998.
- [14] S.R. Reid & C. Peng, *Int. J. of Impact Engng.*, 19, n°5-6, pp. 398-405, 1997.
- [15] J.H. Prindle, the Boeing Co. Report, n°D2-84109-1, 1965.
- [16] E. Wu, W.S. Jiang, *Int. J. of Impact Engng.*, 19, n°5-6, pp. 439-456, 1997.

A viscoplastic modeling of sheet metal in the range of large deformation at low and high strain rates in double shear

A. RUSINEK, J.R KLEPACZKO

Laboratory of Physics and Mechanics of Materials, University of Metz, France, rusinek@lpmm.univ-metz.fr , klepaczko@lpmm.univ-metz.fr

INTRODUCTION

Sheet metal is a primary material used in construction of different component of cars, coaches and other vehicles. Because of probability of collisions, much effort has been recently put to evaluate the crashworthiness by computer simulations. In order to provide experimental data to the industries interested in crashworthiness, special experimental techniques have been recently developed in LPMM-Metz. This method is a combination of two experimental technique that permits to get strain rate varying from 10^{-4} to 10^4 s^{-1} . The first technique use a fast hydraulic machine and the second more original is based on the elastic wave propagation. This last, use the direct impact which reduce the time of rise considerably and permit to obtain high strain rate. The shear scheme of deformation is advantageous in comparison to tensile tests since in shear relatively large deformations can be reached, of the order of 1.0 (that is 100 %) that corresponds to an equivalent strain in traction of 57 %. These two techniques give us various results as the history of loading $\tau(t)$, the history of the strain $\Gamma(t)$

and the history of the strain rate $\dot{\Gamma}(t)$. The experimental data obtained from the shear tests have provided a clear picture of rate sensitivities for some industrial sheet metals. A relatively simple constitutive relation have been proposed which takes into account strain hardening, rate sensitivity and thermal coupling. A general scheme for the identification of parameters is proposed in [2]. The implantation of this constitutive relation will permit to simulate operations and processes appropriate in complex shape as the perforation or the embossing of sheet metal.

I-EXPERIMENTAL TECHNIQUE

The scheme of double shear offers two important advantages in comparison to tensile test. The first one is a possibility to read relatively large deformations which are not accessible in the case of tension test, because of striction. Another advantage is that a wide range of strain rates can be reeached without difficulty, up to 10^4 s^{-1} for the scheme of direct impact. The experimental data gathered could be used in variety of engineering applications, like perforation, dynamic buckling or adiabatic shearing.

This contribution reports on two experimental procedures established in LPMM-Metz which can provide reliable data for sheet materials. The first procedure is based on use of an universal fast hydraulic machine equipped with a special device for double-shear testing. The scheme of this test is show in Fig.1. The range of strain rates accessible for this scheme of loading is from 10^{-4} s^{-1} to 10^2 s^{-1} . The second procedure based on the the concept of direct impact, [1], is shown in Fig. 3. The types of signal are shown in Fig. 2 and 4 respectively. The range of strain rates for this experimental setup is from 10^2 s^{-1} to 10^4 s^{-1} . The same specimen geometry is used in both cases, Fig.5. This experimental setup is composed with the gas launcher, Hopkinson tube, [1], and non-contact, displacement transducer. The double shear specimen is attached to the Hopkinson tube and its central part is loaded by a flat-ended projectile (punch in quasi-static scheme) launched from the gas gun. The impact velocity $V_0 \approx 30 \text{ m/s}$ gives the strain rate $\approx 10^4 \text{ s}^{-1}$ with the shear zone 3 mm. The scheme of electronic measurements developed in LPMM-Metz and a complete theory of this test is given elsewhere, [1]. Measurements of the impact velocity V_0 , displacement of central part of the specimen $U_A(t)$ and the transmitted wave $\epsilon_T(t)$ in the Hopkinson tube permits for obtaining the $\tau(\Gamma)$ at different strain rates, τ is the shear stress and Γ is the shear strain.

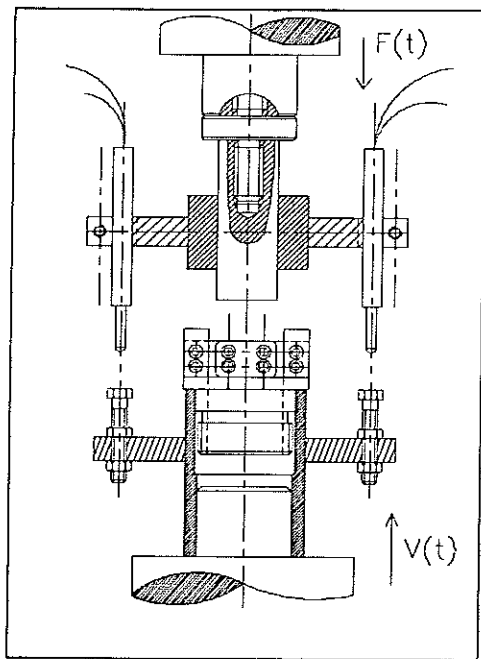


Fig. 1 : Quasi-static loading

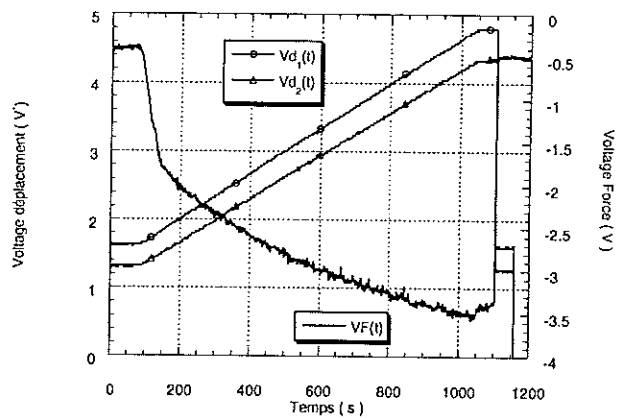


Fig.2 : Type of signals

This results, permits to obtain the variation of the stress with the strain and the strain rate at constant temperature. The strain and the stress are obtained by following relations. Thus, the displacement of the central part of the specimen is :

$$U_{\text{sch}}(t) = \frac{\delta_1(t) + \delta_2(t)}{2} \quad (1)$$

and the shear strain is

$$\Gamma(t) = \frac{U_{\text{sch}}(t)}{h} \quad (2)$$

The shear stress is the force divided by the two cross sections which are deformed during the test.

$$\tau(t) = \frac{F(t)}{2A_s} \quad (3)$$

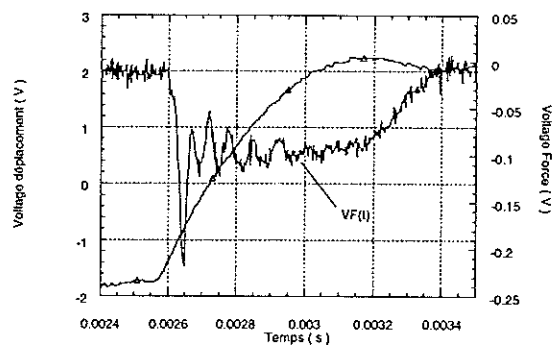
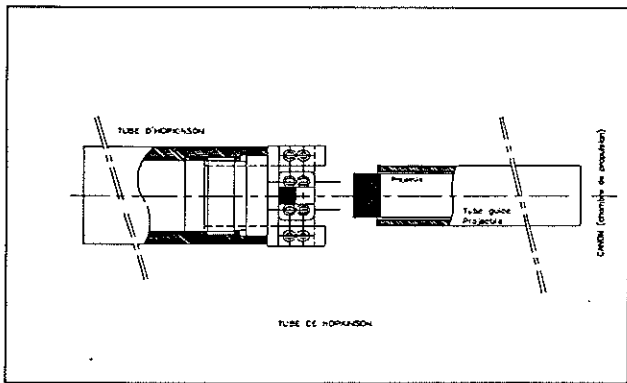


Fig. 3 : Experimental technique in impact loading Fig.4 : Typical signals from impact tests

The geometry of the specimen used in double shear has the following form with thickness of 0.8 mm.

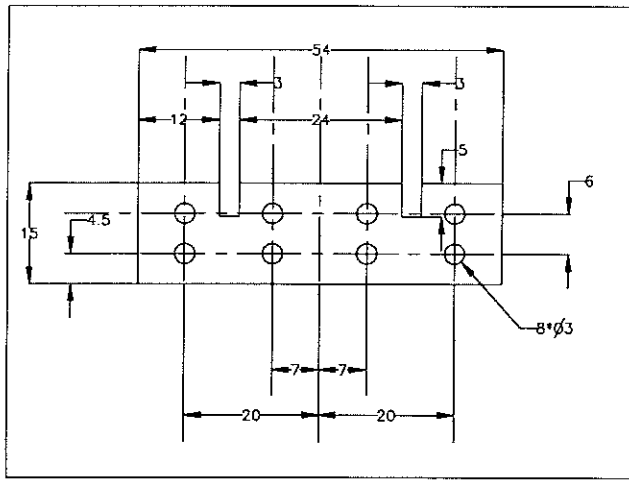


Fig. 5 : Geometry of specimen

In impact loading, the strain and the stress are functions of the amplitude of the transmitted wave ϵ_T with the formulas.

$$\Gamma(t) = \frac{1}{h} \left[U_{ext}(t) - C_0 \int_0^1 \epsilon_T(\zeta) d\zeta \right] \quad (4)$$

C_0 is the elastic wave speed and h the width of the shear zone

$$\tau(t) = \frac{E_{ub} A_{ub}}{2A_s} \varepsilon_\tau(t) \quad (5)$$

II-VISCOPLASTIC MODELING

At present the industry needs a more sophisticated viscoplastic models coupled with temperature, which could be used in numerical codes. Relatively high strain rates and large strains must be covered. A relatively simple constitutive relations have been developed in LPMM-Metz which could be implemented in computer codes, [2]. The relation is based on the Mechanical Equation of state of the form $\tau, \Gamma, \dot{\Gamma}, T=0$, where $\dot{\Gamma}$ and T are respectively the plastic strain rate and absolute temperature. The relations are based on the notion of two components of flow stress τ_μ and τ^* ; where τ_μ is the internal stress and τ^* is the effective stress, thus :

$$\tau = \frac{\mu(T)}{\mu_0} \left[\tau_\mu(\Gamma, \dot{\Gamma}, T) + \tau^*(\dot{\Gamma}, T) \right] \quad (6)$$

The expression of the shear modulus is

$$\frac{\mu(T)}{\mu_0} = 1 - \frac{T}{T_m} \exp\left(\theta^* \left(1 - \frac{T_m}{T}\right)\right) \quad (7)$$

And the expressions of the internal and effective stress are

$$\tau_\mu(\Gamma, \dot{\Gamma}, T) = B(\dot{\Gamma}, T) (\Gamma_0 + \Gamma)^{n(\dot{\Gamma}, T)} \quad (8)$$

$$\tau^*(\dot{\Gamma}, T) = \tau_0^* \left(1 - D_1 \frac{T}{T_m} \log \frac{\Gamma^{\max}}{\dot{\Gamma}} \right)^m \quad (9)$$

where $B(\dot{\Gamma}, T)$ is the plasticity modulus, $n(\dot{\Gamma}, T)$ is the rate and temperature dependent strain hardening exponent, τ_0^* is the effective stress at 0 K, m is the strain rate sensitivity and T_m is the melting temperature. The total number of constants (not shown here) is eight, [2].

To analyze the transition isothermal-adiabatic, the heat equation (10) is used together with other equations.

$$\Delta T = \frac{\beta}{\rho C_v} \int_0^r \tau d\xi \quad (10)$$

III-COMPARISON OF EXPERIMENT AND MODELING FOR DOUBLE SHEAR

To evaluate the qualitative description of this constitutive relation, a comparison was made for four strain rates varying from 10^{-4} to 10^{-3} s $^{-1}$ and from 10^2 to 10^3 . A complete characterization is given in [2].

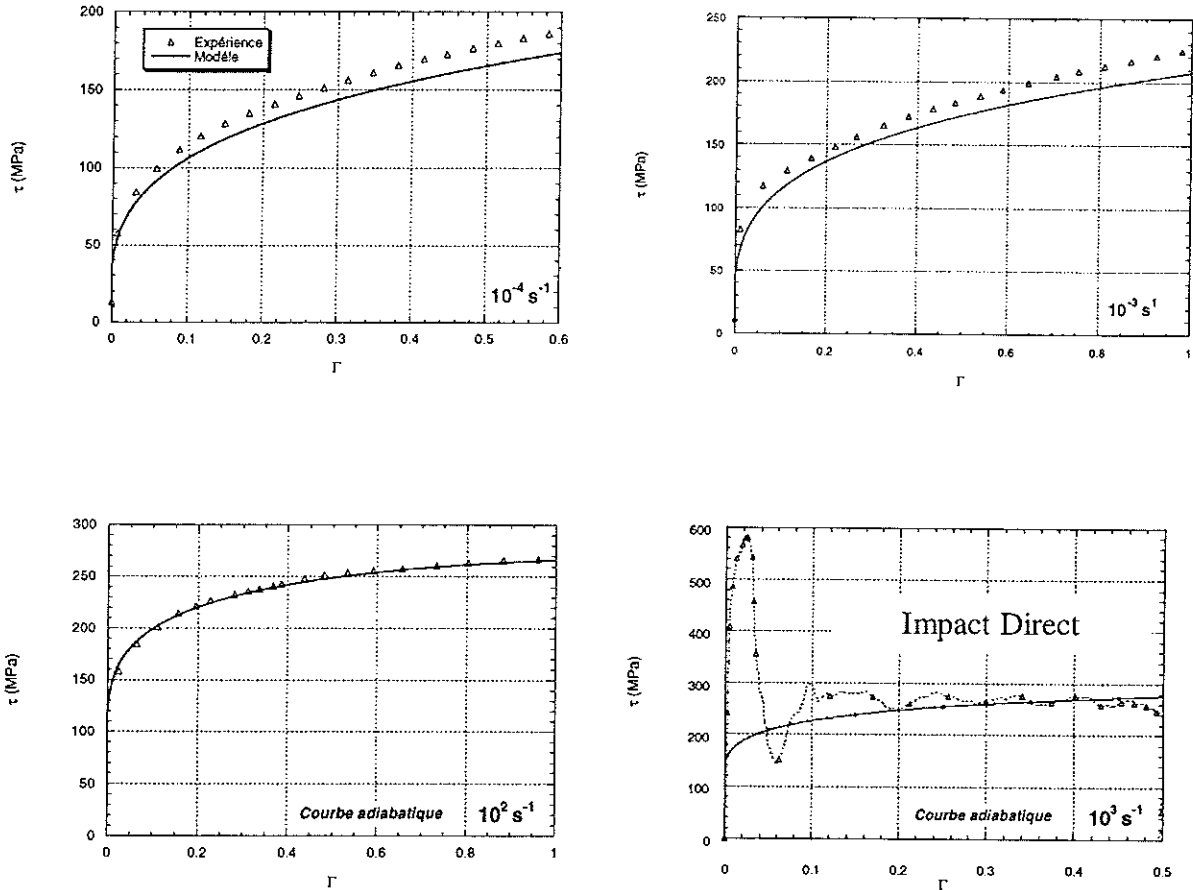


Fig. 6 : Comparison of experiment and modeling

IV- APPLICATION TO PERFORATION

The tensile tests were performed for three directions with respect to the rolling, they have shown almost ideal isotropy of this material. Thus, additional test were made in perforation. A modeling has been proposed using the FE code ABAQUS Standard. Two types of calculations were made. The first is with $\mu \neq 0$ and the second is $\mu \cong 0$, where μ is the friction coefficient (Coulomb). The Coulomb model assumes that no relative motion between two surfaces occurs if the equivalent frictional stress is less than the critical stress which is proportional to the contact pressure p , [3].

$$\tau_{crit} = \mu p \quad (11)$$

In addition, two types of experiments have been performed with a hemispherical punch, with normal and reduced friction. In order to reduce friction the lubrication film of teflon and grease MoS2 are used. The results obtained are shown in Fig. 7.

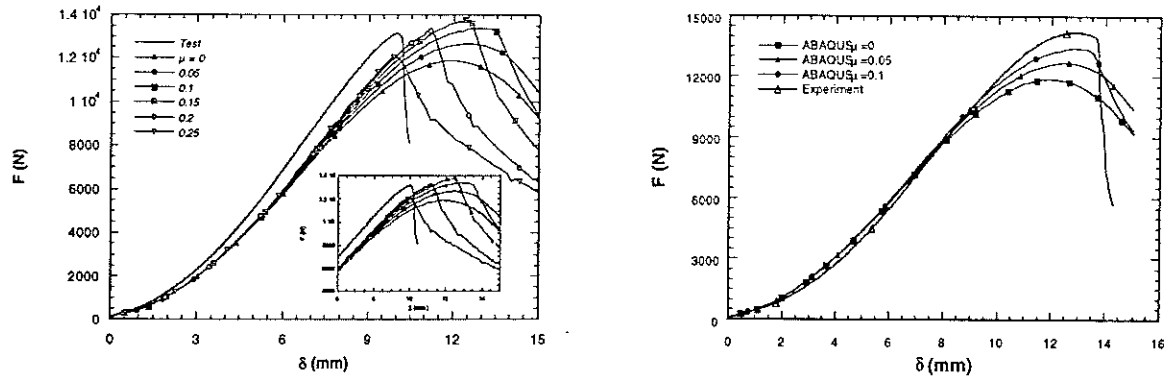


Fig. 7 : Results of punch tests, experiments and FE analysis for different μ .

The constitutive relation developed based on the double shear test (which is one-dimensional) permits to describe correctly the behavior during perforation.

CONCLUSION

The experimental techniques discussed here permit to cover a large spectrum of strain rate in the range of the large strains. Moreover, this constitutive relation gives a good agreement between double shear test and in perforation. This simple model has been equally used in [4] to describe the behavior of a harder alloy like VAR 4340 steel for strain rates up to 7.10^4 s^{-1} .

References

- [1] J.R Klepaczko (1994). *An experimental technique for shear testing at high strain rates. The cas of mild steel, Int. J. Impact Engng.*, **15**, 25-39
- [2] A. Rusinek and J.R Klepaczko (Mars 1998). *Etude expérimentale du double cisaillement des tôles, modélisation de l'écoulement viscoplastique, Rapport interne au LPMM*, 1-27
- [3] ABAQUS Theory Manuel, HKS Inc. Providence, RI (1997)
- [4] J.R Klepaczko, M. Klosak & T. Lodygowski (1998). *Numerical study of inelastic wave propagation and rupture modes in dynamic shearing*, Solmec'98 Poland, 197-198